CENPA

Center for Experimental Nuclear Physics and Astrophysics

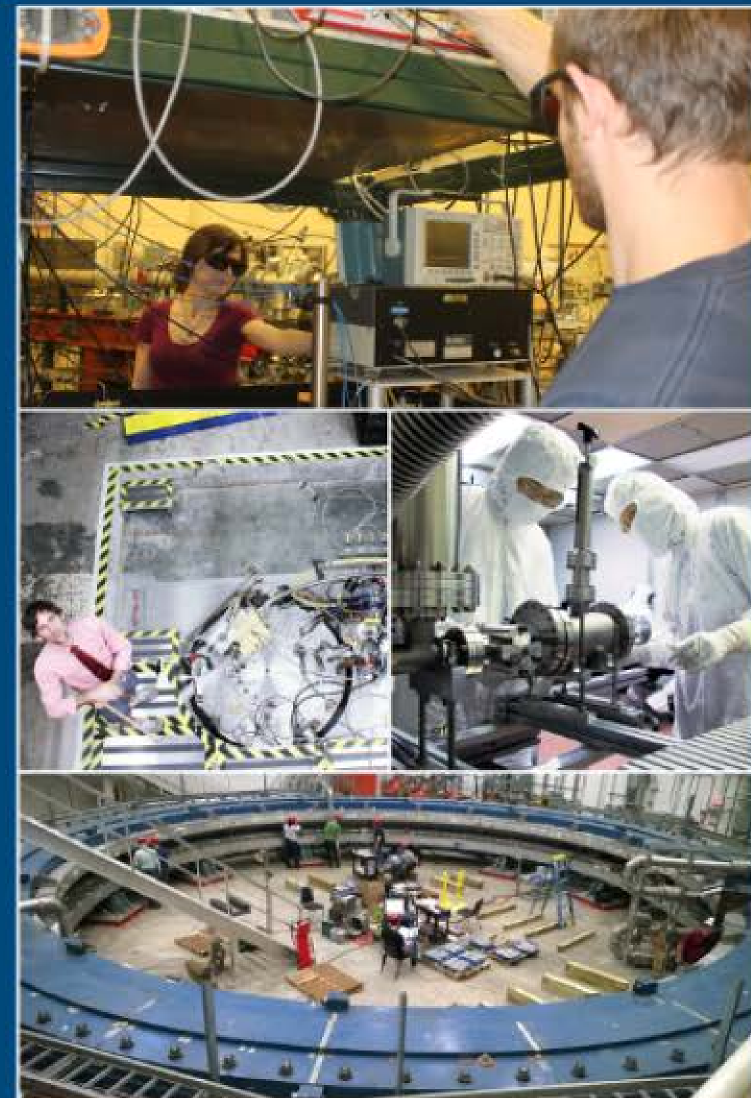

Annual Report 2016

University of Washington

ANNUAL REPORT

Center for Experimental Nuclear Physics and Astrophysics
University of Washington
April, 2016

Sponsored in part by the United States Department of Energy
under Grant #DE-FG02-97ER41020.

Cover design by Gary Holman. In the top photo, Graduate student Yelena Bagdasarova and postdoc Arnaud Leredde working near the laser setup for the ^{6}He experiment (Sec. 3.1) (photo by Amber Cortes). The middle left photo, James V Sloan gestures toward the approximately 8 Tesla main magnet of ADMX which provides virtual photons for the reverse Primakoff process by which axions convert into photons within the experiment's cavity (Sec. 5.1) (photo by Amber Cortes). In the middle right photo, Ying-Ting Lin (L) and Laura Bodine (R) work on the TRIMS vacuum system (Sec. 1.8) (photo by Diana Parno). In the bottom photo, The Muon $g-2$ storage ring at Fermilab is being readied for mapping its magnetic field after pole alignment (Sec. 4.1) (photo by Erik Swanson). The background design on the back cover is a rendering of the recognizable bench and Acer palmatum (Japanese Maple) tree on the front lawn at CENPA.

INTRODUCTION

The Center for Experimental Nuclear Physics and Astrophysics, CENPA, was established in 1998 at the University of Washington as the institutional home for a broad program of research in nuclear physics and related fields. Research activities are conducted locally and at remote sites. The research program emphasis is fundamental symmetries and neutrinos. In neutrino physics, CENPA is the lead US institution in the KATRIN tritium beta decay experiment, the site for experimental work on Project 8, and a collaborating institution in the MAJORANA ^{76}Ge double beta decay experiment. The Muon Physics group has developed the MuSun experiment to measure muon capture in deuterium at the Paul Scherrer Institute in Switzerland. The group has a leadership role in the new project to measure the anomalous magnetic moment of the muon at Fermilab to even higher precision than it is presently known from the collaboration's previous work at Brookhaven. The fundamental symmetries program also includes "in-house" research on the search for a static electric dipole moment in ^{199}Hg, and an experiment using the local tandem Van de Graaff accelerator to measure the electron-neutrino correlation and Fierz interference in ^{6}He decay.

In addition to the research directly supported by DOE's Office of Nuclear Physics through the CENPA core grant, other important programs are located in CENPA, forming a broader intellectual center with valuable synergies. The 'Gravity' group, as it is known, carries out with both DOE and NSF support studies of the weak and strong Equivalence Principles, fundamental precepts of General Relativity, as well as searches for non-Newtonian weak forces such as are predicted by theories with extra dimensions. In addition, they participate in LIGO. The DOE Office of High Energy Physics supports a unique experiment, the ADMX axion search. An unusual spin-off from basic nuclear physics is our program on nanopore sequencing, supported by NIH.

This past year has certainly been a banner year in accomplishment and recognition. Both the 2015 Breakthrough Prize in Fundamental Physics and the 2015 Nobel Prize in Physics recognized achievements in neutrino physics in which CENPA physicists played a strong role. The leader of the Sudbury Neutrino Observatory (SNO) collaboration, Art McDonald, accepted the Nobel in Stockholm in December. He shared the prize with Takaaki Kajita, who led the Super-Kamiokande project. The Breakthrough Prize recognized SNO, Super-Kamiokande, KamLAND, Daya Bay, K2K, and T2K. In this case, individual collaboration members are recognized and directly receive a share of the prize. CENPA physicists Jason Detwiler and Nikolai Tolich were in fact members of two of the collaborations honored, SNO and KamLAND. Other recipients included John Amsbaugh (SNO), Tom Burritt (SNO), Peter Doe (SNO), Sanshiro Enomoto (KamLAND), Greg Harper (SNO), Hamish Robertson (SNO), and Tim Van Wechel (SNO), as well as a large number of former members of CENPA.

Graduate student and NSF Fellow Julieta Gruszko was selected to attend the 66th Lindau Nobel Laureate meeting. Julieta was also honored with a departmental Mentoring Award.

Graduate student Aaron Fienberg won a Department of Energy Office of Science Graduate Student Research Award, to further his work in the Muon g-2 program at Fermilab. Our muon team continues to be highly regarded at Fermilab, as several students received travel grants and Senior Research Scientist Erik Swanson was named Run Coordinator for the magnet-shimming phase.

Electronics Technician David Peterson won a 2016 University of Washington Distinguished Staff Award for his work at CENPA.

The Project 8 demonstration of free cyclotron radiation from single electrons was selected by Physics World as one of the top 10 physics results of 2015.

Gray Rybka accepted a tenure-track Assistant Professorship in the Physics Department and continues his research on ADMX and Project 8. Postdoctoral Fellows Krishna Venkateswara and Martin Fertl have been appointed to the rank of Acting Assistant Professor. Martin devotes his efforts to Project 8 and the Muon g-2 project and Krishna is in the Gravity group.

Seven students successfully defended their PhD theses, Jared Kofron and Dmitry Lyapustin in March (as was mentioned in the 2015 report), Will Terrano in April, Charles Hagedorn in May, David Zumwalt in June, Laura Bodine in August, and Ran Hong in January 2016. Will Terrano received the departmental Henderson Prize for his PhD thesis. We congratulate them all.

Nomie Torres, our Fiscal Specialist, departed in May, and Ida Boeckstiegel joined us in the front office with Administrator Victoria Clarkson in February 2016. Seth Kimes, Research Engineer, moved from Oregon to join Tom Burritt's team of engineers and instrument makers in August. Cliff Plesha, Research Engineer with ADMX, departed in February 2016, and he has been replaced by Nick Force.

Postdoctoral Fellow Frederik Wauters, who worked with Peter Kammel on the MuSun experiment in PSI and the He-6 experiment, and Matt Sternberg, who worked on Project 8 and the He-6 experiment, departed in September. Frederik is now Research Faculty at the University of Mainz, and Matt accepted a position in industry.

In March, 2015, Kim Siang Khaw arrived to join the Muon Group as a postdoc, as was mentioned in the 2015 report. Daniel Salvat from Indiana University joined us as a postdoc in July to work with Peter Kammel in the muon program, and Rakshya Khatiwada, also from Indiana, arrived also in July to work with the ADMX project.

The DOE Office of Nuclear Physics renewed our grant DE-FG02-97ER41020 for FY15-17. The continued support of CENPA by the Office of Nuclear Physics is greatly appreciated.

In the following we record some of the highlights of our past year in research.

- The tritium source and all components of the electron transport system have been delivered and installed at KIT. Commissioning continues apace. The goal is to be ready to accept tritium in early 2017, with the entire KATRIN apparatus working in unison.

- In preparation for the next commissioning phase, the detector system is undergoing upgrades and maintenance. A new, vacuum-compatible, wiring harness has been installed in the detector system. A cracked ceramic preamp card has been replaced and all 148 channels of the detector are fully functional. Installation of the new veto scintillator and readout electronics will begin in June 2016.

- The MAJORANA DEMONSTRATOR collaboration has successfully completed the first of the two modules of 35 Ge detectors, and operations have begun to study backgrounds. The second module is close to completion.

- Project 8 continues the development of the Cyclotron Radiation Emission Spectroscopy method (CRES) and has demonstrated that with tight cuts on pitch angle and radiated power, an energy resolution better than 2 eV can be achieved for 30-keV electrons. A new cell has been designed and constructed for the first tritium studies at small scale.

- A major hardware item for g-2 has been finished and delivered to FNAL for installation, the approximately 450 pulsed NMR probes for the stationary array and the trolley.

- The g-2 Storage Ring is in operation mode at full field. Our UW team is central to the shimming effort, having provided the new NMR probes, control electronics, data acquisition, and much of the analysis and predictive modeling software.

- UW is building the g-2 calorimeter system based on PbF_2 crystals with silicon photo-multiplier readout. All components have arrived and quality control tests are complete or are in progress. Installation at Fermilab begins in Fall 2016.

- With another excellent run at PSI, the MuSun experiment reached its required full statistics.

- The AlCap experiment at PSI had two successful runs in 2015. Pending further detailed analyses, the main objectives of this program have been achieved.

- With many improvements in the production of ^{6}He, the laser trapping efficiency, and detection stability, the ^{6}He experiment is now able to take data steadily at a rate allowing for a $\sim 1\%$ determination of little-a and associated calibrations in less than 3 days. The charge distribution of the Li ions has been measured and comparison to recent calculations shows interesting results that will soon be published.

- The Hg edm experiment completed the analysis of its most recent data set. A new upper limit on the edm of ^{199}Hg was found, 4 times more sensitive than previous work. This work, reported in Phys. Rev. Lett. **116**, 161601 (2016), sets the tightest limits on most sources of CP violation in the hadronic sector (NSF/DOE support).

- The LIGO Scientific Collaboration, of which UW is a part, has detected gravitational waves from a merging Black Hole binary system, proving the existence of such systems and enabling tests of strong-field General Relativity. The UW contribution to Advanced LIGO has been in characterizing charge and pressure noise on the LIGO test masses and in low-frequency seismic isolation using high-precision ground-rotation sensors (NSF support).

- The main construction of ADMX with its dilution refrigerator is now complete, and the collaboration is making the transition into commissioning. Data-taking is expected to start by the end of 2016 (DOE-HEP support).

As always, we encourage outside applications for the use of our facilities. As a convenient reference for potential users, the table on the following page lists the capabilities of our accelerators. For further information, please contact Diana Parno, Associate Director (dparno@uw.edu) or Eric Smith, Research Engineer (esmith66@u.washington.edu) CENPA, Box 354290, University of Washington, Seattle, WA 98195; (206) 543 4080. Further information is also available on our web page: `http://www.npl.washington.edu`.

We close this introduction with a reminder that the articles in this report describe work in progress and are not to be regarded as publications nor to be quoted without permission of the authors. In each article the names of the investigators are listed alphabetically, with the primary author underlined in the case of multiple authors, to whom inquiries should be addressed.

Hamish Robertson, Director
Gary Holman, Technical Editor

Diana Parno, Associate Director, Editor
Victoria Clarkson, Assistant Editor

TANDEM VAN DE GRAAFF ACCELERATOR

Our tandem accelerator facility is centered around a High Voltage Engineering Corporation Model FN purchased in 1966 with NSF funds, with operation funded primarily by the U.S. Department of Energy. See W. G. Weitkamp and F. H. Schmidt, "The University of Washington Three Stage Van de Graaff Accelerator," *Nucl. Instrum. Methods* **122**, 65 (1974). The tandem was adapted in 1996 to an (optional) terminal ion source and a non-inclined tube #3, which enables the accelerator to produce high intensity beams of hydrogen and helium isotopes at energies from 100 keV to 7.5 MeV.

Some Available Energy Analyzed Beams

Ion	Max. Current (particle μA)	Max. Energy (MeV)	Ion Source
^{1}H or ^{2}H	50	18	DEIS or 860
^{3}He or ^{4}He	2	27	Double Charge-Exchange Source
^{3}He or ^{4}He	30	7.5	Tandem Terminal Source
^{6}Li or ^{7}Li	1	36	860
^{11}B	5	54	860
^{12}C or ^{13}C	10	63	860
*^{14}N	1	63	DEIS or 860
^{16}O or ^{18}O	10	72	DEIS or 860
F	10	72	DEIS or 860
* Ca	0.5	99	860
Ni	0.2	99	860
I	0.001	108	860

*Negative ion is the hydride, dihydride, or trihydride.

Several additional ion species are available including the following: Mg, Al, Si, P, S, Cl, Fe, Cu, Ge, Se, Br and Ag. Less common isotopes are generated from enriched material. We recently have been producing the positive ion beams of the noble gases He, Ne, Ar, and Kr at ion source energies from 10 keV to 100 keV for implantation, in particular the rare isotopes ^{21}Ne and ^{36}Ar. We have also produced a separated beam of 15-MeV ^{8}B at 6 particles/second.

Contents

1 Neutrino Research

KATRIN

1.1 KATRIN status and plans

J. F. Amsbaugh, J. Barrett*, A. Beglarian†, T. Bergmann†, L. I. Bodine, T. H. Burritt, P. J. Doe, S. Enomoto, N. Fong, J. A. Formaggio*, F. M. Fränkle†, F. Harms†, L. Kippenbrock, A. Kopmann†, Y.-T. Lin, E. L. Martin, A. Müller†, N. S. Oblath*, D. S. Parno, D. A. Peterson, A. W. P. Poon‡, R. G. H. Robertson, A. Seher†, D. Tcherniakhovski†, T. D. Van Wechel, K. J. Wierman§, J. F. Wilkerson§, and S. Wüstling†

The KArlsruhe TRItium Neutrino experiment will make a direct, model-independent probe of the neutrino mass to an estimated sensitivity of 200 meV. The well-established experimental technique is to make a precision measurement of the electron energy spectra resulting from molecular tritium beta decay. A distortion at the end point of the beta spectrum may be attributed to the neutrino mass. Other interesting physics, such as the existence of sterile neutrinos, may also be addressed by precision measurements of the beta spectrum shape.

The apparatus, shown schematically in Fig. 1.1-1, consists of an intense (10^{11} Bq) windowless, gaseous tritium source. Beta electrons from this source are adiabatically conveyed to spectrometers by a transport system consisting of a train of superconducting magnets. The transport system is also responsible for preventing, by a factor of 10^{14} in partial-pressure reduction, tritium gas from contaminating the spectrometers. This is achieved by a series of turbo-molecular pumps (the Differential Pumping System) and a cold trap consisting of argon frost on the beam pipe walls, (the Cryogenic Pumping System). The electrons then enter the first of two retarding potential spectrometers, the prespectrometer, whose potential is set to reject all electrons typically more than 100 eV below the end point energy. The electrons then enter the main spectrometer, which has an energy resolution of 0.94 eV. Those electrons with sufficient energy to overcome the retarding potential of the main spectrometer are counted in the electron detector located at the exit of the main spectrometer. Operating the spectrometers at various retarding potentials provides the integrated energy spectrum. It is also possible to operate the spectrometers in a time-of-flight mode (TOF), which offers a differential spectrum mode with potential background rejection. This requires a single-electron detector located at the entrance of the spectrometer to provide a start signal for the time-of-flight measurement. Such a detector is under development.

With the delivery of the source to the Karlsruhe Institute of Technology in July 2015, all major components are in hand and commissioning of the source and transport system has begun. The commissioning of the prespectrometer, main spectrometer and detector

*Massachusetts Institute of Technology, Cambridge, MA.
†Karlsruhe Institute of Technology, Karlsruhe, Germany.
‡Lawrence Berkeley National Laboratory, Berkeley, CA.
§University of North Carolina, Chapel Hill, NC.

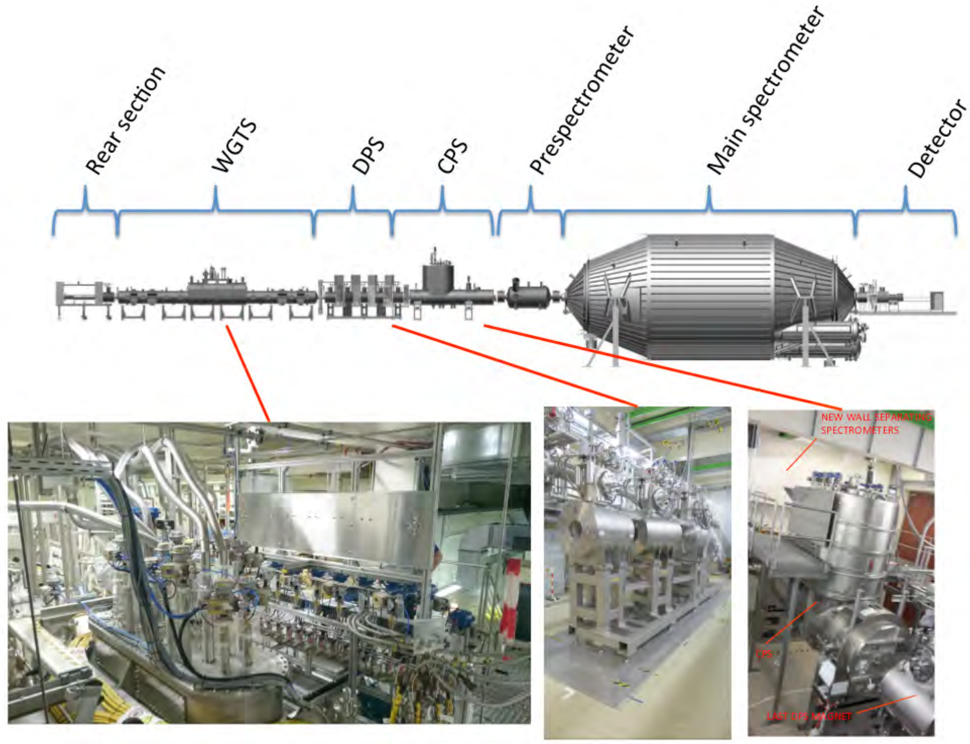

Figure 1.1-1. *Top:* The main components of the KATRIN experiment. *Bottom (left to right):* Shown are pictures of recently installed components, the Windowless Gaseous Tritium Source (WGTS) the Differential Pumping System (DPS) and the Cryogenic Pumping System (CPS).

has yielded a trove of information, aiding design refinement and furthering understanding of the performance parameters. A second commissioning phase of the main spectrometer was completed in August 2015, revealing an unexpected background attributed to the main spectrometer. Analysis of the commissioning data strongly suggests that the background is a result of radon deposited on the interior walls of the spectrometer. The dominant progeny in the decay chain is ^{210}Pb with a half-life of 22.6 years. The alpha decay of ^{210}Po, in the ^{210}Pb decay chain, creates Rydberg atoms (hydrogen dominates the 10^{-11} mbar pressure in the spectrometer). These highly excited, neutral atoms pervade the volume of the spectrometer and are ionized by the blackbody radiation, resulting in a background of electrons and positive ions.

In September 2016 a third spectrometer commissioning phase will begin, with the prespectrometer, for the first time, attached to the main spectrometer. In normal running, the spectrometers operate at different retarding potentials and therefore a Penning trap, a potential source of background, exists between the two spectrometers. The mechanism for clearing this trap will be tested along with further studies of backgrounds and their amelioration. The spectrometer commissioning will run 24/7 until October 2016. During this time the US institutes will undertake remote operation of the experiment. If successful this may become a standard mode of operation, both for further commissioning as well as normal tritium data taking. Safety considerations require that operation of the tritium components remain an on-site controlled activity.

By October 2016, installation and testing of the source and transport components will be complete and commissioning of the entire KATRIN apparatus can begin. Initially this will include alignment of the components using an electron gun located at the far end of the source. Once physically and magnetically aligned, a Kr source, with 17 and 30 keV lines will be used to ensure that the apparatus functions as expected and is ready to accept tritium. This is a critical milestone, since once exposed to tritium, further intervention into the hardware is non-trivial. The goal is to be ready to accept tritium in January 2017.

In addition to participating in the ongoing commissioning, the UW is also spearheading the establishment of data-quality controls and the investigation of ways of controlling backgrounds by developing a time-of-flight electron tagger. These activities are described below.

1.2 KATRIN data quality

S. Enomoto, L. Kippenbrock, and D. S. Parno

As KATRIN prepares for neutrino-mass data-taking (Sec. 1.1), we are working to develop an analysis framework that will allow us to rapidly move from raw data to physics results. In addition to data processing, calibration, comparison against Monte Carlo results, and allowance for a blind analysis protocol that has yet to be finalized, we must also ensure the quality of neutrino-mass data. The KATRIN database presently tracks information from some 6000 slow-controls channels; the installation (and integration) of subsystems is not yet complete, however, and the final number is expected to approach 10,000.

We are therefore coordinating with all subcomponent task groups in KATRIN to identify the limited subset of sensor readbacks with the most direct effect on the neutrino-mass measurement. To take a few straightforward examples, these include the status of a valve that blocks the beamline when closed; a status indicator showing whether a radioactive source has been inserted into the flux tube; and high-voltage readbacks from the main spectrometer. More complex monitoring indicators, including analyzed data indicating the ^{83m}Kr line position in a monitor-spectrometer measurement or magnetic-field reconstructions from multiple sensor readouts, must also be included. The analysis framework must ultimately incorporate all of these necessary quality checks with careful attention to synchronization: some data-quality parameter values can only be determined after monitoring periods of half an hour or longer. The necessary framework is currently under development.

Within this general framework, we are also responsible for determining exactly where data-quality cut thresholds should be set for the Focal-Plane Detector (FPD) system. To accomplish this, we are studying FPD-system slow controls data acquired during the extended commissioning period in 2015. In the process we have identified a persistent slow-controls readout error that affects two channels and must be addressed before the next commissioning period.

1.3 Molecular effects and the KATRIN experiment

L. I. Bodine and D. S. Parno

Our assessment[1] of the molecular final-state distribution (FSD) populated by T_2 beta decay, and its impact on neutrino-mass experiments with molecular tritium sources, identified several *experimental* sources of systematic uncertainty entering into the KATRIN error budget through their effects on the calculated FSD. The original monitoring and measurement plan for the operational parameters of the KATRIN windowless gaseous tritium source (WGTS) was focused on ensuring and quantifying stability. From an FSD perspective, however, the absolute accuracy of source parameters becomes significant, since the initial-state distribution of the tritium-containing parent molecule will affect the final states populated by the daughter. In particular, further work is needed to understand the rotational temperature and isotopic composition of the tritiated gas in the WGTS.

The KATRIN experiment monitors the isotopic composition of the gas in the LARA apparatus using laser Raman spectroscopy. LARA is operated in the inner tritium recirculation loop before the final buffer vessel. The gas circulates through the loop and buffer vessel at 300 K, and is cooled to the WGTS temperature of 30 K as it flows through a 5m capillary tube. Rotational thermalization is incomplete, however: since T2 is a homonuclear molecule, transitions between odd- and even-J states require a nuclear spin flip, and are thus significantly hindered. In fact, the ortho-para ratio in the WGTS is expected to remain characteristic of room temperature. We are working with our LARA collaborators to understand the extent to which the T_2 even-J and odd-J populations will separately thermalize to $J = 0$ and $J = 1$, respectively, via collisions with the walls of the capillary. The rotational distribution of T_2 in the WGTS is not currently well constrained, but must be understood so that the correct theoretical input can be applied to the neutrino-mass analysis. Our collaborators are working to develop a modified LARA system – a capillary LARA, or CLARA – that could be deployed at the WGTS outlet, after the first pumping stage, in order to measure the rotational-state distribution empirically.

The LARA system was specified and designed to measure the relative isotopic purity, with only loose constraints on the absolute uncertainty. The LARA calibration uncertainty has been established at $< 10\%$[2]; the corresponding uncertainty on the tritium purity ϵ_T is much reduced because ϵ_T is very high at 95%. We have worked with the LARA team to build the case for a detailed study of the LARA systematics, which is expected to form part of the thesis work of a KIT student.

[1] L. I. Bodine, D. S. Parno, and R. G. H. Robertson, Phys. Rev. C **91**, 035505 (2015).
[2] M. Schlösser *et al.*, J. Mol. Struct. **1044**, 61 (2013).

1.4 FPD system operation and upgrades

J. F. Amsbaugh, A. Beglarian*, T. Bergmann*, L. I. Bodine, T. H. Burritt, P. J. Doe, S. Enomoto, N. Fong, J. A. Formaggio†, F. M. Fränkle*, F. Harms*, L. Kippenbrock, A. Kopmann*, E. L. Martin, A. Müller*, N. S. Oblath†, D. S. Parno, D. A. Peterson, R. G. H. Robertson, A. Seher*, D. Tcherniakhovski*, T. D. Van Wechel, K. J. Wierman‡, J. F. Wilkerson‡, and S. Wüstling*

The Focal Plane Detector (FPD) has been a key component of the commissioning exercise since it was installed in 2011. With the exception of a failed pinch magnet, replaced in 2015, it has performed reliably on a 24/7 basis and the detailed spatial imaging it provides has been key to understanding the background processes of the spectrometer. With continued use, FPD improvements have been identified and implemented. The detector front-end readout electronics are located in a 10^{-6} mbar vacuum chamber. The wiring harness used to connect the readout components was not vacuum-compatible and exposure to high temperatures resulted in the vacuum chamber being contaminated by plasticizers. A new, vacuum-compatible harness, seen in Fig. 1.4-1, has been installed, a failed preamplifier card replaced and a new detector wafer installed in order to compare wafer performance.

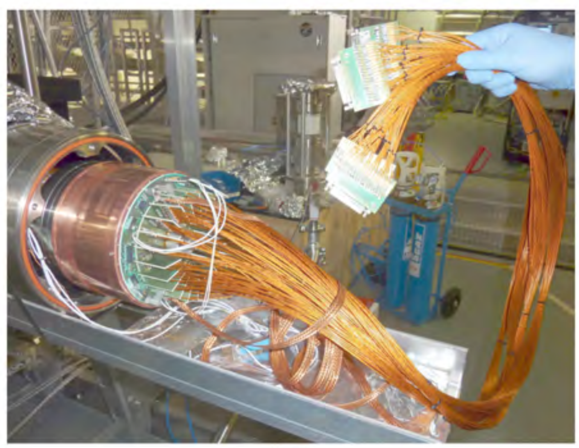

Figure 1.4-1. The new, vacuum-compatible cable harness being installed in the FPD.

The goal is to have the highest resolution wafer, with 100% working pixels, installed in time for the start of the next commissioning phase. A new cosmic-ray veto has been developed that builds on the experience gained with the original veto and takes advantage of improvements in silicon photomultiplier (SiPM) technology, resulting in a more robust, simpler and more efficient veto system. This new veto is described below. It is expected that such improvements and maintenance of the detector system will continue on a yearly basis throughout the planned 5-year operational life of KATRIN.

*Karlsruhe Institute of Technology, Karlsruhe, Germany.
†Massachusetts Institute of Technology, Cambridge, MA.
‡University of North Carolina, Chapel Hill, NC.

1.5 Progress on veto upgrade

T. H. Burritt, P. J. Doe, S. Enomoto, N. Fong, A. Müller*, D. A. Peterson, and T. D. Van Wechel

To control backgrounds, the FPD is surrounded by concentric cylinders of high purity copper and lead to reduce intrinsic backgrounds and an outer layer of plastic scintillator, providing an active veto for cosmic-ray backgrounds. The scintillator is read out by wavelength shifting fibers leading to silicon photomulipliers (SiPMs). SiPMs are chosen to allow operation in the high magnetic fields surrounding the veto. To overcome dark noise, the SiPMs had to be cooled. This resulted in a mechanically complex system for which it was frustratingly difficult to set bias levels and thresholds; the system was also unstable and relatively inefficient.

Building on the experiences of the original veto, a new veto has been designed using thicker scintillator (higher photon yield) and SiPMs directly mounted on the scintillator (lower photon transmission loss in fibers). In addition, significant improvements to SiPM technology have reduced dark noise and inter-pixel crosstalk to a level at which, in conjunction with the increased signal size, cooling is no longer required.

The new veto scintillator configuration consists of eight barrel staves and two semi-circular end caps, all 20 mm thick. Scintillation light in each stave and end-cap is collected by four, 1-mm-diameter wavelength-shifting fibers located in 2 mm deep grooves in the scintillator panels. Fig. 1.5-1 shows these grooves being machined into a stave.

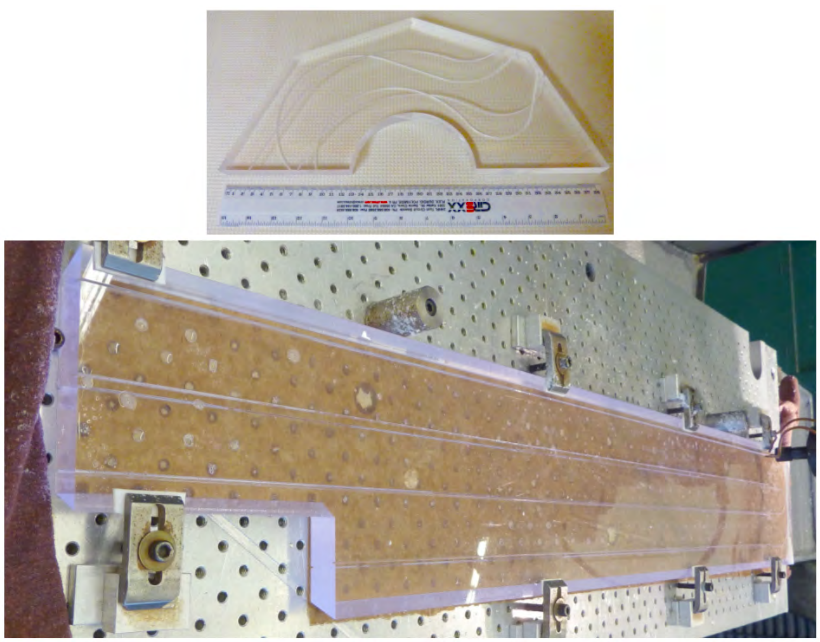

Figure 1.5-1. *Top:* The wavelength shifting fiber grooves in an end-cap. *Bottom:* Grooves being machined in a stave.

*Karlsruhe Institute of Technology, Karlsruhe, Germany.

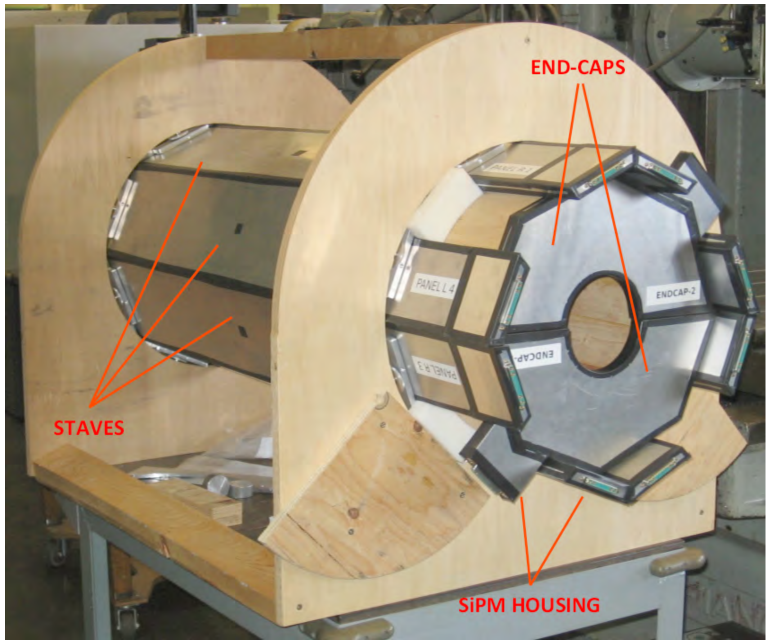

Figure 1.5-2. The scintillator staves and end caps mounted around a wooden mock-up of the shielding and magnet bore.

The scintillator components are covered in reflector material to enhance light collection and clad in thin aluminum sheets to exclude ambient light. Fig. 1.5-2 shows the scintillator staves and end caps being test-mounted around a mock-up of the Cu/Pb shielding. The design allows individual scintillator elements to be removed if necessary. Since fibers are not glued into the scintillator grooves, individual fibers may also be replaced without removing the scintillator. Also seen are the SiPM housings located at the ends of the staves and at the edge of the end-caps. Opening a housing allows the SiPM to be replaced. Signals from the SiPMs are fed via coaxial cables to the readout electronics located downstream of the veto where space is freely available.

Housed in a Weiner NIM chassis, located immediately downstream of the detector magnet, a newly developed set of electronics will provide 40 computer-controlled bias levels, 40 SiPM signal-conditioning circuits and 10 SiPM temperature readouts, before digitization by an identical Data Acquisition (DAQ) system as that used for the FPD. At this signal conditioning stage, a baseline is established above the high rate SiPM thermal pulses, eliminating the possibility of baseline fluctuations due to pulse pileup. All the SiPM bias voltages are individually controlled by computer according to the temperature readout values of each SiPM housing. The system includes two ADCs for self-calibration of the 80 DACs. The entire electronics setup is controlled through a USB interface, to which a Raspberry-Pi single-board computer is connected. The embedded computer implements all the control logic, including automated bias setting and full calibration sequences, and provides a Web-browser based operation environment as well as a set of RESTful HTTP protocols for multiple external controls by ORCA DAQ software and the slow-control system. The electronics modules and a screen shot of the control interface can be seen in Fig. 1.5-3.

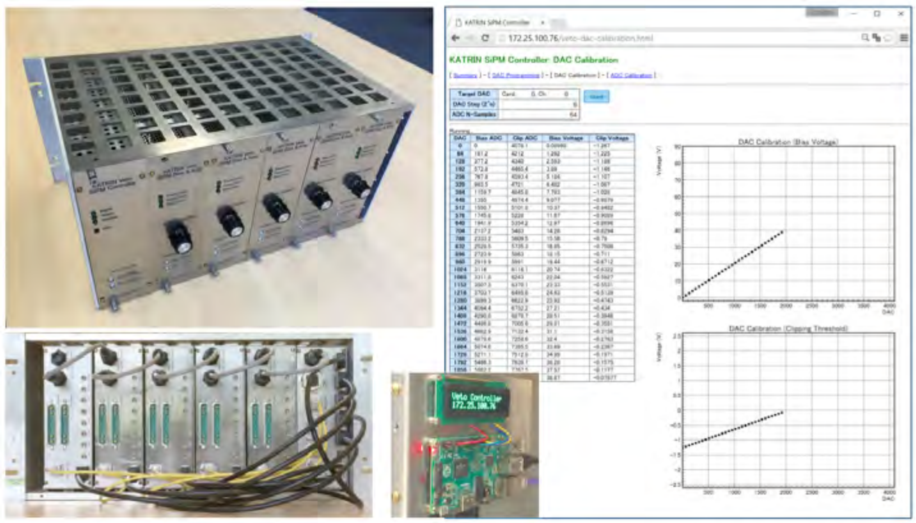

Figure 1.5-3. The veto electronics and user interface. *Upper left:* Front view of the analog and control modules in the NIM chassis. *Lower left:* Rear view of modules. *Lower center:* The Raspberry-Pi with status display. *Right:* Web interface of the embedded calibration system.

Fig. 1.5-4 shows a typical pulse height spectrum for cosmic-ray muons. The muon peak is easily distinguished from backgrounds which are generally attributed to ambient gamma radiation and dark noise. The SiPMs operate at room temperature. Construction of the new veto is complete. The average scintillator response to a muon is 60 - 70 photo-electrons (p.e.)/muon, approximately an order of magnitude improvement over the existing veto. Further commissioning of the readout electronics remains to be done, but we expect to install the veto into the FPD system in June 2016.

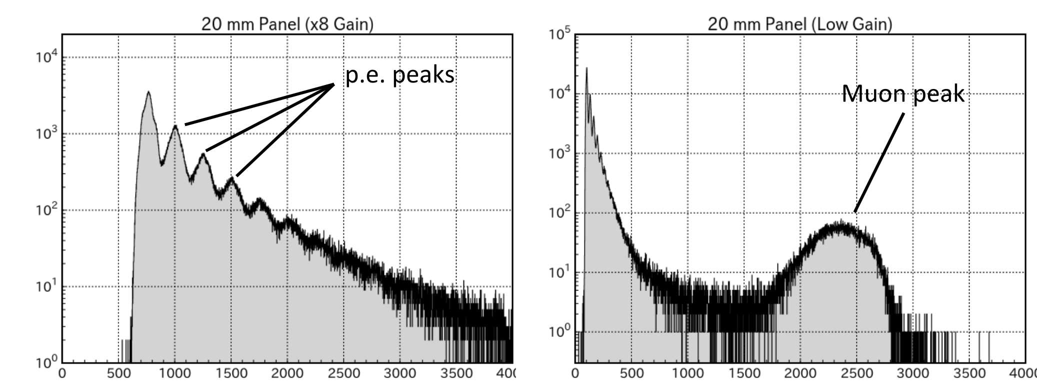

Figure 1.5-4. Typical performance of a scintillator stave. *Left:* High-gain spectrum is shown in which the individual photo-electron peaks can be seen. *Right:* Low-gain spectrum is shown in which the muon peak is clearly discernible above background.

1.6 Main spectrometer background studies

L. Kippenbrock and D. S. Parno

To reach the design sensitivity of 0.2 eV/c^2 on the upper limit of the $\bar{\nu}_e$ mass, KATRIN requires a background rate of less than 10 mcps[1]. However, recent commissioning measurements with the main spectrometer indicate an electron background rate of several hundred mcps. A large amount of effort has been expended looking for the origin of this background and mitigating its effects. In this article, investigations of gamma radiation and cosmic muons as potential background sources are described. Both gammas and muons can produce secondary electrons when passing through the steel hull of the spectrometer vessel.

The decay of radioisotopes in the concrete surrounding the spectrometer vessel is a known source of gamma radiation. In the summer of 2015, two experimental configurations were used to manipulate the gamma flux on the spectrometer surface and look for correlated changes in the focal-plane detector (FPD) rate. First, a strong ^{60}Co source was placed near the vessel to increase the flux of gammas. Second, water was added below the vessel to provide shielding from the concrete floor. In both cases, negligible changes in the FPD rate were observed.

To calculate how much the gamma flux through the vessel hull actually changed in the previously mentioned configurations, a Geant4 simulation of the main spectrometer hall was developed. Measured values for the activity of ^{40}K and the daughters of ^{232}Th and ^{238}U in the concrete were used as input for the simulation. The results showed a significant increase (decrease) in flux with the addition of the ^{60}Co source (water shielding). Because experiment failed to see a similar correlation in terms of background rate, it can be concluded that sources other than environmental gammas must be the major contributors to the spectrometer background.

The muon background has been primarily studied through the use of muon detector panels placed near the spectrometer vessel. Using these panels, a previous analysis showed that the magnetic shielding of the main spectrometer effectively prevents muon induced secondary electrons from reaching the FPD[2]. Nevertheless, to improve KATRIN's knowledge of the muon background, a coincidence analysis of muon panel and FPD data is presently underway. The dataset being analyzed includes runs taken with a special magnetic field configuration that allowed surface electrons to reach the detector. Initial results show a clear excess of FPD events that occur within a 100-μs window following muon panel events, the first time such an unambiguous muon coincidence peak has been seen in data from the main spectrometer.

At present, the favored model to explain the background rate seen by KATRIN is the ionization of hydrogen Rydberg atoms, originating from the spectrometer inner surface. Such

[1] J. Angrik *et al.*, "KATRIN Design Report", 2005.

[2] J. Linek, "Investigation of the muon induced background at the KATRIN main spectrometer". Master's thesis, KIT, 2015.

atoms are neutrally charged but have electrons in highly excited states. Thus, Rydberg atoms are unaffected by the magnetic and electrostatic shielding designed to block electrons and only require a small amount of energy to be ionized. Blackbody radiation, in particular, can be sufficiently energetic to ionize a Rydberg atom; when this occurs in the spectrometer volume, the resultant electron can be magnetically guided to the FPD. A possible production method currently under study is the alpha decay of ^{210}Po in the spectrometer walls, in which the recoiling daughter nucleus may be able to eject Rydberg hydrogen atoms from the surface.

1.7 Single-electron detection for KATRIN time-of-flight operation

T. H. Burritt, P. J. Doe, E. L. Martin, D. A. Peterson, R. G. H. Robertson, and T. D. Van Wechel

Implementing a time-of-flight measurement in the KATRIN experiment could allow measuring the energy spectrum above each retarding potential instead of the total rate of electrons above each retarding potential. This would significantly reduce the data-collection time required to attain the same statistical uncertainty[1].

In time-of-flight mode the energy of each electron is determined from the time it takes to pass through the main spectrometer. As flight time is mostly determined by the slow movement through the analyzing plane, where the remaining transverse momentum on the electron results in reduced energy resolution similar to high-pass-filter mode, the energy resolution in time-of-flight mode can be nearly as good as high-pass-filter mode. The stop signal for time-of-flight is already available from electron impact on the focal-plane detector, but a start signal is still required. The best place for the start signal is between the pre-spectrometer and main spectrometer.

An electron-tagger test setup using a resonant structure was constructed, shown in Fig. 1.7-1. It uses a cylindrical cavity with a large hole through the center for electrons to pass. A ring in the center of the cavity is supported by three coils connected to the can. The ring-to-can capacitance and coil inductance form a resonant-tank circuit. The time-dependent electric field exchanges energy with passing electrons. The cavity is excited and cavity excitation measured using wire loops placed between the ends of the two coils and the can wall. Coupling is adjusted by rotating the loops.

This setup was unable to produce a sufficiently low-noise signal to detect the passing of a single electron. Its estimated noise power is currently about a factor of 700 times the signal power. Changes to the readout electronics to allow a lower-noise readout are being explored.

Electrons trapped between the main spectrometer and pre-spectrometer cause a background at the focal-plane detector. A removal method using a wiper that sweeps across the

[1] N. Steinbrink, V. Hannen, E. L. Martin, R. G. H. Robertson, M. Zacher and C. Weinheimer, New J. Phys. **15**, 113020 (2013).

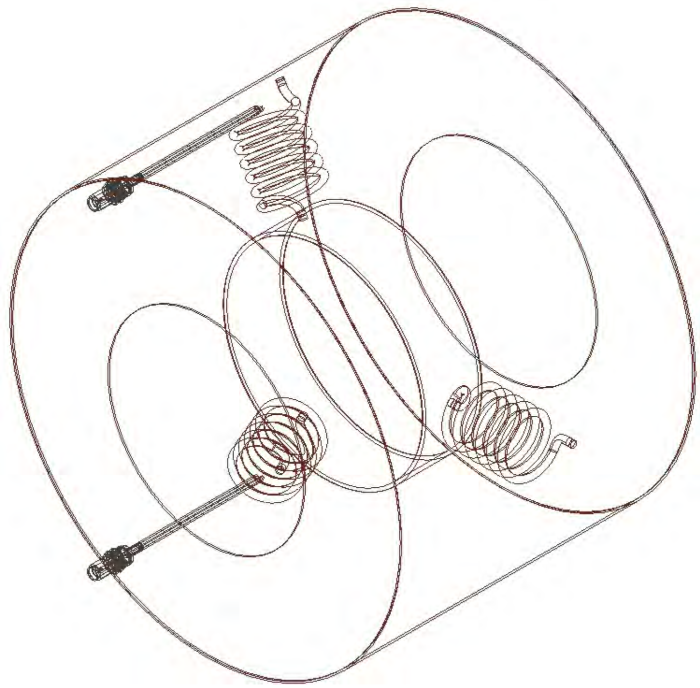

Figure 1.7-1. Ring resonator.

beam line is planned. The tagger performance is suspected to allow the noise from trapped electrons to be used as a signal to trigger the wiper before the appearance of significant background at the focal-plane detector.

1.8 Tritium Recoil-Ion Mass Spectrometer (TRIMS)

L. I. Bodine, T. H. Burritt, S. Enomoto, G. T. Holman, M. Kallander, Y.-T. Lin, E. Machado, D. S. Parno, D. A. Peterson, R. G. H. Robertson, E. B. Smith, T. D. Van Wechel, and D. I. Will

The TRIMS experiment at the University of Washington is designed to measure the branching ratio to the bound molecular ion ^{3}HeT$^+$ following beta decay in the T_2 molecule[1]. This observable has been predicted using the final-state theory on which the KATRIN analysis will rely, but the prediction disagrees with existing 1950s mass-spectrometry measurements. TRIMS will probe this discrepancy with a modern measurement addressing the factors that complicate a comparison of the existing measurements to the theory.

In Summer, 2015, we completed construction of the TRIMS vacuum system, including the installation of two silicon PIPS detectors, and moved it out of the clean room and into a basement lab in the Physics building. After pumpdown, the system reached a base pressure

[1]CENPA Annual Report, University of Washington (2013) p. 15.

of 10^{-8} Torr without bakeout. We designed and implemented a slow-controls monitoring system for our sensors, including automatic updates to a remote database. Using a ^{83}Rb-fed ^{83m}Kr source produced at CENPA in 2014[1], we successfully measured a spectrum with the magnets at their full field value of 2 kG (Fig. 1.8-1). A linear potentiometer was installed to guide the positioning of the beta detector, the ground end of the high-voltage resistor chain was modified to allow a simple diode-based current readout, and the CAEN DT5720 desktop digitizer was integrated into the ORCA data acquisition software with a functional OrcaROOT decoder. A data-processing chain has been implemented on a dedicated server.

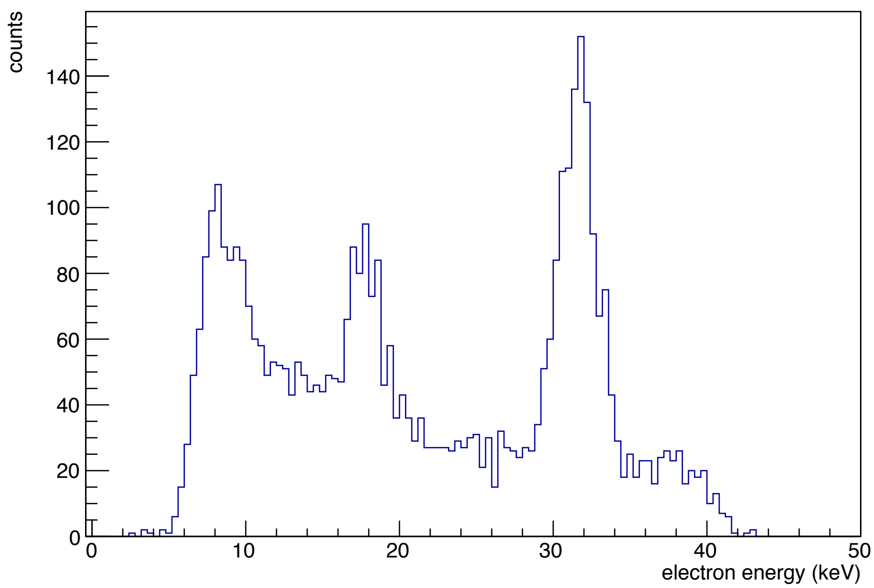

Figure 1.8-1. Preliminary ^{83m}Kr spectrum measured in the TRIMS apparatus with magnetic field but without high voltage. These events were acquired with the beta detector.

Subtle high-voltage problems have delayed data-taking, however. With the magnets on, small, frequent spikes appear in both pressure and current readouts at voltages above about 25 kV; the spikes are correlated with spurious detector events. Even with the magnets off, detailed study has revealed high rates of spurious detector events – even at relatively low voltages – following bright, instigating events. Electrons are emitted near the ion-detector mount, and are then accelerated to the beta end at positive high voltage. When they strike the glass of the decay chamber near that end, we detect X-rays and visible fluorescence. Additionally, a Penning trap has been identified in the system and must be eliminated.

Addressing these problems will require changes to the in-vacuum elements of the high-voltage system. In March, 2016, we disconnected the decay chamber from the rest of the vacuum system, and moved the apparatus to the CENPA Hot Lab where further work on the system will be conducted.

[1]CENPA Annual Report, University of Washington (2014) p. 13.

Majorana

1.9 Construction activities

T. H. Burritt, M. Buuck, C. Cuesta, J. A. Detwiler, Z. Fu, J. Gruszko, I. Guinn, J. Leon, D. A. Peterson, R. G. H. Robertson, K. T. Ton, and T. D. Van Wechel

The CENPA Majorana group has been heavily involved in the construction of the Majorana Demonstrator. In particular, CENPA students and staff have led the development and assembly of low-background cable connectors for the Demonstrator. These connectors are used on the signal cables which run from the HPGe detector array to an electronic feedthrough flange outside of the shielding. Because of their close proximity to the detectors, a novel, spring-free design, shown in Fig. 1.9-1, was necessary to ensure that backgrounds are low enough to meet the goals of the Demonstrator. Over the last year, 90 cables with female connectors were assembled and tested at UW with two main updates to their design. First, the dimensions of the connectors were tweaked to improve the reliability of their fit to male connectors. Second, the cables were soldered at the other end to 50-pin d-sub feedthrough flange connectors to reduce the risk of damaging cables during installation. These connectors are currently in use in both modules 1 and 2.

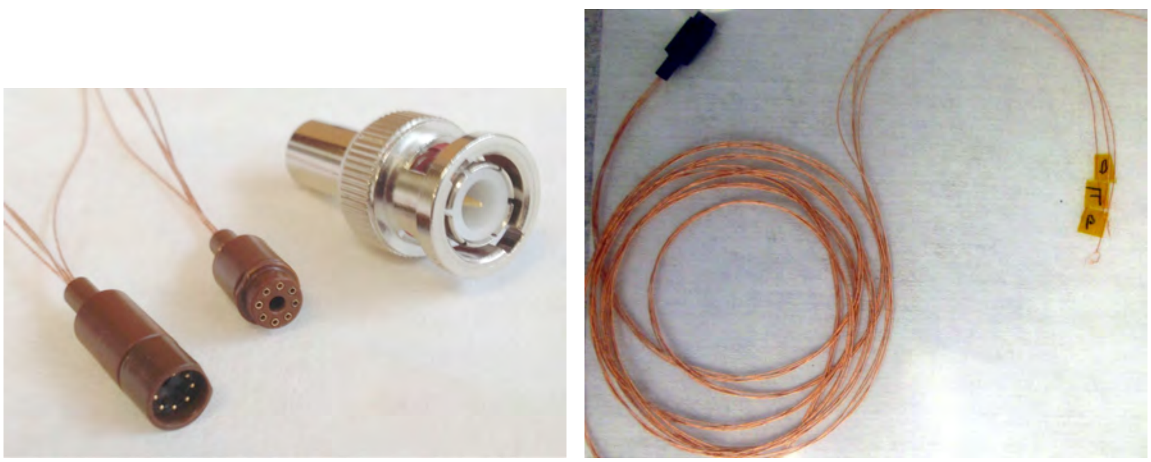

Figure 1.9-1. *Left:* A signal plug pair, with a BNC connector for comparison. *Right:* A signal cable soldered to a signal plug.

In addition, CENPA researchers have been responsible for testing the high-voltage cables and feedthrough flanges used in the Demonstrator. These tests are designed to search for breakdowns and microdischarges either in the cables or across the flange connections. All cables and flanges for the Demonstrator have been tested and suitable cables and flange connectors have been selected for use in both modules 1 and 2. A paper describing the cable testing has been accepted by NIM A[1].

CENPA collaborators have also been heavily involved in construction and operation of the experiment at SURF, enabling the Majorana Demonstrator to reach several important

[1] N. Abgrall *et al.*, Nucl. Inst. Meth. A, **823**, 83 (2016).

milestones. CENPA researchers have spent 2175.5 hrs at SURF. Module 1, shown in Fig. 1.9-2, was installed and operated in-shield in May 2015. In October 2015, Module 1 was removed in order to make several design improvements. These improvements included the replacement of old signal cables with the updated design mentioned in the previous paragraph. In addition, the inner electroformed copper shield was installed along with additional shielding in the cryostat crossarm. Module 1 was reinstalled in the shield in December 2015, and is currently in operation.

Figure 1.9-2. Seven strings are installed in each module of the MAJORANA DEMONSTRATOR.

Construction of Module 2 is also well underway. All seven strings of detectors for Module 2 have been assembled, each containing 3 to 5 detectors, with 29 detectors total. A detector in its mount and a string of detectors are shown in Fig. 1.9-3. The assembly process was improved over that for Module 1 by the implementation of a modernized quality-control procedure developed by Julieta Gruszko and implemented using the elog system[1]. In addition, the cryostat and vacuum hardware for Module 2 have been assembled and commissioned. The strings will be loaded into the cryostat by the end of April 2016, and commissioning of the detectors will begin soon after.

[1]https://midas.psi.ch/elog/

Figure 1.9-3. *Left:* The MAJORANA detector unit holds a P-type point contact HPGe detector and low-mass front end. *Right:* Detector assemblies are stacked to create a string.

1.10 Run selection and data reduction

M. Buuck, C. Cuesta, J. A. Detwiler, J. Gruszko, and I. Guinn

Tools needed to perform the run evaluation and data reduction for the DEMONSTRATOR are currently being developed and applied to the first Module 1 data. First, runs and detectors are evaluated and organized into data-sets, then a data-reduction framework is used to tag the different classes of events allowing the removal of non-physical events.

Run selection criteria are used to create a golden $0\nu\beta\beta$-decay run list using automated checks. Silver and bronze run lists are also created with background runs that can be used in other physics analyses. In order to carry out an automated run selection, run selection bits that record important run information during data-taking were implemented in the acquisition. They indicate which modules were taking data, the type of run (calibration, $0\nu\beta\beta$, maintenance), whether only a partial shield was in place, etc. The runs passing the run selection criteria are organized into data-sets. Module 1 has been taking data from June to October, 2015 and since December, 2015, and the data are divided in two data-sets, one for each of these periods. These are non-blinded data-sets corresponding to engineering runs for which the shielding was not complete. Data-set 0 (DS0) accounts for (47.9900 ± 0.0011) d to be used in the physics analysis and data-set 1 (DS1) for (54.7002 ± 0.0009) d until blind data-taking started. The duty cycles are shown in Fig. 1.10-1. A further selection is performed to select detectors within these runs that are suitable for various analyses. Automatic detector selection is being developed and for the moment only nonoperative detectors are rejected. The detector active masses are calculated taking into account the individual detector dead layers. In DS0 a total active mass of (14.60 ± 0.25) kg is considered, including (10.69 ± 0.16) kg of $^{\mathrm{enr}}$Ge. In DS1, the total active mass is (13.56 ± 0.04) kg and the $^{\mathrm{enr}}$Ge mass is (11.89 ± 0.04) kg.

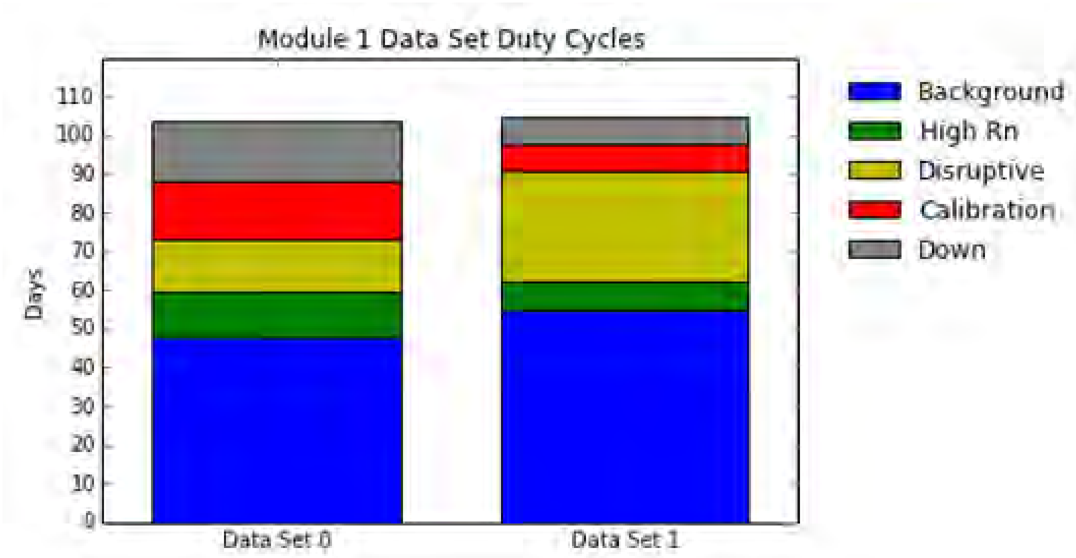

Figure 1.10-1. Duty cycles of the two data-sets corresponding to DEMONSTRATOR Module 1.

A data-reduction framework to tag non-physical events has been developed. The code creates a 32-bit integer for each waveform or event. Selected parameters are evaluated by boolean statements, and those events and waveforms that pass the filter are tagged by flipping one bit of the 32-bit integer. A complementary data-reduction framework that uses neural networks was also developed to help to identify unknown populations of events. An established list of waveform classes is in development, tag values will be refined, and their efficiencies will be quantified. Also, several types of external events may have an impact on the quality of Ge data. In addition to the detector data, there are a number of environmental parameters that are continuously recorded: fluctuations in the particle counts and radon levels in the experimental space, liquid nitrogen fills of a thermosyphon dewar, etc. These environmental data are monitored in a slow controls database, and are readily accessible for a direct comparison against Ge data.

Finally, the live-time measurement is carried out using data taken with a pulser, and using the distribution of inter-event times. A preliminary value of 99.96% live-time has been obtained.

1.11 Simulation and analysis activities for the MAJORANA DEMONSTRATOR

T. H. Burritt, M. Buuck, C. Cuesta, J. A. Detwiler, Z. Fu, J. Gruszko, I. Guinn, D. A. Peterson, R. G. H. Robertson, K. T. Ton, and T. D. Van Wechel

The UW MAJORANA group under the direction of Prof. Jason Detwiler leads the simulations and analysis effort within the MAJORANA collaboration. Much of the low-level software for data input/output, event building, data processing, and simulation was written by CENPA personnel. Members of our group have played a central role in the building and validation of the background model for the MAJORANA DEMONSTRATOR, which informs the radiopurity criteria upon which the experimental design is evaluated. We also participate in the development and implementation of data-analysis techniques, geometrical models for Monte Carlo simulations, and data handling, storage, and database technologies. Our efforts over the past year have focused on workflow management, improvements to data processing and cleaning, and the development and use of analysis tools for data from the first commissioning run of the MAJORANA DEMONSTRATOR Module 1. A significant achievement for the collaboration this past year was the submission for publication of a paper on our muon veto system[1].

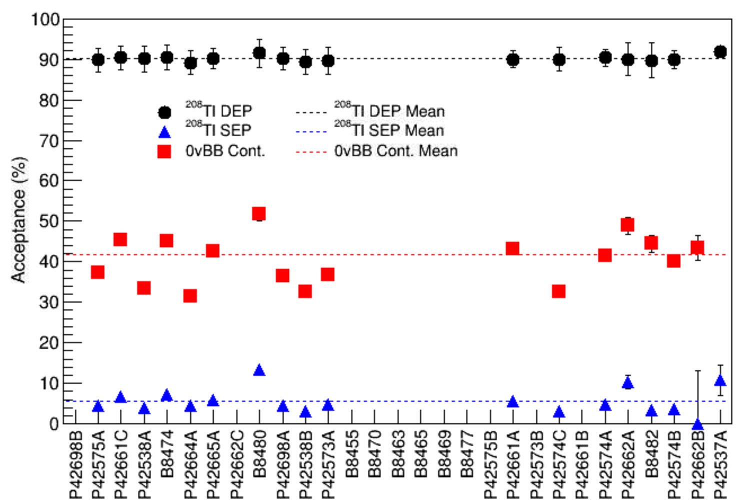

Figure 1.11-1. A/E acceptances for all detectors in Module 1. The black circles show the acceptance in the ^{208}Tl double-escape peak (DEP), which is dominated by single-site interactions. We tune the acceptance there to the expected fraction of $0\nu\beta\beta$ events that are single-site, which is 90%. The technique is very successful at rejecting events in the ^{208}Tl single-escape peak (SEP) (blue triangles), which is dominated by multi-site interactions. The effect of the cut on backgrounds in the ^{76}Ge $0\nu\beta\beta$-decay region-of-interest is given for each detector by the red squares. In the legend the abbreviation Cont. stands for continuum, i.e., the $0\nu\beta\beta$-decay flat background continuum.

Dr. Clara Cuesta has led the development of a pulse-shape-based background-suppression technique called A/E which analyzes the ratio of the maximum current in a pulse to the energy collected. Events that produce a single localized energy deposit – such as most $0\nu\beta\beta$ decays – will have a larger value of A/E than events that deposit energy in multiple locations inside

[1] N. Abgrall *et al.*, submitted for publication in Astropart. Phys., arXiv:1602.07742 [nucl-ex] (2016).

the same detector. We have shown using ^{228}Th calibration data that we are able to reduce our backgrounds using this technique by more than 50% (Fig. 1.11-1).

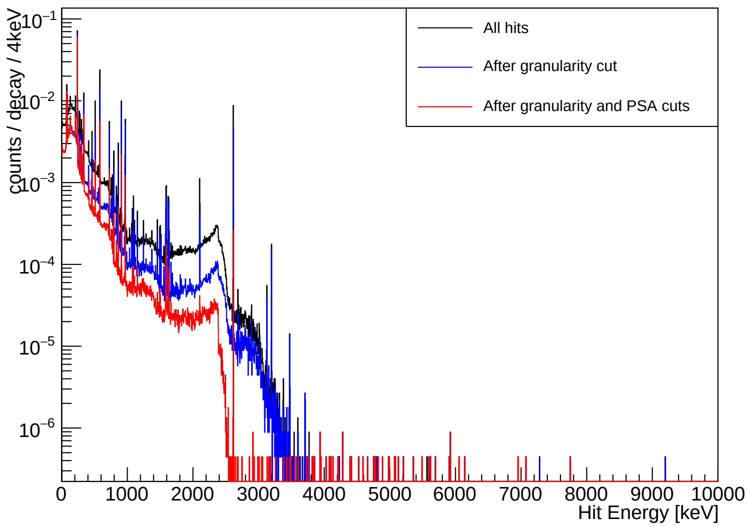

Figure 1.11-2. A simulation of the efficiency of the Module 1 array of Ge detectors for detecting thorium contamination in the copper detector unit pieces. The black line shows all energy depositions recorded by the array that do not occur in the dead layer of a detector. The blue line has removed events occurring in multiple detectors, and the red line has additionally removed events that are detectable as multi-site within a single detector using pulse-shape analysis (PSA).

Micah Buuck has primarily focused this year on two simulation- and analysis-related activities: a pulse-shape-based technique for identifying multi-site backgrounds complementary to A/E, and upgrading the simulation software to produce results on the detector level.

The pulse-shape technique requires the generation of a "basis library" of single-site event pulses, which is then used to accept or reject incoming pulses based on a χ^2 fit. He has successfully implemented the software necessary to generate the basis, and has done so on selected sets of calibration data. He is now in the process of quantifying the acceptance of the technique for various kinds of pulse shapes, and tuning input parameters to achieve optimal distinction between single- and multi-site pulses.

Buuck has also modified and upgraded the Majorana simulation post-processing software to incorporate detector-specific responses. He updated old code that determines which simulated interactions happen in the detector dead layers, and whether an event is likely to be distinguishable as multi-site. Fig. 1.11-2 is a simulation of the efficiency of the Module 1 array for detecting thorium contamination in the copper detector unit pieces. Each detector has a unique dead-layer geometry and drift-time mapping (primarily based on the detector shape) whose effects must be applied, before combining the data into a single spectrum.

Ian Guinn has continued to work on the event builder for the Majorana Demonstrator. The event builder has three main responsibilities. First, it converts the raw data files produced by the data acquisition software (ORCA) into ROOT files, known as built files, that are compatible with the MAJORANA software. Second, it combines waveforms and muon veto events that occur at proximate times into a single event, in order to detect coincidences. Finally, it filters out corrupted data that may confuse the main analysis software, a process known as garbage collection. In the last year, Guinn has implemented a builder for the muon veto data. He has also added a checker for built files, which searches for inconsistencies and errors that occur during the building process. Additionally, the event builder is now capable of building multi-sampled waveforms, in which the baseline and falling-edge waveforms are sampled at a slower rate than the rising edge. Guinn has also made a number of other improvements and bug fixes.

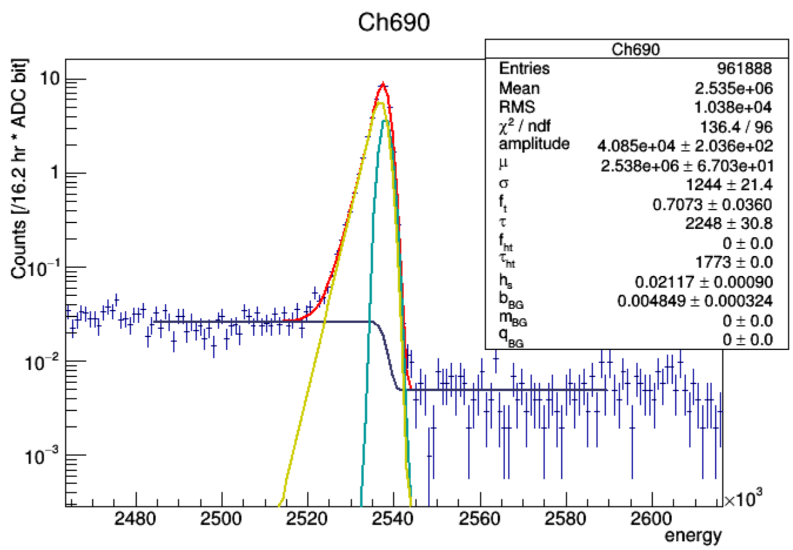

Figure 1.11-3. A 2614 keV ^{208}Th calibration peak fit to the peak shape function (red), which sums together a Gaussian (turquoise), low-energy ExGaussian tail (gold), and step function plus flat background (blue).

Guinn has also implemented a sophisticated algorithm for MAJORANA that fits peaks in the DEMONSTRATOR energy spectrum to an analytic peak shape function (see Fig. 1.11-3 for an example). The peak shape function is composed of a Gaussian, high- and low-energy ExGaussian tails, a step function, and a low-order polynomial background. The peak fitter is currently being used to calibrate the energy spectrum of the detectors from a ^{228}Th line source. Guinn is currently working on extending the peak fitter to fit multiple peaks simultaneously, which will allow an automated and more robust energy calibration.

We are now analyzing the first data to come from the first module of enriched Ge detectors, and have recently commenced blind data-taking. Other major activities include software quality-assurance tests, utilization of run and detector information stored in our databases, automatic data workflow management, refinement of event-building routines, optimization of energy estimation and pulse-shape parameter extraction algorithms, and data-monitoring and cleaning routines.

1.12 Alpha particle discrimination and LAAttE

T. H. Burritt, M. Busch*†, M. Buuck, C. Cuesta, J. A. Detwiler, J. Gruszko, I. Guinn, and D. A. Peterson

Alpha particles pose a problematic background in large granular detector arrays, particularly those alphas that originate from Rn progeny that plate out on the detector surfaces during manufacturing and assembly. The geometry of the p-type point contact (PPC) detectors implemented in the MAJORANA DEMONSTRATOR make the DEMONSTRATOR relatively insensitive to alphas, with the exception of a contribution coming from the passivated surface between the point contact and outer dead layer. In this region, the response to alphas is difficult to characterize. The charge-collection properties near this surface can differ for different detector models. In the MAJORANA DEMONSTRATOR, events have been observed in which alphas originating on this surface are significantly degraded in energy, leading to a potential background contribution in the region of interest (ROI) for neutrinoless double-beta decay.

However, it is also observed that charge mobility is drastically reduced on or near the passivated surface, and is slowly released on the timescale of waveform digitization, leading to a measurable change in slope of the tail of a recorded pulse. This matches the model developed by Mullowney *et al.*[1]. Using a filter that can identify the occurrence of this delayed charge recovery, these events can be identified, allowing for the efficient rejection of passivated surface alpha events in analysis.

To fully characterize the alpha interaction rejection efficiency of such a filter, and therefore understand the backgrounds of the MAJORANA DEMONSTRATOR, requires alpha source scans of the specific detector geometries used. To that end, the CENPA group is making progress on LAAttE, the Large-acceptance Alpha Attenuation Experiment. This internal scanning cryostat will permit alpha source scans of the various detector geometries used in the MAJORANA DEMONSTRATOR and of novel PPC detector geometries that could be used in future low-background experiments.

The Delayed Charge Recovery (DCR) Cut for Alpha Particle Interactions

An alpha-interaction cut, which identifies waveforms with a low-mobility charge component like those of Fig. 1.12-1, has been developed using commissioning data from Module 1 of the DEMONSTRATOR. It has been implemented with a single-site bulk (gamma and double-beta decay) event acceptance efficiency of 99% in the ROI, based on calibration spectra. Further optimization of the DCR cut will continue in the coming year.

*Department of Physics, Duke University, Durham, NC.
†Triangle Universities Nuclear Laboratory, Durham, NC.

[1] P. Mullowney, *et al.*, Nucl. Inst. Meth. A, **662**, 33 (2012).

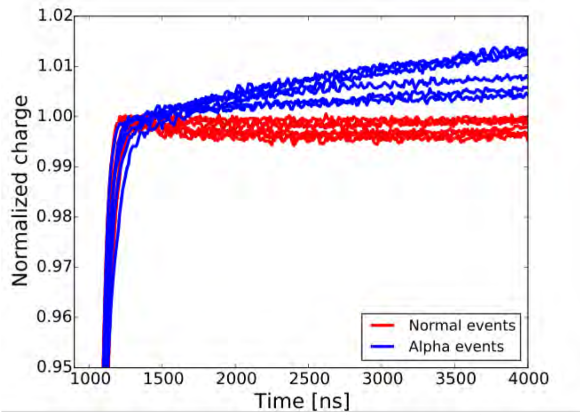

Figure 1.12-1. Example waveforms with pole-zero (pulse decay) correction. The alpha event waveforms show a slow component contribution from the drift of charge along the passivated surface, which is used to identify these events.

LAAttE: the Large-acceptance Alpha Attenuation Experiment

LAAttE is an experiment that is being designed and built at CENPA and will be used to conduct collimated alpha source scans of the surfaces of PPC detectors. It will allow scans at a range of alpha incidence angles, and uses a flexible design that accepts the full range of existing PPC geometries. Work on LAAttE in the past year has focused on two main efforts: (1) continuing design work on the scanning cryostat and (2) characterization of MJ60, the first PPC detector that will be scanned using LAAttE.

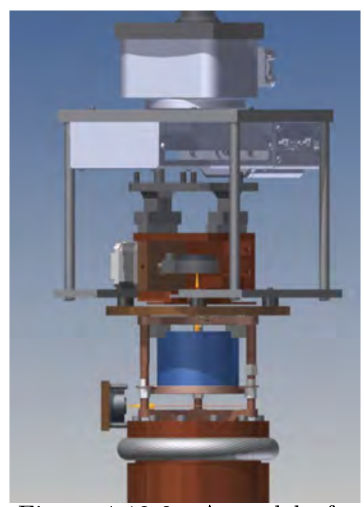

Figure 1.12-2. A model of the LAAttE cryostat. The cryostat itself and the IR shields have been removed to allow the cryogenic elements of the scanning system to be seen.

Changes have been made to an existing design by Marcel Held (a mechanical engineering exchange student to CENPA from Cooperative State University Karlsruhe in Winter Quarter of 2014) and Matthew Busch (Majorana Project Engineer, TUNL/-Duke U) that allow the re-use of components from the Majorana single-string test cryostats that were designed and constructed at CENPA[1]. Further changes, made based on the Majorana Collaboration's experience with germanium detectors, serve to reduce the potential leakage current due to infrared shine (IR) by eliminating, as much as possible, both line-of-sight and reflection paths to warm elements in the cryostat. Elements of the current design can be seen in Fig. 1.12-2.

[1]CENPA Annual Report, University of Washington (2013) p. 26.

Further work has been done to characterize and prepare MJ60. A String Test Cryostat was moved to CENPA and successfully baked, achieving excellent vacuum performance. The detector was removed from its vendor cryostat and mounted in a MAJORANA mount in the String Test Cryostat. The electronics needed to operate the detector were developed and prepared, and the first physics pulses were taken with the detector in its new mount. Current work is focusing on improving the leakage current of the detector through IR shine reduction and a future pump and bake of the crystal.

SNO

1.13 Search for *hep* neutrinos in SNO data

T. J. Winchester and N. R. Tolich

The SNO experiment was mainly sensitive to solar neutrinos produced by decay of ^{8}B atoms, but was also able to detect neutrinos from the *hep* reaction, $^3\mathrm{He}+p \rightarrow ^4\mathrm{He}+\nu+e^+$. The *hep* neutrinos occur with a much smaller flux than ^{8}B neutrinos, but they can be identified by their energy which extends a few MeV higher than the ^{8}B background.

Because the flux of *hep* neutrinos is so small, our ability to detect a signal is limited by the statistics. To increase the number of events in the dataset, we have developed two strategies for using events that were excluded from the ^{8}B analyses. The first strategy is to increase the fiducial volume from the 5.5 m radius used in the previous *hep* analysis to the full 6 m radius of the SNO detector's D_2O region. In order to achieve this increase, we wrote a new event fitter that remains accurate at higher radii and which is able to discern a special class of backgrounds more effectively than previous cuts.

The new fitter, called Cone Fitter, uses a Markov Chain Monte Carlo algorithm and a physics-based model for the spatial and temporal distribution of Cherenkov photons. Comparisons with Monte Carlo (MC) data show a 10% improvement in the position resolution compared to other SNO fitters, and less bias in the direction of the initial electron. Fig. 1.13-1 shows a histogram of residuals for Cone Fitter and FTP (a previous SNO fitter), as well as FTP with the cuts used in SNO applied. The residuals are calculated in the direction of the initial electron.

In SNO, some background events were produced in the acrylic vessel. While the physical origin of these events is not definitively known, a simple model of isotropic photons does a good job recreating these events. Our fitter is able to reliably cut these events using the ratio of the likelihoods of a Cherenkov cone-based model with a model based on isotropic photons. It turns out that this cut is not sensitive to the details of the simulated events such as wavelength and whether the events are produced inside the acrylic or on the surface. Fig. 1.13-2 shows a comparison of MC electron events and backgrounds created with several wavelengths on the surface and within the bulk of the acrylic.

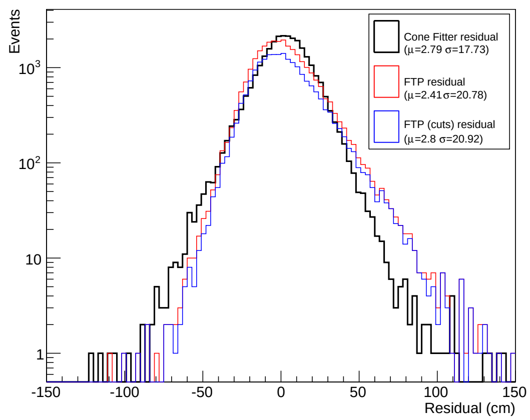

Figure 1.13-1. The difference between the fit position and the true position in the direction of the initial electron's momentum. Cone Fitter is the new fitter for the *hep* analysis and FTP is one of the best existing SNO fitters.

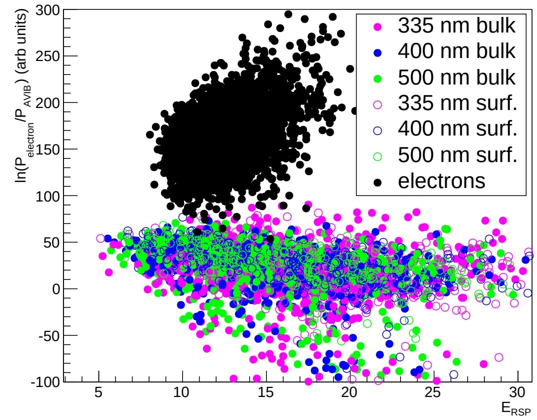

Figure 1.13-2. A fitter parameter that effectively cuts acrylic vessel background events. The separation between electrons and backgrounds is very good at all energies but is best for the higher energies of interest for a *hep* analysis. The details of the background model do not appear to be important for effective separation.

The second strategy to increase the number of events in our data set is to include runs that were excluded from other SNO analyses. These runs include those with low-energy backgrounds or calibration sources and normal data runs excluded previously for a variety of reasons. The total possible gain from these runs was about a 40% increase in run time.

Our criteria for being able to include additional runs are that the distribution of data in the runs must look sufficiently like the "golden" dataset, and that the rate of events must also be consistent. We used a modified Wald-Wolfowitz test to compare the distributions of energy, isotropy, position, and in-time-ratio of events in the candidate runs with those in the golden runs. This test returns a value for how similar the two distributions are. We also compared the rate of events in our region of interest in the candidate runs to that of the golden runs and rejected run types with a high event rate.

After doing this test on an unblinded 1/3 sample of the data, we found that we can definitively rule out most calibration source runs based on both a high rate and a bad result from the Wald-Wolfowitz test. The agreement between these two independent measures gives us confidence that the Wald-Wolfowitz test does identify bad run types. Most of the non-calibration runs pass both of these tests, which results in about a 20% increase in run time. However, it is not clear whether these runs will all pass these tests after unblinding, so the final gains may be smaller.

Project 8

1.14 Status of the Project 8 neutrino mass experiment

A. Ashtari Esfahani, L. De Viveiros*, P. J. Doe, M. Fertl, J. A. Formaggio†, M. Guigue‡ K.M. Heeger§, A. M. Jones‡, J. Kofron, B. H. LaRoque*, E. Machado, B. Monreal*, N. S. Oblath‡, R. G. H. Robertson, L. J Rosenberg, G. Rybka, L. Saldana§, P. Slocum§, M. G. Sternberg, J. Tedeschi‡, B. A. VanDevender‡, M. Wachtendonk, E. Zayas†

Project 8 is an effort toward an improved neutrino mass measurement by using frequency observation of the tritium β-decay electron's cyclotron radiation. The technique, now called Cyclotron Radiation Emission Spectroscopy (CRES), combines the rich history of single-electron trapping with high-resolution analysis techniques to provide a unique avenue to high-resolution electron spectroscopy. The project is organized into four phases to reach the expected sensitivity of 40 meV.

The publication of a highly resolved ^{83m}Kr conversion electron spectrum which includes conversion from the K, L, M, and N shells of krypton marked the completion of Phase I of the experimental effort[1]. This was the first demonstration of the CRES technique. Fig. 1.14-1 shows a high-resolution spectrum of ^{83m}Kr internal-conversion lines, with cuts to select high-power emission and near-maximum pitch angles. A thorough study of krypton lines has also been conducted to facilitate a probe of the extended magnetic bottle trap and lay the groundwork for a CRES measurement of the full β-decay spectrum of tritium.

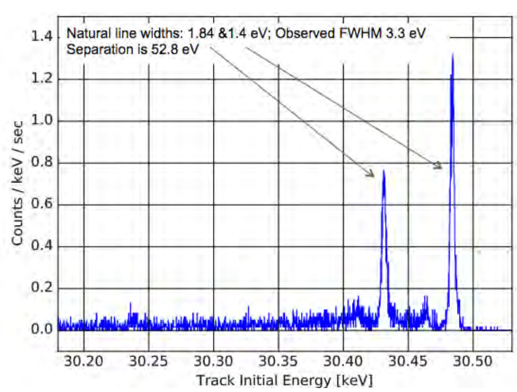

Figure 1.14-1. Spectrum of the ^{83m}Kr lines at 30.4 keV (bins are 0.5 eV wide).

In addition to the completion of Phase I, the engineering design for Phase II cell, shown in Fig. 1.14-2, is progressing. The new cell is designed with a circular cross section increasing

*University of California at Santa Barbara, CA.
†Massachusetts Institute of Technology, Cambridge, MA.
‡Pacific Northwest National Laboratory, Richland, WA.
§Yale University, New Haven, CT.

[1] Phys. Rev. Lett. **114**, 1162501 (2015).

both the signal-to-noise ratio and effective volume of the system. The magnetic trap consists of five "Z^2" coils, which can act independently as harmonic traps, or in concert to form a broad flat region with pinches at the end (termed a "bathtub" trap). A new electron spin resonance (ESR) probe has also been added to probe the magnetic field along the trapping region. This new system, which will contain tritium, is expected to be installed soon. Success in this step will lead the project to extraction of the first β-decay spectrum data.

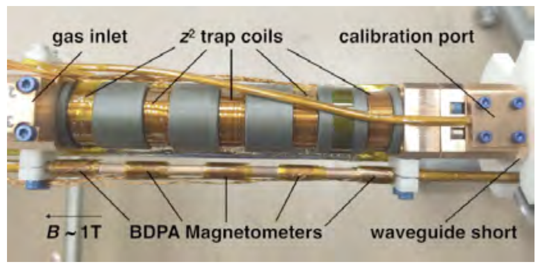

Figure 1.14-2. Phase 2 cell with five trapping coils, ready to be installed.

Phase III will have a larger volume, requiring a larger magnet to reach a better sensitivity. Plans for this Phase are also proceeding with the purchase of a 1.5-T MRI magnet system, shown in Fig. 1.14-3. The design for this Phase is being developed with the expectation of beginning construction after the completion of Phase II.

Figure 1.14-3. Phase III MRI magnet.

The project's ultimate goal of 40-meV sensitivity will be achieved in Phase IV, using the atomic tritium. This ideal sensitivity will cover the full range of neutrino masses in the inverted mass hierarchy scenario. Research and development for this Phase are also progressing.

COHERENT

1.15 The COHERENT experiment

A. Cox, C. Cuesta, J. Detwiler, A. Eberhardt, D. S. Parno, and A. Zderic

This year we received a UW Royalty Research Fund Award to perform R&D toward fielding an array of NaI(Tl) scintillating detectors at the Spallation Neutron Source (SNS) in Oak Ridge. The SNS produces a pulsed source of stopped pions, which decay to neutrinos with energies reaching tens of MeV. One goal of the experiment would be to measure the coherent elastic neutrino-nucleus scattering (CEνNS) cross section of these neutrinos with the ^{23}Na nucleus, a Standard Model process that has yet to be observed. Another goal would be to perform an improved measurement of the charged-current interaction cross section of neutrinos with ^{127}I. This measurement would test several aspects of nuclear physics relevant to nuclear-matrix-element uncertainties for neutrinoless double-beta decay, for example the potential quenching of g_A. These goals are being pursued in conjunction with the COHERENT Collaboration, who plans to additional deploy detector targets for the CEνNS search, including CsI(Tl) scintillating crystals, an array of Ge detectors, and a liquid xenon time projection chamber.

CENPA came into possession of a large number of NaI(Tl) crystals that became available to the US nuclear science community when they were surplussed from the failed Department of Homeland Security Advanced Spectroscopic Portal (ASP) program. We received 130 crystals of dimension 2" $\times$ 4" $\times$ 16" with photomultiplier tubes (PMTs) attached, giving a total mass of 1.0 tons (see Fig. 1.15-1). Preliminary testing of the crystals at UW and elsewhere showed that they are high quality. The PMTs require high-voltage (HV) power supplies and a voltage divider (PMT base) to operate. We have designed a PMT base that incorporates the socket and HV power supply recovered from the custom bases produced for ASP. A prototype implemented on a perfboard is being tested. Once tested successfully, the final design will be implemented on printed circuit boards. The detectors will be held in a compact array surrounded by steel and water shielding to block neutrons from the SNS beam as well as natural gamma radiation in the environment surrounding the detector. The water boxes required for the shielding are already in hand at the SNS. Should the sensitivity studies deem that additional shielding is required, pallets of existing steel and/or lead bricks from CENPA and Duke can be used to augment the shield.

We are also validating and upgrading the neutrino source-simulation code, originally written in Geant4 by H. Ray and collaborators at the University of Florida. The detector locations are now expected to be somewhat different from those anticipated in the original simulation, so new detector locations are being implemented in the code and we are checking the layout of the modeled corridor against building surveys provided by Oak Ridge. We are also reconfiguring the output data format to improve flexibility, reliability and readout speed. Separately, we are working on simulations of both large and small (24 crystals) NaI(Tl) detectors, in preparation for a test deployment.

Figure 1.15-1. One ton of NaI detectors surplussed from the DHS's Advanced Spectroscopic Portal program.

The COHERENT Collaboration's CsI(Tl) detector has been installed at the SNS and is already operational. We are collaborating on the design of the required analysis tools. A good knowledge of the detector response function for real scintillation events in the active volume, a good characterization of other anomalous or noise event populations contributing in that energy range, and the development of convenient filtering procedures for the latter are mandatory in order to achieve the required low background at low energy. In addition to an standard pulse-shape analysis, an alternate method led by P. Barbeau at Duke is being developed. It consists of fitting the signals in the CsI(Tl) waveforms and attempts to incorporate information from all parts of the waveform and integrate the full pulse shape. To do that we are designing an algorithm to find single photoelectrons in the trace and record the location of every photoelectron.

2 Fundamental symmetries and non-accelerator-based weak interactions

Torsion-balance experiments

2.1 Progress on a high-precision ground-rotation sensor to improve Advanced LIGO

J. H. Gundlach, C. A. Hagedorn, D. Larsen, M. Ross, and K. Venkateswara

The discovery of gravitational waves by Advanced LIGO (aLIGO) has begun the era of gravitational wave astronomy. Both LIGO detectors work well with individual duty cycles of about 60-70 percent and a network duty cycle of about 43% for the first observation runs. A significant problem limiting duty cycle is the influence of seismic conditions such as high microseismic motion, high winds and earthquake-induced ground-motion. The primary limitation in the active seismic isolation under these conditions is the tilt-horizontal coupling, which is the inability of conventional seismometers to separate ground rotation (tilt) and ground translation at frequencies below 0.1 Hz. This limits their ability to correct for ground translation as required to keep the interferometer stably locked. Thus, aLIGO needs a ground-rotation sensor to accurately distinguish between horizontal-ground translation and rotation. Such an instrument is not commercially available and the required sensitivity of the rotation sensor is challenging to reach.

Over the last two years, we have developed and installed two prototype instruments that meet a significant part of the requirement specified by the seismic-isolation team in aLIGO in the frequency range of 40 to 400 mHz. Each device consists of a low-frequency flexure-beam-balance. Its angle is measured using a multi-slit autocollimator mounted rigidly to the ground. Above its resonance frequency, the balance remains inertial, thus the autocollimator measures ground rotation. Torque from horizontal acceleration is rejected by locating the center of mass at the pivot point of the flexure. The prototype beam-balance consists of a 0.75-m aluminum tube with 1.8-kg copper weights attached at each end. It is suspended by two, 15-μm-thick, copper-beryllium flexures. The entire balance is surrounded by an aluminum-heat shield and is placed in high vacuum to minimize thermal effects.

One rotation sensor each was installed at both the X and Y end-stations at the LIGO Hanford Observatory. They are referred to as the Beam Rotation Sensors (BRS). Under windy conditions, tilt as measured by the BRS has been shown to be very coherent with a seismometer output at frequencies below 0.1 Hz, and has been used to remove tilt-induced noise from the seismometer output. Fig. 2.1-1 shows an example of a measurement taken with the new sensor when wind speeds were between 20-30 mph. The plot shows the amplitude spectral density of tilt data recorded by BRS-Y (labelled as BRS2) and the translation measured by a seismometer (labelled as STS2), converted to angle units. The blue/green trace shows the raw/processed tilt as measured by BRS, the red curve shows the seismometer output, and the cyan curve shows the tilt-subtracted ground translation signal. At frequencies greater than 0.1 Hz, the cyan curve follows the red, but below that frequency, tilt dominates the seismometer output, which can be subtracted well using the BRS.

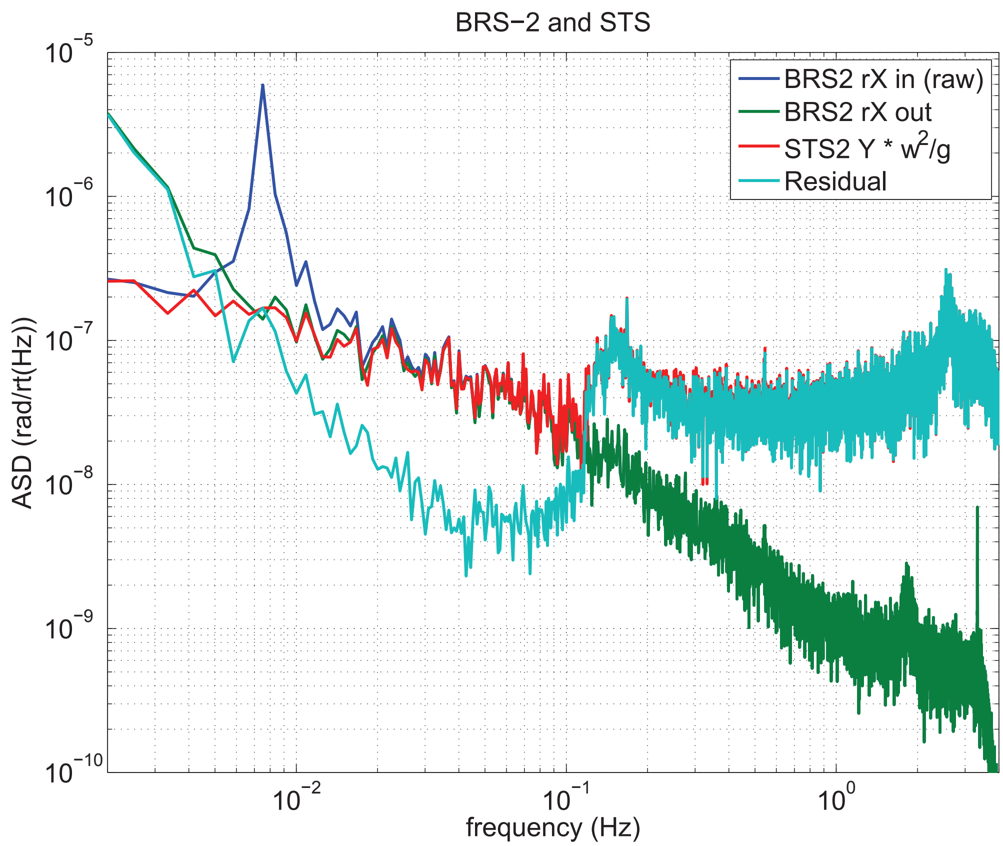

Figure 2.1-1. Seismic data measured at LIGO Hanford Observatory. The plot shows the ground rotation recorded by our sensor (BRS2, blue/green) in comparison to a seismometer (STS2, red). The tilt-subtracted translation signal is shown in cyan.

At the Hanford site, it has been shown that the differential arm-motion of the interferometer at low frequencies is dominated by the motion of the End-Station platforms under windy conditions. Hence it is expected that the duty cycle could be significantly improved with the two BRS instruments. Further testing and characterization of the control system to use these instruments is underway at LIGO Hanford Observatory (LHO).

At our lab, we are also developing a new compact version of the BRS with improved readout using two fiber-optic interferometers and a cross shape to reduce sensitivity to gravity gradient noise. This instrument is designed to be mounted directly to the optical platforms in aLIGO, which can potentially lead to much better angular control of the platforms than is possible with external ground rotation sensors. These sensors also have sufficient sensitivity at 10 Hz to be able to measure seismic tilt signals, which would allow better subtraction of direct gravitational noise on the LIGO test masses caused by seismic motion.

2.2 Progress and commissioning of wedge-pendulum experiment for testing short-range gravity

E. G. Adelberger, S. Fleischer, B. R. Heckel, W. J. Kim, J. G. Lee, and H. E. Swanson

Upgrades for the Fourier-Bessel short-range experiment began in May upon completion of the short-range spin-spin experiment. Improvements mentioned in previous annual reports[1] include a set of three motorized actuators for leveling the electrostatic screen to the rotating attractor, an improved gluing procedure for manufacturing the test masses, an increased vacuum conductance, a more rigid vacuum vessel, a larger calibration turntable, and automated apparatus leveling.

Both pendulum and attractor platinum test masses were fabricated from wire-EDM-cut foils and epoxied to glass annuli. Installation of the new motorized actuators, vacuum vessel, pump line, optics parts, and pendulum took approximately 6 months as parts and designs were adjusted to improve ease of operation.

The addition of the in-situ screen leveling allowed for an improved measurement of attractor-to-screen separation and leveling. The leveling procedure consists of rotating the screen through several small angles while monitoring the attractor to screen capacitance and searching for the minimum in capacitance. The separation measurement procedure is akin to previous pendulum-to-screen separation measurements. The screen is lowered on the motorized actuators while monitoring the capacitance and fitting to a COMSOL model of the capacitance as a function of separation.

In addition to the previously mentioned upgrades, we have also increased the height of the pendulum and installed a more effective swing and bounce damper. Previous measurements with the wedge-pendulum balance experienced increased torque noise at its closest separations suspected to be due to electrostatic patch-field noise. By increasing the size of the copper slug in our eddy-current damper and the length of the damper from 14.6cm to 27.6cm we have lowered the swing damping coefficient from 108s to 11s and limited the amount of random patch-field sampling. The current effort is now in bringing the balance to a point of operating near the thermal-limit noise floor.

2.3 Short-range, spin-dependent interactions of electrons: a sensitive probe for exotic pseudo-Goldstone bosons

E. G. Adelberger, B. R. Heckel, J. G. Lee, and W. A. Terrano*

Spontaneously broken global symmetries play an important role in particle physics. When the underlying symmetry is exact, the process always produces massless pseudoscalar Goldstone bosons whose coupling to a fermion with mass m_f is $g_{\rm p}=m_{\rm f}/F$, where F is the energy scale of the spontaneously broken symmetry. If the symmetry is not exact but explicitly broken

*Presently at Technical University of Munich, Munich, Germany.

[1] CENPA Annual Report, University of Washington (2015) p. 27.

as well, as in the chiral symmetry of QCD, the fermionic couplings are unchanged, but the resulting pseudo-Goldstone bosons, such as the QCD pions, acquire a small mass $m_{\rm b} = \Lambda^2/F$ where Λ is the explicit symmetry-breaking scale of the effective Lagrangian. Searches for the ultra-weak, long-range interactions mediated by exotic pseudo-Goldstone bosons, therefore, provide very sensitive and general probes for new hidden symmetries broken at extremely high energies. However, the tree-level potentials from pseudoscalar boson exchange are purely spin-dependent. The classic pseudoscalar potential is the dipole-dipole interaction

$$V_{\rm dd} = \frac{g_{\rm p}^2 \hbar^2}{16\pi m_e^2 c^2 r^3}\left[(\hat{\sigma}_1 \cdot \hat{\sigma}_2)\left(1+\frac{r}{\lambda}\right) - 3(\hat{\sigma}_1 \cdot \hat{r})(\hat{\sigma}_2 \cdot \hat{r})\left(1+\frac{r}{\lambda}+\frac{r^2}{3\lambda^2}\right)\right] e^{-r/\lambda} , \qquad (1)$$

where $\lambda = \hbar/(m_{\rm b}c)$. Axion-like bosons with an additional scalar coupling, $g_{\rm S}$, can also generate a CP-violating monopole-dipole interaction

$$V_{\rm md} = \frac{\hbar g_{\rm s} g_{\rm p}}{8\pi m_e c}\left[(\hat{\sigma} \cdot \hat{r})\left(\frac{1}{r\lambda}+\frac{1}{r^2}\right)\right] e^{-r/\lambda} . \qquad (2)$$

Both potentials vanish for unpolarized bodies so that traditional searches for new macroscopic forces are essentially insensitive to such bosons. Motivated by theoretical conjectures[1] that propose additional pseudo-Goldstone bosons such as axions, familons, majorons, closed-string axions and accidental pseudo-Goldstone bosons, we developed a generic "pseudo-Goldstone detector" with high sensitivity to both $V_{\rm dd}$ and $V_{\rm md}$ interactions.

Previous annual reports[2] discussed the basic principles and development of the instrument. During the period covered by this report the analysis of the second data set (which achieved a torque signal sensitivity of few aN m, substantially better than any of our previous torsion balance studies) was completed. Will Terrano, who designed the instrument, successfully defended his thesis[3], and the work was published[4]. The abstract and two figures from the published paper, reproduced below, summarize our results.

[1] A. Ringwald, arXiv:1407.0546v1 (2014).
[2] CENPA Annual Report, University of Washington (2015) p. 32.
[3] W. A. Terrano, *Torsion Pendulum Searches for Macroscopic Spin-Interactions as a Window on New Physics*, PhD thesis, University of Washington, 2015.
[4] W. A. Terrano, E. G. Adelberger, J. G. Lee and B. R. Heckel, Phys. Rev. Lett. **115**, 201801 (2015).

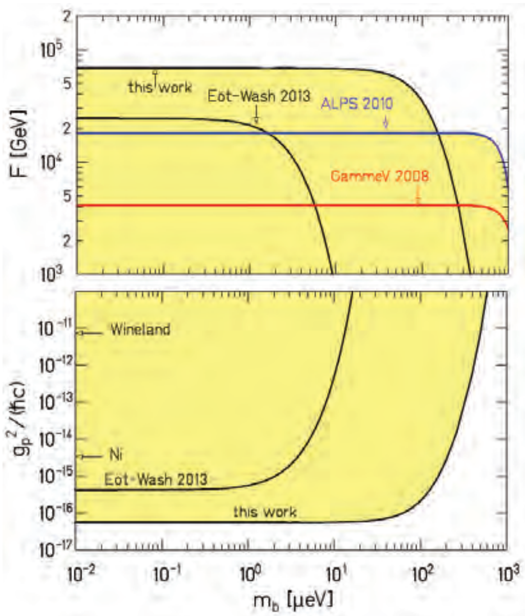

Figure 2.3-1. *Bottom:* $V_{\rm dd}$ limits from this work and from Ref.[1]. Arrows indicate the infinite-range constraints from other work and from Ref.[2]. Electron $g-2$ constraints are at the 10^{-10} level[3] *Top:* limits on the symmetry-breaking scale from this work and from FermiLab[4] and DESY[5]. The shaded areas are excluded with 95% confidence.

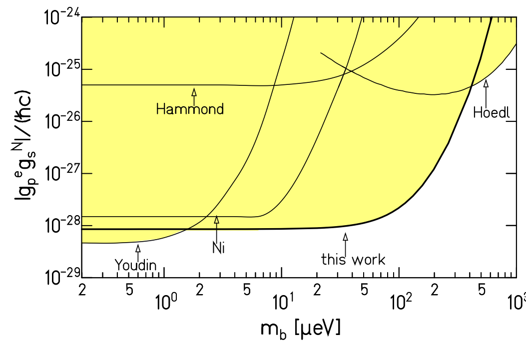

Figure 2.3-2. Monopole-dipole constraints from this work[6]. The shaded region is excluded with 95% confidence. The $m_{\rm b}=0$ limit[7] is 2×10^{-36}.

We used a torsion pendulum and rotating attractor with 20-pole electron-spin distributions to probe dipole-dipole interactions mediated by exotic pseudo-Goldstone bosons with $m_{\rm b}c^2 \leq 500$ μeV and coupling strengths up to 14 orders of magnitude weaker than electromagnetism. This corresponds to symmetry-breaking scales $F \leq 70$ TeV, the highest reached in any laboratory experiment. We used an attractor with a 20-pole unpolarized mass distribution to improve laboratory bounds on CP-violating monopole-dipole forces with 1.5 μeV$< m_{\rm b}c^2 <$ 400 μeV by up to a factor of 1000.

[1] B. R. Heckel, W. A. Terrano and E. G. Adelberger, Phys. Rev. Lett. **111**, 151802 (2013).

[2] D. J. Wineland *et al.*, Phys. Rev. Lett. **67**, 1735 (1991); W.-T. Ni *et al.*, Physica B **194-196**, 153 (1994).

[3] D. Hannecke, S. Fogwell and G. Gabrielse, Phys. Rev. Lett. **100**, 120801 (2008).

[4] A.S. Chou *et al.*, Phys. Rev. Lett. **100**, 080402 (2008).

[5] K. Ehret *et al.*, Phys. Lett. B **689**, 149 (2010).

[6] A. N. Youdin *et al.*, Phys. Rev. Lett. **77**, 2170 (1996); W.-T. Ni *et al.*, Phys. Rev. Lett. **82**, 2439 (1999); G. D. Hammond *et al.*, Phys. Rev. Lett. **98**, 081101 (2007); S. A. Hoedl *et al.*, Phys. Rev. Lett. **106**, 041801 (2011).

[7] B. R. Heckel *et al.*, Phys. Rev. D **78**, 092006 (2008).

2.4 Wedge-pendulum test-mass magnetic measurements

E. G. Adelberger, G. Benson, S. Fleischer, B. R. Heckel, J. G. Lee, and H. E. Swanson

A giant magnetoresistance (GMR) probe with rotating turntable was developed for the investigation of stray magnetic fields for the spin-dependent force experiment[1]. After a period of disuse, we began its rebuild to investigate a possible magnetic contamination in the platinum foils cut with wire EDM for the wedge-pendulum upgrade. A new stepper motor and driver were installed, additional mu-metal shielding was added to decrease background fields, slight timing errors in the data acquisition system were corrected, and a 250× amplifier and 3s low-pass filter were added to the GMR-probe output.

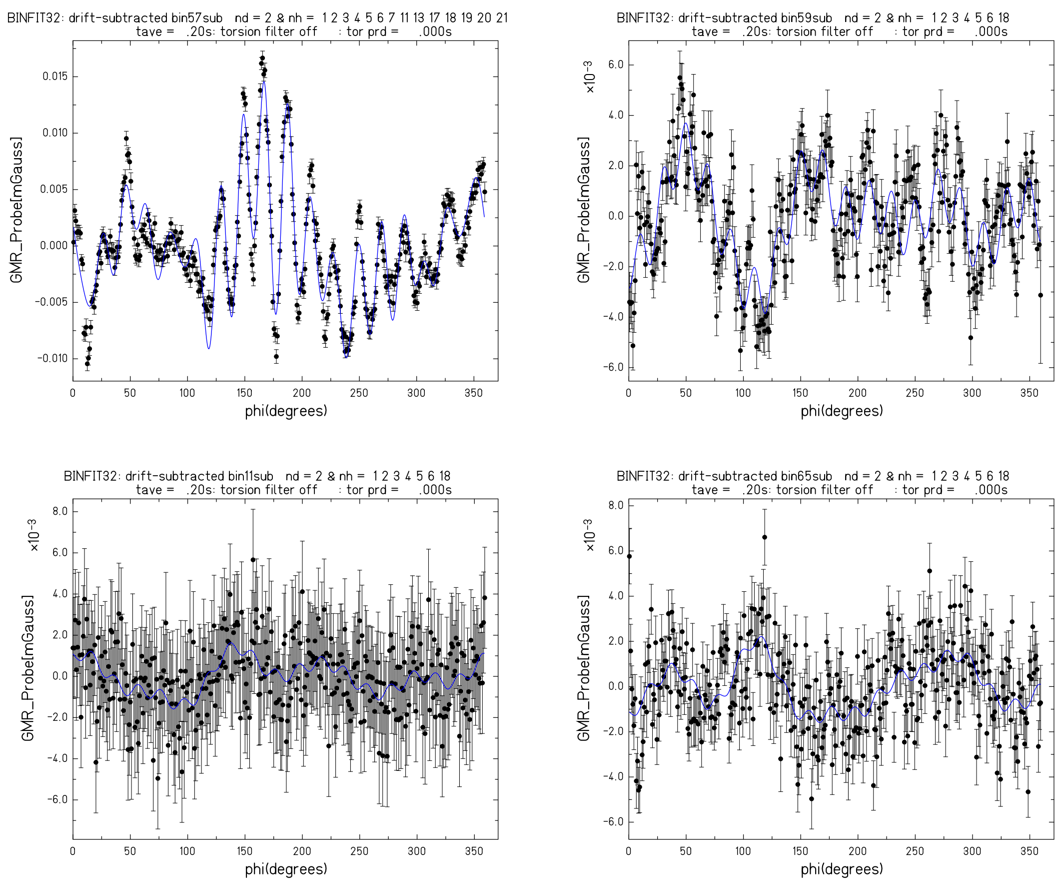

Figure 2.4-1. Measurements of the stray fields of the wedge-pendulum test masses (clockwise starting from top left: tungsten attractor, tungsten pendulum, platinum pendulum, and platinum attractor). Data are background, subtracted filtered, and then binned by turntable angle. Blue curves show fits to several low-order harmonics and to the 18th harmonic, which is associated with a pattern in the foils.

New measurements of the previous tungsten wedge-pendulum test masses and the new

[1] CENPA Annual Report, University of Washington (2015) p. 32.

platinum wedge-pendulum foils were taken. Measurements consisted of rotating the turntable under the GMR probe with and without the test sample, filtering out harmonics associated with the stepper motor, binning the data by turntable angle, and fitting harmonics to the difference of the two measurements. Two of the four platinum foils cut with the wire EDM showed significant signs of magnetic contamination, $\sim$1 mGauss. However, the two foils prepared for the upgrade showed comparable stray fields to the tungsten pendulum test mass and 10-20$\times$ smaller stray field in the 18-fold pattern of the tungsten attractor, Fig. 2.4-1.

2.5 Progress on silica fibers for improved equivalence-principle test

J. H. Gundlach, C. A. Hagedorn, J. G. Lee, E. A. Shaw, and K. Venkateswara

Last year we determined how to fabricate fused silica fibers up to a length of 20 inches and demonstrated a mechanical quality factor of Q=270,000 in the LISA apparatus[1]. This was achieved by adding magnetic shielding. Without any shielding Qs were limited to around 10,000. Compared to the Qs of tungsten fibers with maximum $Q \sim 6000$, these fibers have lower thermal torque noise, $\tau(f) = \sqrt{2k_BT\kappa/(\pi Q f)}$, where k_B is Boltzman's constant, f frequency, T the fiber temperature, and κ the fiber torsion constant[2]. The torsion constants of the fibers are comparable to those of tungsten, so the possible improvement in noise is around a factor of 5 to 10.

Over the last year we investigated what else could be limiting the Q. In particular, we observed that we could change the Q by tipping the apparatus and by rotating the pendulum. It turned out that the pre-hanger stage was causing this effect. The pre-hanger consists of a metal disk in a inhomogeneous magnetic field suspended from leaf springs by a tungsten fiber. The pendulum is then suspended from this disk, which damps both bounce and swing modes of the pendulum through eddy-current damping. Undesirably, this sets a limit on the Q of the coupled oscillator based on the relative torsion constants and Qs of the two fibers. Replacing the fiber with a rod resulted in measured Qs of around 500,000 and no observable dependence on the orientation of the pendulum in the apparatus.

[1] CENPA Annual Report, University of Washington (2015) p. 30.

[2] C. A. Hagedorn, S. Schlamminger, and J. H. Gundlach, 2006 Proc. 6th Int. LISA Symp. (AIP Conf. Proc. **873**) (New York, 2006) pp 189-193.

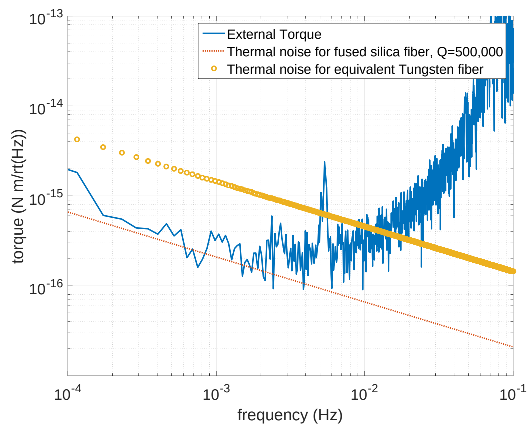

Figure 2.5-1. Characterization of external torque noise on the fused-silica-fiber-based torsion pendulum, shown in blue. Also shown are the expected thermal noise curves for a tungsten fiber of the same length and the current fused-silica fiber. The small peak at 5.3 mHz may be caused by aliased higher-frequency noise.

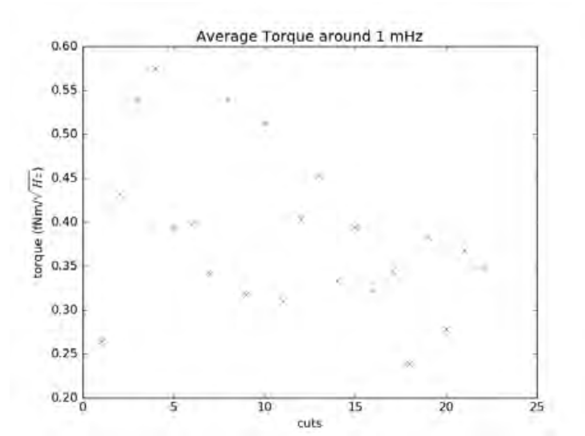

Figure 2.5-2. Average torque noise in 10 bins around 1 mHz after installation of ion pump in subsequent cuts. Each cut is around 20,000 seconds. This does not include weekday construction and seismic events. There appears to be no increase in noise over the course of almost 2 weeks.

Having established high Q in the torsion pendulum, we are investigating whether we can reach the thermal noise limit reliably. Another outstanding question is whether having an electrically isolated pendulum will affect the noise. While we had not noticed any effect on the noise before, it was important to test whether using an ion pump would change anything. This is because an ion pump is necessary in NewWash, our equivalence-principle test setup. Fig. 2.5-1 and Fig. 2.5-2 show tentative results that are promising. In parallel, we are also working on pulling fibers of the length required for installation in NewWash. Currently, we can pull fibers of the right length ($\sim$ 40 inches) with a torsion constant on the order of 1 nJ. This is comparable to tungsten, but as of yet these fibers do not have the requisite tensile strength to hold a pendulum. Soon we should be able to install a fiber in NewWash and start a test science run to evaluate the actual impact of these fibers.

2.6 Parallel-plate test of gravity at sub-millimeter scales

J. H. Gundlach, C. A. Hagedorn, S. Schlamminger*, M. D. Turner, and K. Venkateswara

Our first parallel-plate test of gravity[1] is complete. A titanium torsion pendulum with tantalum inlays was used to measure the uniformity of the gravitational field of a planar tantalum/aluminum attractor as a null test of Newton's Inverse-Square Law. In the Yukawa

*Presently at National Institute of Standards and Technology, Gaithersburg, MD.

[1] CENPA Annual Report, University of Washington (2015) p. 31.

parametrization ($V(r) = -G\frac{m_1 m_2}{r}(1 + \alpha e^{-r/\lambda})$), we constrain $|\alpha| < 1$ with 95% confidence for 104 μm$< \lambda <$ 1320 μm. Our limits on $|\alpha|$ are shown in Fig. 2.6-1.

The parallel-plate design offers the potential for both greater signal and complementary systematic uncertainties to our on-going "wedge pendulum" experiment. In addition, this experiment incorporated important new elements:

- An infrared interferometer directly monitored the motion of the stretched CuBe foil that isolated the pendulum from the attractor, a major source of systematic uncertainty in all parallel-plate experiments.
- The analysis is reproducible – one computer command leads from raw data to finished thesis[1], making audits or exploration straightforward. Our code is publicly available[2].
- The analysis was performed blind and unblinded[3] in public. When the blind was lifted, initially puzzling results were traced to the accidental incorporation of a few systematic-test data with the science dataset. The results are discussed in great depth in the thesis[1].

Straightforward improvements, notably nulling the pendulum-foil voltage and a flatter pendulum, would allow substantial improvements in performance.

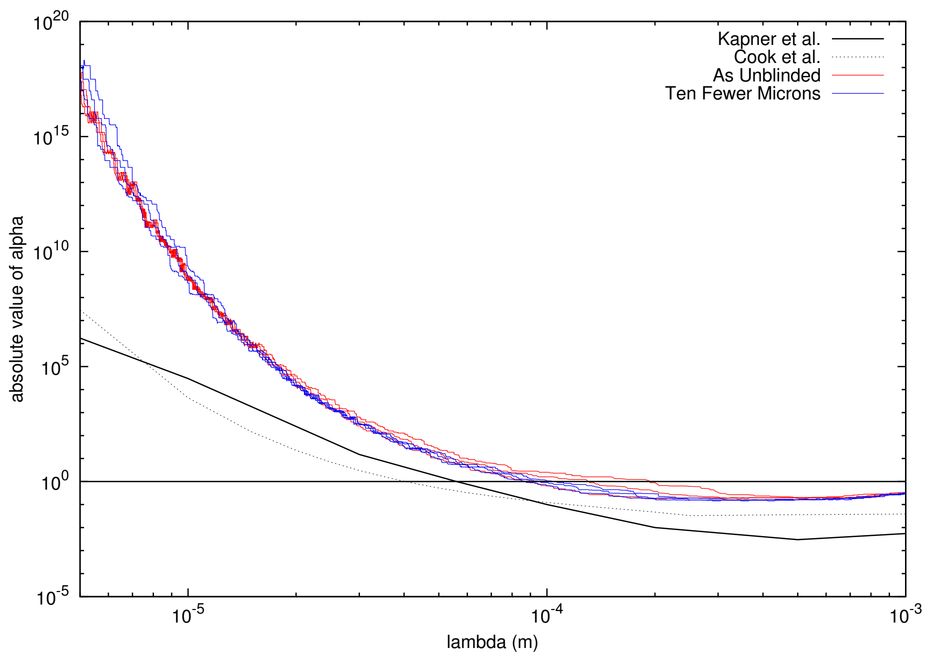

Figure 2.6-1. Limits on $|\alpha|$. "10 fewer microns" reflects a post-unblinding cut of the data.

[1] C. A. Hagedorn, *A Sub-Millimeter Parallel-Plate Test of Gravity*, PhD thesis, University of Washington, 2015.

[2] https://github.com/4kbt/PlateWash

[3] https://twitter.com/CharlieHagedorn/status/591782911860285440

2.7 Development of a rotating differential-tiltmeter gravity gradiometer

E. G. Adelberger, J. H. Gundlach, C. A. Hagedorn, E. A. Shaw, and H. E. Swanson

Figure 2.7-1. View of the upgraded lower tiltmeter column on our rotating EP apparatus. The torsion pendulum is located within the gravity-gradient compensator at the height of approximate up-down symmetry.

Among the leading sources of systematic uncertainty in equivalence-principle (EP) measurements are gradients in the gravitational field. In past tests of the EP, we have measured the most important gravity gradients before and after each stretch of EP data[1]. These gradients change with time; any improvement in uncertainty requires a continuous monitor.

We are commissioning an upgrade, begun in 2014, to install and operate sensitive co-rotating tiltmeters placed symmetrically above and below the torsion balance. The difference between the tiltmeter signals measures, to a reasonable approximation, the change in the horizontal component of gravity with height. The most-important Q_{21} gradient has substantial overlap with Δg_{xz}, allowing us to track gradients over time. In addition to upgrading the lower column, shown in Fig. 2.7-1, we have modified the experiment's rotating thermal shields to accommodate the column.

Using a plastic turntable placed beneath the lower column, we have demonstrated the sensitivity of the differential sensor to the presence of lead bricks near the lower tiltmeter. The sensitivity of the gradiometer is better than ~ 200 nrad/$\sqrt{\text{Hz}}$ when rotating at 2 mHz.

Furthermore, we have re-implemented the experiment's leveling feedback system on our new data-acquisition system and begun an extended campaign of comparing simultaneous gravity-gradient signals from both a gradiometer torsion pendulum and the tiltmeters.

[1] T. A. Wagner, *Rotating Torsion Balance Tests of the Weak Equivalence Principle*, PhD thesis, University of Washington, 2014.

2.8 Continued development of the cryogenic balance

J. H. Gundlach, C. A. Hagedorn, M. P. Ross, and K. Venkateswara

We have continued development of the cryogenic torsion balance that has been described in previous reports.[1] Cryogenic torsion balances have the potential to improve the sensitivity of many of our room-temperature torsion-balance experiments by reducing Brownian motion noise in the fiber.

The experiment was partly limited by excess noise in the autocollimator. The autocollimator measures the angle of the torsion balance with respect to a beam-splitter placed in the optical path, referred to as the reference mirror. Several autocollimator noise sources were addressed. We installed thermal insulation around the autocollimator body to reduce slow thermal drifts in angle. In addition, we increased the apertures for the optical beam to reduce beam-clipping.

We studied how the reference mirror location changes the ability to subtract common noise. The reference mirror was originally placed on the outside of the vacuum can. This allowed easier alignment but it was more sensitive to ambient thermal gradients, hence did not serve well as a reference. We moved the reference mirror from the vacuum can to different stages of the thermal shielding that are closer to the pendulum. We have found the best common-noise subtraction while the reference mirror was placed on the outer thermal shielding, which is at a slightly warmer temperature than the pendulum but is mounted more rigidly than the inner shielding.

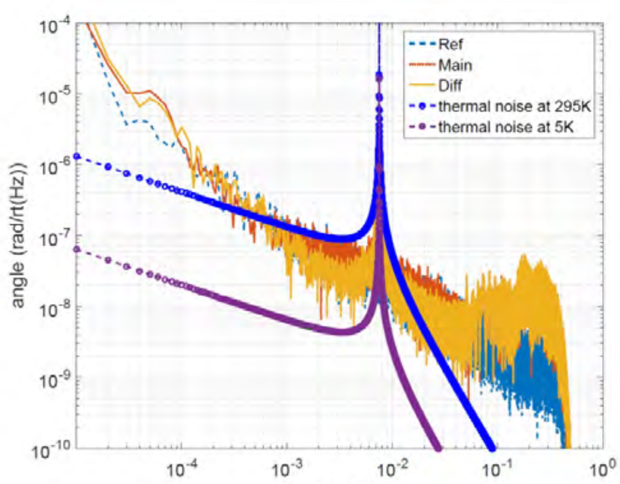

Figure 2.8-1. Amplitude spectral density with the reference mirror on the outer thermal shield. The blue dashed line shows the motion of the reference mirror, the red line shows the motion of the pendulum, and the yellow line shows the difference of these two signals which removes any common motion between apparatus and the pendulum. The blue dotted line shows the thermal noise limit at room temperature and the purple dotted line shows the thermal noise limit at the temperature of the pendulum, 5 K.

[1] CENPA Annual Report, University of Washington (2013) p. 46.

Additionally, we have installed a section of copper bellows at the fiber connection point which acts as a vertical spring to allow vertical damping with the previously developed magnetic damper. The combination of these two improvements decreased broadband noise.

Fig. 2.8-1 shows an amplitude spectral density (ASD) of the pendulum's angular motion as a function of frequency with the mirror on the outer shielding. The curves labeled 'Ref' and 'Main' are the angular positions of the reference mirror and the mirror on the torsion balance, respectively. 'Diff' represents the difference between the two showing a subtraction of the common-mode noise. Also shown are the expected angle ASD for a Brownian-motion-noise-limited pendulum at 295K and 5K. The 'Diff' curve lies between the two curves, which shows that the pendulum's motion is lower than room temperature thermal noise in the 1 mHz to 10 mHz range but has not yet attained the expected limit at 5K.

Non-accelerator-based weak interactions

2.9 The mercury electric-dipole-moment experiment

Y. Chen, B. Graner, B. Heckel, and E. Lindahl

The ^{199}Hg electric-dipole-moment (EDM) apparatus uses uv laser light to polarize and measure the spin precession frequency of ^{199}Hg atoms in a stack of 4 vapor cells, 2 of which (the inner pair) have oppositely directed electric fields, as illustrated in Fig. 2.9-1. A pump-probe sequence is employed, with the electric fields reversed between each pump-probe cycle. A blind frequency offset is added to the inner cell frequency difference to mask the EDM signal until the analysis of the entire data set is complete. EDM data collection is divided into "sequences", groups of 16 days of data distinguished by the ordering and orientation of the 4 vapor cells. Each sequence includes equal numbers of runs with electric-field magnitudes of 6 kV/cm and 10 kV/cm, magnetic field normal and reversed, and slow and fast electric field ramp rates.

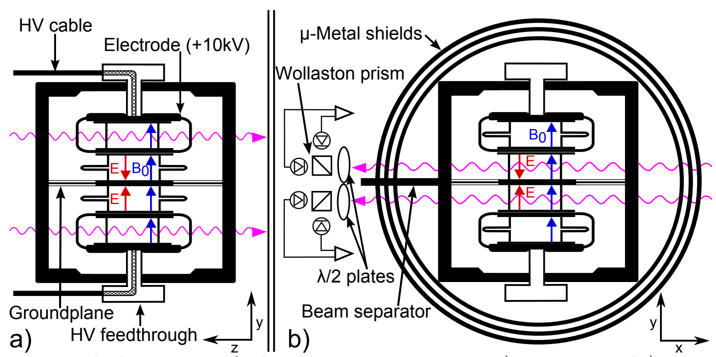

Figure 2.9-1. Cross-sectional diagram of the EDM apparatus (not to scale) showing the light paths through the outer cells and electric field directions (a) and the light paths and optics for the inner cells (b).

In 2015, we completed 12 sequences of EDM data, a complete set of data for 3 vapor cells cycling through the EDM-sensitive positions in the apparatus. Analysis of the (blinded) data revealed a new systematic error that was traced to a small motion of the stack of 4 mercury vapor cells due to electrostatic forces created by the application of high voltage (HV) to the stack of cells. HV-correlated cell motion in a magnetic field gradient can lead to a false EDM signal. To determine the feedthrough of cell motion onto the EDM signal, correlation analyses were performed and careful field maps of the magnetic-field gradients were completed.

After all known systematic errors were accounted for, the EDM data were unblinded, leading to a new ^{199}Hg EDM result: $d(^{199}\mathrm{Hg}) = -(2.20 \pm 2.75_{stat} \pm 1.59_{syst}) \times 10^{-30} e\,\mathrm{cm}$, which we interpret as a new upper limit of: $|d(^{199}\mathrm{Hg})| < 7.5 \times 10^{-30} e\,\mathrm{cm}$ (95% C.L.). This result represents a factor-of-4 reduction of the upper limit on the ^{199}Hg EDM over previous work.

The ^{199}Hg EDM project is primarily supported by NSF Grant 1306743 (P. I. Heckel).

3 Accelerator-based physics

Accelerator-based weak interactions

3.1 Overivew of the ^{6}He experiments

Y. S. Bagdasarova, K. Bailey*, D. Carlton, X. Fléchard†, A. García, R. Hong‡, M. Kossin, A. Knecht§, A. Leredde*, E. Liénard†, G. Leum, P. Müller*, O. Naviliat-Cuncic¶, T. P. O'Connor*, J. Pedersen, E. Smith, M. G. Sternberg, J. Stiebritz, D. W. Storm, H. E. Swanson, F. Wauters**, and D. W. Zumwalt

We are carrying out an experiment to search for tensor currents by measuring the correlation coefficient between the momenta of electron and the antineutrino (called "little a") from ^{6}He beta decay. The tensor currents flip chirality and are forbidden in the standard model but predicted by some extensions of it. Our present effort aims at determining the $e - \nu$ correlation coefficient at the level of 0.1 % (about 1 order of magnitude improvement over previous) by trapping ^{6}He in a laser Magneto-Optical Trap (MOT). The electron is detected via a combination of a multi-wire proportional chamber and a scintillator. The recoiling Li ions are detected via a focusing electric field that guides them onto a position-sensitive Micro-Channel Plate detector. By measuring the time of flight and the landing position of the Li ion its momentum can be reconstructed. Both the electron and Li momenta can be used for reconstructing the anti-neutrino momentum.

During the past year much progress has occurred in all fronts of the experiment. Graduate student David Zumwalt graduated in the Summer quarter of 2015: he worked on developing a very stable Li target, on improvements to deuterium beam monitoring and on laser-systems-related projects to improve trapping efficiency. Graduate student Ran Hong graduated in the Winter quarter of 2016: he produced a working multi-wire proportional chamber with excellent energy and position resolution and a scintillator to detect position and energy of beta hits; he developed calibration procedures that yielded unprecedented precision on our micro-channel plate detector and set up simulation software to begin the data analysis for the whole experiment.

We now can get data for a $\sim 1\%$ determination of the $e - \nu$ correlation coefficient in less than 3 days of running time, including calibrations. The experiment runs in a stable fashion. This has had immediate impact in our mode of operation and allowed us to begin a program for understanding and fixing sources of systematic uncertainties towards determination of the $e - \nu$ correlation coefficient.

*Physics Division, Argonne National Laboratory, Argonne, IL.
†LPC-Caen, ENSICAEN, Université de Caen, Caen, France.
‡Presently at Argonne National Laboratory, Argonne, IL.
§Paul Scherrer Institute, Villigen, Switzerland.
¶Department of Physics and Astronomy and National Superconducting Cyclotron Laboratory, Michigan State University, East Lansing, MI.
**Presently at Institut für Kernphysik, Johannes Gutenberg-Universität Mainz, Mainz, Germany.

In addition, we have made a first test of recent calculations of the Li charge distribution: we found good agreement on the ratio of $q = 2$ to $q = 1$ intensities, but the $q = 3$ to $q = 1$ ratio is much smaller than expected.

On a different front, we are exploring the possibility of using the Project8 idea to determine the shape of the ^{6}He beta spectrum. An article at the end of this section describes progress toward doing measurements in the P8 setup with a gaseous ^{131m}Xe source.

3.2 Improvements of the ^{6}He laser trapping efficiency

Y. S. Bagdasarova, K. Bailey*, D. Carlton, X. Fléchard†, A. García, R. Hong‡, M. Kossin, A. Knecht§, A. Leredde*, E. Liénard†, G. Leum, P. Müller*, O. Naviliat-Cuncic¶, T. P. O'Connor*, J. Pedersen, E. Smith, M. G. Sternberg, J. Stiebritz, D. W. Storm, H. E. Swanson, F. Wauters**, and D. W. Zumwalt

This past year, the ^{6}He setup[1] has reached its full potential in terms of trapping efficiency after numerous upgrades of the vacuum and laser systems. The acquisition of a new CMOS camera has allowed a 3-dimensional view of the first Magneto-Optical Trap (MOT) once added to the existing CCD camera. By precisely centering the trap in the vacuum chamber, the trapping efficiency, which differs for the isotopes ^{4}He and ^{6}He if the trap is not centered, became more reliable. As a consequence, we were able to trap ^{6}He with the same efficiency as ^{4}He after optimizing the trapping parameters thus obtaining a much higher number of trapped ^{6}He. In an optimized configuration, the peak production rate is $\sim 2 \times 10^{10}$ ^{6}He/s and the trapping efficiency is usually greater than 1×10^{-7} which leads to a number of trapped atoms >2000. Shortly after this upgrade, we focused on the high-sensitivity detection system for a trap containing a very small number of atoms (as is always the case with ^{6}He) using a 706 nm laser beam tuned on resonance with the 2^3P_2 to 3^3S_1 transition. The scattered light is then detected by an imaging system made of a telescope and an iris in order to increase the signal-to-noise ratio (SNR). The optimized signal of 5 Hz/atom allows for a detection threshold down to 20 trapped atoms and translates into a very clean signal on which fine tuning of the trap parameters can be performed to further increase the efficiency.

Other improvements have been made to improve the overall SNR of the β-recoil-ion detection system. Among them, a recirculation system of the ^{6}He atoms inside the discharge source increases the probability for the atoms to be excited to their metastable state in order to be trapped. Switching to recirculation mode consists of closing the valve V2 (Fig. 3.2-1) going to the roughing pump and redirecting the exhaust of the 250 l/s turbo pump towards

*Physics Division, Argonne National Laboratory, Argonne, IL.
†LPC-Caen, ENSICAEN, Université de Caen, Caen, France.
‡Presently at Argonne National Laboratory, Argonne, IL.
§Paul Scherrer Institute, Villigen, Switzerland.
¶Department of Physics and Astronomy and National Superconducting Cyclotron Laboratory, Michigan State University, East Lansing, MI.
**Presently at Institut für Kernphysik, Johannes Gutenberg-Universität Mainz, Mainz, Germany.

[1] CENPA Annual Report, University of Washington (2015) p. 36.

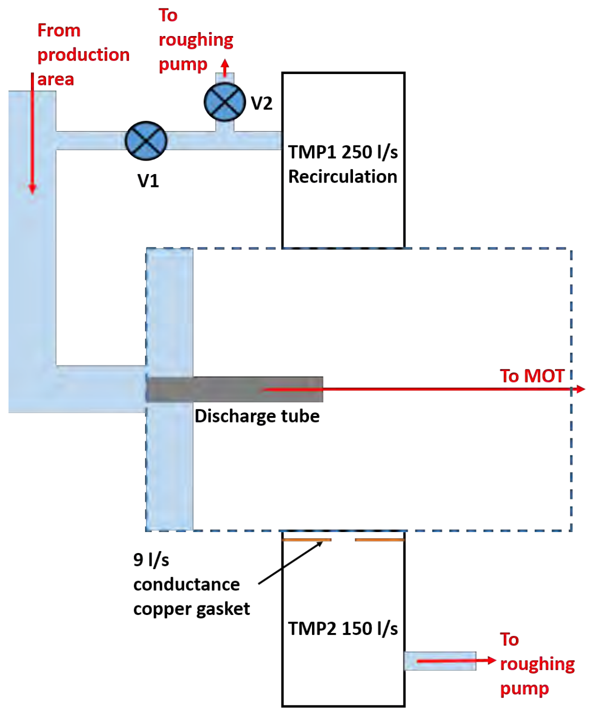

Figure 3.2-1. Sketch of the discharge chamber and the recirculation setup. The recirculation mode is activated by opening V1 and closing V2 while the turbomolecular pump (TMP2) constantly pumps on the chamber with a reduced pumping speed.

the entrance of the discharge source. In addition, the conductance of the 6" flange of the 150 l/s turbo pump is limited by an initially blank copper gasket which has been drilled with a 1-cm-diameter hole resulting in a 9 l/s conductance. This last modification increases the number of passes of the helium atoms inside the discharge before their decay. A single pass in the recirculation system is expected to be short compared to the 807 ms lifetime of ^{6}He. As a result, the gain factor before limiting the conductance of the 150 l/s turbo pump was approximately 2 and increased to 2.7 after adding the copper gasket.

In the next chamber, the 150 l/s turbo molecular pump has been replaced by a 360 l/s pump in order to compensate for the reduced pumping speed in the discharge chamber. ^{6}He test runs have shown that the reducing factor of the diffuse background due to the higher pumping speed was equal to the ratio of the final to initial pumping speed: 360/150=2.4.

On the MOT-to-MOT transfer, the atomic shutter, which opened periodically each time the trapped atoms were pushed to the second MOT, has been removed as its outgasing rate started to reduce significantly the lifetime of the first MOT and reduced the overall efficiency. To compensate for the background reduction factor (~ 3.75) from this shutter on the diffuse ^{6}He rate, the 1-cm-diameter-aperture tube on which it was clamped was replaced by a tube with a conductance 4 times lower. Unfortunately, the reduced diameter of the new tube also impacts the transfer efficiency by about a factor of two, leaving it at $\sim$10%.

Since September 2015, the detection rate has increased from 0.75 Hz to 4 Hz corresponding to a number of trapped atoms in the second MOT > 1000. A first data set was taken in October 2015 over four days leading to 100,000 good coincidences at the end of the data analysis. More recently, in March 2016, a set of about 450,000 good coincidences has been taken in less than 3 days. The stability of the system is now good enough such that a 1% measurement of $a_{\beta\nu}$ can be obtained within 3 days.

Further improvements of the laser system are under investigation to further improve the SNR. The largest gain would be a 2-dimensionnal optical dipole trap, confining the atoms radially as they transfer from MOT1 to MOT2. At most, this could result in a gain factor of 10 if the transfer efficiency reaches 100 %. Along with this improved transfer, the conductance between the two MOTs could be reduced, leading to a SNR close to what is needed for a 0.1% measurement of $a_{\beta\nu}$.

3.3 Determination of the electric field, MOT shape, and position

Y. S. Bagdasarova, K. Bailey*, D. Carlton, X. Fléchard†, A. García, R. Hong‡, M. Kossin, A. Knecht§, A. Leredde*, E. Liénard†, G. Leum, P. Müller*, O. Naviliat-Cuncic¶, T. P. O'Connor*, J. Pedersen, E. Smith, M. G. Sternberg, J. Stiebritz, D. W. Storm, H. E. Swanson, F. Wauters**, and D. W. Zumwalt

Systematic studies using MC simulations have shown that a is particularly sensitive to uncertainties in the electric field parameters, the magneto-optical trap (MOT) position (X_{MOT}, Y_{MOT}, Z_{MOT}), and the MOT shape (σ_X, σ_Y, σ_Z). We are exploring and comparing the various ways to measure these parameters. These methods along with their known uncertainties are listed in Table 3.3-1.

The main improvements for the electric field over the last year involved noise-filtering the electrode voltages, studying transient times for voltage stability, and preparing a high-voltage (HV) divider system to monitor all the electrode voltages simultaneously. With the new micro-channel plate (MCP) configuration where the MCP is mounted directly to the bottom electrode, excessive high-frequency noise (10 MHz) was being picked up by the MCP when the HV was on. To attenuate the noise, we built a low-pass filter box containing 100-kΩ resistors for each HV lead, where the choice of resistance assumed pF capacitance for the cables. This reduced the noise to the typical 20-30 kHz seen for the old configuration. Additionally, we used the HV probe to measure the stabilization time of the voltages upon ramping. Fig. 3.3-1 shows the probe reading on the highest voltage over 2.5 hours once the supplies have been ramped to 23 kV from a "cold" state, meaning they were powered on but outputting zero for days prior to ramp. The voltage initially increases by about 5 V in the first hour since the ramp but then steadily relaxes at a rate of -0.8V/11 hrs (0.004%/11 hrs).

*Physics Division, Argonne National Laboratory, Argonne, IL.
†LPC-Caen, ENSICAEN, Université de Caen, Caen, France.
‡Presently at Argonne National Laboratory, Argonne, IL.
§Paul Scherrer Institute, Villigen, Switzerland.
¶Department of Physics and Astronomy and National Superconducting Cyclotron Laboratory, Michigan State University, East Lansing, MI.
**Presently at Institut für Kernphysik, Johannes Gutenberg-Universität Mainz, Mainz, Germany.

Item	Calibration	Purpose	δx Achieved	$\delta x/x$	δx Goal
1	HV Monitoring	Electrode Voltages (EField)	0.5 V	0.02%	0.5 V
2	Mechanical Measurement of Electrode Array	Electrode Spacing (EField)	13 μm	0.05%	13 μm
3	MOT Imaging	Z_{MOT} σ_Z	33 μm 24 μm	0.04% 2.7%	10 μm 10 μm
4	^{4}He/^{6}He Penning Ion MCP Image	X_{MOT} Y_{MOT} σ_X σ_Y	7 μm 7 μm 6 μm 6 μm	0.4% 1% 0.7% 0.8%	20 μm 20 μm 20 μm 20 μm
5	^{4}He Photoion TOF in Non-uniform E Fields	Array Geometry (EField) Z_{MOT}	- -	- -	13 μm 10 μm
6	^{4}He Penning Ion Rate in Hill Potentials	Z_{MOT} σ_Z	- -	- -	10 μm 20 μm

Table 3.3-1. List of calibrations for the determination of the electric field and MOT parameters.
-Dashes signify studies still in progress.

Based on this we conclude that the HV should be ramped an hour prior to data-taking to ensure a constant electric field. Eventually, more irregular fluctuations can and do occur. To observe and account for these fluctuations, each electrode will be monitored with the HV-divider design described in (Sec. 3.5) of this annual report.

In addition to the electrode voltages, the array geometry must be known accurately in order to model the field correctly in the MC simulation. The mechanical measurement of the electrode thicknesses and spacings for this purpose (Item 2) is described in section 3.3 of the previous annual report[1]. This year we have calibrated the CCD camera imaging of the ^{4}He MOT (Item 3) in order to measure Z_{MOT} to 33 μm with respect to the MCP position.

One method in progress to cross-check the field and MOT parameters obtained with the calibrations above is to measure the time-of-flight (TOF) spectra of photoionized ^{4}He and ^{6}He atoms in the MOT (Item 5). The atoms are photoionized with a pulsed nitrogen laser that is hand-aligned with the MOT by maximizing the rate of photoions on the MCP. The pulse from the laser is also fed into a photodiode to serve as a trigger for the TOF measurement. The resulting TOF spectra are then compared to the simulated spectra for the parameters obtained using calibrations 1-3. In order to decouple the many parameters that define the field, such as the individual electrode positions and voltages, from Z_{MOT}, the ions must be transported through several different non-uniform fields. The largest source of uncertainty in this calibration comes from the shape of the N2 laser profile and its alignment with the center of the MOT. Presently, we have issues reproducing data with the MC simulation.

[1]CENPA Annual Report, University of Washington (2015) p. 39.

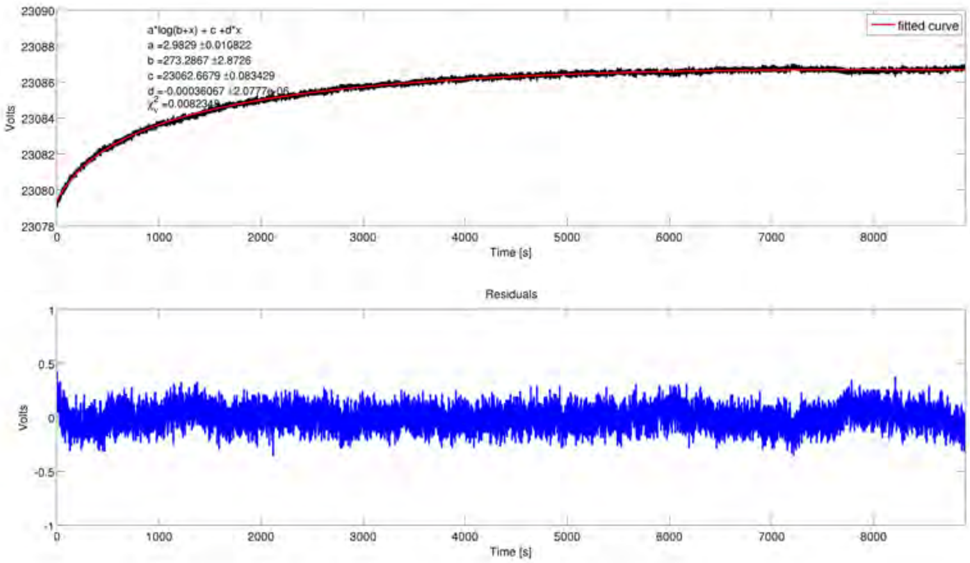

Figure 3.3-1. Probe reading of highest voltage over time after ramping HV supplies to 23 kV from 0 kV.

We are also in the process of evaluating a new laser-independent way to measure Z_{MOT} and σ_Z (Item 6). In this method we create a smooth hill-like potential at the position of the ^{4}He MOT, as pictured in Fig. 3.3-2 (*left*), and scan it across the MOT by adjusting the voltage of the top electrode (E6). Only the penning ions below the potential maximum (located at Z_0) will travel to the MCP, which allows us to obtain the time-averaged MOT cummulative distribution as a function of Z_0 ($CDF(Z_0)$) and fit Z_{MOT} and σ_Z. The change in Z_0 per kV on E6 is ~ 0.6 mm/kV. Due to the narrow output range of the HV supplies (5 kV), two different voltage configurations (labeled Lo and Hi) were needed to scan through the entire MOT profile ($\sim$ 4 mm). The resulting $CDF(Z_0)$ is shown in Fig. 3.3-2 (*right*). The 100 μm jump between the Lo and Hi configurations has not yet been explained but is under investigation.

One advantage of the "hill potential" calibration is that Z_0 is much less sensitive than the ^{4}He TOF spectra to systematic scaling or individual offsets of the electrode voltages ($<$ 10 μm/0.05% on closest electrode, based on simulation). Z_0 is also insensitive to offsets of X_{MOT} and Y_{MOT} ($<$ 1 μm/1 mm). However, it may be sensitive to the modeling of the electrode array geometry which will be determined by simulation. Throughout the scan, the magnetic field increasingly deflects the penning ions which causes the collected image to move across the MCP up to 1 mm. Since the image partially falls on the MCP mask, this motion affects the accuracy of the measured rate, and thus the CDF profile. The severity of this effect will be determined by simulation and accounted for in the analysis.

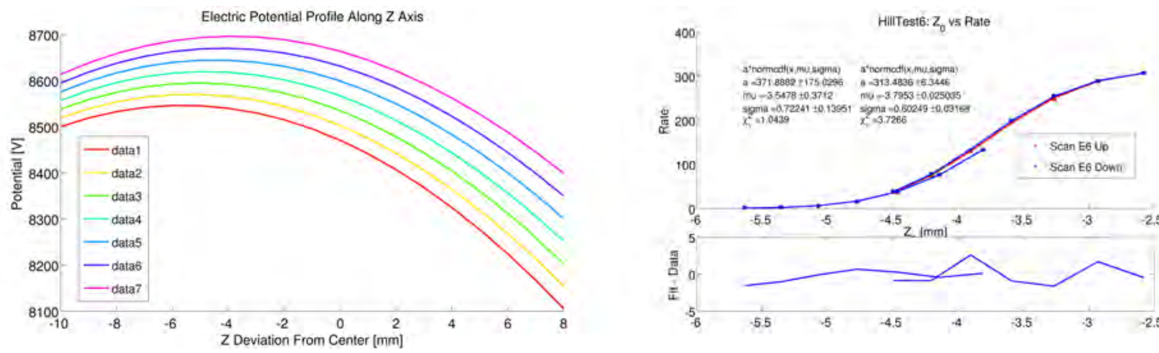

Figure 3.3-2. Hill potential calibration with ^{4}He penning ions. *Left:* $V(Z)$ for the hill potentials where position of maximum Z_0 $(E_z(Z_0) = 0)$ is scanned through the MOT region. Different colors represent different settings on E6. *Right:* Fit and residuals of the ^{4}He penning ions rate as a function of potential maximum position $Z_0$for the Lo and Hi MOT region field sweeps.

The X_{MOT}, Y_{MOT}, σ_X, and σ_Y are obtained by fitting the MCP image of the H_2^+ residual gas ionized by collisions with the MOT (penning ions) (Item 4). The thermal broadening of the MOT due to initial momentum of the penning ions ($\sigma_{Th} = 170$ μm)[1] is subtracted from the widths. The uncertainty in the position is from the fit and the MCP position accuracy determined from calibration.This calibration allows a direct comparison of these parameters for ^{4}He and ^{6}He, as well as a method to monitor them throughout the experiment as seen in Fig. 3.3-3.

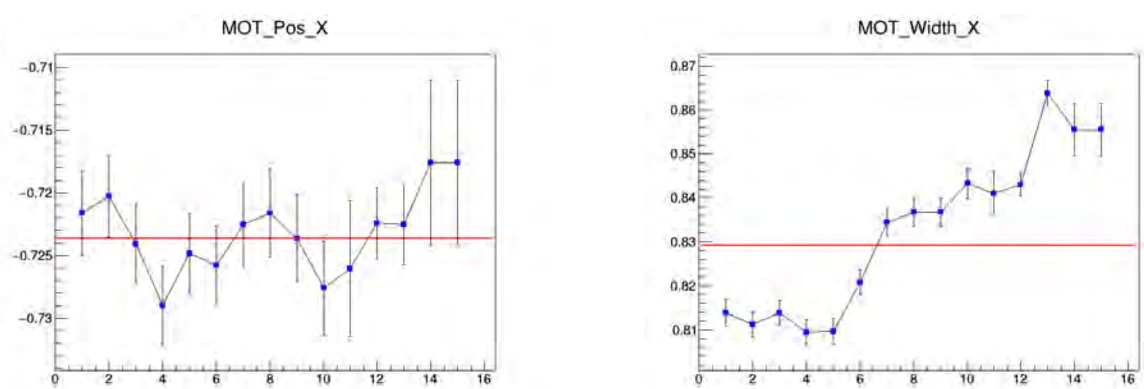

Figure 3.3-3. Monitoring of the position and shape of the MCP penning ions image during the most recent ^{6}He run on 03/07/2016. Horizontal axis marks consecutive runs, about 1-2 hours apart.. *Left:* MCP penning ions image position in X [mm] vs run number. *Right:* MCP penning ions image σ in X [mm] vs run number.

[1]Ran Hong, *Developments for a measurement of the β-ν correlation and determination of the recoil charge state distribution in ^{6}He β decay*, PhD Thesis, University of Washington, 2016.

3.4 Simulation and data analysis

Y. S. Bagdasarova, K. Bailey*, D. Carlton, X. Fléchard†, A. García, R. Hong‡, M. Kossin, A. Knecht§, A. Leredde*, E. Liénard†, G. Leum, P. Müller*, O. Naviliat-Cuncic¶, T. P. O'Connor*, J. Pedersen, E. Smith, M. G. Sternberg, J. Stiebritz, D. W. Storm, H. E. Swanson, F. Wauters**, and D. W. Zumwalt

Significant additions to the data analysis in the last year were the micro-channel plate (MCP) position reconstruction calibration, measurement of the background contribution from untrapped ^{6}He, the time-of-flight (TOF) spectrum timing calibration, and monitoring of the MOT position and shape with the MCP penning ion image and the photion TOF (Sec. 3.3). Much of this work has been performed by Ran Hong and is described in further detail in his PhD thesis[1].

The hit position of an event on the front MCP is proportional to the difference of charge-pulse arrival times at the two ends of the delay line anodes underneath the MCP plates. Calibrating the position reconstruction consists of locally correcting distortions of the reconstructed image of the MCP mask to match the true geometry of the mask (Fig. 3.4-2a).

The MCP mask image is generated by diffuse (untrapped) ^{6}He decays. In the calibration, the grid cross points and three points in between are first located for each grid square as shown by the crosses in Fig. 3.4-2b. Coefficients of local 2nd-order polynomials are then fit in order to transform the cross points of each grid square to their ideal locations. The local coefficients for each square are then imported into the Analyzer to apply the corrections to subsequent experiment runs. To correct the reconstructed MCP position using the position calibration, the Analyzer algorithm first identifies which square each event belongs to before applying the transformation. In the process, it enforces a fiducial grid area cut as shown in Fig. 3.4-2c.

To determine the accuracy of the MCP position calibration, grid cross point locations from two corrected MCP images are compared with one another. Fig. 3.4-2d is a histogram of the differences in corresponding cross point locations, with a mean deviation $\mu = 7.8$ μm and $\sigma_{rms} = 4.4$ μm. The MCP resolution is taken as the mean of the Gaussian smearing widths of the rising and falling edges of the grid lines and is $\sigma = 36$ μm. The resolution is input as a detector response parameter in the MC simulation. Much of the background from scattered and untrapped events can be eliminated by reconstructing the total energy (Q-values) of the events assuming they belong to either the first or second charge state of ^{6}Li,

*Physics Division, Argonne National Laboratory, Argonne, IL.
†LPC-Caen, ENSICAEN, Université de Caen, Caen, France.
‡Presently at Argonne National Laboratory, Argonne, IL.
§Paul Scherrer Institute, Villigen, Switzerland.
¶Department of Physics and Astronomy and National Superconducting Cyclotron Laboratory, Michigan State University, East Lansing, MI.
**Presently at Institut für Kernphysik, Johannes Gutenberg-Universität Mainz, Mainz, Germany.

[1] Ran Hong, *Developments for a measurement of the β-ν correlation and determination of the recoil charge state distribution in ^{6}He β decay*, PhD Thesis, University of Washington, 2016.

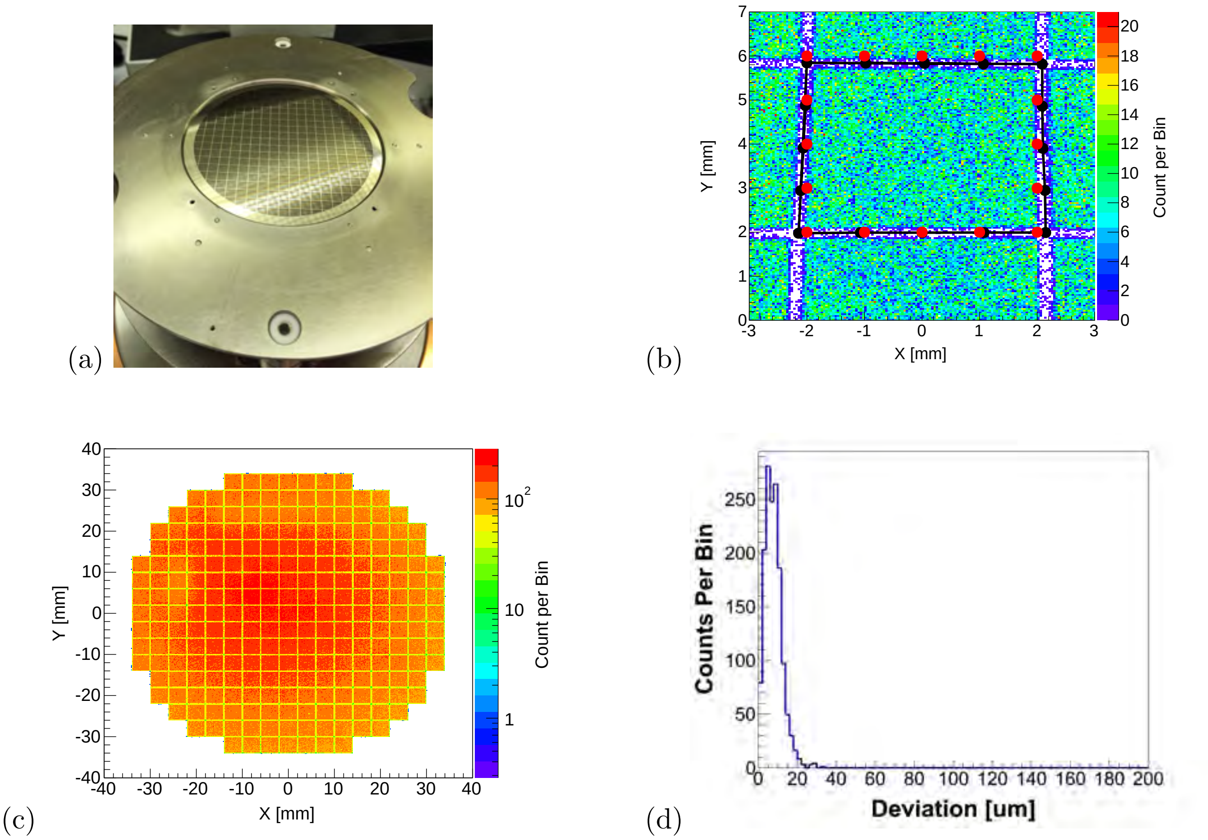

Figure 3.4-1. (a) MCP mask. (b) Identification of grid points (black) and correction to ideal (red). (c) Fiducial area cut from MCP position calibration. (d) Histogram of differences in grid point locations for two calibrated MCP images. $\mu = 7.8$ μm and $\sigma_{rms} = 4.4$ μm.

and then cutting out events with Q-values that are not within 3σ of the endpoint of the decay. However, some events from untrapped ^{6}He decays survive this Q-cut. To remove them from the sample, we measure the triple-coincidence TOF spectrum of untrapped ^{6}He decays and normalize it to the data in the TOF range where no contributions from the untrapped atoms can occur (10 ns $<$ TOF $<$ 110 ns) before applying the Q-cut (Fig. 3.4-2 *left*). We apply the Q-cut to both data and background and subtract the normalized background spectrum from the data (Fig. 3.4-2 *right*). After the Q-cut, the subtracted background is 0.6% of the spectrum.

In a true coincidence event, $0 = T_{MCP} - T_{PMT} - T_{zero}$, where T_{MCP} and T_{PMT} are the readout times for events reaching the MCP and the photomultiplier tube (PMT), respectively, and T_{zero} is the correction for the delay introduced by the detectors and electronics, such as electron transport through the scintillator and signal transport through cables. Two different calibrations were performed to determine T_{zero}. In the first calibration we measured the coincidence emission of γs and conversion electrons in the cascade decay of ^{207}Bi to the nuclear ground state of ^{207}Pb. After correcting for delays caused by the lifetime of the 1st excited state and the travel time of the electron, T_{zero} was determined to be -83.819 ns.

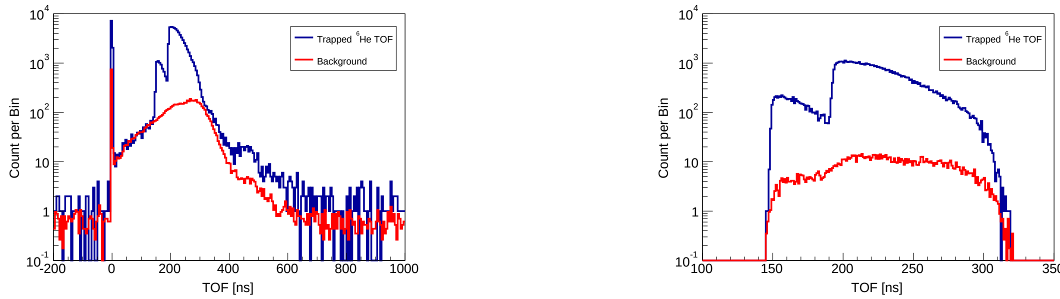

Figure 3.4-2. *Left:* Comparison of triple-coincidence TOF spectra from trapped and untrapped decays before the Q-cut is applied. The untrapped spectrum is normalized to the trapped spectrum in the region 10 ns < TOF < 110 ns. The S:B ratio is 28. *Right:* Comparison of TOF spectra from trapped and untrapped decays after normalization and the Q cut is applied. The red curve constitutes the background to be subtracted from the blue curve. The S:B is increased to 175.

For the second calibration, we analyzed the two coincidence TOF peaks of fast particles (backscattered βs, cosmic rays, beam-related background) detected by the MCP and PMT in sequence during the ^{6}He data run. The left and right peaks in Fig. 3.4-3 (*right*) correspond to those particles that hit the scintillator before the MCP and vice-versa. The difference between the left and right peak locations in the TOF is twice the time it takes a relativistic particle to travel the distance between the detectors, so T_{zero} is the midpoint between the left and right peaks and is determined to be -83.689 ns. For either method, we estimate uncertainties on the order of 200 ps due to the unknown penetration times of the detectors for different particles. Since the ^{6}He timing calibration data is included in every set of ^{6}He data, we use it to measure T_{zero} and estimate its uncertainty to be 200 ps. Ultimately, this level of accuracy is not enough to fix T_{zero} in the final fit of a, so we leave T_{zero} as a floating parameter in the fits.

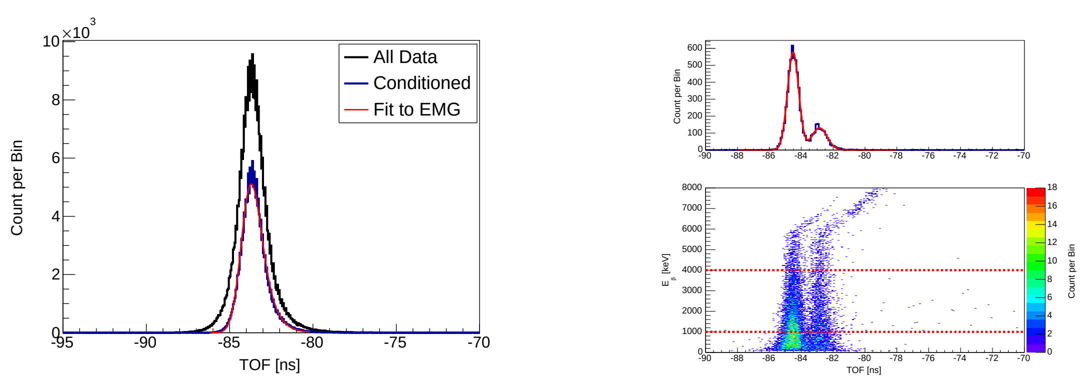

Figure 3.4-3. *Left:* TOF Spectrum for the ^{207}Bi cascade decay. The blue curve is data conditioned with a cuts on the scintillator energy (200 keV $< E_\beta <$ 1 MeV). The red curve is a fit to an exponentially-modified gaussian (EMG). *Right:* TOF-E_β histogram and projection for the timing-zero peaks from ^{6}He data run.

3.5 Monitoring of the high-voltage supplies for the electric field

Y. S. Bagdasarova, K. Bailey[*], D. Carlton, X. Fléchard[†], A. García, R. Hong[‡], M. Kossin, A. Knecht[§], A. Leredde[*], E. Liénard[†], G. Leum, P. Müller[*], O. Naviliat-Cuncic[¶], T. P. O'Connor[*], J. Pedersen, E. Smith, M. G. Sternberg, J. Stiebritz, D. W. Storm, H. E. Swanson, F. Wauters[**], and D. W. Zumwalt

Fig. 3.5-1 shows the high-voltage (HV) electrode system for the second ^{6}He Magneto-Optical Trap (MOT2). It consists of six Spellman MP Series regulating 5-kV supplies which are floated and stacked using Ultravolt EFL 30-kV isolators in order to provide about 30 kV on the sixth electrode. The supplies are remotely controlled via the isolators, which limit the accuracy of the high voltage output to 0.2% for each supply. If this uncertainty is systematic across all supplies, it registers as an overall uncertainty in the electric-field strength. If this uncertainty differs across supplies, it registers as an uncertainty in the electric-field shape.

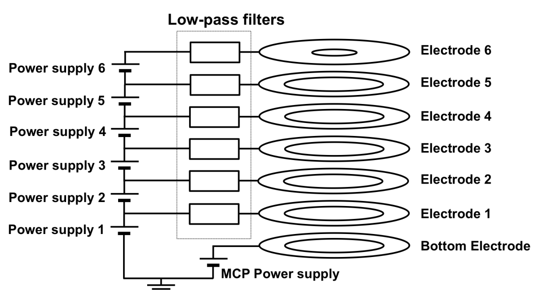

Figure 3.5-1. High voltage electrode array for the MOT2 chamber, where the decay of ^{6}He atoms are observed.

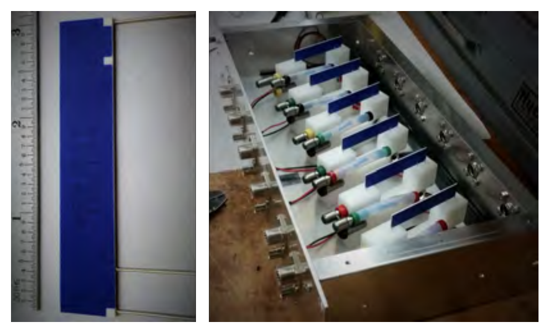

Figure 3.5-2. *Left:* A 1:10,000 high voltage divider for the new supply monitoring system. *Right*: Installation of monitoring system components in low-pass filter box.

To achieve the desired 1% measurement of a, the uncertainty in the absolute accuracy of the individual supply voltages must be reduced to 0.05%. Currently, a 0.02% accuracy HV probe is used to calibrate the supplies one by one for a single setting and then set to continuously monitor the top electrode voltage over time. However, this does not provide a way to measure or monitor the individual supplies all at once, *in situ*, which is needed to discriminate fluctuations in the field strength vs field shape over time and to ensure that the conditions measured during calibration stay reliable for the duration of the experiment run.

To make this possible, we are developing a monitoring system capable of simultaneously measuring the outputs of all six supplies with respect to ground via six high-voltage dividers. These dividers are specified for a voltage ratio of 1:10,000 with a voltage coefficient

[*] Physics Division, Argonne National Laboratory, Argonne, IL.
[†] LPC-Caen, ENSICAEN, Université de Caen, Caen, France.
[‡] Presently at Argonne National Laboratory, Argonne, IL.
[§] Paul Scherrer Institute, Villigen, Switzerland.
[¶] Department of Physics and Astronomy and National Superconducting Cyclotron Laboratory, Michigan State University, East Lansing, MI.
[**] Presently at Institut für Kernphysik, Johannes Gutenberg-Universität Mainz, Mainz, Germany.

of resistance (VCR) of >0.07 ppm/V and a temperature coefficient of resistance (TCR) of 10 ppm/°C (Fig. 3.5-2 *left*). Although their absolute tolerance is quoted as 1%, we will calibrate them individually against our 0.02% accurate HV probe.

In order to obtain the most reliable measurements of the electrode voltages, the monitoring system is being installed on the far side of the low-pass filters in Fig. 3.5-1, the closest feasible location to the electrodes themselves. To allow easy removal and minimize handling of the HV dividers during calibration, we sought a removable terminal block configuration to hold the monitoring system in place within the low-pass filter enclosure. However, since the filters are tightly housed in a grounded aluminum box and run at high voltages, off-the-shelf solutions were not readily usable without a redesign of the filter system.

Instead, we designed and fabricated a terminal block configuration in-house for the new monitoring system (Fig. 3.5-2 *right*). Acetal resin was chosen as an insulating material for its machinability and high surface resistivity, and rounded steel rods and banana jack fittings were used for conductive contacts to minimize corona discharge. Thus far, the system has been tested up to 23 kV without breakdown, and has made it through a series of short experimental runs without incident.

3.6 Recent data summary

Y. S. Bagdasarova, K. Bailey[*], D. Carlton, X. Fléchard[†], A. García, R. Hong[‡], M. Kossin, A. Knecht[§], A. Leredde[*], E. Liénard[†], G. Leum, P. Müller[*], O. Naviliat-Cuncic[¶], T. P. O'Connor[*], J. Pedersen, E. Smith, M. G. Sternberg, J. Stiebritz, D. W. Storm, H. E. Swanson, F. Wauters[**], and D. W. Zumwalt

Since last year, the production, the vacuum system and the laser setup of the ^{6}He experiment have significantly improved to finally achieve a high β-recoil ion coincidence rate and low background rate (Sec. 3.2). Triple coincidences, MWPC+PMT+MCP events (multi-wire proportional chamber, photo-multiplier tube, micro-channel plates), from trapped ^{6}He were first observed in late 2013 with a low rate of about 0.15 Hz. At this time, our first data set was made of about 1,500 events. In October 2014, a new set of about 4,000 events was taken followed by a 20,000 event run in February 2015. For these experiments, the rates were not reproducible and the detection system was not fully equipped with calibration tools. The game changed in September 2015 when the upgrades mentioned earlier improved the detection rate up to 1 Hz. Shortly after, fine tuning allowed us to progressively increase it up to 4 Hz. The two largest sets of data were taken in October 2015 (100,000 events) and March 2016 (450,000 events). A detailed analysis of the October data has been performed allowing us to test our data analysis tools and better understand our experimental setup.

[*]Physics Division, Argonne National Laboratory, Argonne, IL.
[†]LPC-Caen, ENSICAEN, Université de Caen, Caen, France.
[‡]Presently at Argonne National Laboratory, Argonne, IL.
[§]Paul Scherrer Institute, Villigen, Switzerland.
[¶]Department of Physics and Astronomy and National Superconducting Cyclotron Laboratory, Michigan State University, East Lansing, MI.
[**]Presently at Institut für Kernphysik, Johannes Gutenberg-Universität Mainz, Mainz, Germany.

The latest and highest-statistic-run is currently under analysis with the upgraded tools from the previous analysis.

A typical ^{6}He run starts in late afternoon after starting the ion source and the tandem Van de Graaff, starting and optimizing the laser system to achieve a high trapping and transfer efficiency and finally turning on all the detectors for a warming-up period. The trapped ^{6}He data are accumulated overnight until early morning the next day. Between an overnight run and the next one, day time is dedicated to calibration runs. First, a diffuse ^{6}He run is taken using the bypass described in the last CENPA annual report[1] for about 30 mn. The high number of single events on the MCP ($> 1 \times 10^7$) is used to calibrate the position response of the MCP looking at the shadow of a precision mask. Then a run of about 1h is taken with a ^{207}Bi calibration source in order to calibrate the energy response of the β detector. Finally, the laser system is switched to ^{4}He and a photoion time-of-flight (TOF) study is performed using the optimized uniform electric field of our experiment and weaker uniform fields in order to extract the time offset induced by various parameters such as cable length and time delays from the detectors and the data acquisition system. Knowing the electric field along the path of the photoions and measuring the time offset from this scaling study gives the absolute distance between the trap and the recoil ion detector.

October 2015 run

In October, the production was $\sim 1 \times 10^{10}$ ^{6}He/s, the trapping efficiency of the laser system was on the order of 8×10^{-8} and the transfer efficiency between the MOTs was $\sim 20\%$. Over 4 days of data taking, the detection rate fluctuated from 1 to 2 Hz mostly due to fluctuations of the trapping efficiency. After studying the possible sources of background, it turned out that the dominant one comes from diffusion of non-trapped ^{6}He into the detection chamber. This diffuse background was not affected by the trapping efficiency since only a very small fraction of the atoms are trapped. The signal-to-noise ratio (SNR) followed the fluctuations of the detection rate dominated by events coming from trapped atoms.

Each one of the four run days has been analyzed individually as conditions may have changed from one run to another. We match the TOF of a diffuse ^{6}He run to a TOF from trapped atoms in a non-physical region (10 ns $<$ TOF$<$ 110 ns) with no cut on the reconstructed kinematics to obtain the overall SNR. The kinematic cut on the reconstructed Q-value of the decay is then applied to both diffuse and trapped events and gives the final SNR for the meaningful TOF window. The best SNR was obtained on October 25th with a value of 13:1 before the Q-value cut and 64:1 after the Q-value cut. In the worst case, the SNR after the Q-value cut was only 28:1. After extracting the various parameters from the data such as the X, Y and Z positions and widths of the MOT and calibrating the detector responses, the TOF templates for $a_{\beta\nu} = -1/3$ and $a_{\beta\nu} = +1/3$ were generated and used to fit the experimental TOF spectra for each day. The four days give a value of $a_{\beta\nu}$ consistent with each other but off by about 10% compared to the expected value of $-1/3$. As a first high-statistics run, this was also the first opportunity to test and debug the analysis tools.

[1]CENPA Annual Report, University of Washington (2015) p. 36.

At the end, we concluded that higher statistics were required to split the data in different ways and search for sources of systematic effects. As the analysis was under way, the setup kept improving to eventually reach a higher efficiency and a reduced background by the end of February 2016.

March 2016 run

The latest and highest-statistics run with trapped ^{6}He was taken on March 7th, 8th and 9th with detection rates up to 4 Hz and a reduced background as compared to the October 2015 runs. The data-taking procedure was the same as before. Approximately 450,000 good coincidences were recorded in less than three days. This corresponds to a statistical uncertainty of about 1% for $a_{\beta\nu}$. The analysis is currently ongoing but preliminary results are already available. The SNR has been extracted for each day and is much higher than previously, with a peak value at 34:1 without the Q-value cut and > 200:1 after the cut. The associated systematic uncertainty, inversely proportional to the SNR, is thus strongly reduced. Currently, the experimental parameters are being extracted from the data to input into the simulation and generate the TOF templates needed to finalize the data analysis and obtain a value for $a_{\beta\nu}$.

3.7 Improvements of the ^{6}He production target

Y. S. Bagdasarova, K. Bailey[*], D. Carlton, X. Fléchard[†], A. García, R. Hong[‡], M. Kossin, A. Knecht[§], A. Leredde[*], E. Liénard[†], G. Leum, P. Müller[*], O. Naviliat-Cuncic[¶], T. P. O'Connor[*], J. Pedersen, E. Smith, M. G. Sternberg, J. Stiebritz, D. W. Storm, H. E. Swanson, F. Wauters[**], and D. W. Zumwalt

Over the last year the reliability of the Li target system has been improved. A technique was developed to cool the target continuously instead of following the feedback on temperature that tended to stress the air-cooling connections through vacuum and led to vacuum leaks in the past. A system to monitor the position of the stirring device has been implemented to avoid problems with the mechanical devices. A system to control valves for guiding the ^{6}He atoms either towards our counting station for monitoring production or to the discharge region for laser trapping was developed. The latter has allowed the monitoring and quick diagnosis of problems.

The last target was installed before the October 2015 runs and is still currently yielding excellent production in a stable manner in April 2016.

[*]Physics Division, Argonne National Laboratory, Argonne, IL.
[†]LPC-Caen, ENSICAEN, Université de Caen, Caen, France.
[‡]Presently at Argonne National Laboratory, Argonne, IL.
[§]Paul Scherrer Institute, Villigen, Switzerland.
[¶]Department of Physics and Astronomy and National Superconducting Cyclotron Laboratory, Michigan State University, East Lansing, MI.
[**]Presently at Institut für Kernphysik, Johannes Gutenberg-Universität Mainz, Mainz, Germany.

3.8 Recoil-ion charge-state distribution in the ^{6}He β-decay

Y. S. Bagdasarova, K. Bailey*, D. Carlton, X. Fléchard†, A. García, R. Hong‡, M. Kossin, A. Knecht§, A. Leredde*, E. Liénard†, G. Leum, P. Müller*, O. Naviliat-Cuncic¶, T. P. O'Connor*, J. Pedersen, E. Smith, M. G. Sternberg, J. Stiebritz, D. W. Storm, H. E. Swanson, F. Wauters**, and D. W. Zumwalt

Orbital electron shake-off is the process by which orbital electrons are excited into the continuum after a sudden change of the nuclear charge due to processes like β decay. The shake-off process results in different recoil-ion charge states in β decays and therefore affects the ion-momentum reconstruction in the ^{6}He experiment. The ion-energy dependence of the charge-state distribution affects the time-of-flight (TOF) spectral shape, so for the high-precision measurement of $a_{\beta\nu}$ it is important to know with high precision how the shake-off probability depends on the ion energy. As a ballpark estimate, completely ignoring this effect causes a $\sim 0.6\%$ shift in the extracted value of little a.

Theoretical calculations[1,2] of shake-off probabilities for ^{6}He decay for atoms in the ground state or the 2 $^3S_1$ metastable state, have been performed by Wauters and by Vaeck and Schulhoff and Drake. Interestingly, Schulhoff and Drake noticed that previous estimates of the ion-energy dependence of the charge distributions had neglected a contribution that interferes destructively with other processes and implies a much smaller overall effect. Until now, there are no measurements of the shake-off probabilities in the decay of ^{6}He atoms in the 2 $^3S_1$ metastable state, which is important for experiments with laser-trapped ^{6}He atoms. Therefore, we analyzed data taken in October 2015 with trapped ^{6}He atoms. The statistics we gathered are not yet enough to give support to one of the calculations over the other regarding the ion-energy dependence. However, Schulhoff and Drake's calculations predict about 2% of the decays should produce Li with charge state $q = 3$. We were able to establish an upper limit about 2 orders of magnitudes lower. In what follows we give more details on our findings.

To determine the ratio of events with charge state 3, an E_β threshold of 1 MeV is applied so that events under this condition are not lost due to the fiducial cut of the MCP. A TOF cut of 146.5 ns is used to separate out those events with charge state 3 as shown in Fig. 3.8-1. Due to the overlap between the charge states 2 and 3 in TOF, the number of events with TOF $<$ 146.5 ns is 85.5% of the number of all events with charge state 3 according to Monte Carlo simulations. This collection factor is used to correct the observed number of charge-state-3 events. The TOF spectrum including all three charge states is shown in Fig. 3.8-2

*Physics Division, Argonne National Laboratory, Argonne, IL.
†LPC-Caen, ENSICAEN, Université de Caen, Caen, France.
‡Presently at Argonne National Laboratory, Argonne, IL.
§Paul Scherrer Institute, Villigen, Switzerland.
¶Department of Physics and Astronomy and National Superconducting Cyclotron Laboratory, Michigan State University, East Lansing, MI.
**Presently at Institut für Kernphysik, Johannes Gutenberg-Universität Mainz, Mainz, Germany.

[1] L. Wauters, and N. Vaeck, Phys. Rev. C **53**, 497 (1996).
[2] E. E. Schulhoff and G. W. F. Drake, Phys. Rev. A **92**, 050701(R) (2015).

with the corresponding background TOF spectrum generated by the non-trapped ^{6}He atoms. After the background subtraction and correction due to the collection factor, the measured ratio between the number of events with $q = 3$ and the number of events with $q = 1$ or 2 is $(0.37 \pm 1.3) \times 10^{-4}$. This number is also the probability ratio of ending in these charge states: $P_3/(P_1 + P_2)$. We then calculated the upper limit of this ratio at the 90% confidence level, which is 2.4×10^{-4}.

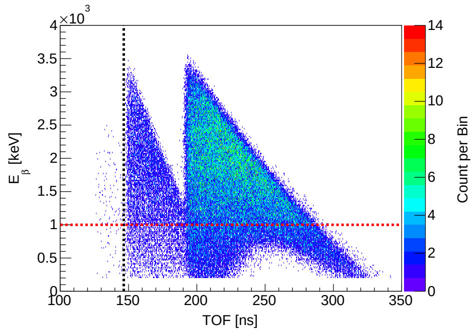

Figure 3.8-1. E_β-vs.-TOF 2D histograms for trapped-^{6}He data taken in October 2015. Q-value cuts are applied, while the background subtraction is not applied.

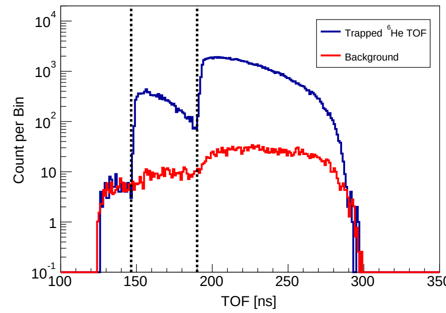

Figure 3.8-2. TOF spectra with the Q-value cuts. The background spectra (red curve) is overlaid. The vertical lines indicate boundaries between (low to high TOF) charge-state-3, charge-state-2, and charge-state-1 populations

To study the ion-energy dependency of the shake-off probabilities, one needs to reconstruct the initial energy of the recoil ions (E_{ion}). Therefore, for each event its charge state should be determined with no ambiguity. Because the upper limit of the probability of having an ion with $q = 3$ is at the 10^{-4} level, and the probability of having an ion with $q = 2$ is approximately 10%, we neglected the charge state $q = 3$ in this study. To separate the charge states 1 and 2, the E_β threshold was raised to 1500 keV, and the TOF cut for charge-state separation was 190.0 ns. The recoil-ion energy of each event is reconstructed, and the ion-energy spectra (Γ_1 and Γ_2) for the two charge states are shown in Fig. 3.8-3 and Fig. 3.8-4.

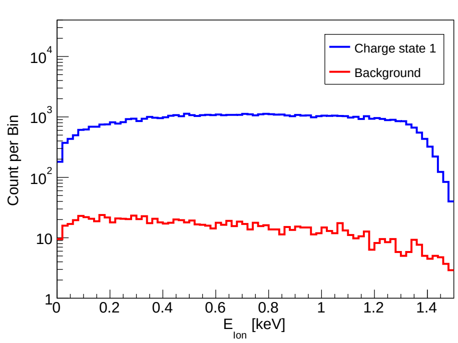

Figure 3.8-3. ^{6}Li recoil ion initial energy distributions the charge state 1. Background spectrum is plotted in red.

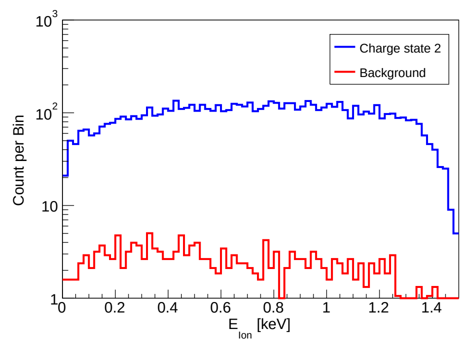

Figure 3.8-4. ^{6}Li recoil ion initial energy distributions for charge state 2. Background spectrum is plotted in red.

To first order the probability of having a recoil ion with charge state i depends on the ion energy (E_{ion}) linearly as $P_i(E_{ion}) = A_i + B_i E_{ion}$ $(i = 1, 2)$. $P_1(E_{ion}) + P_2(E_{ion}) = 1$ because the charge state 3 is neglected. When taking the ratio of background-subtracted Γ_2 and Γ_1, the intrinsic ion-energy distribution which depends only on the decay kinematics cancels because it is common to both charge states. The detector response also cancels if the MCP efficiency non-uniformity and the area of the calibration mask are neglected. Therefore, we fit the ratio Γ_2/Γ_1 to

$$R(E_{ion}) = \frac{A_2 + B_2 E_{Ion}}{1 - A_2 - B_2 E_{Ion}} \tag{1}$$

as shown in Fig. 3.8-5. The extracted values of A_2 and B_2 are $A_2 = 0.091(3)$ and $B_2 = 0.0084(45)$ keV^{-1}.

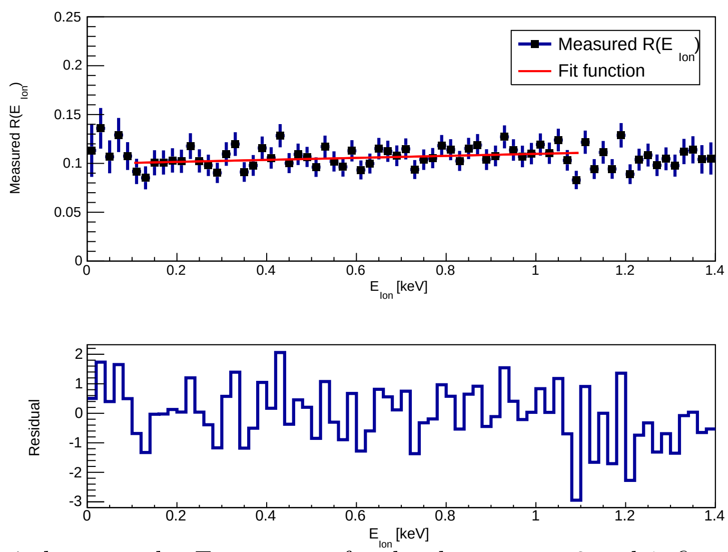

Figure 3.8-5. Ratio between the E_{ion} spectra for the charge state 2 and 1, fit to Equation 1 in the range 0.1 keV< E_{ion} <1.1 keV. Statistical uncertainties are shown, and residuals are plotted in the lower panel. The fitting domain was chosen to minimize dependence on systematic uncertainties.

The systematic uncertainties on $P_3/(P_1 + P_2)$, A_2 and B_2 are all negligible compared to their statistical uncertainties according to studies using Monte Carlo simulation. We compared these results to the calculation by Schulhoff and Drake. The calculated values of A_2 and B_2 are $A_2 = 0.0942(7)$ and $B_2 = 1.04(6) \times 10^{-3}$ keV^{-1} which agree with the extracted values from this measurement within 1σ and 1.6σ. However, the calculated value of $P_3/(P_1+P_2)$ is $1.86(7)\times10^{-2}$, approximately 100 times higher than this measurement. This disagreement is significant for the $a_{\beta\nu}$ measurement and needs to be addressed by improved atomic theory calculations. On the other hand, measurements of A_2 and B_2 with higher statistics are also important for determining the systematic uncertainty of $a_{\beta\nu}$ related to the shake-off effect. Furthermore, the population of trapped atoms in the 2 $^3P_2$ state and the calculations of shake-off probabilities for the 2 $^3P_2$ state are needed for more precise comparisons between calculations and measurements.

3.9 Development of a ^{131m}Xe source for a P8-style measurement of the beta spectrum

D. Carlton, A. García, D. Hamlin*, A. Leredde†, P. Müller†, M. G. Sternberg, H. E. Swanson, S. Wilbur†, D. M. Will

A possible way to search for tensor currents with enhanced sensitivity is to measure the shape of the beta spectrum and look for the interference between the axial vector and tensor currents. We are considering the possibility of measuring the beta energy spectrum of ^{6}He (extending up to $E_e \sim 3.5$ MeV) using a setup similar to that of Project 8 (focusing on detection of electrons with $E_e \sim 18$ keV). To test the response of the P8 system for electrons with higher energies we will use ^{131m}Xe which yields monoenergetic electrons with $E_e \sim$ 25, 129, 160 keV.

This will provide for a good comparison between the detection system response at 25 keV and 129 and 160 keV. By varying the magnetic field we plan to receive signals at about the same frequency for all energy ranges.

The isotope ^{131m}Xe ($t_{1/2} \sim 11$ d) is naturally produced in the decay of ^{131}I ($t_{1/2} \sim 8$ d) with a yield of about 1%. We estimate that a source of about 500 μCi of ^{131m}Xe is needed which implies about 50 mCi of ^{131}I. Because of the tendency of retention of iodine in the thyroid, 30 μCi of ^{131}I is already a safety concern, so we are developing a series of procedures to satisfy radiation safety requirements. We have been able to show that radioactive iodine from a solution of Na ^{125}I in 0.1 N NaOH can be precipitated and contained using silver loaded zeolite [1]. Plans for further tests using 5 mCi of ^{131}I are under review by the radiation safety officers at UW. With approval we expect to show that the appropriate amount of ^{131m}Xe is released and that the overall pressure remains below about10^{-6} Torr as needed for measuring the electron spectrum.

---

*Department of Radiation Oncology, University of Washington, Seattle, WA.
†Physics Division, Argonne National Laboratory, Argonne, IL.

[1] AGZB58 from F&J Specialty Products.

4 Precision muon physics

4.1 Overview of the muon physics program

M. Fertl, A. T. Fienberg, A. García, N.S. Froemming, D. W. Hertzog, R. Hong*, P. Kammel, J. Kaspar, K. S. Khaw, E. Muldoon, M. H. Murray, R. E. Osofsky, D. J. Prindle, R. A. Ryan, D. Salvat, M. W. Smith, H. E. Swanson, and F. Wauters†

The Precision Muon Group is involved in fundamental experiments that determine Standard-Model parameters or low-energy effective-field-theory constants, or provide sensitive tests for new physics. With strong CENPA support, the group has carried out a significant number of hardware development projects and has led several important data-taking periods. Our current experimental campaign involves the MuSun and AlCap experiments at the Paul Scherrer Institute, (P. Kammel, Co-Spokesperson) and the Muon $g-2$ experiment at Fermilab (D. Hertzog, Co-Spokesperson).

At PSI, we had three runs in 2015. MuSun acquired the balance of its muon capture on deuterium physics production data, enjoying a highly successful and smooth 12-week-long run. These data are being analyzed at present by Ph.D. students and new postdoc D. Salvat. We are scheduled for one more limited run in fall 2016 to carry out a set of systematics measurements. The AlCap experiment will determine key background rates and normalization procedures of low-energy protons and neutrons following muon capture on Al. These data directly affect the design of the muon-to-electron convertion experiments COMET and Mu2e. In 2015 the collaboration performed two runs at PSI and, pending ongoing data analysis, achieved the main objectives of this experiment.

The $g-2$ Project completed CD2/3 in June 2015 and a final progress review in March 2016. The construction is 70% complete. A major achievement has been the successful commissioning of the superconducting storage ring. Our UW team plays a leading role in field shimming, modeling, and measuring activities with Deputy Field Team Leader and Run Coordinator E. Swanson guiding the on-site team. CENPA built more than 400 new pNMR probes, which are used to measure the field. On the detector activities, we have received and tested all 1300 PbF_2 crystals and completed production of the SiPM readout boards. Together they form the core of the 24 calorimeter stations. We have built an extensive quality control testing process ensuring smooth assembly of components. Graduate student Fienberg led a test beam run at Frascati in February, providing the final confirmation of system performance. The UW group is leading the development of the offline analysis software in anticipation of data taking in spring 2017. We also continue to carry out a wide range of simulation efforts on many topics.

*Presently at Argonne National Laboratory, Argonne, IL.

†Presently at Institut für Kernphysik, Johannes Gutenberg-Universität Mainz, Mainz, Germany.

Two review articles[1] were published in the past year, along with several technical papers on detectors for $g-2$[2] and the isotope purification system for MuSun[3]. The thesis work of MuCap Ph.D. student S. Knaack was published in PRC[4]. Highlights of our research program are described in the reports that follow this introduction.

g-2

4.2 Overview of the $g-2$ experiment

M. Fertl, A. T. Fienberg, A. García, N. S. Froemming, D. W. Hertzog, P. Kammel, J. Kaspar, K. S. Khaw, R. E. Osofsky, G. Plunkett, M. W. Smith, and H. E. Swanson

Context

Muon $g-2$ is a special quantity because it can be both measured and predicted to sub-ppm precision, enabling the so-called $g-2$ test for new physics defined by $a_\mu^{\mathrm{New}} \equiv a_\mu^{\mathrm{Exp}} - a_\mu^{\mathrm{SM}}$. As a flavor- and CP-conserving, chirality-flipping, and loop-induced quantity, a_μ is especially sensitive to new physics contributions[5]. The current $g-2$ test gives:

$$\Delta a_\mu^{\mathrm{New}} = [(263 - 289) \pm 80] \times 10^{-11} \quad (3.3 - 3.6)\,\sigma. \tag{1}$$

The range here represents different, but standard, evaluations[6,7,8] of hadronic vacuum polarization (HVP) loops, and a common averaged value for hadronic light-by-light (HLbL) scattering. In fact, the range is even wider if all efforts to evaluate the SM are considered. If $\Delta a_\mu^{\mathrm{New}}$ is confirmed at a greater significance, the positive sign and relatively large magnitude – several times greater than the electroweak contribution – will provide important clues to the physics it is trying to reveal. This highly cited discrepancy continues to generate new physics speculations from supersymmetry (SUSY) to Dark Photons and beyond. To this end our UW group is helping to lead a next-generation $g-2$ experiment (E989) at Fermilab which aims to improve the BNL E821 final result[8] by a factor of 4, thereby reaching a relative precision of 140 ppb on a_μ.

The standard model (SM) contributions to a_μ are usually listed in five categories:

$$a_\mu^{\mathrm{SM}} = a_\mu^{\mathrm{QED}} + a_\mu^{\mathrm{Weak}} + a_\mu^{\mathrm{HVP}} + a_\mu^{\mathrm{Had-HO}} + a_\mu^{\mathrm{HLbL}} \tag{2}$$

[1] D. W. Hertzog, Annalen Phys. **528**, 115 (2016); T. P. Gorringe and D. W. Hertzog, Prog. Part. Nucl. Phys. **84**, 73 (2015).

[2] A. T. Fienberg *et al.*, Nucl. Instrum. Meth. A **783**, 12 (2015); A. Anastasi *et al.*, Nucl. Instrum. Meth. A **788**, 43 (2015).

[3] I. Alekseev *et al.*, Rev. Sci. Instrum. **86**, 125102 (2015).

[4] V. A. Andreev *et al.* [MuCap Collaboration], Phys. Rev. C **91**, 055502 (2015).

[5] A. Czarnecki and W. J. Marciano, Phys. Rev. D **64**, 013014 (2001); D. Stöckinger, J. Phys. G **34**, R45 (2007).

[6] K. Hagiwara *et al.*, J. Phys. G **38**, 085003 (2011).

[7] M. Davier *et al.*, Eur. Phys. J. C **71**, 1515 (2011).

[8] Muon g-2 Collaboration: G.W. Bennett *et al.*, Phys. Rev. D **73** 072003, (2006).

with a quadrature summed total uncertainty of $\sim 50 \times 10^{-11}$. The QED and Weak term uncertainties are totally negligible owing to impressive calculations. The hadronic vacuum polarization (HVP) contribution is determined from experiment through a dispersion relation that amounts to an energy-weighted integral of $e^+e^- \rightarrow hadron$ total cross sections. The uncertainty at 42×10^{-11} is non-negligible and dominates the overall δa_μ(SM). This contribution depends on the accuracy of the reported data. Its quoted uncertainty is arrived at from reported cross section errors and, when necessary, errors have been expanded to account for independent data sets that differ beyond statistical expectations. At the sub-percent level of needed precision, radiative correction uncertainties also are important. New experimental campaigns at BESIII and the upgraded VEPP-2000 facility in Novosibirsk, along with continued analyses of the large and varied BaBar data set, can be counted on to reduce the HVP uncertainty going forward. Higher-order HVP diagrams contribute a value of -98.4×10^{-11} to a_μ(SM), with negligible uncertainty.

An interesting new approach to determining the leading-order HVP contribution is emerging based on modern lattice calculations that are performed at the physical pion mass. Recently Chakraborty *et al.* reported a competitive 2% precision result for the dominant connected HVP diagrams[1]. The disconnected diagrams have been estimated to be quite small.

Higher-order hadronic light-by-light (HLbL) at present can only be estimated using hadronic models, which typically contain various strengths, weaknesses, and limitations. Assigning an uncertainty is almost a guess. We use 26×10^{-11}, which is a consensus reached by comparing models, but one could as well chose an uncertainty 50% larger, which many people do. More troubling is that these models could be badly wrong. Fortunately intense efforts using lattice QCD have been making rapid progress toward a prediction of HLbL with an uncertainty goal below 10%. Most recently, a collaboration started by T. Blum has achieved a breakthrough determination of HLbL connected diagrams at the physical pion mass[2]. The group's ambitious plans will include the disconnected diagrams to obtain a complete result at the desired precision.

Experiment

The muon anomaly is proportional to the ratio ω_a/ω_p, where ω_a is the anomalous precession frequency of the muon spin in a magnetic field and ω_p is a measure of that average magnetic field carried out using proton nuclear magnetic resonance (NMR). Both frequency measurements must control systematic uncertainties to 70 ppb. The statistics required to determine ω_a exceed those at Brookhaven by a factor of 20. Our UW group is involved in both the ω_a and the ω_p measurements. We are designing and building a significant array of hardware tools in both cases. Additionally, we have been modeling the optimization of muon storage in the ring, including tuning strategies of the superconducting inflector and the kicker field

[1] B. Chakraborty, *et al.*, arXiv:1601.03071.

[2] see, for example, L. Jin, T. Blum, N. Christ, M. Hayakawa, T. Izubuchi and C. Lehner, arXiv:1511.05198 and more recent seminar updates.

strengths, and the quadrupole and collimator geometries. A set of entrance imaging counters is also being designed to aid in the tuning phase.

The past year has again seen great progress with the experiment as a whole. Most notable is the successful commissioning of the storage ring and the beginning of precision field operations. Here, UW's Swanson — who won an Intensity Frontier Fellowship — has been named the experiment's first Run Coordinator. Our on-site UW team is carrying out a major role in shimming the magnet, which involves iterations of measuring and analysis, followed by small adjustments to various field-shaping components in the ring. Locally, we have been completing preparation of the electromagnetic calorimeters, which are the heart of the ω_a measuring system. As reported previously, we have published accounts of our success with prototypes of both lead-fluoride crystals and SiPM readout. The final design of the enclosures is being made now and installation of the system is scheduled for fall, 2016.

The Collaboration has grown to include 35 institutions and > 160 collaborators from 8 countries. D. Hertzog was recently re-elected as Co-Spokesperson and J. Kaspar has been named Detector Coordinator, a task that oversees all detector, electronic and DAQ systems operations once installation has been complete. E. Swanson will continue as Deputy Field Team Leader. The collaboration construction work has been divided around the generically named: Beam, Ring, Field, and Detector Teams. Recently, a significant Simulation / Offline Team has been created. Progress from all teams has been substantial as we summarize briefly.

The Beam design includes the booster, recycler, transfer lines, target station, decay beamline, and delivery ring subsystems that are necessary to create and deliver a bunched, 3.1 GeV/c polarized muon beam, which is purified of background pions and protons. This effort is led by Fermilab accelerator physicists with collaboration members providing some of the modeling. The installation of the new beamlines is in good shape and on schedule. A new end-to-end modeling effort is producing files of muon phase space and spin information at the end of the beamline; that is, at the entrance to the storage ring where our modeling programs take over to optimize the muon storage fraction.

The Ring team is responsible for building and operating the storage ring. They also provide the inflector, quadrupoles, collimator, and kicker subsystems. The team carries out simulations of muon storage and evaluates beam dynamic systematic uncertainties. UW student Froemming's exquisitely detailed Geant4 model of the storage ring and its components has led to modifications of the E821 Q1 outer electrostatic quadrupole plate material and support system and to the optimization of new asymmetric collimators, and it has provided the needed simulation justification to warrant construction of a new open-ended inflector magnet. These changes are all being implemented. Recently our studies and presentation of a first-order commissioning plan highlighted the need for a series of imaging devices along the path from the storage-ring entrance to just past the inflector. P. Kammel has designed these detector systems using SiPM technology with thin scintillating fibers. Lab tests are promising and we will report the design and progress in next year's report.

The Field team is presently shimming the magnet to ultra-high uniformity. The work involves mapping the field around the ring in the absence of vacuum chambers, using a suite of pulsed NMR (pNMR) probes incorporated into a rough-shimming trolley that circumnavigates the ring. UW grad student M. Smith developed the DAQ, the analysis routines, and a field modeling program that recommends mechanical adjustments of poles, top hats, and wedge shimming knobs following a complete field-map acquisition. The UW team built 400 new fixed pNMR probes and we are also in charge of preparing the NMR electronics. Grad student R. Osofsky and postdoc M. Fertl have recently been working on the design of a critical radial-field measuring system.

The Detector team provides the instrumentation to monitor the stored muon distribution and to measure the decay positrons from which the characteristic precession signal histograms are built. The UW group led a six-university consortium proposal to NSF to secure funding for the precession-frequency measurement. We are responsible for the electromagnetic calorimeter system, which consists of 24 stations, each having arrays of 54 PbF_2 crystals with large-area SiPM readouts. The electronics, testing, and mechanical supports are all developed and built at CENPA. At this time, all 1300 crystals have been received and carefully evaluated for quality control. Final optimization of the custom electronics is complete and all SiPM boards have been built. J. Kaspar is leading the design and production of these central detector systems. They are scheduled to be installed at Fermilab in fall, 2016.

Figure 4.2-1. Photo of the nearly 100 participants at the first $g-2$ Physics Week held in July, 2015 at the University of Washington.

The CD2/3a review of the Project was completed in June, 2015 and a final progress review was carried out in April, 2016. The construction Project is 70% complete and the supporting Accelerator Improvement Projects (AIP) and General Plant Projects (GPP) that underwrite beamline preparations and building infrastructure are either complete or making excellent progress. First beam commissioning is scheduled to begin in April 2017; this date has not changed in three years. With the construction nearly complete, the Collaboration has increasingly turned its attention toward the physics measurement program. To that end, we sponsored the first "Physics Week" here in Seattle in the summer of 2015, see Fig. 4.2-1. Nearly 100 participants enjoyed a week of talks ranging from theory to systematic uncertainties to analysis strategies.

4.3 PbF_2 calorimeter with SiPM readout

J. F. Amsbaugh, A. T. Fienberg, D. W. Hertzog, M. Huehn, J. Kaspar, K. S. Khaw, D. A. Peterson, G. J. Plunkett, W. Shaffer, M. W. Smith, and T. D. Van Wechel

After a stored muon decays into a positron and a neutrino, the positron curls inward through the opening in the C-shaped magnet. Twenty-four calorimeter stations are positioned along the inside storage-ring radius at discrete locations to intercept the positrons. Each calorimeter is composed of lead fluoride (PbF_2) crystals. Light from the positron showers is read out using silicon photo-multipliers (SiPMs). The signal provides positron energy and hit-time information. The characteristic $g-2$ spectrum — with its precession-frequency oscillation imprinted on an exponential decay — is built from the arrival times of the higher-energy positrons; that is, those above 1.8 GeV, where $E_{\max} = 3.1$ GeV.

Over the past year, we received and tested all 1300 PbF_2 crystals from the vendor and completed a meticulous set of quality control measurements related to optical transmission and physical dimensions. Crystals corresponding to an individual calorimeter station will be arranged in 6×9 arrays. A sorting program was used to associate crystals with specific calorimeters based on their common transverse dimensions. The choice of lead fluoride was based on its high density and intrinsically fast temporal response to energy deposition. In February we completed a test-beam run using the 450 MeV electron beam at Frascati. This final test re-confirmed the good light yield of ~ 1 pe/MeV using our "black-wrapped" crystal preparation. Because the Frascati beam time structure emits electrons over a 10 ns bunch width, events with multiple electrons exist, which can be studied to identify "pile-up" resolution vs. pulse-separation time. The resolution depends on the intrinsic light-collection time and the speed of the readout device (see below). Such events were analyzed and we demonstrated that we can resolve two electrons separated by 4 ns or more with nearly 100% confidence. This exceeds the $g-2$ detector performance specification.

Silicon photo-multipliers collect Čerenkov photons from showering positrons. They were selected because their operation is not disturbed by the 1.45 T magnetic field of the storage ring. We previously reported on the development of the pre-amplifier board designed by CENPA engineers[1]. It conveys the needed bias voltage to the 16-channel SiPMs and performs summing and amplification of the channel signals. Over the past year, this board was perfected through a number of prototype iterations. An external company was then contracted to mass-produce and stuff 1350 units, all of which have been received. At UW, we complete the job by gluing a custom-shaped heat sink to the board and then processing each through

[1]CENPA Annual Report, University of Washington (2015) p. 65.

a rigorous quality control station, see Section 4.6. Fig. 4.3-1 shows the final board from both sides.

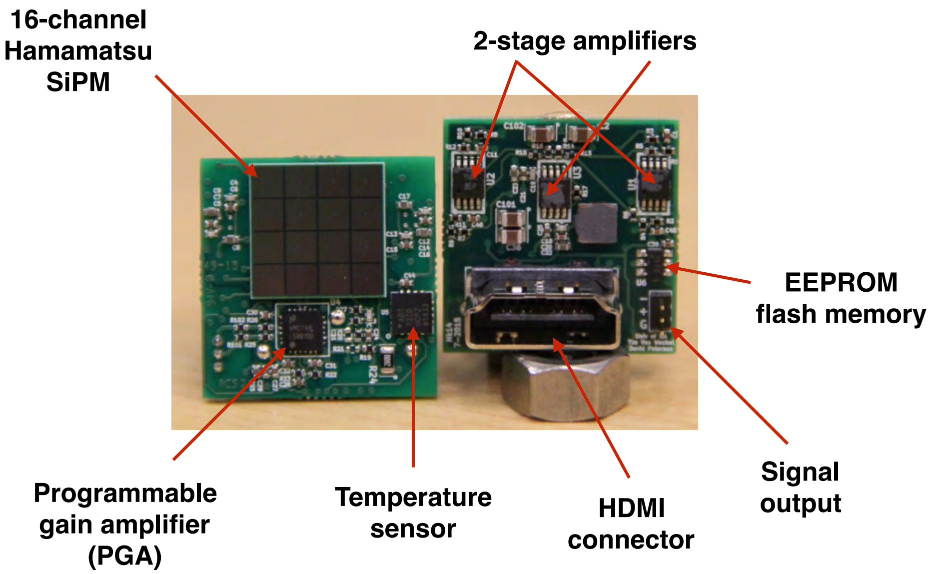

Figure 4.3-1. The final SiPM production board. The 16 channels of the SiPM are first summed in four sub-groups, then those groups are eventually summed and amplified with a user-controlled variable gain. An onboard temperature sensor provides key monitoring information which is important for gain stabilization. An EEPROM allows identification of modules and storage of gain settings. We have built 1350 of these boards and quality-control testing is in progress.

The pre-amplifier is based on a concept of the multi-staged transimpedance amplifier. In the first step, current pulses from four SiPM channels are added together and converted into voltage pulses in a fixed-gain transimpedance amplifier. In the second stage, the four partial sums are added together using a THS3201 op-amp operated at unity gain in voltage mode. The output stage drives an AC-coupled differential pair of coaxial cables, and is designed using a LMH6881 digitally controlled variable-gain amplifier. The multi-staged design provides a PMT-like pulse width of better than 5 ns, and it can be operated at very high (many MHz) rates, while exhibiting excellent gain stability. We have also worked closely with our Cornell colleagues to match the impedance between the SiPM output and the analog front-end motherboard for their 800 MSPS waveform digitizers.

Each SiPM is glued to a PbF_2 crystal using a high-index-of-refraction optical epoxy having good optical transmission above 300 nm. A gluing assembly line is shown in Fig. 4.3-2. These completed "detectors" are then wrapped in black Tedlar and mounted in a temperature-controlled calorimeter box, the final design of which is shown in Fig. 4.3-3. This box performs many important functions and hosts various services. At the front face, a calibration plate is mounted. It is built by our Italian colleagues and contains 54 small prisms that deflect laser light from individual fibers emanating from a fabricated fiber bundle that is uniformly illuminated by a diffuser lens, which in turn has been lit by light from a pulsed 407-nm laser, located externally. The detector signals, either from positron showers or from laser flashes,

Figure 4.3-2. Production setup demonstrating how SiPMs are glued to PbF_2 crystals using a high index-of-refraction optical epoxy.

are conveyed to the digitizers along a shielded and light-tight corridor; the signal path does not include any patch panels. The SiPM pre-amplifer boards are controlled using HDMI cables that connect each to a breakout board mounted within the box service compartment. The boards distribute the bias voltage levels and route the communication information which is controlled by an on-board BeagleBone computer. The housing around the crystal SiPM ends is cooled from the bottom by air fans and a duct-work corridor internal to the box.

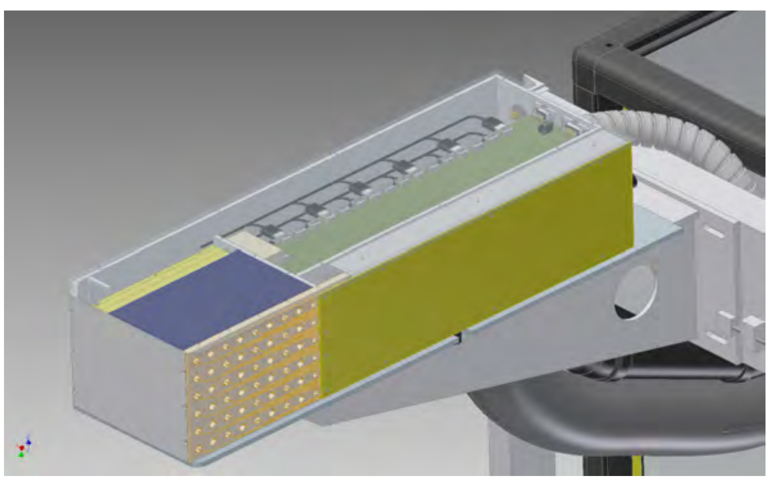

Figure 4.3-3. Inventor model of final calorimeter housing. The crystals are mounted in a 6×9 array on the left side of the box. The front panel holds 54 prisms that deflect laser light into the upstream ends of each crystal. The SiPMs (rear side, not visible) are powered and controlled by four breakout boards housed in the utility compartment to the right of the crystals. Visible below are cooling tubes to maintain constant temperature. The housing resides on the partially visible chariot that contains the readout electronics, power supplies, and other services.

4.4 Muon beam injection and storage studies

N. S. Froemming, D. W. Hertzog, J. Kaspar, and K. S. Khaw

The new muon $g-2$ experiment at Fermilab will require a 21-fold increase in the number of decay-positron events recorded compared to the previous experiment at BNL. Based on the studies that will be discussed in the subsequent paragraphs, the collaboration is moving forward to implement novel ideas such as a new open-ended superconducting inflector magnet design, better pulsed kicker magnets, thinned electrostatic quad plates, etc., in order to drastically improve the fraction of muons stored in the ring per injected muon bunch compared to the previous E821 experiment at Brookhaven. All these decisions have been made as a direct result of UW's efforts in simulating candidate designs using the *art* framework (see Section 4.5).

Components of the experiment relevant to muon injection and storage studies are modeled to reasonably high accuracy. Examples of storage-ring components include the superconducting inflector magnet refurbished from experiment E821 (Fig. 4.4-1(a)), the E989 pulsed magnetic field kicker plates (Fig. 4.4-1(b)), the electric quadrupole and new asymmetric collimator (Fig. 4.4-1(c) and (d)). The importance of the geometry, and hence the materials, cannot be overstated: the momentum acceptance of the storage ring is about $\pm 0.25\%$ $\Delta p/p_0$ (RMS), for example, so a small amount of material like the 2 mm NbTi-Cu-Al conductor coil of the inflector's end winding can result in multiple scattering, induce energy loss and hence reduce significantly the amount of storable muons.

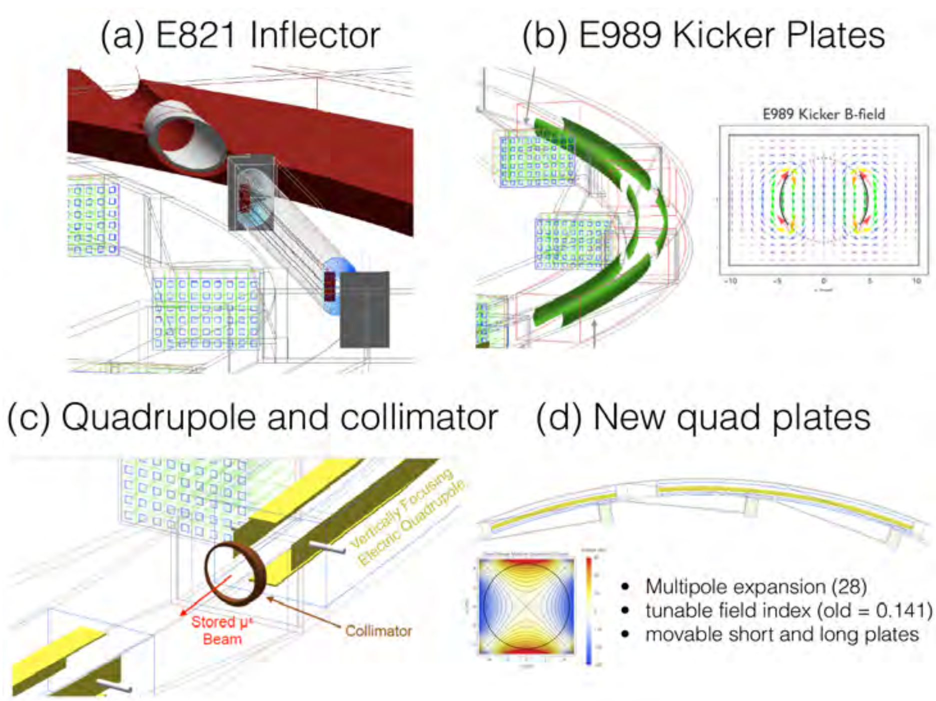

Figure 4.4-1. Sketches of the models implemented in the simulation.

Several important parameters that affect the beam dynamics at the end of the inflector are $(\Delta x, \Delta x^{'}, B_{\text{inf}}, R_{\text{inf}})$, where Δx and $\Delta x^{'}$ are the deviation in (x, $x^{'} = P_x/P_z$) from the centerline of the inflector, B_{inf} the inflector magnetic field and R_{inf} the rotational angle of the inflector. To maximize the number of muons injected into the storage ring, the mean position of the beam should be as close as possible to the inflector axis to avoid scattering and energy loss, as the inflector is very narrow (18 mm wide, 46 mm tall) and long (1.7 m). From a geometrical point of view, as the kickers are located in one quarter of the storage ring circumference downstream of the injection point, an ideal configuration for the kickers will be (x_{inf}, $x^{'}_{\text{inf}}$)=(0, 0) at the injection point. Sets of $(\Delta x, \Delta x^{'}, B_{\text{inf}}, R_{\text{inf}})$ satisfying this condition were found and were used for the subsequent studies related to the designs of the inflector, quadrupole plates and standoffs.

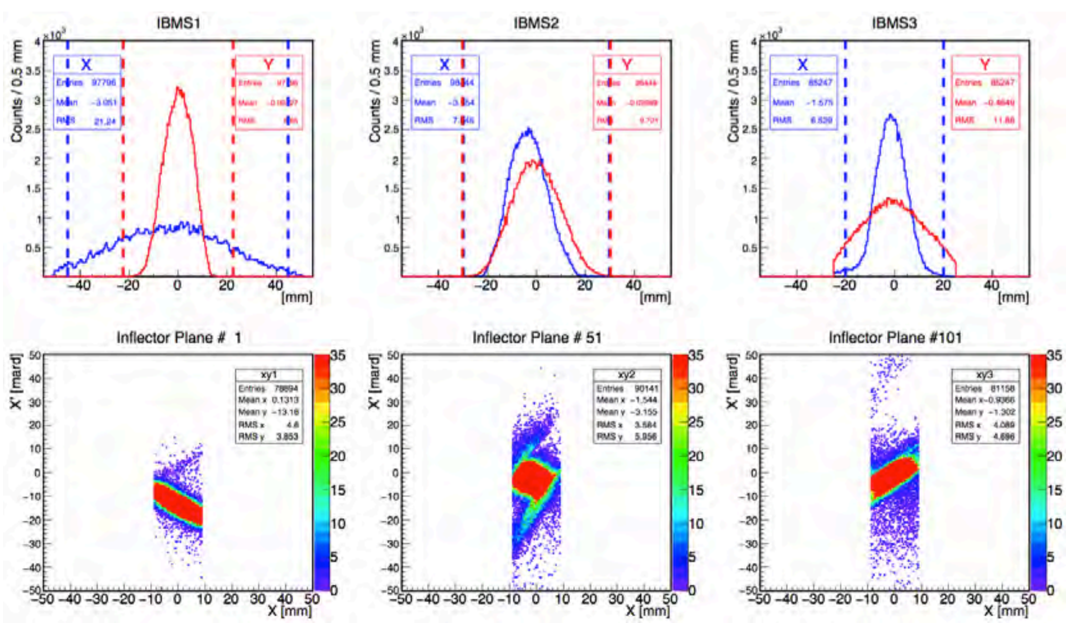

Figure 4.4-2. Beam profiles (x and y) at the IBMS detectors (1,2,3) and inflector planes (entrance, midpoint and exit) for P2 injection benchmark points.

In order to guide the beam through the tiny aperture of the inflector, a system of detectors known as the *Inflector Beam Monitoring System* (IBMS) was proposed by our group and will be installed at 3 different locations—at the backleg yoke (IBMS1), upstream of the inflector entrance (IBMS2), and downstream of the inflector exit (IBMS3). It is possible then to infer (Δx, $\Delta x^{'}$) from IBMS1, (x_{inf}, $x^{'}_{\text{inf}}$) from IBMS2 and ($x_{\text{inj}}, x^{'}_{\text{inj}}$) from IBMS3. The proof of principle was done using Geant4 simulation by defining virtual tracking planes at the IBMS locations. An example of the muon beam profiles that will be measured by the IBMS is shown in Fig. 4.4-2.

The dependence of the muon storage fraction on a) the kicker timing relative to the time the muon beam is injected into the ring and b) the kicker B-field magnitude (around 250 G) was also investigated. A weak dependence was observed. However, the effect of changing B_{kicker} is visible in the mean and RMS of the muon position, due to the large coherent-betatron-oscillation (CBO) amplitude introduced when the muon beam leaves the kicker at a non-zero $x^{\prime}$. The importance of materials to the storage fraction was also studied by changing the quadrupole materials like the plates and the standoffs. It was found that by moving them away from the region through which the muon will pass at injection, an extra 50% in the storage fraction can be achieved. A more realistic realization of extra stored muons is to build the outer plates of the first quadrupole (Q1) using thinner material and to switch the horizontal standoffs to vertical ones with some horizontal offsets. A similar factor can be achieved by making the inflector upstream and downstream windows open at both ends. A new inflector is being designed based on the outcome of this study.

4.5 MC simulation and offline data analysis framework

A. T. Fienberg, N. S. Froemming, D. W. Hertzog, J. Kaspar, K. S. Khaw, and G. J. Plunkett

The Monte Carlo (MC) simulation and offline data analysis for the muon $g-2$ experiment are implemented in *art*, an event-processing framework for particle physics experiments developed at Fermilab. The framework itself is written in the C++ language and is compatible with the Geant4 simulation package and the ROOT analysis framework. In addition to the *art* framework, a "tier-based" data analysis framework as shown in Fig. 4.5-1 is proposed and is currently being implemented. It is a conceptual framework that provides context for the data and computing algorithms that makes organization and collaboration of this scale possible.

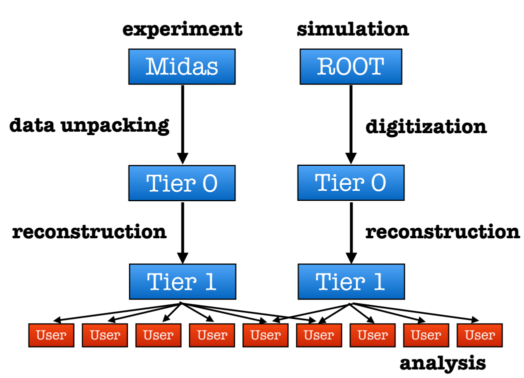

Figure 4.5-1. Offline data-analysis framework in the "Tier" structure. Tier 0 data from the experiment and the simulation are stored in the same format, allowing common reconstruction tools at Tier 1.

As shown in Fig. 4.5-1, the raw data for the experiment is stored in the MIDAS file format. A "MIDAS to art" module is implemented to convert the Midas banks to the *art*/ROOT format. This is the Tier 0 dataset. Then a series of reconstruction modules runs through the Tier 0 datasets to prepare the Tier 1 datasets which are for user analyses. On the other hand, for the MC simulation, the truth information generated by the Geant4 simulation is stored in the *art*/ROOT format. The truth information is then digitized and converted to the format as if coming from the experiment (Tier 0). The digitized datasets are processed with the same reconstruction algorithms as in the experiment and are stored as Tier 1 datasets.

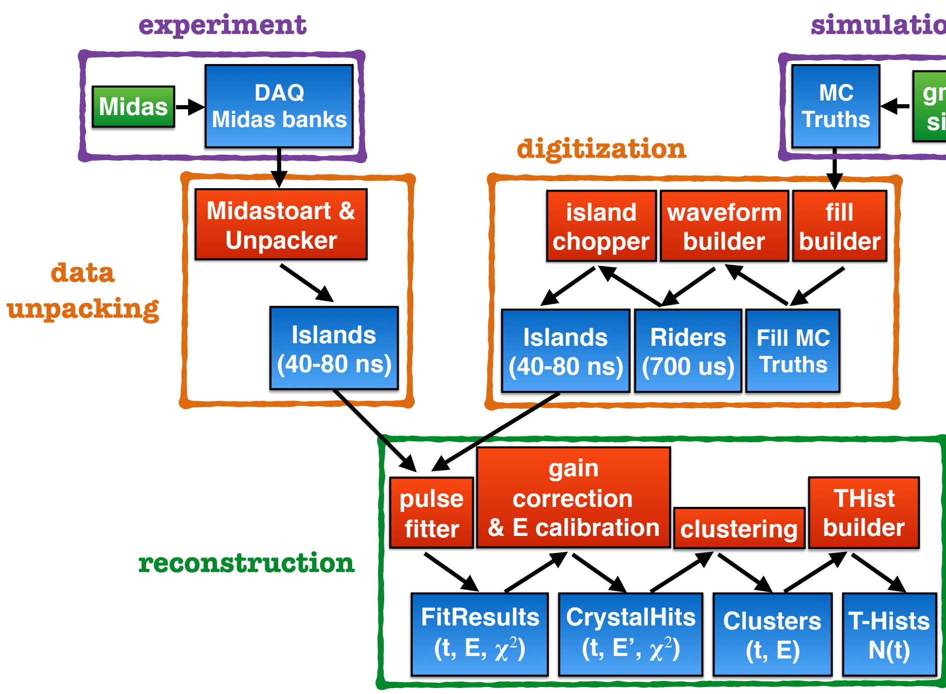

Figure 4.5-2. A detailed version of the framework. Boxes in blue are the data structures where the outputs from previous algorithms are stored and boxes in red are the processing algorithms.

A more complete picture of the offline analysis framework is shown in Fig. 4.5-2. Each stage of data processing (digitization, reconstruction) consists of a series of algorithms and data products. For example, the digitization stage starts with a fill builder which collects 10^4 muon decays and converts them into a single fill event. A waveform builder is then used to implement the SiPM responses and the digitizer behavior. Finally an island chopper is used to filter out regions of interest for further analysis. The reconstruction stage starts with the pulse fitter and ends with the T-histogram builder. Each algorithm will output a data product that serves as input to the next algorithm. By having this modularity, it is convenient to insert alternative reconstruction algorithms developed by different collaborators.

A series of mock data challenges is in place to test the readiness of the offline computing model. This includes the feasibility of generating large datasets (10^{11} muon decays) in terms of computational time and data storage, large dataset handling, and also exercising pulse fitting algorithms, calibration routines and clustering algorithms. The first mock data challenge, MDC0, began in January 2016 and is focused on testing the new offline analysis framework and on the unpacking of the DAQ data for data analysis. About 10^7 muon decays were generated and several glitches in the simulation were found and fixed. MDC0 helped us to better understand our simulation model and flaws in the reconstruction chain. All the digitization and reconstruction algorithms are now in place and are heading towards performance tuning stage. MDC0 will be concluded at the end of April 2016 and we will move on to MDC1, where we will utilize fast electromagnetic showers to speed up the simulation and to generate the large datasets expected for Run 2017 (about 10^{11} muon decays) which is equivalent to the experiment E821.

4.6 Quality control of production SiPM boards

M. Huehn, J. Kaspar, and K. S. Khaw

The core of the PbF_2 calorimeter is the silicon photomultiplier (SiPM) board that measures the Cerenkov photons produced by charged shower particles in the PbF_2 crystal. The functionality of 1400 of such boards must be thoroughly investigated and the characteristic breakdown voltages must be measured to validate the values provided by the vendor to ensure the full understanding of the calorimeter system.

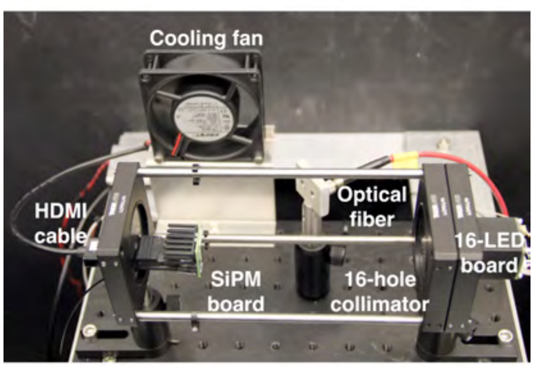

Figure 4.6-1. *Left:* SiPM QC station. During a L0 measurement, the collimator is pushed to the left to fully cover the SiPM surface. *Right:* Custom-made LED board and collimator.

A dedicated quality-control (QC) station as shown in Fig. 4.6-1(left) has been constructed. Two tests, level zero (L0) and level one (L1) are conducted using this station. The main purpose of L0 is to check the functionality of each of the 16 individual channels (4 by 4 array) of the SiPM board, where the outputs of these channels are summed to provide a single signal. To shine lights on each of the channels one at a time, a custom-made 16-channel light-emitting diode (LED) board and a Delrin collimator are used (see Fig. 4.6-1 *right*). In addition, we also tested the temperature sensor, programmable gain amplifier (PGA) and the flash memory (EEPROM) installed on the board. The purpose of L1 is to measure roughly the average breakdown voltage V_{bd} of the SiPM as a whole, as we need to glue the SiPM boards to the PbF_2 crystals based on their breakdown voltage values. A pulsed laser is used, where the light is guided using an optical fiber (see Fig. 4.6-1 *left*) to illuminate the entire 16-channel SiPM at once. The bias voltage V_{bias} applied to the SiPM board is varied from 66 V to 69 V and the output signal's amplitude is plotted as a function of V_{bias}, as shown in Fig. 4.6-3 (*right*).

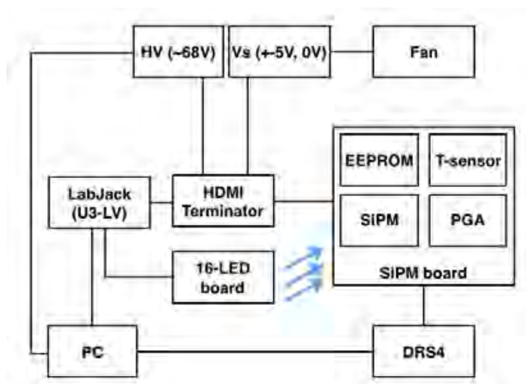

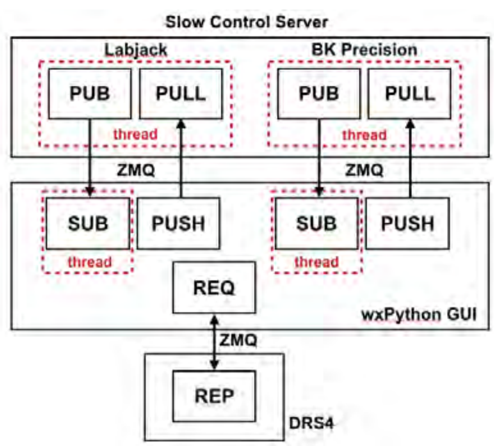

Figure 4.6-2. *Top:* An overview of the hardware connection of the QC station. *Bottom:* Fast and slow DAQ of the SiPM QC Station using Zeromq communication sockets.

The DAQ and communication of the QC station is shown in Fig. 4.6-2 (*top*). While the low-voltage supply is set manually, the bias-voltage supply is controlled through a serial communication. The fast DAQ system of the QC station is based on the DRS4 digitizer developed at PSI and the slow control DAQ system is based on a Labjack I/O device. Both of them are running on separate instances and the communication with a SiPM QC graphical user interface (GUI) frontend is done using Zeromq, a high performance asynchronous messaging library, see Fig. 4.6-2 (*bottom*). The GUI is developed based on the wxPython toolkit. Readouts of the temperature, flash memory, gain and LED channel are fully automated; once

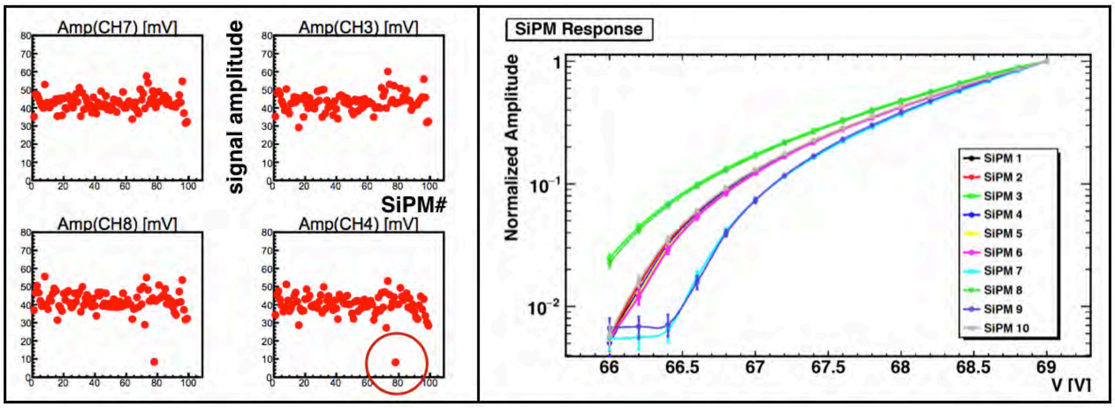

Figure 4.6-3. *Left:* Example results from the L0 test. Shown are the SiPM output signal's amplitude when only one of the channels (3, 4, 7, 8) is illuminated with the LED pulse, as a function of SiPM number (from 1 to 100). One of the SiPMs has below-average output amplitudes (for example CH4 with a circle) indicating that these channels are not functioning properly. *Right:* Example result from the L1 test. The normalized output amplitude is plotted as a function of applied bias voltage. It is obvious that 3 groups of breakdown voltages exist in this sample.

a SiPM board is connected to the HDMI connector, all the readings are shown on the GUI control panel. Once a measurement is done, all the results are stored in a JSON (JavaScript Object Notation) file and an embedded sqlite3 database for redundancy. A single measurement takes about 3 s and a full LED scan or V_{bias} scan takes about a minute. The average signal waveform and the signal-amplitude distribution are computed on the fly.

The first 100 production SiPM boards were tested using the QC station and the L0 test results are shown in Fig. 4.6-3 (*left*). Out of 100 SiPMs, 99 of them passed the functionality tests and one has some faulty channels. Results from the L1 tests are shown in Fig. 4.6-3 (*right*). Tests on the second batch of production SiPM boards (1300 of them) will be conducted soon.

4.7 Offline analysis of calorimeter data

A. T. Fienberg, D. W. Hertzog, J. Kaspar, K. S. Khaw, and G. J. Plunkett

The output of each of our 54 photodetectors in each of our 24 calorimeters will be digitized. We must extract pulse heights and times from these traces to find the energy deposition in each calorimeter segment (pulse finding) and then combine these segment energies and times to obtain a decay positron energy and time (clustering). The developed pulse finding and clustering algorithms should be robust against systematic effects and perform consistently at event rates anywhere between 5 MHz at the beginning of a muon fill and 100 Hz at the end. This past year, our group has made significant progress on development of these offline algorithms and has had the opportunity to test them on both real and simulated data.

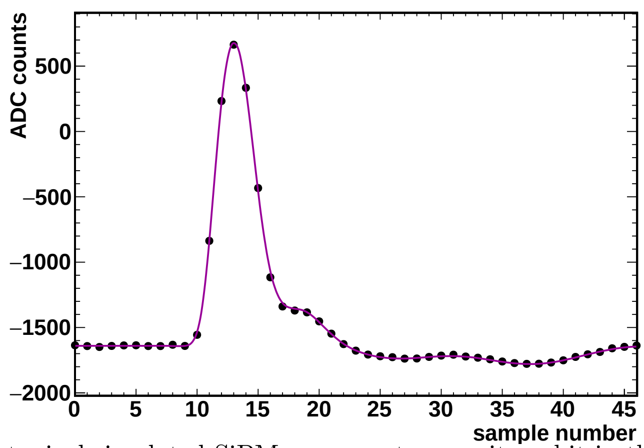

Figure 4.7-1. A typical simulated SiPM response to a positron hit in the calorimeter. This trace is fit with a pulse template.

Before processing signals from the photodetectors, an empirical description of their electrical response must be obtained. This description is called a pulse template. Pulse templates are generated from large sets of acquired digitized waveforms sorted by peak time, which is determined through an interpolation of the peak three samples. The pulses are then separated into groups based on their phase relative to the digitizer clock, aligned, and averaged. Sorting by phase allows a pulse template that is defined with much finer time spacing than initially provided by the digitizer. An example of a template fit is shown in Fig. 4.7-1.

Once a satisfactory pulse template has been generated, it can be used to extract energies and times from digitized waveforms. This is accomplished through a least-squares fit with three parameters: time, scale, and baseline. The technique yields precise measurements of the desired parameters, but beyond that it provides a natural technique for resolving multiple pulses in a single waveform (pileup). If a single pulse fit is not good, more pulses can be added until an acceptable result is achieved. Simulation studies have suggested that the $g-2$ SiPM pulse shape combined with this pulse-fitting technique will reliably separate all pulses with a time difference greater than 5 ns, and we have measured approximately 99% separation efficiency for pulses separated by between 4 and 5 ns. The correct energy is extracted for all pulses in a simultaneous fit. Minimizing pileup is critical to keeping the $g-2$ systematic error under control. For an example of a double-pulse template fit, see Fig. 4.7-2.

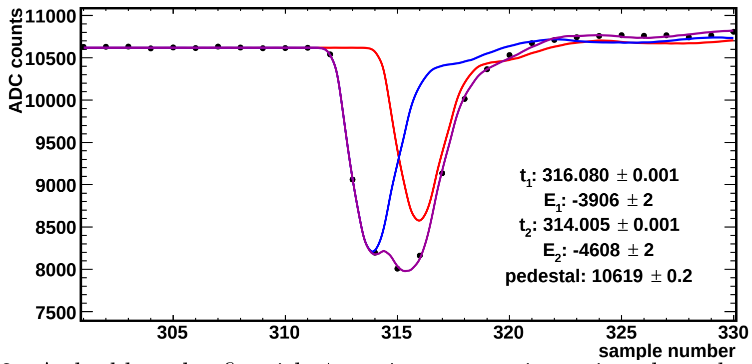

Figure 4.7-2. A double-pulse fit with 4 ns time separation using the pulse-template technique. Each pulse is from a 450 MeV electron delivered by the Laboratori Nazionali di Frascati accelerator. This waveform was acquired by a 500 MSa/s CAEN DT5730.

After pulse fitting comes clustering. Clustering is the combination of pulse-fit results that are localized in space and time into one summary energy and time. The energy and time obtained in the clustering step is interpreted as a decay-positron event. Based on the distribution of pulses in space and time, one can further separate pileup events and accomplish an impact position and angle measurement. Approximately two-thirds of the pileup events that are not detected in the pulse-fitting stage are detected in the clustering stage.

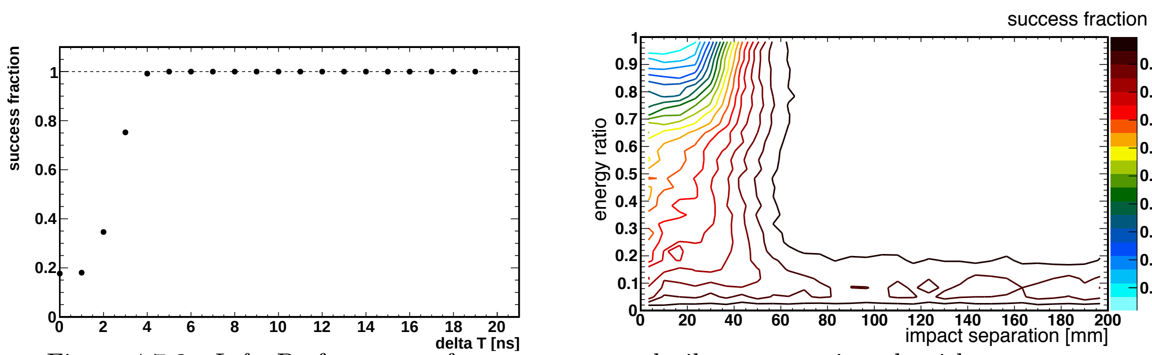

Figure 4.7-3. *Left:* Performance of current temporal pileup separation algorithm, as measured through simulation. Success rate reaches 100% for events separated by more than 5 ns. *Right:* Performance of current spatial pileup separation algorithm. Success rate is well over 90% for impacts of high-energy pulses separated by more than 60 mm.

Over the past year, the analysis routine described above has been implemented in the Fermilab *art* framework and is performing well according to initial tests. The pulse-finding routine was tested both on 450 MeV electron pileup pulses from the accelerator at Laboratori Nazionali di Frascati, Italy and on simulated pulses. The Frascati accelerator provided pulses separated by between 0 and 10 ns. The clustering routine was tested on simulated calorimeter showers from a Geant4 model of the $g-2$ ring. Results from these tests are shown in Fig. 4.7-3. Over the next year, the offline analysis routine will be evaluated for systematic effects and exercised in a high-statistics mock data challenge.

4.8 Muon $g-2$ precision field overview

M. Fertl, A. García, J. Grange*, B. Kiburg†, R. Ortez, R. Osofsky, M. Smith, H. E. Swanson, and P. Winter*

In June 2015, UW precision field team members Rachel Osofsky, Matthias Smith and Erik Swanson headed for Fermilab to work on the re-assembled E821 storage ring and make it a precision research magnet. The goal is to keep field fluctuations around the ring to less than ± 25 parts per million by shimming, an iterative process that involves tailoring the field profile by positioning iron shimming elements within the magnet. When we arrived the superconducting coils had just been cooled to 5K for the first time in over 10 years. Initial ramping of the current showed there was insufficient cooling for the dissipation in the power coupler and its repair required first warming up the magnet. In the down time we built up the field measurement apparatus. A cylindrical matrix of 25 UW nuclear magnetic resonance (NMR) probes was installed in a custom trolley, see Fig. 4.8-1, that rides between rail-like shims on the inner and outer pole radii. Refurbished E821 electronics are used to control and readout probes. A laser system at the center of the ring tracks retro reflectors on the trolley and provides real-time angle and height coordinates. The trolley is pulled forward by fishing line routed around an upstream pulley to a stepping-motor-controlled drum located in the ring. The DAQ system, developed at the UW, was extended to include trolley motion control, position and field readouts. We then developed visualization techniques to show the multipole nature of the field over the entire ring.

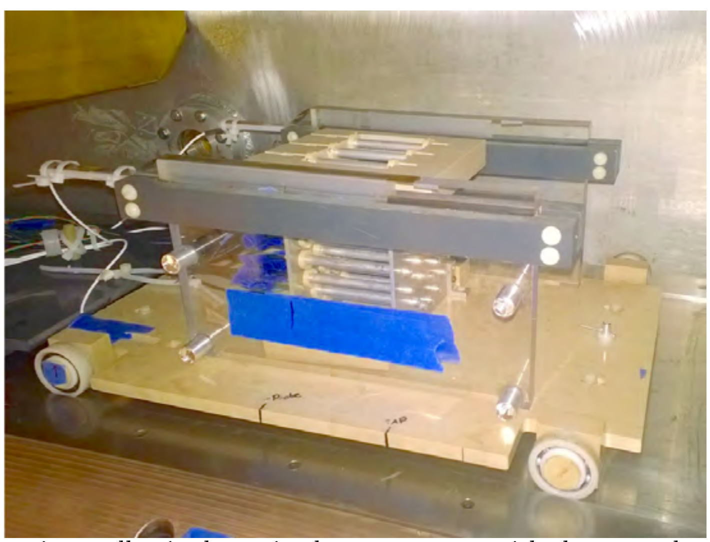

Figure 4.8-1. The shimming trolley is shown in the magnet gap with the top pole removed. 25 NMR probes sample the central volume, home of future muons. Vertical quartz plates front and back have proximity sensors on top and bottom to measure the gap. The 4 retro reflectors on the front plate are targets for the laser tracking system. Additional probes on top sample the field close to the poles where fixed probes will have to operate during the experiment.

---

*Physics Division, Argonne National Laboratory, Argonne, IL.
†Fermi National Accelerator Lab, Batavia, IL.

With repairs completed the magnet was again cooled and was successfully powered to full field. We obtained the first field map with our NMR probes and it showed the restored storage ring still works. It looks remarkably similar to the first map made in 1996 as seen in Fig. 4.8-2. In the next weeks of operation the magnet quenched twice and field measurements again stopped until the cause could be determined. Investigation found a significant Helium leak into the cryostat vacuum that was being pumped by cryopanels installed when the coils were built. These periodically released enough gas to quench the magnet through increased heat conductivity. A workaround allowed us to energize the magnet for up to 8 hours at a time deferring permanent repairs until the completion of shimming. The magnet operated stably in this mode and we were able to characterize each of the shimming elements and apply them to reduce some of the larger field fluctuations.

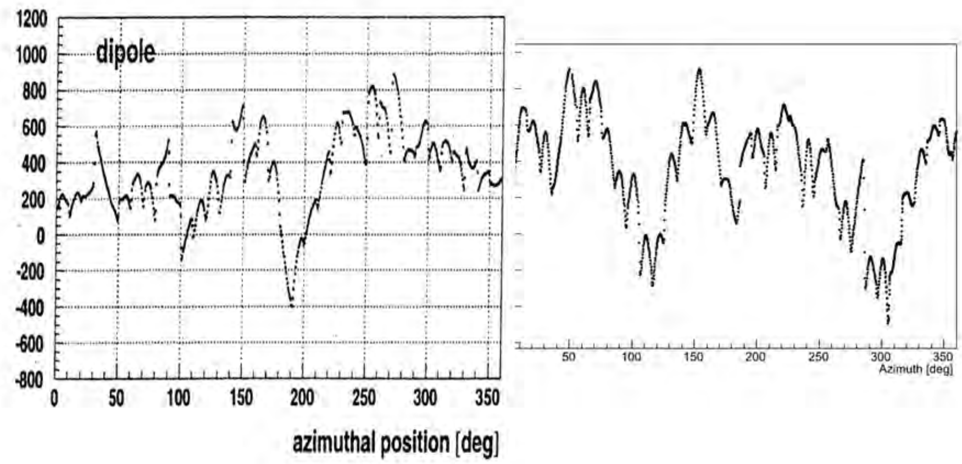

Figure 4.8-2. The left plot is the field map taken at Brookhaven National Laboratory when the magnet was first turned on in 1996. The right plot shows our first field map at Fermilab in 2015. Figures are scaled to use the same left axis which is in ppm. Field variations over ring azimuth are about 1300 ppm.

As seen in the plots, the field varies significantly across individual poles. Using commercial electrolytic bubble levels, we constructed a tilt sensor to measure alignments of individual poles to understand these field variations. Plotting pole tilts as a function of azimuth showed the ring was tilted out of the horizontal plane such that heights of opposite sides differed by a couple of millimeters. Additional metrology confirmed that the building had in fact settled in the direction of nearby new construction. Field measurements and shimming were again paused while the entire ring was jacked back into the horizontal plane. Despite delays our experiences over the past months have taught us how to use the shimming tool kit designed into the magnet.

Shimming elements have a full width half maximum (FWHM) range comparable to the size of poles and cannot effectively smooth field variations across poles or pole boundaries. We began a program to measure and correct alignments of all 72 poles. A global model of the pole surfaces was developed that gave the amount each of the supporting feet would have to be shimmed to achieve desired tilt angles and maintain minimal differences in relative heights between poles at their boundaries. At the time of this report most bottom pole boundaries are within 0.0005 inches and we are working to achieve similar alignment precision with the top set of poles. Once this is complete, shimming elements can be used to continue bringing the field to the desired homogeneity. This will be facilitated by our optimization code which uses measured effects of shimming elements and determines the positions of all individual elements to best null observed field variations. We expect this rough shimming phase to be finished in July 2016, about a year after our arrival at Fermilab.

4.9 Construction and delivery of pNMR probes for the muon $g-2$ experiment

M. Fertl, A. García, C. Helling, R. Ortez, R. E. Osofsky, M. W. Smith, and H. E. Swanson

A successful measurement of the muon anomalous magnetic moment, $a_\mu = (g-2)/2$, crucially relies on a precise knowledge of the magnetic-field distribution seen by the muons orbiting in the storage ring. While this distribution can be measured with a special magnetic field mapper several times a week, this mapping trolley has to be retracted into its storage position during muon operation. To track changes of the magnetic field between trolley measurements a stationary array of pulsed proton nuclear magnetic resonance (pNMR) probes is distributed along the outside of the storage ring's vacuum chambers. Over the last year the magnetic-field team at CENPA built more than 450 new pNMR probes for the stationary array as well as the trolley, to replace the probes used in the BNL E821 experiment[1]. This was necessary because the vast majority of probes used in the BNL E821 experiment were found to be dysfunctional (details in a previous report[2]).

The mechanical design of the new probes is shown in Fig. 4.9-1. The new features include a crimp connection between the radiofrequency cable braid and the base piece of the probe instead of a conduction epoxy joint used in the E821 experiment. This new connection has proven to provide a very reliable electrical connection even under repeated exposure to mechanical stress and water. All NMR probes are filled with the same petroleum jelly which was characterized before by NMR measurements and replaces the copper-sulfate-doped water samples. This eliminates the risk of corrosion of aluminum parts due to leaking of the water sample. All parts for the new pNMR probes were produced in the workshops of CENPA and the Department of Physics in batches of about 80 probes at a time. This allowed us

[1] G. W. Bennett *et al.*, Phys. Rev. D **73**, 072003 (2006).
[2] CENPA Annual Report, University of Washington (2014) p. 69.

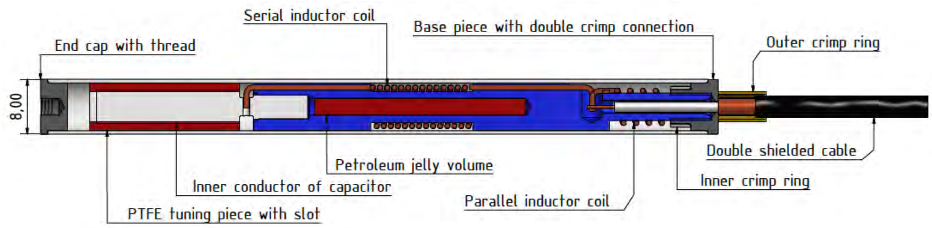

Figure 4.9-1. A cut-away view of the final design of the new pNMR probes. The double shielded radiofrequency cable is crimped to the base piece of the probe. This base piece holds the support structure for the serial and parallel inductors and the inner conductor of the capacitor, and connects to the aluminum sleeve that forms the ground plate of the capacitor. The easily removable end cap provides fast access to the PTFE tuning piece. By screwing the PTFE piece on or off the inner conductor the resonance frequency of the pNMR probe can be adjusted.

to establish a parallel production and assembly line for the new probes. To standardize the assembly among the different people involved, an assembly manual was written which describes all assembly steps in detail. After delivery of the pieces a thorough cleaning was performed and the parts were distributed among so-called assembly kits as shown in Fig. 4.9-2. All parts necessary to assemble one complete probe were included in an assembly kit. This made the assembly of probes straightforward and avoided a time consuming search for parts. After the mechanical assembly of a probe its resonance frequency was tuned and its impedance matched to the cable impedance. All control measurements have been recorded and stored for documentation in the $g-2$ Traveller database. The production and quality

Figure 4.9-2. All parts necessary to assemble a complete pNMR probe are contained in an assembly kit. Once a probe is completely assembled it is marked with a unique number on a shrink tube.

control of all probes was successfully finished in early 2016. Subsequently the pNMR probes have been shipped to FNAL where they will be installed in the allocated slots on the vacuum chambers later this year.

4.10 Preliminary concepts for a radial field measurement for the $g-2$ experiment at Fermilab

M. Fertl, A. García, R. Osofsky, and H. E. Swanson

The magnetic field in the $g-2$ storage ring influences the motion of muons in the ring. Radial and azimuthal field components cause muons to deviate from their nominal orbit and "swim" vertically and radially as they move around the storage ring azimuthally. An average radial or azimuthal field in the muon storage region can be corrected using correction coils on the pole surfaces, but before this can be done, the variation around the ring must be less than ± 50 parts per million, known to 10 parts-per-million precision.

The field in the storage region is normally mapped using pulsed nuclear magnetic resonance (pNMR) probes. However, NMR probes are only sensitive to field magnitude, not field direction, and cannot be used to measure non-vertical field components. For this reason, a separate measurement of these small field components must be done using Hall probes.

In general, the voltage across a Hall probe has 3 contributions (the normal Hall effect, the planar Hall effect, and an ohmic offset voltage) and is given by

$$V = k_1 B_\perp I + k_2 \vec{B}_{||}^2 I \sin(2\psi) + V_0 \tag{1}$$

where k_1 and k_2 are the normal and planar Hall coefficients, I is the Hall current, $B_\perp$ is the magnitude of the component of the magnetic field normal to the Hall probe active region, $\vec{B}_{||}$ is the magnetic field component in the plane of the Hall probe active region, ψ is the angle between the Hall current and $\vec{B}_{||}$, and V_0 is the ohmic offset voltage.

In order to only measure a radial or azimuthal field component without contamination from the other 2 field components, a series of measurements will be undertaken at each azimuthal location where a radial and azimuthal field value is desired. The offset voltage contribution can be subtracted away by rotating the Hall probe by 180° and taking half the difference of the 2 measurements. To minimize the planar Hall contribution, Hall probes with an ultra-low planar Hall coefficient were purchased, but we will additionally use the spinning-current technique, in which the voltage and current taps on a Hall probe are interchanged. Assuming the voltage and current taps are perpendicular to one another, this is equivalent to rotating the Hall probe by 90° about its normal vector, changing the sign of the planar Hall contribution.

The precision we will be able to achieve is directly related to how well we can align the Hall probe active region with respect to gravity and how well the necessary rotations can be executed. A rotation by slightly more or less than 180° about the main field direction results in contamination between the radial and azimuthal field component measurements. In doing this rotation, if there is also some additional small rotation about either of the other 2 coordinate axes, the main dipole field will contribute to the small field measurement. We will minimize this source of error by using electrolytic tilt sensors mounted on the same platform as the Hall probe. Using fine-threaded adjustable screws we will adjust the platform to be at the same tilt, both radially and azimuthally, after a rotation as it was before.

Before taking measurements of the field components, we will measure the Hall and planar Hall coefficients for our Hall probe. As seen in the above equation, the planar Hall contribution varies with the angle between the current and the parallel component of the magnetic field. This angle can be varied by rotating the Hall probe about its normal axis, resulting in a sinusoidally varying plot with contributions not only from the varying planar Hall effect (which has a period of π), but also an overall offset from the offset voltage and the normal Hall effect, and a sinusoidal contribution (period 2π) if the axis of rotation is not exactly parallel to the Hall probe normal vector. Fig. 4.10-1 shows an apparatus for rotating the Hall probe about its normal vector. The Hall probe is mounted to a plate, which is attached to a cube. This cube then sits inside of a cylinder which rotates about its central axis.

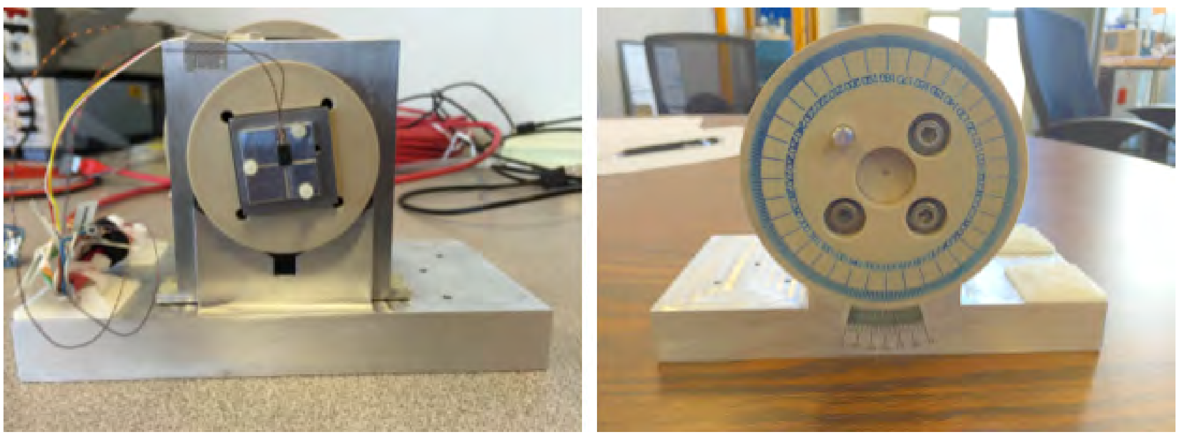

Figure 4.10-1. A Hall probe is mounted on a plate, which is in turn mounted on a cube. This cube fits in the back of a cylinder which can be rotated a full 360 degrees around its axis. Electrolytic tilt sensors will be installed on the platform, next to the rotating cylinder, to monitor the tilt of the apparatus with respect to gravity.

The normal Hall contribution varies as a function of field strength. To measure the Hall coefficient, the Hall probe will be set up in an orientation so as to measure the main field, either in a region where the magnetic field is very homogeneous, or in the homogeneous field of the $g-2$ test magnet at Argonne National Laboratory. By tilting the Hall probe away from this orientation, the magnitude of the field seen by the Hall probe can be changed, and from this data the normal Hall coefficient can be extracted.

Another important systematic to consider is the effect of temperature drifts and fluctuations on Hall probe measurements. In particular, due to the temperature coefficient of the ohmic offset voltage, temperature differences between 180° rotations must be well understood and corrected for. A PT100 temperature sensor will be mounted near the Hall probe and its output recorded through every measurement sequence. During the calibration process, various temperature studies will be performed, informing what, if anything, needs to be done to correct for temperature changes during final measurements.

4.11 Shimming the $g-2$ storage magnet at Fermilab

R. Bjorkquist*, M. Fertl, A. García, J. Grange†, M. Farooq‡, D. Flay§, D. Kawall§, B. Kiburg¶, R. Ortez, R. Osofsky, M. W. Smith, H. E. Swanson, D. Sweigart*, and P. Winter†

The muon $g-2$ experiment powered the magnetic field in its storage ring for the first time at Fermilab in September of 2015. The same storage ring was used in the previous muon $g-2$ experiment experiment at Brookhaven National Lab, and the initial homogeneity of the magnetic field was similar despite efforts to recreate the final configuration of the ring at Brookhaven. Since powering the magnet, the field team has been studying the field and the tools available to improve the uniformity of the field in a process referred to as rough shimming. After rough shimming has been completed, the collaboration will proceed to install the vacuum chambers and other detector systems.

In the previous $g-2$ experiment, the field team achieved extraordinary magnetic-field uniformity, and the new experiment needs to be even more extraordinary in its field uniformity. Before discussing the uniformity constraints, though, there needs to be an explanation of the terms used to describe it. The measurements are taken using a suite of 25 nuclear magnetic resonance (NMR) probes that are set in concentric rings. The layout allows the measurement to sample the magnetic field in the muon storage volume and decompose the data into symmetry components called multipoles. Examples are shown in Fig. 4.11-1: the average field is the dipole field, the inner-radius to outer-radius asymmetry is the normal quadrupole, and the vertical vs. radial asymmetry is the normal sextupole. The uniformity specification for the current $g-2$ experiment is a uniformity of $\pm$ 25 ppm for the average field around the ring and $\pm$ 10 ppm and with average less than 5 ppm for the higher order multipoles.

Figure 4.11-1. Examples of multipoles. *Left:* The average field is the dipole field. *Center:* The inner-radius to outer-radius asymmetry is the normal quadrupole. *Right:* The vertical vs. radial asymmetry is the normal sextupole.

The rough shimming is currently in an intermediate phase, but the field's future looks

*Physics Department, Cornell University, Ithica, NY.
†High Energy Physics Division, Argonne National Laboratory, Argonne, IL.
‡Physics Department, University of Michigan, Ann Arbor, MI.
§Physics Department, University of Massachusetts Amherst, Amherst, MA.
¶Muon Department, Fermi National Accelerator Laboratory, Batavia, IL.

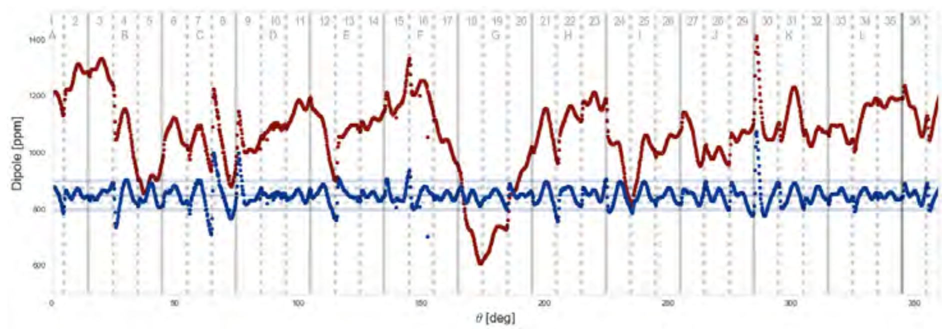

Figure 4.11-2. The plot above shows the current average magnetic field vs azimuth in red. The blue points are the predicted field after adjusting our shim knobs, and the light blue bands are the uniformity spec on the average. One can see that the current state can approach the specification after tuning the shims.

promising. There are many knobs available which affect the field multipoles differently, such as the wedge shims (dipole + normal quadrupole) and top-hat shims (just dipole). The orientation of the large metal arcs, the pole pieces, that focus the magnetic field is the primary determiner of the field. An arduous process of adjusting the radial tilt, azimuthal tilt, shape, and boundaries between these pole pieces has recently finished, and the field looks to mostly be in range of the secondary shimming knobs. The current state of the field is shown in Fig. 4.11-2.

4.12 Development of the $g - 2$ field data acquisition system

R. Bjorkquist[*], M. Fertl, A. García, J. Grange[†], M. Farooq[‡], D. Flay[§], D. Kawall[§], B. Kiburg[¶], R. Ortez, R. Osofsky, M. W. Smith, H. E. Swanson, D. Sweigart[*], and P. Winter[†]

Over the past year the data acquisition (DAQ) system for field measurements in the muon $g-2$ experiment at Fermilab has gone from prototype to practice. The DAQ aggregates data from several devices into two data streams of synchronous and asynchronous events using the MIDAS framework. The DAQ system has been integral to the field team during the ongoing rough shimming process.

The complete DAQ system integrates components that were developed at several different institutions, a real collaborative effort. The University of Washington group designed the overall format for the collection of software comprising the DAQ. The core of the DAQ is the MIDAS framework originally developed at the Paul Scherrer Institute, currently developed and maintained by TRIUMF. MIDAS front-ends for the synchronized triggering of multiple devices, controlling the movement of the devices around the ring, and reading out the pulsed

[*]Physics Department, Cornell University, Ithica, NY.
[†]High Energy Physics Division, Argonne National Laboratory, Argonne, IL.
[‡]Physics Department, University of Michigan, Ann Arbor, MI.
[§]Physics Department, University of Massachusetts Amherst, Amherst, MA.
[¶]Muon Department, Fermi National Accelerator Laboratory, Batavia, IL.

nuclear magnetic resonance (pNMR) probes were developed at UW. Readout front-ends for Capacitec distance measurements sensors and a Metrolab commercial NMR device were developed by colleagues at Argonne. Temperature probes were integrated into the MIDAS slow-control bus by a collaboration member at Northern Illinois University. The API laser tracker front-end was developed by a Fermilab colleague. Together all of these components deliver data that allows the field team to build geometric models, magnetic field models, and make informed decisions about adjusting storage-ring hardware.

The data from the DAQ machinery come in two basic flavors. The instruments essential to mapping the field need to be read out synchronously, so that all the data are properly correlated. Each data point in the field map contains timestamps, position information from the laser tracker, pole gap information from capacitive distance sensors above and below the pNMR probes, and of course the frequency from the suite of 25 concentric pNMR probes which maps to a magnetic-field strength. The asynchronous data stream includes Metrolab NMR measurements which can be used to verify and calibrate the UW pNMR measurements. There are also several temperature sensors that are constantly read out which provide environmental information, as well as tilt-sensor measurements which are used in determining the geometry (tilt angles and planes) of ring hardware. After processing the raw data into calibrated measurements and performing some analysis to extract multipoles from the field data, the field team has a detailed map of the field over the storage volume for the muons. The plot below depicts a set of pNMR measurements around the ring which make up the field map.

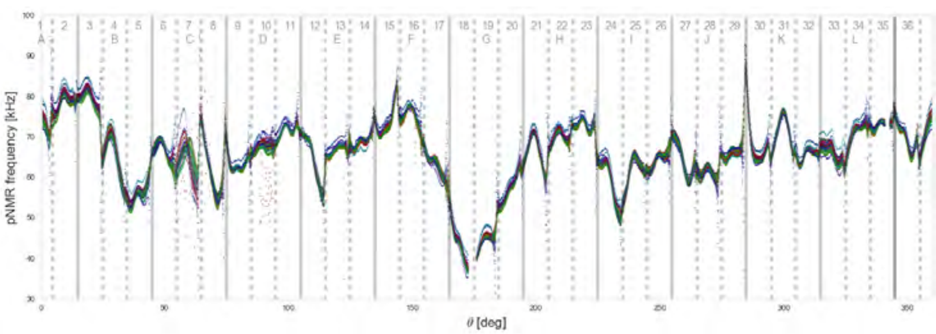

Figure 4.12-1. A plot of a full set of pNMR measurements over the muon storage volume which make up a field map. Notice how closely packed all the frequencies are at any point.

4.13 NMR electronics upgrade

M. Fertl, R. Osofsky, D. Peterson, H. E Swanson, and T. Van Wechel,

Magnetic-field measurements in the muon $g-2$ experiment take advantage of the extraordinary precision obtained from pulsed nuclear magnetic resonance (NMR) techniques. Precession in a proton-rich sample is excited with a short radiofrequency (RF) pulse and the frequency of the resulting induced signal, the free induction decay or FID, is proportional to the magnetic field. The electronics used to generate these signals in the previous $g-2$ measurement were developed back in the 1990s with components now over 20 years old. Our original plan to refurbish these electronics hit a snag when we found some modules were missing and replacement parts were no longer available. Rather than reverse-engineering these old designs for the missing modules we embarked on a program to develop an NMR system from scratch.

Our new design is conceptually similar but built from the ground up using modern off-the-shelf components. Like the previous design it is organized around three different functional blocks: the pulser/mixer, RF power amplifier, and multiplexer/preamplifier.

The pulser/mixer maintains the NIM module form factor of its predecessor. The input from a reference clock is split between send and receive channels. The send channel determines the width of the RF pulse and outputs the switched reference clock, adjustable to +10 dBm. The receive channel mixes the amplified FID from the multiplexer with the reference clock and selects only the difference frequency with a filter. This is scaled to the input range of the waveform digitizer.

The RF power amplifier replaces a class C design that used many hand-wound inductors. The power required is 10 Watts but the average dissipation of class C amplifiers is small, proportional to the pulse duty cycle. Our design is a broadband linear amplifier which we can bias between 10 Watts and off with a TTL gate signal. Additional logic allows the same low average dissipation controlled by duty cycle. It is a self-contained single-circuitboard layout mounted in the multiplexer enclosure.

The multiplexer/preamplifier selects among 20 channels of NMR probes. The switchyard uses broadband surface-mount FET switches and connects selected probes to the power amplifier or the preamplifier dependent on the state of the output from the pulser/mixer module. The output of the preamplifier is the FID signal sent back to the pulser/mixer. The module enclosure follows the same general design as its older counterpart.

All three designs have been prototyped and parts have been ordered for 22 production units to be completed by fall.

MuSun

4.14 Muon capture on deuterium, the MuSun experiment: Overview

D. W. Hertzog, P. Kammel, E. Muldoon, M. H. Murray, D. J. Prindle, R. A. Ryan, D. J. Salvat, and F. Wauters*

The goal of the MuSun experiment is the determination of the rate of the weak semi-leptonic process

$$\mu + d \to n + n + \nu. \tag{1}$$

to 1.5% precision.

This process can be precisely calculated in the Standard Model, apart from a poorly known low-energy constant (LEC) involved in modern – QCD-based – effective field theory (EFT)

*Presently at Institut für Kernphysik, Johannes Gutenberg Universität Mainz, Mainz, Germany.

calculations of weak nuclear reactions. MuSun plans to measure this LEC with 5 times better precision than presently available from the two-nucleon system. This LEC is an important ingredient in developing an EFT-based theory of nuclear forces and is needed for calculating more complicated weak nuclear processes of topical interest, like double beta-decay rates. Regarding the family of two-nucleon weak-interaction processes, the determination of this LEC in muon capture will provide the required input for model-independent calculations of astrophysical processes of fundamental importance, like pp fusion or νd scattering, whose rates have never been measured directly.

MuSun measures Λ_d, the capture rate from the doublet hyperfine state of the muonic deuterium atom in its 1S ground state, by determining the negative muon decay rate λ_- in a time projection chamber (TPC) filled with deuterium gas. The capture rate is derived from the difference $\Lambda_d \approx \lambda_- - \lambda_+$, where λ_+ is the positive muon decay rate.

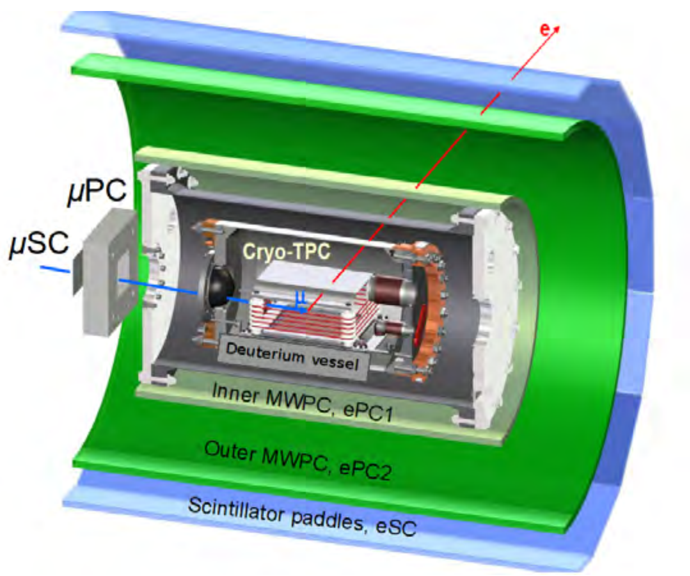

Figure 4.14-1. MuSun detector model. Muons pass through entrance detectors to stop in a deuterium target TPC. The decay electron is detected in two cylindrical wire chambers (green) and a 16-fold segmented scintillator array.

In a simplified overview (see Fig. 4.14-1), the detector consists of muon detectors (muSC, muSCA, TPC), electron detectors (ePC1/2, eSC) and neutron detectors (not shown). For a more detailed discussion of the novel experimental strategy and the physics aspects of this field we refer to a recent review[1].

Experimental challenges were numerous, as this program attempts to improve the measurement Λ_d by about an order of magnitude beyond earlier experiments. A key aspect was the development of a cryogenic high-density TPC operating with ultra-pure deuterium, which needed an extensive development phase followed by significant upgrades to attain reliable operation over long running periods and excellent energy resolution.

[1] P. Kammel and K. Kubodera *Annu. Rev. Nucl. Part. Sci.* **60**, 327 (2010).

A main step towards the experimental goal was achieved in the 2014 run, in which an upgraded TPC designed at UW operated flawlessly over three months of data taking. The 2015 run followed suit. The TPC remained unchanged in clean conditions between the runs and worked perfectly. The purification system (CHUPS) maintained high purity at the 1 ppb level throughout the run. Improved gas chromatography (GC) system produced consistent results. A method for the controlled introduction of impurities was tested after the run, and promises to calibrate the GC to better than 1 ppb. The neutron detectors were replaced with larger, high-efficiency detectors, optimized for monitoring the stability of and background to the observed capture events. The πE1 muon beam at the Paul Scherrer Institute (PSI) was stable and provided a high event rate throughout the beam time, ultimately leading to 7×10^9 candidate events.

MuSun needs to measure Λ_d with an uncertainty $\delta\Lambda_d = 6$ Hz. The capture rate is derived from the difference between the negative and positive muon decay rates, with the latter well-known from MuLan[1]. Thus the uncertainty in $\delta\Lambda_d$ is dominated by the MuSun measurement of λ_- in deuterium. If we assume equal statistical and systematic contributions to the final result, the statistics requirement for the number of fully reconstructed $\mu - e$ decays amounts to $\approx 1.2 \times 10^{10}$ events.

Combining the statistics of 2014 and 2015 we obtain an estimated number of 1.3×10^{10} fully reconstructed events. The statistics quoted comes from preliminary analyses. We still have to establish the final analysis cuts which might lead to some losses. Nevertheless, we are optimistic that the collected statistics comes close enough to the design goal of our experiment and the main data taking phase of MuSun is successfully concluded. The priority in the coming year will be on data analysis to fully evaluate the data consistency and the systematic uncertainties as well as the statistics after all cuts. This will determine whether systematics and statistics balance in the final result.

Thus our beam request for 2016 is very limited. We have requested and were approved for a shorter 6 weeks run in late fall, which is dedicated to study systematic effects.

4.15 2015 production run

D. W. Hertzog, P. Kammel, E. Muldoon, M. H. Murray, D. J. Prindle, R. A. Ryan, D. J. Salvat, and F. Wauters*

The MuSun 2015 production run was the most successful to date, resulting in 7×10^9 μ^- and 1×10^9 μ^+ candidate events after data-selection cuts. Near the end of the run, one week of μ^+ data was taken, and the last two days of beam time were used for systematic effect and beam-quality studies. The accumulation of candidate events throughout the run is shown in Fig. 4.15-1.

---

*Presently at Institut für Kernphysik, Johannes Gutenberg-Universität Mainz, Mainz, Germany.

[1] V. Tishchenko et al. *Phys. Rev.* D **87**, 052003 (2013).

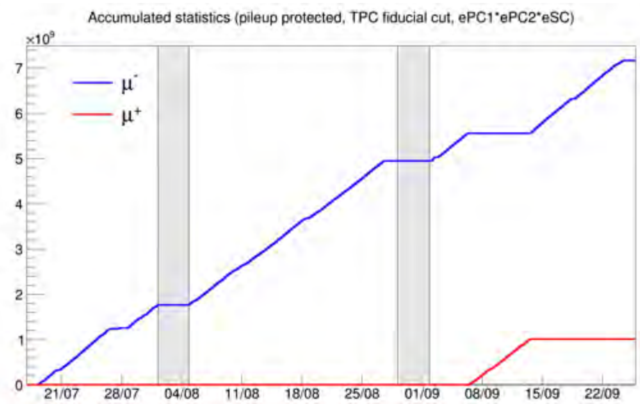

Figure 4.15-1. Number of fully reconstructed decay events with selection cuts acquired over the 2015 run period. The gray bands indicate scheduled accelerator shutdown periods. The beam was utilized efficiently, averaging a collection rate of $\sim 10^9$ good events per week.

Many of the core components of the experiment were unchanged from the previous year, and continued to perform well. In particular, the upgraded time projection chamber (TPC) introduced in 2014[1] continued to perform reliably with excellent energy resolution throughout the 2015 production run. Some components were improved, most notably the muon entrance telescope, fast neutron detectors, and data acquisition.

The muon entrance detectors were improved by replacing the beam-defining μSCA detector and collimator. The μSCA, consisting of a thin scintillator with a hole in the center, is designed to detect and veto muons that are off beam-axis. The original design measured muon signals using a photomultiplier tube mounted to one side, which resulted in large differences in light-collection efficiency across the area of the scintillator. The new design collects the scintillation light in two rows of silicon photomultipliers on opposite sides, the outputs of which are summed into one signal for each side. The improved detector is shown in Fig. 4.15-2(left). This provides a more uniform signal regardless of the location of the incident particle and more reliable discrimination between muons and electrons. The new design also contains a pair of temperature sensors and a variable-gain amplifier for each output signal, all of which can be monitored and controlled remotely. Finally, the beam collimator is now mounted directly to the μSCA, creating a compact shielded package which can be simply and precisely mounted. The final μSCA and collimator assembly is shown in Fig. 4.15-2(right).

Muons in MuSun can produce neutrons via muon-catalyzed fusion or by muon capture in the deuterium gas or other materials[2]. The capture neutrons allow for the assessment of systematic effects due to muon stops in the walls of the TPC. Fusion neutrons are produced mono-energetically at 2.45 MeV, so at higher energies the capture neutrons dominate. To better detect capture neutrons, the existing detectors were replaced with large-volume liquid-scintillator neutron detectors from the DEMON collaboration, offering improved efficiency for high-energy neutrons. All eight detectors used in the 2015 run were calibrated with ^{60}Co and ^{137}Cs gamma sources. Pulse-shape discrimination (PSD) is used to reject γ-ray events:

[1]CENPA Annual Report, University of Washington (2015) p. 85.
[2]V. Andreev *et al.* (MuSun Collaboration), arXiv:1004.1754.

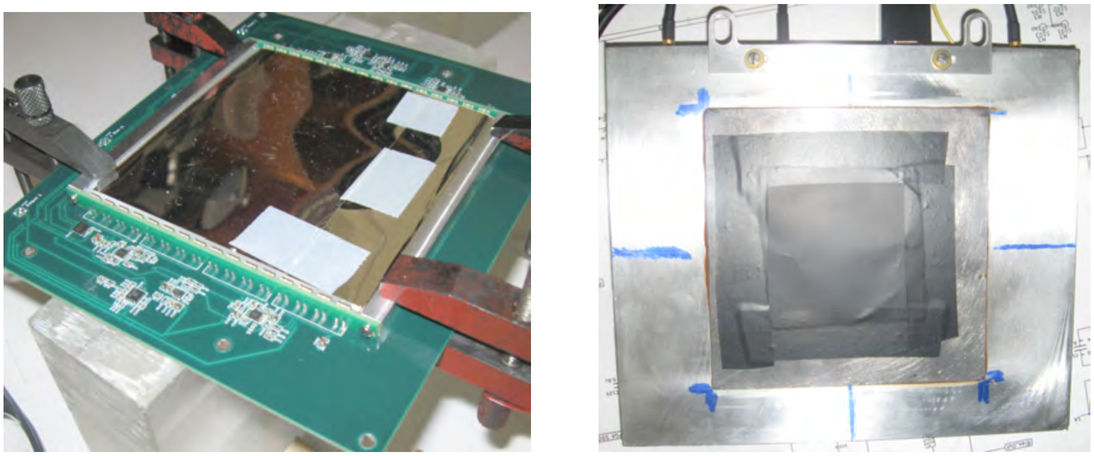

Figure 4.15-2. The new μSCA detector with (right) and without (left) its outer casing.

in particular, the PSD parameter is defined as the ratio of the area of the pulse tail to the total area of the pulse, and this parameter can be used to reduce the γ-ray background for fusion and capture neutron analysis. Fig. 4.15-3 shows the PSD parameter versus total pulse energy, with capture neutrons visible well above the energy limit for fusion neutrons. Analysis of neutron-detector data from the 2015 run is currently underway.

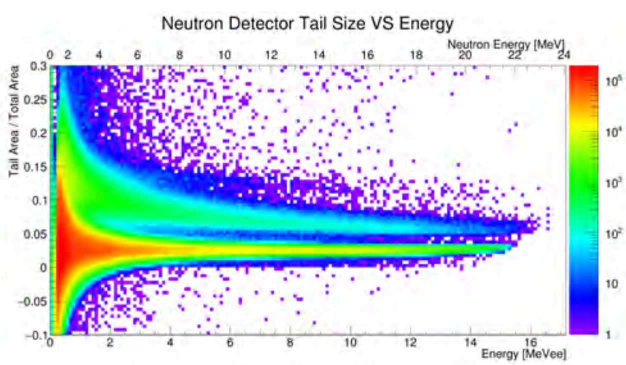

Figure 4.15-3. An example neutron PSD plot. The upper band corresponds to neutrons, while the lower band corresponds to γ-rays

4.16 Fusion interference in the TPC

D. W. Hertzog, P. Kammel, E. Muldoon, M. H. Murray, D. J. Prindle, R. A. Ryan, D. J. Salvat, and F. Wauters*

Fusion interference is a challenging source of systematic error in the measurement of the muon lifetime in MuSun. The products of muon-catalyzed fusion reactions combine with muon tracks to produce a time projection chamber (TPC) response ambiguously indicating the muon stop position. Since fusion events have a smaller disappearance rate than non-

*Presently at Institut für Kernphysik, Johannes Gutenberg-Universität Mainz, Mainz, Germany.

fusion events, cuts on the muon stop position, such as defining a fiducial volume, will cause a shift in the measured lifetime.

To minimize this effect, tracking algorithms are designed to determine identical stop positions for identical muon tracks with or without fusion products. The algorithms differ primarily in determination of the Z-coordinate, parallel to the incoming muon beam. The *Threshold* tracker sets a threshold, above which any signal is assumed to indicate the Bragg peak of the muon stop. This method reconstructs the wrong Z-coordinate of the stop when fusion protons travel upstream, putting the pad before the muon stop above threshold. The *PDir* tracker compares the energy deposited in the last two Z-rows of the muon track (see Fig. 4.16-1) to distinguish events where the proton goes upstream from those where it travels downstream. With the Z-coordinate determined, only the energy deposited on pads upstream from the stop is used to determine the Y- and X-coordinates. A projection of this part of the track into the stop pad is used for the Y-coordinate and the pad just before the stop pad for the X-coordinate.

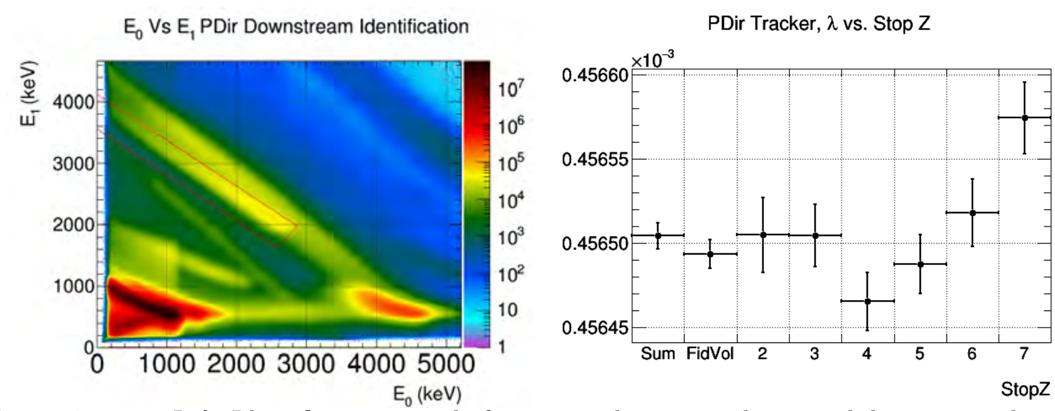

Figure 4.16-1. *Left:* Identification in red of events with protons that travel downstream by distribution of energy on the last two pads in the muon track. E_0 is the energy deposited in last pad, E_1 is that deposited in the next-to-last. The muon only deposits energy in the next-to-last pad for downstream-going protons, so overall energy deposition is lower. *Right:* Muon lifetime for slices of the TPC volume in the Z-direction. The fiducial volume cut includes only bins 2-6. The fit start time is 1000 ns. Non-statistical lifetime shifts are due to the difference in acceptance for fusion and non-fusion events.

The success of this procedure is measured using scans of the measured lifetime as a function of the muon stop position in the TPC. Since a reconstruction error only affects event acceptance if it causes the event to be erroneously rejected or accepted by the fiducial volume cut, the lifetime shift due to incorrect Z reconstruction can be enhanced by considering the lifetime for events in slices of the TPC along the Z-direction. Using the *PDir* tracker, this scan of the lifetime is shown in Fig. 4.16-1. Based on the enhanced lifetime shift for TPC slices, the shift for the full fiducial volume is preliminarily estimated to be < 6 Hz for a fit start time of 1000 ns after the muon enters the apparatus.

4.17 Monitoring of trace impurities in the TPC

D. W. Hertzog, P. Kammel, E. Muldoon, M. H. Murray, D. J. Prindle, R. A. Ryan, D. J. Salvat, and F. Wauters*

Trace contamination in the deuterium gas at the levels of 3 ppb for O_2 and 1 ppb for N_2 will have an effect on our measurement of μ^- capture on the deuteron. MuSun has developed a custom gas-chromatography system to perform these challenging low-concentration measurements. The presence of ~100 keV energy deposited after a μ^- stop in the time projection chamber (TPC) also provides a signal for muon capture on impurities. Besides impurity recoils there are three important contributions to the 100 keV region that we must quantify; energy deposition in the TPC due to Michel electrons, the tail of the ^{3}He from the $\mathrm{d} + \mu^- + \mathrm{d} \to \mu^- + \mathrm{n} + {}^3\mathrm{He}$ reaction extending to low energies, and deuteron recoils from neutrons produced during μ^- capture, $\mu^- + d \to \nu_\mu + n + n$. The contribution due to the Michel electrons is important at lower energies but essentially disappears by 100 keV.

The ^{3}He has a kinetic energy of 800 keV but the observed energy is peaked near 350 keV with a long tail toward lower energy. By tagging the neutron in an electron scintillator we determine the direction of the ^{3}He and can select it to be perpendicular or nearly aligned with the TPC drift field. Shown in the first panel of Fig. 4.17-1 we see the perpendicular ^{3}He with a narrow peak around 350 keV while the aligned ^{3}He have a long tail extending nearly to 100 keV. This is the first observation of an electron-ion recombination dependence on the particle direction with respect to the drift field, although it has long been expected theoretically. We will better constrain the angle of the ^{3}He with respect to the drift field using the timing difference of the electron scintillator photomultiplier tubes (PMT).

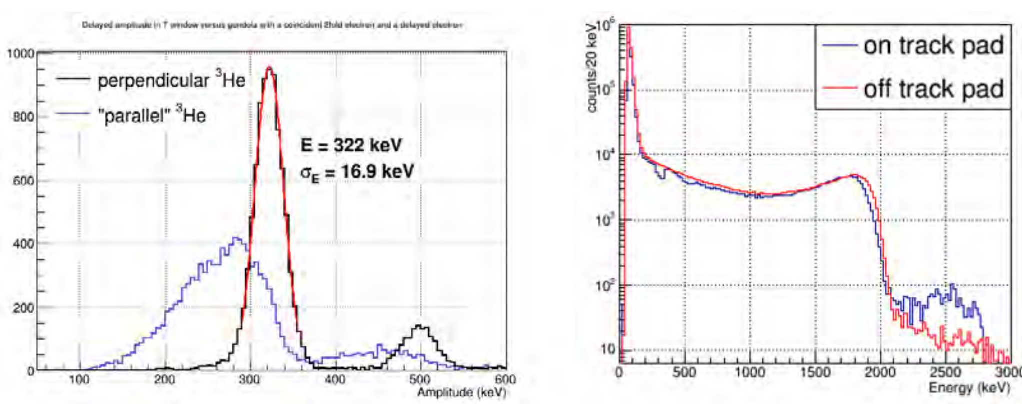

Figure 4.17-1. *Left:* ^{3}He direction tagged by a neutron in the electron scintillators demonstrating an angular dependence to electron-ion recombination. The black line shows ^{3}He perpendicular and the blue line shows aligned events. *Right:* Deuteron energy deposition from neutron recoil. The blue line is delayed energy on the stop pad and the red is energy in a single pad away from the muon track. The shoulder near 2 MeV is the maximum energy that can be deposited by the 3 MeV neutron from the $\mathrm{d} + \mu^- + \mathrm{d} \to \mu^- + \mathrm{n} + {}^3\mathrm{He}$ reaction.

Deuteron recoils, mostly from neutrons from the $\mathrm{d} + \mu^- + \mathrm{d} \to \mu^- + \mathrm{n} + {}^3\mathrm{He}$ reaction, are shown in the right panel of Fig. 4.17-1. The blue line corresponds to delayed energy

*Presently at Institut für Kernphysik, Johannes Gutenberg-Universität Mainz, Mainz, Germany.

on the muon stop pad, and the red to off-track energies. The Monte Carlo prediction (not shown here) is in excellent agreement. The ^{3}He neutrons are strongly reduced by selecting events for which no Michel electron was observed in the scintillators, leaving neutrons from μ^- capture as the dominant source of background for the impurity recoil measurement. We have generated a Monte Carlo sample enhanced in $\mu^- + d \rightarrow \nu_\mu + n + n$ events and used this to determine the ratio between the stop-pad and off-track neutrons. This ratio is applied to the off-track energy measured in data to determine the absolute neutron-recoil contribution to the stop pad. This is a non-negligible contribution to the impurity capture region; we estimate neutrons are typically one third of the yield.

4.18 Analysis of production run 2014

D. W. Hertzog, P. Kammel, E. Muldoon, M. H. Murray, D. J. Prindle, R. A. Ryan, D. J. Salvat, and F. Wauters*

The 2014 production run collected six weeks of μ^- data, amounting to an estimated 6×10^9 events after all selection cuts. In December 2015, a first analysis was completed over all high-quality data collected under nominal conditions.

The 41 TB of R2014 data are currently stored on a mass storage facility at the Texas Advanced Computing Center (TACC). A two-stage analysis is performed using TACC's Stampede computing cluster. Several upgrades were introduced to both analysis stages before the production pass of the R2014 data. More robust error-checking algorithms were introduced to monitor data quality. About 10% of the R2014 data suffered from DAQ-related issues, which are flagged with the upgraded software and taken out of the final lifetime histograms. Additional software was implemented to study the effect of the muon entrance detector efficiency. The first data pass revealed an overall pileup inefficiency of 10^{-5} for all entrance detectors, leading to a negligible lifetime shift. Several new diagnostic histograms were also added to study aspects of the decay-electron definition and readout, including variations in software threshold and coincidence requirements within the anode and cathode layers of the wire chamber.

A preliminary pass of the highest-quality data through both analysis stages resulted in 4×10^9 muon-electron pairs after the application of all selection cuts. Initial high-statistics lifetime fits and the corresponding fit residuals reveal no irregularities as seen in the example fit in Fig. 4.18-1.

The decay curve is also fitted as a function of different experimental parameters, and these studies can be used to quantify the sensitivity of the result to the final cuts. Such studies include scans of the fit start time, the muon stop position, and the electron track reconstruction method. The stability of the lifetime result over the muon stop position is a reflection of the robustness of the upgraded muon tracking algorithm, discussed in (Sec. 4.16). The scans over the fit start time revealed an unexpected dependence on the electron track direction, which indicates an increased beam-electron background in R2014 data. There

*Presently at Institut für Kernphysik, Johannes Gutenberg Universität Mainz, Mainz, Germany.

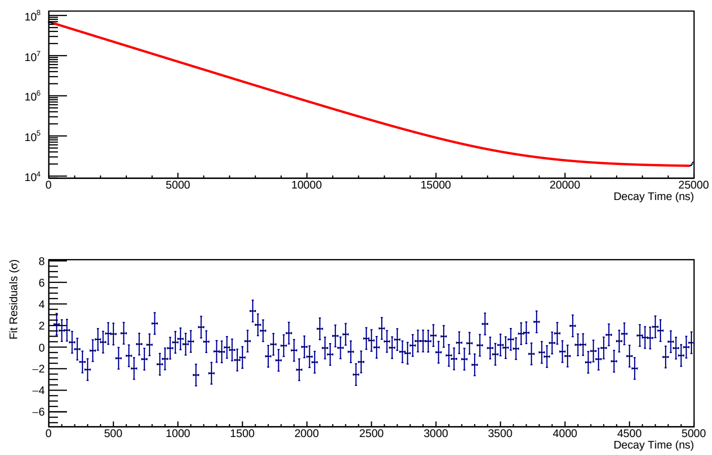

Figure 4.18-1. *Top:* Exponential fit of high-statistics decay curve from recent R2014 data pass with corresponding fit residuals (*bottom*).

was no observed dependence of the lifetime on the electron track definition. Ultimately, the analysis revealed no major issues and a second, complete analysis of R2014 is underway.

AlCap

4.19 AlCap experiment: Nuclear physics input in the search for charged lepton-flavor violation

D. W. Hertzog, R. Hong*, and P. Kammel

As the predicted charged-lepton flavor violation (CLFV) within the Standard Model including massive neutrinos is tiny, the observation of this process would be an unambiguous signal of new physics with an energy reach beyond the LHC. Accordingly, searches for CLFV are of high priority in the worldwide program to explore the limits of the Standard Model. The Mu2e[1] (FNAL) and COMET[2] (J-PARC) experiments seek to determine the branching ratio for the charged-lepton flavor-violating process $\mu^- N \to e^- N$ to better than 10^{-16}, which is a factor of 10,000 improvement compared to the current best limit.

The AlCap experiment is a combined effort of the Mu2e and COMET collaborations to study important nuclear-physics reactions in candidate target materials (Al, Ti) and to establish reliable means of normalizing to the number of stopped muons. This information is required to optimize these new muon-electron conversion experiments. Kammel is the US spokesman of this collaboration, based on his extensive experience with the relevant muon

*Presently at Argonne National Laboratory, Argonne, IL.

[1]Mu2E collaboration, http://mu2e.fnal.gov
[2]COMET collaboration: http://comet.kek.jp

capture reactions. The UW muon group has been a member of the Mu2e collaboration since it inception, but, because of its main commitments, has been careful to limit its involvement on targeted efforts where it has significant expertise, like the AlCap experiment.

When a low-energy negative muon stops in a target material, it quickly becomes bound in atomic orbits. As it cascades through lower orbitals, X-rays are emitted. Once the muon arrives in the 1S orbital, it can decay or it can capture on the nucleus. The relative importance of the two processes depends on Z; for aluminum the breakdown is 39% decay and 61% capture. When the muon captures, it can knock neutrons and protons out of the nucleus, and it can create prompt gamma rays as well as delayed gamma rays from activation.

2015 was a major year of activity for AlCap, with two running periods at PSI. The goal of the first campaign was the measurement of gammas and neutrons from muon capture in aluminum and titanium. The second campaign aimed to corroborate the surprising findings of the first AlCap run in an upgraded set-up and extend the measurement to titanium. Pending further detailed data analysis, both runs appear highly successful.

Below we summarize the main findings, following the structure of the AlCap work packages (WPs).

WP1: Charged Particle Emission after Muon Capture. The goal of WP1 is to measure the rate and spectrum of protons emitted after nuclear muon capture. These protons have never been measured for candidate Mu2e/COMET stopping targets (aluminum and titanium) in the relevant low-energy regime of 2.5 to 15 MeV. Protons in this energy range generate a significant rate in the cylindrical trackers of the experiments, leading to tracks, noise hits and radiation damage. An absorber reduces their rate in the tracker, but also deteriorates its energy resolution.

Preliminary data from the AlCap 2013 run, analyzed in two PhD Theses[1,2], show that the rate is considerably smaller in aluminum than previously estimated, which would have a significant impact on the designs of Mu2e and COMET.

The basic layout of the proton experiment is shown in Fig. 4.19-1. For 2015 several upgrades were implemented: i) electronic noise reduction with new flange and shielding of silicon detector electronics designed at UW, ii) improved geometric precision and survey, iii) precise measurement of beam profile at target location with a 16-strip silicon detector, iv) beam counter inside the vacuum vessel to minimize effect of multiple scattering for low-energy muons, v) three-fold silicon telescope to extend the observed proton energy range, vi) measurement of emitted proton distribution with thin 16-strip dE/dx detector in silicon telescope and vii) new high-rate waveform digitizers.

Measure i) allowed much lower thresholds and dramatically improved the stability com-

[1]Tran Nam, *A study of proton emission following nuclear muon capture for the COMET experiment*, PhD Thesis, Osaka University, 2014.

[2]A. W. J. Edmonds, *An Estimate of the Hadron Production Uncertainty and a Measurement of the Rate of Proton Emission after Nuclear Muon Capture for the Comet Experiment*, PhD Thesis, University College London, 2015.

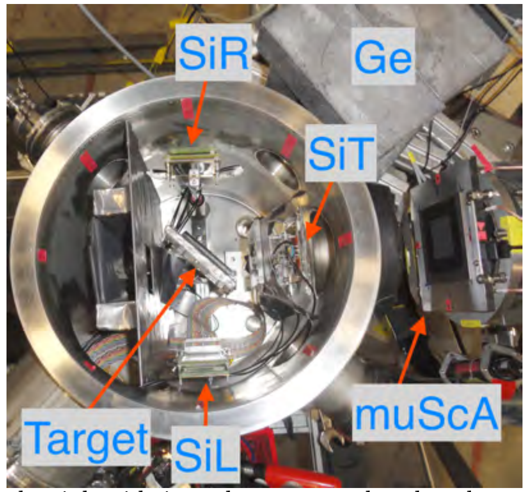

Figure 4.19-1. Muons enter from the right side into the vacuum chamber, by passing through the veto counter muSCA and SiT detectors. The silicon detector packages, labeled SiL and SiR (left and right of the entering beam) are composed of multiple detectors for the identification of charged particles emitted from the target. The Ge detector observes muonic X-rays and gamma rays.

pared to our first run. The improvement in the beam counters iv) increased the muon stopping fraction by a factor of 3, the total statistics was increased by a similar amount. The other improvements will increase the precision and reliability of the analysis and the Monte Carlo simulation to determine the final absolute rate.

WP2: Gamma and X-ray Emission after Muon Capture. The emphasis of WP2 is to measure the spectra of low-energy photons (<6 MeV) emitted when muons stop in materials. This has several purposes: i) Normalization of the number of stopped muons in AlCap; this is primarily done by observing the number of muonic X-rays. ii) Identifying and establishing the intensity of X-ray and gamma-ray lines that could be used for normalization to the number of stopped muons in candidate target materials aluminum and titanium. iii) Identifying X-ray and gamma-ray lines from muons stopped in structural materials that could introduce backgrounds.

Fig. 4.19-2 provides an example of the data. The Mu2e baseline option is to normalize to the 347 keV muonic X-ray observed with a high-resolution Ge detector. If the background rates are too high an alternative option is the delayed 844 keV line or a prompt high-energy gamma line at 1.8 MeV, which could be observed with a fast, lower-resolution detector.

WP3: Neutron Emission after Muon Capture. Neutron emission from the stopping target in the Mu2e experiment is an important background to be understood and controlled. For example, the Monte-Carlo-predicted gamma background from neutron capture in the proton attenuation shield surrounding the target caused it to be redesigned. Further, the front-end electronic systems are placed within the detector solenoid, and neutron-induced single-event-upsets (SEU) in the readout electronics require detailed attention. Time-to-failure in memory and logic components has shown to be significant and this must be evaluated using accurate neutron-flux calculations.

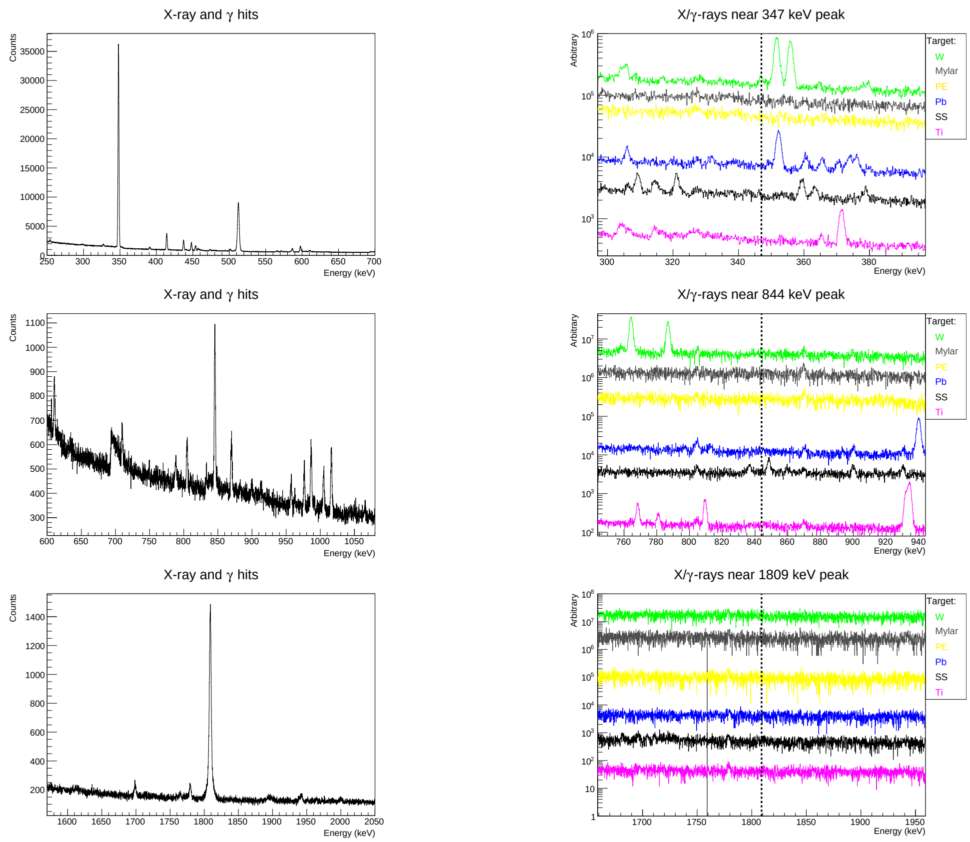

Figure 4.19-2. Germanium signals from aluminum (*left*) compared to possible backgrounds (*right*). From the top down, the 347 keV X-ray, the 844 keV delayed γ-ray from activation, and the 1.8 MeV γ-ray prompt with capture.

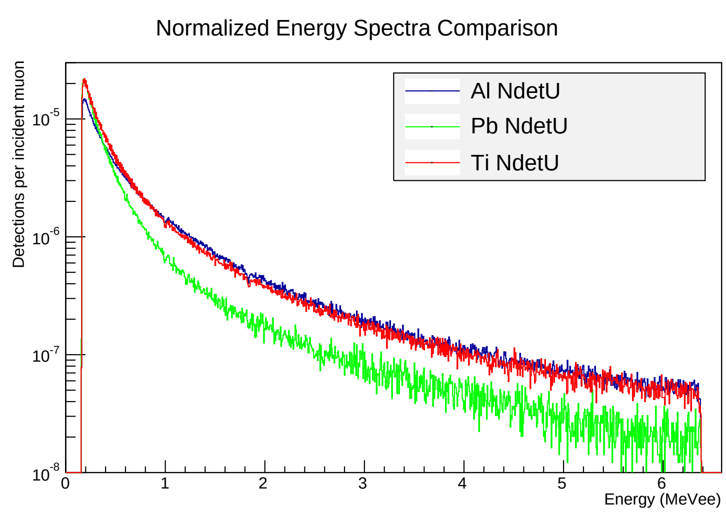

Figure 4.19-3. Preliminary proton-recoil spectra measured by neutron detectors for different targets as shown in legend. Energy calibrated in equivalent gamma energy (MeV$_{ee}$).

Neutrons were detected in an optimized geometry which included beam telescopes, targets, a Ge detector and most importantly, two 5" x 2" BC501a detectors, which could discriminate between neutrons and gammas based on pulse shape. All targets (Al, Ti and Pb) were sufficiently thick to stop the muon beam at momenta up to 40 MeV. As shown in Fig. 4.19-3, excellent high-statistics proton-recoil spectra were obtained. These spectra have to be converted to primary neutron-emission spectra by an unfolding procedure. Although standard codes exist, the specific detector properties (i.e. the response matrix), have to be carefully described. This analysis is currently underway.

5 Axion searches

ADMX (Axion Dark Matter eXperiment)[1]

5.1 Status of ADMX

C. Boutan, N. Crisosto, N. Force, R. Khatiwada, E. Lentz, H. LeTourneau, D. Lyapustin*, A. Malagon, R. S. Ottens, C. Plesha†, L. J Rosenberg, G. Rybka, J. V. Sloan, and D. I. Will

The Axion Dark Matter eXperiment (ADMX) is a search for galactic dark-matter axions whose detection apparatus is an implementation of Pierre Sikivie's axion haloscope[2]. The ADMX collaboration has operated a series of axion searches since the mid-1990s. The experiment has been located at CENPA since 2010. Following a data run in 2013-2014, ADMX has been undergoing a series of upgrades, most notably the addition of a dilution refrigerator, to enter phase "Gen 2." At the time of writing, April 2015, the dilution refrigerator had been installed in the experimental insert and ADMX was preparing for an imminent data run. The upgrades will complete an unprecedentedly low-noise system; ADMX will be sensitive to even the most pessimistically coupled QCD axions and will search at an increased frequency scan rate in the range of $1 - 10$ μeV.

The axion first emerged in the late 1970s as a consequence of a solution to the "strong CP problem." The strong CP problem can be concisely stated as: An exceedingly fine, arguably unnatural, tuning of the Standard Model is required to account for the conservation of the discrete symmetries P (parity) and CP (charge conjugation times parity) within quantum chromodynamics (QCD). The amount of CP violation in QCD is encoded in a phase θ which appears in the QCD Lagrangian. When θ differs from zero, QCD violates P and CP. Since the strong interactions appear to be P- and CP-symmetric in the laboratory, θ must be very small, namely, the upper limit on the neutron electric-dipole moment requires $|\theta| < 10^{-10}$. However, in the Standard Model, P- and CP-violation by the weak interactions feeds into the strong interactions so that the expected value of θ is of order unity. Peccei and Quinn proposed a solution to this problem in which the Standard Model is modified so that θ becomes a dynamical field and relaxes to zero, thus conserving CP in a natural way[3]. The theory's underlying broken continuous symmetry dictates existence of a particle: the axion. The axion is the quantum of oscillation of the θ field and has zero spin, zero electric charge, and negative intrinsic parity. So, like the neutral pion, the axion can decay into two photons. Soon after the initial proposal of the axion, it was realized within a certain range of possible masses the axion is an ideal dark-matter candidate. Experiments and astronomical

*Presently at Crane Aerospace & Electronics in Redmond, WA.
†Presently at University of Waterloo in Waterloo, Ontario, Canada.

[1]ADMX is supported by the DOE Office of High-Energy Physics and makes use of CENPA resources by recharge to the cost center.
[2]P. Sikivie, Phys. Rev. Lett. **51**, 1415 (1983).
[3]R. D. Peccei and H. R. Quinn Phys. Rev. Lett. **38**, 1440 (1977).

observations have since constrained the axion's mass to fall within a range in which the axion contributes a significant portion of dark matter; this mass range corresponds to microwave photons.

ADMX operates by stimulating the decay of local dark-matter axions into photons via Primakoff conversion and detecting the resulting photons. The experiment consists of a large tunable microwave cavity immersed in a static magnetic field. The resonance of the cavity further enhances the conversion, and the resonance is tuned to search for axions of varying mass. A radiofrequency (RF) receiver records the power spectrum of the cavity for each tuning configuration as ADMX scans in frequency. However, despite the prodigious predicted local density of dark-matter axions (approximately 10^{14}/cc), the expected electromagnetic signal is extraordinarily weak, around 10^{-22} W in the ADMX apparatus. Our present ADMX collaboration (University of Washington, LLNL, University of Florida, University of Sheffield, NRAO, University of California Berkeley, PNNL, LANL, and FNAL) has constructed and is operating the first, and presently only, experiment sensitive to plausible dark-matter axions.

ADMX is essentially an extraordinarily low-noise radio receiver with a tunable RF cavity forming a tuned resonance circuit. A short electric-field probe couples power from the cavity into a cryogenic amplifier which is cooled to near the cavity temperature.

The dominant background in ADMX comes from thermal noise; the system noise temperature is the noise temperature of the amplifier plus the cavity physical temperature. The motivation for lowering the system noise temperature is clear: (i) for a given axion-photon coupling, the frequency scan rate decreases as the square of the system temperature and (ii) for a given scan rate, the power sensitivity increases as the system temperature drops. ADMX reduces its thermal noise by using low-noise first-stage amplifiers and cooling the cavity. ADMX collaboration members developed superconducting quantum interference device (SQUID) amplifiers in the $100 - 1000$ MHz range specifically for ADMX; this development allowed more than an order-of-magnitude reduction in system noise temperature.

The previous version of ADMX, ADMX Phase 1, was located at LLNL and operated from 2002-2009. The Phase 1 apparatus was fitted with SQUID amplifiers and operated at about 2 K physical temperature via a pumped ^{4}He system. ADMX Phase 1 completed a scan of the $1.9 - 3.5$ μeV axion-mass range and the results for conservative estimates of dark-matter density were published[1]. After further analysis the ADMX collaboration published a search for axions assuming a non-virialized dark-matter distribution within our galaxy[2].

Starting in 2010, ADMX was entirely redesigned and rebuilt at CENPA. The 2013-2014 data runs of ADMX (henceforth referred to as "Phase 2a") were the first data collected by ADMX at CENPA. Throughout the 2014 data runs ADMX employed a pumped ^{4}He system, achieving physical temperatures of about 1.2 K and SQUID amplification. The success of Phase 2a demonstrated full functionality of the new ADMX design and success of the closed-loop helium liquefaction system in maintaining ADMX operations through order-months extended data runs. Additionally, Phase 2a was the first time an axion haloscope had taken

[1] S. Asztalos *et al.*, Phys. Rev. Lett. **104**, 041301 (2010).
[2] J. Hoskins *et al.*, Phys. Rev. D **84**, 121302 (2011).

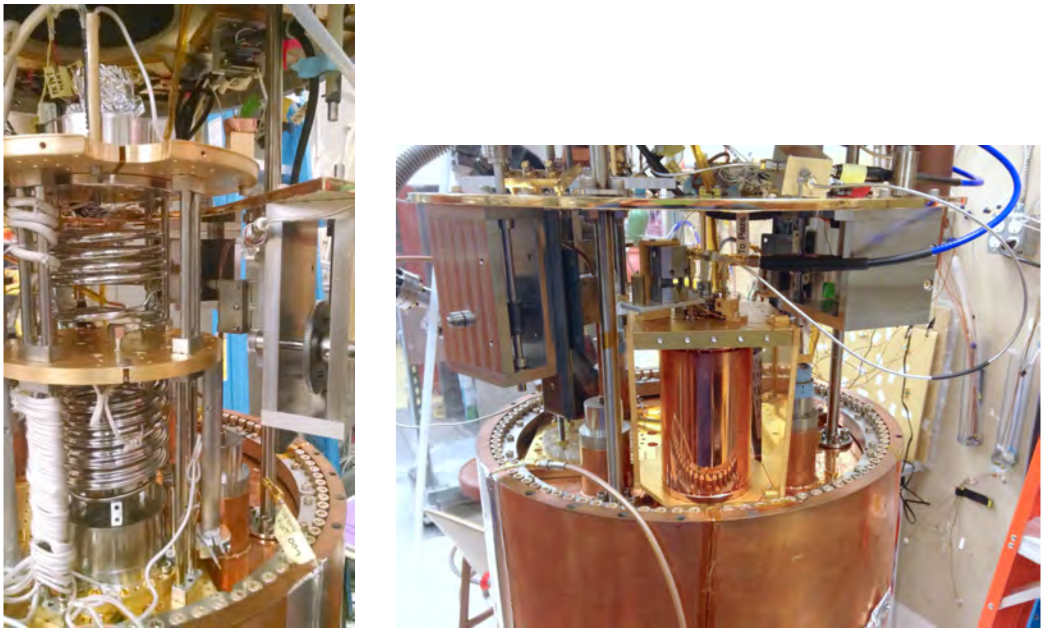

Figure 5.1-1. New additions to ADMX insert. *Left:* Dilution refrigerator. *Right:* Sidecar cavity. Piezoelectric actuators are visible on top of the cavity's gold-plated mechanical support.

data through two independent receiver chains simultaneously and the first time a nonfundamental cavity mode achieved sensitivity to plausible QCD axions. New axion exclusion limits were set in two frequency regimes: $600 - 720$ MHz (corresponding to the "TM010" mode) and $1050 - 1400$ MHz ("TM020" mode), with benchmark QCD axion sensitivity in select frequency ranges.

ADMX entered phase "Gen 2" in fall 2014 and began a period of design, build, and upgrade. Among the major upgrades are: the installation of a dilution refrigerator and supporting plumbing and infrastructure, a smaller cavity that will take data in parallel with the main cavity (named "Sidecar"), a redesigned RF system including Josephson Parametric Amplifier and SQUID amplifiers, and substantial redesign of the thermal linkages and connections in the experiment to achieve the lowest possible operating temperature.

The dilution refrigerator was designed and built by Janis Cryogenics in Woburn, Massachusetts, USA to meet the unusual needs of ADMX. The refrigerator, as well as its associated pumps and gas handling system (GHS), arrived on March 30 2015. The refrigerator was required by ADMX to achieve a stable temperature of 100 mK with a 800 μW heat load applied to the mixing chamber; 100 mK is the target operating temperature for ADMX Gen 2. The dilution refrigerator, its GHS and vacuum pumps, and the vacuum plumbing installed at CENPA were extensively tested by operating the refrigerator in a cryostat isolated from other ADMX systems. On 5 March 2016, the refrigerator was physically moved to the ADMX insert and, at the time of writing, integration of the refrigerator into ADMX was underway.

The addition of Sidecar, the thesis project of graduate student Christian Boutan, will allow ADMX to simultaneously search for axions in a third frequency range. Sidecar is a small $4-6$ GHz cavity that is mounted to the top of the main ADMX cavity. Sidecar shares mechanical supports and cryogenics with the main experiment, but has an independent receiver chain and is tuned by piezoelectric motors. Piezoelectric motors have been a topic of R&D for ADMX for several years, and Sidecar is the first implementation of piezoelectric motors in an ADMX axion search. At the time of writing, Sidecar was ready to take data with anticipated sensitivity approaching plausible QCD axions.

A newly designed RF stand that houses the quantum amplifiers and associated electronics within the ADMX insert was assembled. Quantum amplifiers are very sensitive to magnetic flux; accordingly, an important aspect of the ADMX insert's design is to provide a "field-free" region for the quantum amplifiers. This is not a trivial challenge, as the field of the main magnet reaches a maximum 8 T in the vicinity of the cavity. To this end, the RF stand features magnetic shielding and is situated within the bore of a superconducting so-called "bucking coil." The bucking coil is installed in the insert and, via feedback of magnet field measurements near the quantum amplifiers, dynamically cancels the field of the main magnet at the location of the RF stand. The new RF stand was designed to accommodate the addition of Josephson Parametric Amplifiers (JPAs) for amplification of frequencies higher than the current reach of SQUIDs. SQUID amplifiers have been used in previous versions of ADMX; Gen 2 is the first time ADMX has acquired and tested JPAs. Use of a JPA is planned for channel 2 ("TM020" data) during the next data run. In addition to the physical redesign/rebuild of the RF stand and the tests of JPAs, a liquid-helium test cryostat dedicated to cold tests of the RF has been installed at the ADMX site. The cryostat has been used reliably to test RF and provides a dramatically increased capability to perfect electronics prior to installation in the main insert.

Throughout the last year, ADMX has been rapidly expanding as a collaboration. New institutions officially joining the ADMX collaboration since the 2015 CENPA annual report are Pacific Northwest National Laboratory, Los Alamos National Laboratory, and Fermi National Accelerator Laboratory. At CENPA, ADMX has had numerous personnel changes. Graduate student, then post-doc, Dr. Dmitry Lyapustin has entered private industry in the greater Seattle area. Longtime engineer Clifford Plesha moved to Canada to pursue a masters of science at the University of Waterloo. New post-docs include Dr. Rakshya Khatiwada and Dr. Richard Ottens. Nick Force joined as an engineer. University of Florida graduate student Nicole Crisosto moved to Seattle to work on ADMX at CENPA. Erik Lentz joined as a UW graduate student. Additonally, Dr. Gray Rybka was promoted from research assistant professor to assistant professor.

With the addition of the dilution refrigerator, ADMX Gen 2 will take data at an unprecedented frequency scan rate, over 100 times faster than during the 2013-2014 data runs. JPAs will increase sensitivity to an extended range of axion masses. Further, ADMX will take data simultaneously in three frequency regimes with independent receivers for the main cavity's "TM010" mode, the main cavity's "TM020" mode, and Sidecar's "TM010" mode. The Gen 2 data run should begin in summer 2016, and ADMX is on track to discover or exclude the dark-matter QCD axion.

Figure 5.1-2. *Left:* The RF-testing insert for 4K test of electronics. The silver dewar to right is the cryogenic home for the insert. *Right:* Select members of the ADMX collaboration, 15 January 2016.

6 Relativistic Heavy Ions

6.1 UW URHI program overview

T. A. Trainor

The UW program has addressed the structure and interpretation of hadron yields, spectra, correlations and fluctuations from high-energy p-p, p-A and A-A collisions over a broad range of collision energies. It is observed consistently that minimum-bias (MB) dijets play a major role in all high-energy collisions down to low transverse momentum p_t, and most RHIC and LHC data near mid-rapidity are described accurately by a three-component model (TCM): (a) longitudinal dissociation of projectile nucleons (soft), (b) fragmentation of large-angle-scattered low-x partons (gluons) to dijets (hard), and (c) a nonjet (NJ) azimuth quadrupole. NJ quadrupole systematics are incompatible with hydrodynamic (flow) theory expectations.[1]

Recently we conducted a detailed study of the charge-multiplicity and energy dependence of p-p collisions to establish a reference for larger collision systems and to challenge claims that "collectivity" (flow) is manifested even in the smallest collision systems. A high-statistics data sample from 200 GeV p-p collisions was the basis for a study of 2D angular correlations vs charge multiplicity n_{ch}.[2] A NJ quadrupole component is clearly evident and follows a trend much like that in A-A collisions in terms of participants and binary collisions, but with "participants" in this case being low-x gluons within projectile protons rather than nucleons within projectile nuclei. The NJ quadrupole is probably the source of a "ridge" phenomenon reported for 7 TeV LHC p-p collisions. A related study of η density vs n_{ch} determined the η density of the spectrum hard component, also consistent with the hadron source being MB dijets from low-x gluons. Details are presented in Secs. 6.2 to 6.6.

To extend the TCM to higher energies a study of p_t spectra vs n_{ch} at LHC energies was undertaken.[3] To relate the *spectrum ratio* technique applied to LHC data to the TCM the well-understood 200 GeV p-p spectra were analyzed with the spectrum-ratio method and an algebraic relation established. The result is a simple parametric representation of the energy dependence of both soft and hard components from SPS to top LHC energies in terms of QCD parameter $\log(s/s_0)$. The soft-component trend suggests a manifestation of Gribov diffusion within projectile protons. Another novel outcome is significant n_{ch} dependence of the spectrum hard-component shape consistent with the underlying jet spectrum being biased by an increasing n_{ch} condition to a harder jet spectrum, producing more hadron fragments per jet. That parametrization is also simple. Details are presented in Secs. 6.7 to 6.11.

As part of the latter study a comparison was made between the TCM description of p_t spectra and a so-called power-law model function ("Tsallis statistics") commonly claimed to describe both p-p and A-A spectra accurately. The revised TCM is very accurate, the (data − model) residuals consistent with statistical errors. Residuals in the same form for the power-law model are many tens of statistical error bars, indicating that data model should

[1] D. T. Kettler, D. J. Prindle and T. A. Trainor, Phys. Rev. C **91**, 064910 (2015).
[2] T. A. Trainor and D. J. Prindle, Phys. Rev. D **93**, 014031 (2016).
[3] T. A. Trainor, arXiv:1603.01337.

be rejected. Presentation of such comparisons in the form of data/model or data/fit *ratios* tends to suppress large deviations, especially at lower p_t. The *differences* should always be compared directly to statistical errors for proper evaluation of theory or data models.

6.2 Model fits to 2D angular correlations from 200 GeV *p-p* collisions

D. J. Prindle and T. A. Trainor

2D angular correlations are obtained from *p-p* collisions at $\sqrt{s}$ = 200 GeV for seven event-multiplicity classes, the charge-density $\bar{\rho}_0$ range being approximately 2-20 particles per unit η. This high-statistics analysis is based on 6 million events. The 2D histogram statistical uncertainties for the present study are more than 4.5 times smaller than for previous studies.

Fig. 6.2-1 shows data histograms and model fits for the first and sixth multiplicity bins. 2D angular-correlation histograms are fitted with a six-element model function, the simplest model that provides a reasonable description of all minimum-bias *p-p* data and Au-Au data for all centralities. The 2D model function on $(\eta_\Delta, \phi_\Delta)$ for this analysis includes (i) a same-side (SS) 2D Gaussian, (ii) an η_Δ-independent away-side (AS) azimuth dipole $\cos(\phi_\Delta - \pi)$, (iii) an η_Δ-independent azimuth quadrupole $\cos(2\,\phi_\Delta)$, (iv) a ϕ_Δ-independent 1D Gaussian on η_Δ, (v) a SS 2D exponential and (vi) a constant offset. The azimuth-quadrupole (v_2) element required to describe Au-Au data is retained in the fit model for this *p-p* study.

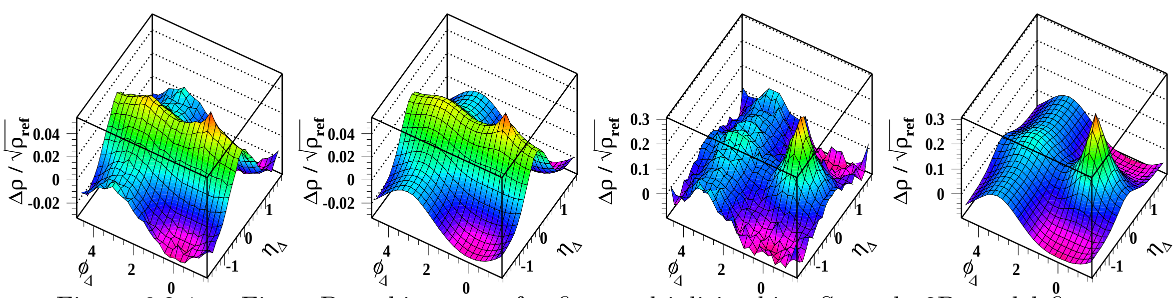

Figure 6.2-1. First: Data histogram for first multiplicity bin. Second: 2D model fit to data. Third: Data histogram for sixth multiplicity bin. Fourth: 2D model fit to data.

The 2D fit model is then the sum of those six elements (in the same order):

$$\frac{\Delta\rho}{\sqrt{\rho_{\rm ref}}} = A_{2D}\,\exp\left\{-\frac{1}{2}\left[\left(\frac{\phi_\Delta}{\sigma_{\phi_\Delta}}\right)^2 + \left(\frac{\eta_\Delta}{\sigma_{\eta_\Delta}}\right)^2\right]\right\} + A_{\rm D}\,\{1+\cos(\phi_\Delta - \pi)\}/2 \tag{1}$$

$$+ \quad A_{\rm Q}\,2\cos(2\,\phi_\Delta) + A_{\rm soft}\,\exp\left\{-\frac{1}{2}\left(\frac{\eta_\Delta}{\sigma_{\rm soft}}\right)^2\right\} + A_{BEC,e\text{-}e}(\eta_\Delta,\phi_\Delta) + A_0.$$

The symmetrized 25 × 25-bin data histograms include more than 150 degrees of freedom and strongly constrain all model parameters. Based on measured parameter trends and comparisons with QCD theory, elements (i) and (ii) together have been attributed to dijet production, (iii) is conventionally identified with elliptic flow in A-A collisions, (iv) is attributed to projectile-nucleon dissociation and element (v) models Bose-Einstein correlations and gamma-conversion electron pairs. The amplitudes of features (i) and (ii) increase with multiplicity n_{ch} much more rapidly than that of (iv), and a significant quadrupole amplitude (iii) is observed for the first time in *p-p* angular-correlation data for larger n_{ch}. Details on jet-related (i), (ii) and nonjet (iii), (iv) correlations are provided in separate articles.

6.3 Systematics of dijet production in 200 GeV *p-p* collisions

D. J. Prindle and T. A. Trainor

Fig. 6.3-1 (first, second) shows fit-parameter trends for jet-related correlations vs charge density $n_{ch}/\Delta\eta$. The same-side (SS) 2D peak per-particle amplitude A_{2D} increases nearly ten-fold with a similar increase of n_{ch}, consistent with a hard-component scaling trend derived from p_t spectra, and remains strongly elongated on azimuth ($\sigma_{\phi_\Delta} > \sigma_{\eta_\Delta}$) even for larger multiplicities. The away-side (AS) 1D peak amplitude on azimuth A_D follows a similar trend, as expected for back-to-back jets. We can relate those trends directly to jet physics.

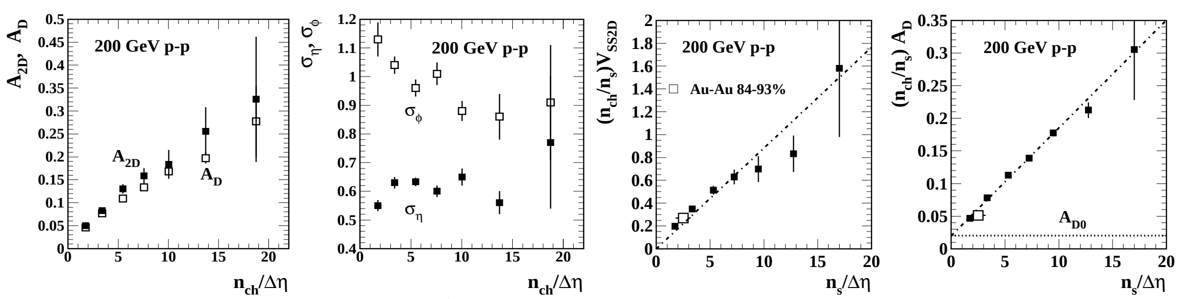

Figure 6.3-1. First: SS and AS peak amplitudes. Second: SS peak widths. Third: Per-participant SS amplitude and Eq. (2) trend. Fourth: AS amplitude with proportional scaling.

Assuming the SS peak represents jet correlations $j^2 = 2\epsilon(\Delta\eta)\, n_j\, \overline{n_{ch,j}^2(\Delta\eta)}/\overline{n_{ch}(n_{ch}-1)}$ is an event-wise pair ratio (number of jet-correlated hadron pairs over total number of pairs in acceptance $\Delta\eta$). The factor $2\epsilon(\Delta\eta)$ (≈ 1.3 for $\Delta\eta = 2$) includes the probability that the recoil partner jet of a dijet also appears within $\Delta\eta$ and $n_j(n_{ch}) = \Delta\eta f(n_{ch})$ is the average number of dijets within $\Delta\eta$. The volume of the SS 2D peak modeled as a 2D Gaussian is

$$V_{SS2D} \equiv 2\pi\sigma_\eta\sigma_\phi A_{2D} \approx n_{ch} j^2 \equiv n_{ch} 2\epsilon(\Delta\eta) n_j(n_{ch}) \frac{\overline{n_{ch,j}^2}}{n_{ch}^2}. \tag{1}$$

The *per-participant-parton* correlation measure (assuming low-x partons $\propto \bar{\rho}_s$) is then

$$\frac{n_{ch}}{n_s} V_{SS2D} = 2\epsilon n_j \overline{n_{ch,j}^2} \times 1/n_s = 2\epsilon(\Delta\eta) f_{NSD} \frac{\bar{n}_{ch,j}^2(\Delta\eta)}{\bar{\rho}_{s,NSD}^2} G^2(\Delta\eta)\bar{\rho}_s, \tag{2}$$

where the $O(1)$ factor $G^2 = \overline{n_{ch,j}^2}/\bar{n}_{ch,j}^2$ accounts for fluctuations in jet fragment multiplicity $n_{ch,j}$, $\bar{\rho}_{s,NSD} = 2.5$ and the measured $f_{NSD} = (1/\sigma_{NSD}) d\sigma_j/d\eta = 0.028$ for 200 GeV *p-p* collisions. Fig. 6.3-1 (third) shows per-participant jet-related SS 2D peak volume vs soft multiplicity density $n_s/\Delta\eta = \bar{\rho}_s$. The solid squares are V_{SS2D} derived from SS peak amplitude A_{2D} combined with measured widths σ_{η_Δ} and σ_{ϕ_Δ} from the first and second panels. The dash-dotted line represents Eq. (2) with mean fragment multiplicity $\bar{n}_{ch,j} = 3.3$ and fluctuation parameter $G^2 = 1.5$. Fig. 6.3-1 (fourth) shows per-participant amplitudes for the AS 1D peak (solid squares) interpreted to represent back-to-back jet pairs. The dashed line is Eq. (2) times a factor of 1/5 adjusted to accommodate the A_D data, confirming that $A_D \propto V_{SS2D}$ within data uncertainties, modulo a fixed offset $A_{D0} \approx 0.02$ representing global transverse-momentum conservation. These results confirm a quantitative relation between published data from event-wise reconstructed jets and jet-related 2D angular correlations.

6.4 Evidence for a nonjet quadrupole in 200 GeV *p*-*p* collisions

D. J. Prindle and T. A. Trainor

Nonjet (NJ) 2D angular correlations of interest include a nonjet quadrupole component (iii) and a soft component (iv) interpreted to represent projectile-nucleon dissociation via low-x gluons to charge-neutral hadron pairs. Fig. 6.4-1 (first) shows measured per-charged-hadron correlation amplitudes. The NJ quadrupole per-particle amplitude increases approximately as n_{ch}^2 and the soft-component amplitude remains approximately constant.

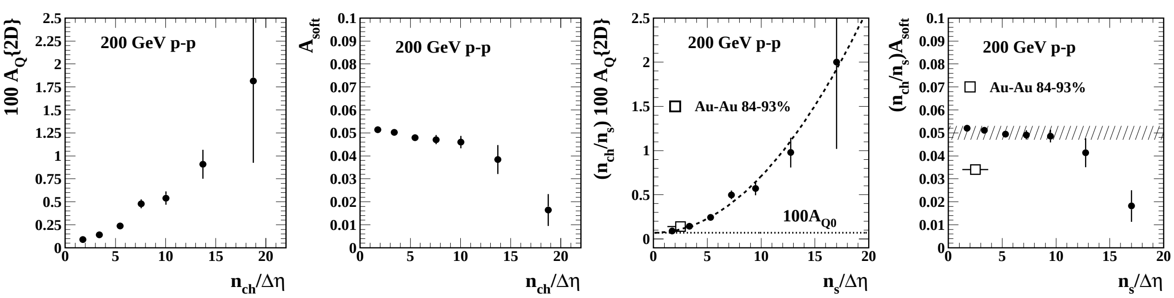

Figure 6.4-1. First: Nonjet quadrupole per-particle amplitude. Second: Soft-component amplitude. Third: Per-participant quadrupole amplitude and Eq. (3) trend. Fourth: Per-participant soft-component amplitude consistent with a constant value: low-x partons $\propto \bar{\rho}_s$.

For Au-Au collisions the following centrality trend is observed for the NJ quadrupole (number of correlated pairs) valid over a large energy interval above 13 GeV ($\bar{\rho}_0 = n_{ch}/\Delta\eta$):

$$V_2^2(b) \equiv \bar{\rho}_0(b)A_Q(b) \quad \propto \quad N_{part}(b)N_{bin}(b)\epsilon_{opt}^2(b), \tag{1}$$

where for A-A collisions $N_{bin} \propto N_{part}^{4/3}$ (eikonal approximation within the Glauber model). For *p*-*p* collisions dijet production scales $\propto \bar{\rho}_s^2$ relative to soft hadron density $\bar{\rho}_s$ suggesting that $N_{part} \sim \bar{\rho}_s$ and dijets $\propto N_{bin} \propto N_{part}^2 \sim \bar{\rho}_s^2$ (eikonal approximation not valid for *p*-*p*). The corresponding form of Eq. (1) for the NJ quadrupole in *p*-*p* collisions should then be

$$V_2^2(n'_{ch}) = \bar{\rho}_0(n'_{ch})A_Q(n'_{ch}) \quad \propto \quad N_{part}^3\langle\epsilon^2\rangle, \tag{2}$$

since there is apparently no systematic dependence on impact parameter b and therefore no b-dependent *p*-*p* eccentricity $\epsilon(b)$. With $N_{part} \sim \bar{\rho}_s$ (representing low-x gluons) we obtain

$$V_2^2(n'_{ch})/\bar{\rho}_s = (\bar{\rho}_0/\bar{\rho}_s)A_Q(n'_{ch}) \quad \propto \quad \bar{\rho}_s^2 \tag{3}$$

as a predicted trend for the NJ quadrupole in p-p collisions based on measured Au-Au quadrupole systematics. Fig. 6.4-1 (third) shows the per-participant amplitude (solid points) compared to Eq. (3) (dashed curve). Modulo a small offset (global momentum conservation), the description is good. The open square is a measured point from 200 GeV Au-Au collisions. We conclude from those results that the nonjet azimuth quadrupole is a universal feature of all high-energy nuclear collisions with $V_2^2 \propto N_{part} N_{bin}$, where N_{part} represents low-x gluons in p-p and nucleons in A-A collisions. It is unlikely that this universal quadrupole phenomenon represents a hydrodynamic flow; it is more likely a novel long-wavelength QCD phenomenon.

6.5 Hadron density on η near mid-rapidity in 200 GeV p-p collisions

D. J. Prindle and T. A. Trainor

Hadron production integrated over azimuth can be represented by the joint charge density

$$\rho_0(y_t, \eta; n'_{ch}) \;=\; S(y_t, \eta; n'_{ch}) + H(y_t, \eta; n'_{ch}) \approx \rho_{s0} S_0(\eta) \hat{S}_0(y_t) + \rho_{h0} H_0(\eta) \hat{H}_0(y_t) \quad (1)$$

describing a two-component (soft + hard) model (TCM) of hadron production. The expression at right in Eq. (1) invokes factorization of the soft and hard components, but hard component $H(y_t, \eta; n'_{ch})$ may include significant y_t-η covariances related to jets. The spectrum model functions $\hat{S}_0(y_t)$ and $\hat{H}_0(y_t)$ on y_t were defined previously. The model functions $S_0(\eta)$ and $H_0(\eta)$ on η are newly defined here, and the ρ_{x0} represent hadron densities at $\eta = 0$.

Fig. 6.5-1 (first) shows corrected y_t-integral charge densities on η for seven multiplicity classes. The dashed curve is the newly inferred TCM soft component. The second panel shows a common instrumental asymmetry (dashed curve) removed from all data due to malfunctions in a small fraction of TPC readout electronics unequal in two halves of the time projection chamber (TPC). The slope at the origin is due to the collision vertex distribution along the TPC z axis.

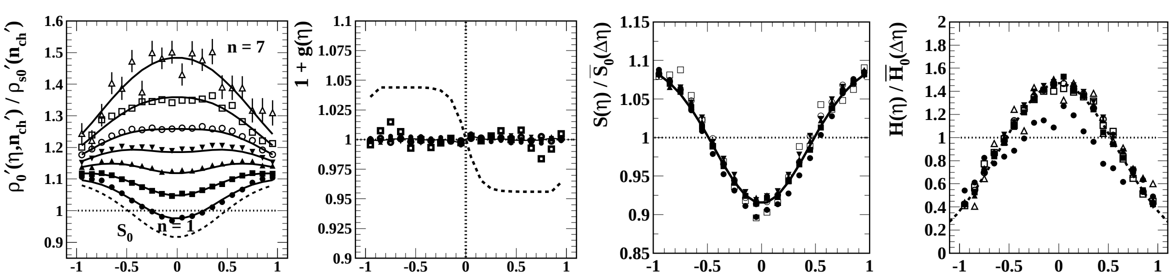

Figure 6.5-1. First: Corrected η densities. Second: Corrected instrumental asymmetry (dashed). Third: TCM η-density soft component. Fourth: η-density hard component.

Fig. 6.5-1 (third) shows data compared to the soft-component model (bold solid curve):

$$\tilde{S}_0(\eta; \Delta\eta) \equiv \frac{S_0(\eta)}{\bar{S}_0(\Delta\eta)} \;=\; 1.09 - 0.18 \exp[-(\eta/0.44)^2/2]. \quad (2)$$

The form of the soft component appears to be unchanging over a large n_{ch} interval. The small data deviations from the model are consistent with statistical errors. The minimum at $\eta = 0$ is expected given the Jacobian for $\eta \leftrightarrow y_z$. An approximately uniform distribution on y_z is expected within the corresponding limited Δy_z acceptance. Fig. 6.5-1 (fourth) shows data compared to the inferred hard-component model function (bold dashed curve)

$$\tilde{H}_0(\eta;\Delta\eta) \equiv \frac{H_0(\eta)}{\bar{H}_0(\Delta\eta)} \quad = \quad 1.47\exp[-(\eta/0.6)^2/2]. \tag{3}$$

The hard-component form is, within statistical errors, approximately independent of n_{ch} over a 10-fold multiplicity increase implying a 100-fold increase in the dijet production rate. This TCM hard-component density suggests that low-momentum hadron fragments from minimum-bias (MB) dijets are strongly peaked within $\Delta\eta = 2$ about $\eta = 0$, consistent with the dominant MB dijet source being low-x gluons within projectile nucleons scattering at large angles to small y_z or η and consistent with results from previous p-p spectrum analysis.

6.6 CMS "ridge," nonjet quadrupole and same-side azimuth curvature

D. J. Prindle and T. A. Trainor

The so-called "CMS ridge" (a SS ridge in p-p collisions at zero azimuth) appears in CMS 2D correlation data for certain cut combinations including large n_{ch} and higher p_t. A previous study[1] demonstrated that extrapolation of NJ quadrupole trends from Au-Au data to N-N (p-p) collisions and from RHIC to LHC energies accounts quantitatively for the observed phenomenon. Given the properties of 200 GeV p-p angular correlations, the CMS ridge at 7 TeV may result from competition between two curvatures on ϕ_Δ within $|\eta_\Delta| > 1$. A ridge appears when structure near $\phi_\Delta = 0$ becomes concave downward (negative *net* curvature). A small *relative* change in certain correlation amplitudes may result in the appearance of a ridge. Fig. 6.6-1 (first) shows curvatures k_X at $\phi_\Delta = 0$ vs soft density $\bar{\rho}_s$ (a proxy for the number of participant low-x gluons). AS dipole curvature k_D is positive and increases linearly while NJ quadrupole curvature k_Q is negative and increases (in magnitude) quadratically. The net curvature $k_D + k_Q$ (solid triangles) is also shown. Fig. 6.6-1 (second) shows the ratio $-k_Q/k_D = 16A_Q/A_D$ vs $\bar{\rho}_s$ increasing linearly (solid line) from zero and passing through unity near the highest-multiplicity class. As noted, for ratios significantly greater than 1 (significant negative net curvature) a SS ridge should appear within $|\eta_\Delta| > 1$. At higher collision energies and with additional p_t cuts the slope of the linear trend should increase, resulting in the appearance of a significant SS ridge even for lower charge densities.

Fig. 6.6-1 (third,fourth) shows 2D angular correlations for $n = 1$ (third) and 6 (fourth) multiplicity classes. Fit-model elements for other structure have been subtracted leaving only the jet-related and NJ quadrupole components. In the region $|\eta_\Delta| > 1$ near $\phi_\Delta = 0$ the curvature varies from large and positive ($n = 1$) to consistent with zero ($n = 6$). Near $\phi_\Delta = \pi$ (AS) the negative curvature approximately doubles, but that important associated phenomenon is typically not acknowledged. Results from the present study describe reported

[1] T. A. Trainor and D. T. Kettler, Phys. Rev. C **84**, 024910 (2011).

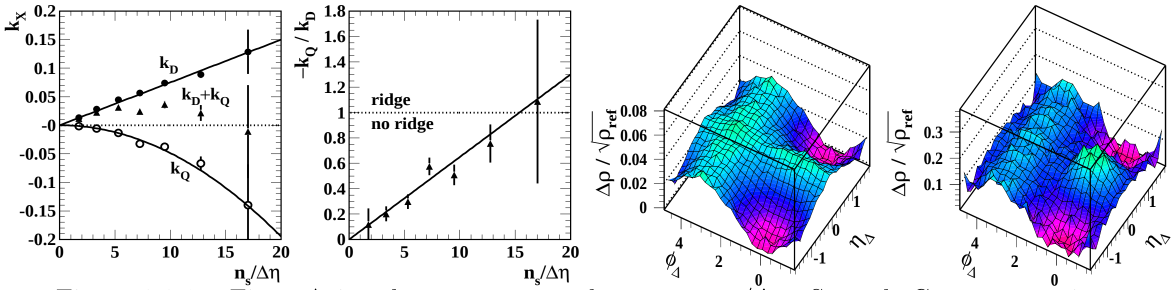

Figure 6.6-1. First: Azimuth curvature trends vs $\bar{\rho}_s = n_s/\Delta\eta$. Second: Curvature ratios. Third: 2D angular correlations for $n = 1$. Fourth: 2D angular correlations for $n = 6$.

7 TeV CMS 2D angular correlations quantitatively but also provide insight into the physical origins of the reported SS ridge. The large collision-energy increase combined with imposed p_t and multiplicity cuts increases the p-p NJ quadrupole amplitude eight-fold relative to the AS 1D jet peak, changing the SS net-curvature sign and producing an apparent SS ridge. In effect, the SS azimuth curvature functions as a comparator, switching from valley to ridge as one competing amplitude increases relative to another. A quantitative curvature change is transformed into a qualitative shape change (mis)interpreted as a novel phenomenon at higher energy, whereas the important "new" phenomenon is the universal nonjet quadrupole.

6.7 Two-component spectrum ratios from 200 GeV *p-p* collisions

T. A. Trainor

The two-component model (TCM) of p-p y_t spectra (conditional on uncorrected n'_{ch} integrated over 2π azimuth and averaged over some η acceptance $\Delta\eta$) is represented by

$$\bar{\rho}_0(y_t; n'_{ch}) \approx \bar{\rho}_s(n'_{ch})\hat{S}_0(y_t) + \bar{\rho}_h(n'_{ch})\hat{H}_0(y_t), \tag{1}$$

where $\bar{\rho}_s = n_s/\Delta\eta$ and $\bar{\rho}_h = n_h/\Delta\eta$ are η-averaged soft and hard hadron densities and $y_t = \ln[(p_t + m_t)/m_h]$. The inferred soft and hard y_t spectrum shapes [unit normal $\hat{S}_0(y_t)$ and $\hat{H}_0(y_t)$] are initially assumed to be independent of n'_{ch}, the parametrized forms being a Lévy distribution on m_t (soft) and a Gaussian with exponential tail on y_t (hard). The 200 GeV TCM should be extended to higher energies, but spectrum n_{ch} dependence at LHC energies has been published only in terms of spectrum *ratios* for which some spectrum information is discarded. Spectrum-ratio data can be used to estimate the TCM model ratio

$$T_0(p_t) \equiv \frac{\hat{H}_0(p_t)}{\hat{S}_0(p_t)} \tag{2}$$

assuming fixed hard-component model $\hat{H}_0(p_t)$, but the individual model components are not accessible from spectrum ratios alone. LHC spectrum-ratio data can be better interpreted by applying a similar ratio analysis to 200 GeV data where the spectrum structure is already well understood in terms of the TCM.

The TCM for a ratio of two uncorrected spectra $\bar{\rho}'_0(p_t; n'_{ch})$ (from seven multiplicity classes) normalized by corrected soft-component densities $\bar{\rho}_s$ (first line) is the second line below

$$\begin{aligned} X(p_t; n'_{ch1}, n'_{ch2}) &\equiv \left(\frac{\bar{\rho}_{s2}}{\bar{\rho}_{s1}}\right) \frac{\bar{\rho}'_0(p_t; n'_{ch1})}{\bar{\rho}'_0(p_t; n'_{ch2})} \\ &\approx \left(\frac{\bar{\rho}_{s2}}{\bar{\rho}_{s1}}\right) \frac{\bar{\rho}_{s1}\hat{S}_0(p_t) + \bar{\rho}_{h1}\hat{H}_0(p_t)}{\bar{\rho}_{s2}\hat{S}_0(p_t) + \bar{\rho}_{h2}\hat{H}_0(p_t)} \\ &= \frac{1 + \alpha\bar{\rho}_{s1}T_0(p_t)}{1 + \alpha\bar{\rho}_{s2}T_0(p_t)} \\ &\to \frac{\bar{\rho}_{s1}}{\bar{\rho}_{s2}} \quad \text{for larger } p_t, \end{aligned} \tag{3}$$

where it is assumed that p_t-dependent tracking efficiencies cancel in the spectrum ratio, and the assumed relation $\bar{\rho}_h = \alpha\bar{\rho}_s^2$ with $\alpha = O(0.01)$ is based on spectrum-data systematics.

Fig. 6.7-1 (first) shows a spectrum ratio for multiplicity class $n = 2$ over $n = 6$ (open circles) and its inverse (solid points) for illustration. Results for other combinations are similar. The soft-component densities are $\bar{\rho}_s = 3.4$ and 12.6 respectively (NSD is $\bar{\rho}_s \approx 2.5$). The TCM in Eq. (3) (third line) is represented by the solid and dashed curves. The density ratios (fourth line) are represented by upper and lower dotted lines as limiting cases of the TCM $X(p_t; n_1, n_2)$. The discrepancy between spectrum data and the TCM at larger p_t indicates that the assumption of a fixed hard component $\hat{H}_0(y_t)$ independent of n_{ch} is incorrect.

Fig. 6.7-1 (second) shows ratios of spectrum data to the corresponding TCM expressions with fixed hard component. Above $y_t = 3$ significant systematic variation (10% increase per multiplicity class at 4 GeV/c) suggests a requirement for a decreasing $\hat{H}_0(y_t; n'_{ch})$ power-law exponent q with increasing n_{ch}, as might be expected if demand for larger event multiplicities biases to more jet fragments from harder jets at higher p_t. Although the ratio deviations from unity at lower y_t are smaller in absolute magnitude they are statistically more significant.

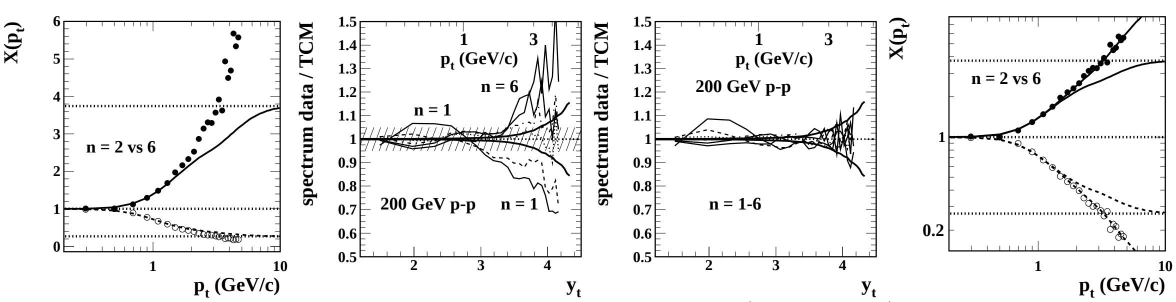

Figure 6.7-1. First: Spectrum ratio for $n = 2$ over $n = 6$ (open points) and its reciprocal (solid points). Second: Ratio of data spectra to TCM spectra for six multiplicity classes assuming fixed $\hat{H}_0(y_t)$. Third: Same ratios but with varying $\hat{H}_0(y_t; q, \sigma_{y_t})$. Fourth: As in the first panel with varying $\hat{H}_0(y_t; q, \sigma_{y_t})$ and log-log format revealing reciprocal systems.

Fig. 6.7-1 (third) shows data/TCM ratios based on a revised TCM with two hard-component $\hat{H}_0(y_t)$ parameters varying. Whereas $\hat{H}_0(y_t)$ was previously held fixed with power-law index $q = 5$ and Gaussian width $\sigma_{y_t} = 0.465$ those parameters are now varied to accommodate individual spectra. The modified TCM describes data *above the hard-component mode* within statistics (symmetric solid curves). Substantial spectrum deviations from the fixed TCM correlated with n_{ch} appear below the mode, but the corresponding manifestations in spectrum ratios below $y_t = 3$ are strongly suppressed by the ratio format. Further modifications to $\hat{H}_0(y_t; n'_{ch})$ could also accommodate those deviations (with the exception of the $n = 1$ high solid curve), but they do not play a significant role for these spectrum ratios.

Fig. 6.7-1 (fourth) repeats Fig. 6.7-1 (first) with the revised TCM including varying $\hat{H}_0(y_t; q, \sigma_{y_t})$. The updated TCM ratios (new solid and dashed curves) pass through all data points (modulo statistical fluctuations), but the asymptotic limit in Eq. (3) is no longer $\bar{\rho}_{s1}/\bar{\rho}_{s2}$ (dotted lines), but instead $\bar{\rho}_{s1}\hat{H}_0(p_t; q_1, \sigma_{y_t1})/\bar{\rho}_{s2}\hat{H}_0(p_t; q_2, \sigma_{y_t2})$, confirming that dijet production changes significantly with increasing event multiplicity as described in a separate article. The log-log format reveals the reciprocal relation of the two spectrum ratios.

6.8 Two-component spectrum ratios from 13 TeV *p*-*p* collisions

T. A. Trainor

LHC spectrum ratios are defined in terms of spectra normalized by total multiplicity

$$R(p_t; n'_{ch}) \equiv \frac{\bar{\rho}'_{00}(\Delta\eta)}{\bar{\rho}'_0(n'_{ch}, \Delta\eta)} \frac{\bar{\rho}'_0(p_y; n'_{ch}, \Delta\eta)}{\bar{\rho}'_{00}(p_y; \Delta\eta)} \approx \left(\frac{1 + \alpha' \bar{\rho}'_{s0}}{1 + \alpha' \bar{\rho}'_s}\right) \left(\frac{\bar{\rho}'_{s0}\bar{\rho}_s}{\bar{\rho}'_s \bar{\rho}_{s0}}\right) \frac{1 + \alpha \bar{\rho}_s T(p_t)}{1 + \alpha \bar{\rho}_{s0} T_0(p_t)}. \quad (1)$$

Fig. 6.8-1 (first) shows 13 TeV spectrum-ratio data (points) for three n'_{ch} conditions (multiplicity bins A, B and C) relative to a reference spectrum. TCM curves are defined by Eq. (1) with reference $T_0(p_t)$ (dashed) and n_{ch}-dependent $T(p_t; n'_{ch})$ (solid) defined below. The dash-dotted curves emulate MC results (e.g. PYTHIA) by increasing the $\hat{H}_0(p_t)$ centroid from 2.4 to 2.7. Fig. 6.8-1 (second) shows a first intermediate quantity $X(p_t; n'_{ch})$ extracted from $R(p_t; n'_{ch})$ data (points) for conditions n'_{ch}. For 200 GeV data $X(p_t)$ emerges directly from the spectrum ratio, thus bypassing the quantity $R(p_t)$ because of the choice of normalization. A further intermediate ratio quantity is

$$Y(p_t) \equiv \frac{1}{\bar{\rho}_s/\bar{\rho}_{s0} - 1} \left[X(p_t; n'_{ch}) - 1\right] \approx \frac{(\bar{\rho}_s/\bar{\rho}_{s0})T(p_t)/T_0(p_t) - 1}{\bar{\rho}_s/\bar{\rho}_{s0} - 1} \left(\frac{\alpha \bar{\rho}_{s0} T_0(p_t)}{1 + \alpha \bar{\rho}_{s0} T_0(p_t)}\right) \quad (2)$$

with reference $Y_0(p_t)$ defined by the quantity in parentheses.

Fig. 6.8-1 (third) shows the estimated hard/soft ratio $T(p_t)$ (points) obtained from spectra via data transformations $R(p_t; n'_{ch}) \rightarrow X(p_t; n'_{ch}) \rightarrow Y(p_t; n'_{ch}) \rightarrow T(p_t; n'_{ch})$ in the form

$$\alpha \bar{\rho}_s T(p_t) = \alpha \bar{\rho}_{s0} T_0(p_t) \left[\left(\frac{\bar{\rho}_s}{\bar{\rho}_{s0}} - 1\right) \frac{Y(p_t)}{Y_0(p_t)} + 1\right] \quad (3)$$

with $T_0(p_t)$ (upper dashed curve) obtained from the single 13 TeV spectrum fit below. A parametrization for $T_0(p_t)$ is adjusted to fit the 13 TeV $T(p_t)$ data ($\bar{y}_t = 2.4$, $\sigma_{y_t} = 0.52$ and $q = 7$), is back transformed to generate model curves in these figures, and is used to obtain

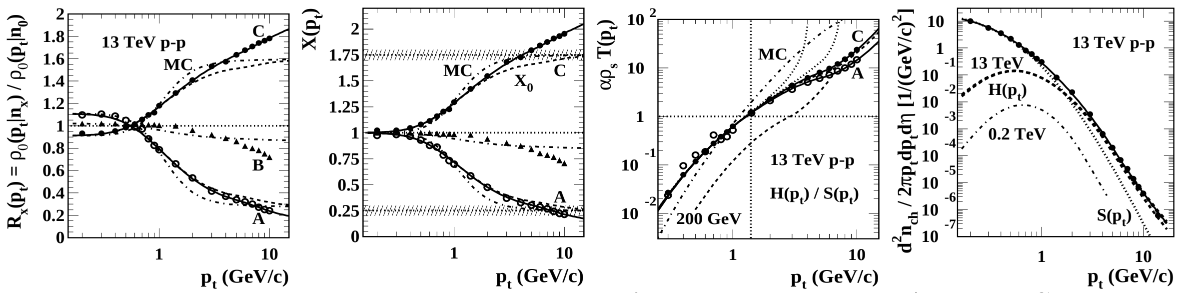

Figure 6.8-1. First: 13 TeV spectrum ratios for multiplicity classes A, B and C vs a minimum-bias reference. Second: Rescaled spectrum ratios. Third: Hard/soft ratio $T(p_t)$ for two multiplicity classes. Fourth: 13 TeV TCM for reference spectrum (solid) and multiplicity classes A and C (dashed) with hard components for 13 TeV and 200 GeV.

the final 13 TeV TCM model functions. The lower dashed curve is $T_0(p_t)$ for 200 GeV, the change in $H(p_t)/S(p_t)$ at 13 TeV indicating the larger role played by jets there at *lower* p_t. The dash-dotted curve (MC) reveals major discrepancies between Monte Carlo and data.

Fig. 6.8-1 (fourth) shows a 13 TeV reference spectrum (points). The TCM (solid) is

$$\bar{\rho}_{00}(p_t) \quad = \quad \bar{\rho}_{s0}\hat{S}_0(p_t; T, n)\,[1 + \alpha\bar{\rho}_{s0}T_0(p_t)] \tag{4}$$

with $\alpha\bar{\rho}_{s0}T_0(p_t)$ represented by the dashed curve in the third panel. The only TCM adjustment to fit the spectrum data is variation of the exponent n in the usual Lévy form of $\hat{S}_0(m_t; T, n)$, with slope parameter $T = 145$ MeV held fixed. The fitted Lévy exponent $n \approx 7.8$ at 13 TeV can be compared with $n \approx 12.5$ at 200 GeV. Two parameters for $T(p_t; n'_{ch})$ are adjusted to match the ratio data, the variations being consistent with a 200 GeV analysis. The result is a complete TCM for 13 TeV with varying $T(p_t; n'_{ch})$ that defines the upper and lower dashed curves at higher p_t in the fourth panel and passes through all the ratio data in other panels.

6.9 Energy evolution of p_t spectrum components from p-p collisions

T. A. Trainor

Fig. 6.9-1 (first) shows soft-component exponents n in the form $1/n$ inferred from spectrum data for three collision energies (solid points) at the SPS, RHIC and LHC respectively. The solid curve is an algebraic hypothesis based on variation of the soft component due to Gribov diffusion. Low-x gluons result from a virtual parton splitting cascade within projectile nucleons whose mean depth on x is determined by the collision energy. Each step of the cascade adds transverse-momentum components in a random-walk process. The depth of the cascade is proportional to $\ln(s/s_0)$, and $\sqrt{s_0} \approx 10$ GeV is inferred from dijet systematics. Given the properties of a random walk and with $1/n$ as a measure of transverse-momentum excursions its trend is estimated as $\propto \sqrt{\ln(\sqrt{s}/10\text{ GeV})}$ (solid curve). The open circles at 0.9, 2.76 and 7 TeV are interpolations of the Lévy exponent to $n = 9.82$, 8.83 and 8.16 respectively.

Fig. 6.9-1 (second) shows inverse values (solid points) of hard-component exponents $q = 5.15$ for 200 GeV and $q = 3.65$ for 13 TeV, plotted vs the quantity $\Delta y_{max} \equiv \ln(\sqrt{s}/6\text{ GeV})$, observed to describe the energy trend for jet-spectrum widths from NSD p-p collisions based on a jet-spectrum infrared cutoff near 3 GeV. Such a relation is expected given that the p-p p_t-spectrum hard component can be expressed as the convolution of a fixed p-p fragmentation-function ensemble with a collision-energy-dependent jet spectrum. The hatched band indicates an inferred cutoff to dijet production from low-x gluon collisions near 10 GeV. That the same relation applies to the ensemble-mean-p_t hard component has been verified. Inverse values of $q = 3.80$ for 7 TeV, $q = 4.05$ for 2.76 TeV and $q = 4.45$ for 0.9 TeV (open circles) are then obtained by interpolation.

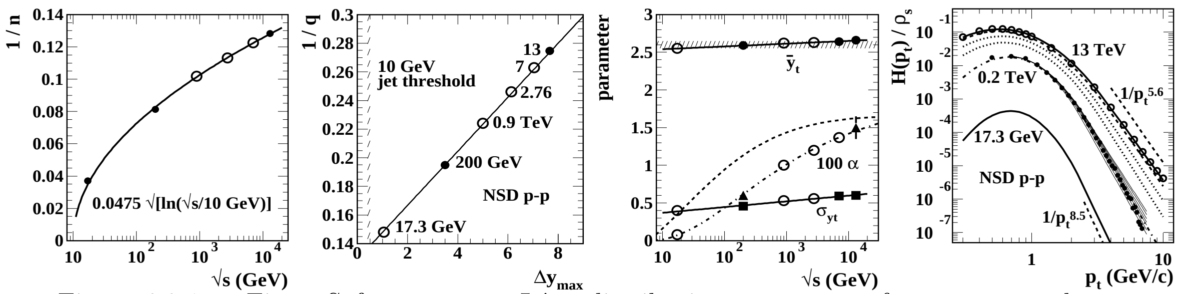

Figure 6.9-1. First: Soft-component Lévy distribution exponent n for spectra at three energies (solid points). Second: Hard-component parameter q inferred for two energies (solid points). Third: Hard-component parameters $\bar{y}_t$ and σ_{y_t} inferred for three energies and soft-hard parameter α for two energies (solid points). Fourth: TCM hard-component model for six collision energies (curves) compared to data for 200 GeV and 13 TeV (points).

Fig. 6.9-1 (third) shows TCM hard-component model parameters (points) vs collision energy. The solid points are derived from data. The open points are interpolations or extrapolations derived from the inferred or predicted trends in the figure (curves). The trends for $\bar{y}_t$ and σ_{y_t} are straight lines. Whereas σ_{y_t} increases with energy by 50%, the upper limit on $\bar{y}_t$ variation is five percent. The soft-hard parameter α is defined by $\bar{\rho}_h = \alpha\bar{\rho}_s^2$. Its energy dependence can be inferred from differential analysis of p_t spectra as for 200 GeV and for 13 TeV in the present study. It is also related to jet systematics by

$$\bar{\rho}_{h,NSD} \quad = \quad \epsilon(\Delta\eta) f_{NSD} 2\bar{n}_{ch,j} \tag{1}$$

for a given collision energy, where $2\bar{n}_{ch,j}$ is the mean hadron fragment multiplicity per dijet averaged over the jet spectrum for that energy and $f_{NSD} = (1/\sigma_{NSD}) d\sigma_{jet}/d\eta$. The energy trends for those quantities, inferred from reconstructed-jet data, and $\bar{\rho}_s$ from spectrum data can be used to predict an energy trend for α. Certain defined kinematic quantities are useful: $y_{max} = \ln(2E_{jet}/m_\pi)$ is a logarithmic representation of jet energy, and $y_b = \ln(\sqrt{s}/m_\pi)$ represents the p-p collision energy. $\Delta y_b = \ln(\sqrt{s}/10 \text{ GeV})$ represents an observed cutoff of dijet production near $\sqrt{s} = 10$ GeV, and $\Delta y_{max} = \ln(\sqrt{s}/6 \text{ GeV})$ responds to an inferred infrared cutoff of jet spectra near $E_{jet} = 3$ GeV. A comprehensive analysis of jet spectra provides the relations $d\sigma_{jet}/d\eta \approx 0.026\Delta y_b^2 \Delta y_{max}$ and $\sigma_{NSD} \approx 0.83(32 + \Delta y_b^2)$. $\bar{\rho}_{s,NSD} \approx 0.81\Delta y_b$ is inferred from spectrum analysis and charge-density trends. The dijet acceptance factor $\epsilon \approx 0.6$ is estimated for $\Delta\eta = 1.5$ - 2. Combining various elements the $\alpha(\sqrt{s})$ trend is

$$\alpha(\sqrt{s}) \quad \approx \quad \frac{\epsilon(\Delta\eta)}{\sigma_{NSD}} \frac{d\sigma_{jet}}{d\eta} \frac{2\bar{n}_{ch,j}}{\bar{\rho}_{s,NSD}^2} \tag{2}$$

$$\approx \frac{0.6 \times 0.026\Delta y_b^2 \Delta y_{max} \times 2\bar{n}_{ch,j}}{0.83(32 + \Delta y_b^2) \times (0.81\Delta y_b)^2}$$
$$\approx \frac{0.03\Delta y_{max}}{32 + \Delta y_b^2} \times 2\bar{n}_{ch,j}(\sqrt{s}).$$

The systematic variation of $\bar{n}_{ch,j}$ with *p*-*p* collision energy can be represented by the simple proportionality $2\bar{n}_{ch,j}(\sqrt{s}) \approx 0.7\Delta y_{max}$. When inserted into Eq. (2) that relation produces the dash-dotted curve in the third panel describing well the soft-hard $\alpha(\sqrt{s})$ trend inferred from spectrum analysis. This comparison establishes an absolute relation between jet fragments within reconstructed dijets and jet fragments appearing as spectrum hard components.

Fig. 6.9-1 (fourth) shows the ratio $H(p_t; E)/\bar{\rho}_s(E) \approx \alpha(E)\bar{\rho}_s(E)\hat{H}_0(p_t; E)$ measuring the spectrum hard component *per soft-component yield* corresponding (by hypothesis) to dijet production per participant low-x gluon. The two dotted curves are for 0.9 and 2.76 TeV and the dashed curve is for 7 TeV. The thin solid curves for 200 GeV show the n_{ch} dependence of the hard component reported in a separate article. Isolated hard components rather than spectrum ratios clarify spectrum energy evolution and its relation to dijet production. The TCM described here provides an accurate *p*-*p* spectrum description for all presently available collision energies for which dijet production is relevant. The separate soft and hard components can be compared directly with QCD theory and with related experimental data.

6.10 n_{ch} dependence of spectrum hard component from *p*-*p* collisions

T. A. Trainor

In previous two-component-model (TCM) analysis of *p*-*p* p_t spectra the spectrum hard component was assumed to be approximately independent of n_{ch}, although significant variation below the hard-component mode was obvious in spectrum data. Analysis of 200 GeV spectra with a spectrum-ratio method applied to LHC data revealed statistically significant variation above the hard-component mode. The hard-component model was then revised to allow variation of two parameters with n_{ch} to accommodate spectrum-ratio data.

Fig. 6.10-1 (first) shows the variation of two $\hat{H}_0(y_t)$ parameters with soft-component charge density $\bar{\rho}_s$ that provides the most accurate description of spectrum ratios for all multiplicity classes. The optimized 200 GeV parameters follow simple $\bar{\rho}_s$ trends:

$$\begin{aligned} 2/q &= 0.373 + 0.0054\bar{\rho}_s \quad \text{(solid)}, \\ \sigma_{y_t} &= 0.385 + 0.09\tanh(\bar{\rho}_s/4) \quad \text{(dashed)}. \end{aligned} \tag{1}$$

The nominal parameter values for the 200 GeV fixed $\hat{H}_0(y_t)$ model are represented by the dotted and dash-dotted lines. The variation of two parameters in combination serves to broaden the hard-component model above the mode toward higher p_t. Such $\hat{H}_0(p_t)$ broadening could represent hardening of the underlying parton spectrum and/or modified jet formation. The parameter variations with n_{ch} for 13 TeV follow trends similar to Eqs. (1). Fig. 6.10-1 (second) shows the result of further modification of the hard-component model. Gaussian widths

σ_{y_t+} above and σ_{y_t-} below the mode are treated separately to accommodate data below the mode as well (except for $n = 1$). The values in the left panel are retained for σ_{y_t+} but values for σ_{y_t-} are varied independently in the form $1/\sigma^2_{y_t-} = 13.5 \tanh[(\bar{\rho}_s - 3)/5]$.

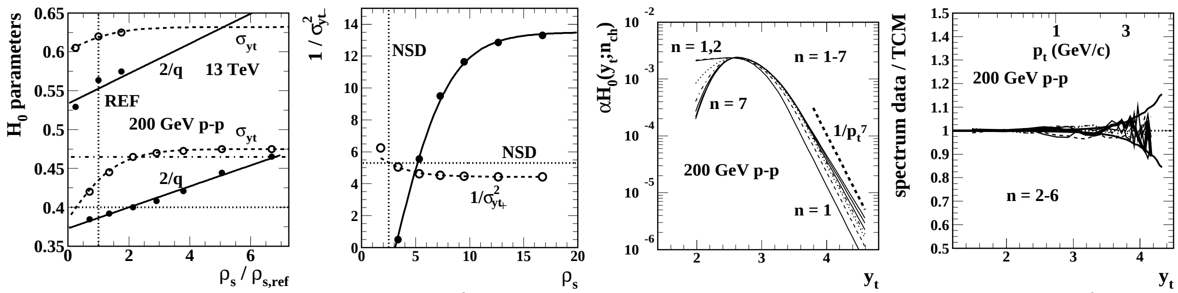

Figure 6.10-1. First: Variation of two hard-component parameters q and σ_{y_t+} with soft-component density $\bar{\rho}_s$ at 200 GeV and 13 TeV. Second: Variation of a third hard-component parameter σ_{y_t-} with soft-component density $\bar{\rho}_s$ at 200 GeV. Third: Summary of 200 GeV hard-component n_{ch} dependence for seven multiplicity classes. Fourth: Data/TCM residuals with varying $\hat{H}_0(y_t)$ for five multiplicity classes consistent with statistical errors.

Fig. 6.10-1 (third) summarizes the revised 200 GeV TCM hard-component model for seven multiplicity classes. The model for class $n = 1$ cannot accommodate data below the mode: the trend for $1/\sigma^2_{y_t-}$ requires a negative entry for $n = 1$, and the shape of the model function would remain very different from the data. The value of σ_{y_t-} for $n = 2$ is retained for $n = 1$. Fig. 6.10-1 (fourth) shows data/TCM residuals consistent with statistical errors (bold solid curves symmetric about unity) over a y_t range relevant to the hard component.

6.11 Model comparison for p_t spectra from high-energy p-p collisions

T. A. Trainor

It is claimed that p_t spectra from high-energy nuclear collisions can be well described by a so-called power-law function (similar to a Lévy distribution or "Tsallis statistics"). The power-law model, also described as a "modified Hagedorn function," is commonly defined as

$$\bar{\rho}(p_t; n'_{ch}) \quad = \quad \frac{p_t}{m_t} \frac{A(p_{t0}, b)}{(1 + p_t/p_{t0})^b}. \tag{1}$$

I demonstrate here with 200 GeV p-p data that the claim is incorrect. This issue is of central importance because claims to measure "radial flow" are based on strong assumptions about the appropriate model function for p_t spectra. Equation (1) is a basis for the so-called blast-wave model used to infer radial flow, and strong jet contributions are thereby ignored.

Fig. 6.11-1 (first) shows the result of varying the two-component model (TCM) hard component. Gaussian widths σ_{y_t+} above and σ_{y_t-} below the mode are treated separately. Exponent q and width σ_{y_t+} are varied to accommodate data above the mode while width σ_{y_t-} is varied independently to accommodate data below the mode (except for $n = 1$). The residuals for n = 2-6 are consistent with point-to-point systematic errors (about 1 per mil of data values). Fig. 6.11-1 (second) shows residuals from fits to the same data with Eq. (1)

(the prefactor p_t/m_t is unimportant), processed in the same manner as in the first panel. The deviations for lower multiplicities are tens of statistical error bars (denoted by the narrow hatched band) over the entire y_t range.

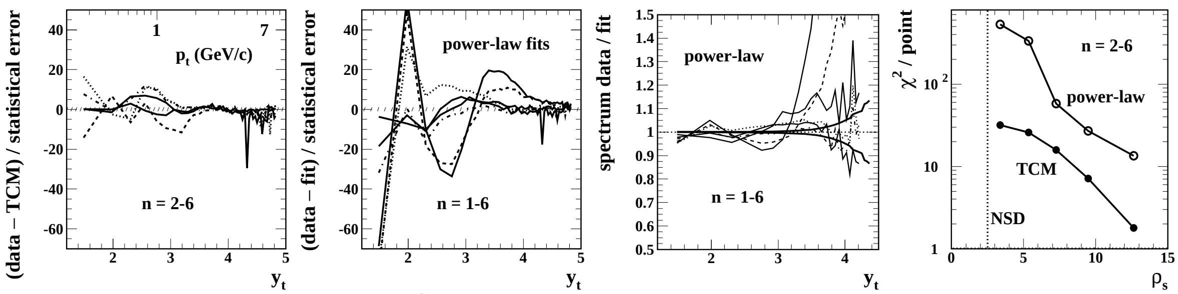

Figure 6.11-1. First: Data-TCM residuals relative to statistical errors with varying hard component. Second: Data-TCM residuals with power-law fit function. Third: Data/fit ratios with power-law fit function. Fourth: χ^2/point for power-law fit function and TCM.

Fig. 6.11-1 (third) shows the same residuals in the more conventional spectrum-ratio format. The bold solid curves symmetric about unity indicate one-sigma statistical errors for such ratios. Fig. 6.11-1 (fourth) shows mean-squared values of residuals in the second panel for five multiplicity classes (open circles). The equivalent for TCM residuals in the first panel are included for comparison (solid points). Those values approximate χ^2 per degree of freedom but the number of model parameters is not included in the ratio, only the number of fitted data points (23). It could be argued that there are more parameters for the TCM (six) than for the power-law model (three), but the nominal number of TCM parameters is substantially reduced by their simple algebraic trends over multiplicity classes and collision energies. The few TCM model parameters are not determined independently by free fits to individual spectra yet they predict accurately hundreds of data points in many spectra.

7 Education

7.1 Use of CENPA facilities in education and course work at UW

E. B. Smith

CENPA has always maintained a prominent role in broad-scope, practical, hands-on training for both undergraduate and graduate students at the University of Washington. One of the most significant and unique advantages that our students enjoy is direct participation in the ongoing local research at CENPA and the engineering contributions to our off-site collaborations.

We have maintained a presence in the UW curriculum since 2011, and currently offer an accelerator-based laboratory course in nuclear physics. This graduate course in physics is entitled "Nuclear Physics: Sources, Detectors, and Safety", Phys 575/576 (Sec. 7.3).

We continue to provide extensive hands-on training for both undergraduate and graduate students. Our electronics shop (Sec. 8.4) is available for use by the students to learn electronic design and assembly. In the student shop (Sec. 8.5) all users are trained in machine-tool operation and safety. Additionally, CENPA has a longstanding and unique history of teaching students how to operate the tandem accelerator and ion sources (Sec. 7.2).

7.2 Student training

G. T. Holman, D. R. Hyde, J. R. Pedersen, D. A. Peterson, E. B. Smith, and D. I. Will

Students at CENPA receive training in a variety of technical laboratory skills that include accelerator operation, machining, and electronics. Graduate and undergraduate students receive accelerator operation training (a.k.a. "crew training") in which the students are taught to operate the duoplasmatron ion source and the 9 megavolt tandem Van de Graaff accelerator. These students practice generating an ion beam, charging the tandem, and tuning the beam through the accelerator. Frequently, these individuals also gain experience with vacuum systems and cryogenics as dictated by the needs of the experiment on which they are working.

CENPA student-shop training is received by staff, graduate students, undergraduate students, and REU students on a continuing basis. These individuals are instructed on how to safely operate a variety of machines including lathes, milling machines, drill presses, saws, grinders, metal shears and breaker, hand tools, and power tools. Some are even trained to use an oxygen/acetylene cutting torch. Additionally, training is given on the student-shop NC 2-Axis Trak milling machine and on the KERN HSE large-format laser cutter system, both of which provide computer-controlled fabrication of complicated parts for research projects.

In the electronics shop, instruction is provided in soldering, wiring, and the use of basic electrical and electronic components. Training in the use of a UV ProtoLaser is given to individuals wanting to fabricate prototype circuit boards for research projects.

7.3 Accelerator-based lab class in nuclear physics

A. García, J. R. Pedersen, E. B. Smith, and D. I. Will

We have developed a graduate-level lecture and laboratory class for the purpose of teaching aspects of nuclear theory and techniques for nuclear physics experiments[1]. This includes student operation of the tandem accelerator to achieve an ion beam on experimental targets.

The class met twice a week during the Winter 2016 quarter, once for a 1-1/2 hour lecture and again in groups for a 1-1/2 hour lab session. The list of subjects we covered were:

1. Atomic nucleus. Basics of nuclear physics, nuclear energy, orders of magnitude.
2. Attenuation of photon radiation. Solid-state detectors (Ge and Si).
3. Ranges of ions and electrons. The weak interaction. Radioactivity and radiation damage and health risks (α, β, γ, and neutron activity).
4. Deciphering a mystery γ spectrum measured using a Ge solid-state detector. Gauging the level of radioactivity and assessing health risks.
5. 9 megavolt tandem accelerator function, duoplasmatron ion source function, and ion beam optics. Tuning beam through tandem accelerator.
6. Rutherford back-scattering (RBS) spectra measured by scattering accelerated protons off foil targets and into Si solid-state detectors. Deciphering a mystery spectrum and the contents of a mystery foil.
7. Fission and fusion. The functioning of reactors.
8. Nuclear astrophysics: nucleosynthesis in stars.
9. Sources of positrons for positron emission tomography.
10. Resonance energy of (p,γ) nuclear reaction determined by irradiating a target with accelerated protons and detecting resulting γs in a Ge solid-state detector.

Thirteen students attended the Winter Quarter 2016 sessions. They engaged enthusiastically in discussions during lectures and in laboratory sessions. A tour of the Boeing Radiation and Effects Laboratory (BREL) in Seattle was arranged by one of the Phys 575/576 students who was an employee of that facility.

[1] Phys 575/576, Nuclear Physics: Sources, Detectors, and Safety, http://faculty.washington.edu/agarcia3/phys576.

8 Facilities

8.1 Facilities overview

E. B. Smith and D. I. Will

CENPA constantly updates and improves its facilities and provides the best possible resources and research environment for its users as new experiments emerge and as the demands of research change with time. In addition we maintain high-quality shop services that are available to the faculty, staff, and students.

The computational facilities at CENPA remain at the front edge of technology. As always, personal desktop and portable computers are maintained and the technology kept current. The NPL Data Center (NPLDC), which previously contained a single high performance cluster, ATHENA, now provides the infrastructure to multiple clusters and department appliances (Sec. 8.3).

The laboratory facilities that surround, support, and include the FN tandem Van de Graaff accelerator are constantly evolving, and provide hands-on training for students in operation of the accelerator and ion sources (Sec. 8.2). A graduate physics course using the accelerator to perform nuclear-physics experiments has been developed (Sec. 7.3). Additionally, we have begun an upgrade project to replace the existing control hardware and software used by the accelerator system.

The CENPA electronics shop provides modern surface-mount technology and miniature cable-manufacturing equipment on site and in appropriately clean areas. The shop continues to do custom design work for specialty preamplifiers as well as dedicated multichannel data-acquisition (DAQ) systems. The shop also interacts with the on-campus Washington Technology Center, taking advantage of much of the capital-intensive, high-tech equipment there that is more effectively used as a cost-shared facility. The electronics-shop staff also provides training for students and other staff members (Sec. 8.4).

The CENPA instrument shop (main instrument shop) is manned by four highly skilled instrument makers with vast knowledge of metallurgy, welding, and fabrication (Sec. 8.5). This shop has CNC machines, mills, lathes, and large-capacity machines. The instrument shop can provide engineering for all research projects. The CENPA student shop is headed by an instrument maker who provides safety training and instruction to students, staff, and faculty. This shop includes mills, lathes, drill presses, a laser cutter, and 3D printer.

Much effort is now being made to remove equipment and structures belonging to the long decommissioned UW Booster LINAC in the west end of the accelerator tunnel. The cleared space will be used for the newly planned ADMX collaboration experiment ORPHEUS.

8.2 Van de Graaff accelerator and ion-source operations and development

M. J. Borusinski, A. T. Eberhardt, B. E. Hamre, G. H. Leum, S. D. MacDonald, J. E. Oppor, J. R. Pedersen, D. A. Peterson, J. G. Reyes, S. S. Sexton, E. B. Smith, T. D. Van Wechel, and D. I. Will

Only two tandem entries were required during this annual report period. The first entry, on May 19, 2015, was required due to steering instability of the beam emitted from the tandem together with arcing observed in accelerator column #2 on the low energy (LE) end of the accelerator. Additionally, both LE electrostatic quadrupole triplets and the XM2/YM2 steerer required dramatically different-from-normal values in order to transport beam through the tandem. Upon entry, it was determined that the resistor jumper between accelerating planes #16 and #17 on LE column #2 had fallen from position and was shorting the electrostatic hoops of planes #18 and #19. The result was arcing between planes #16 and #17. New resistors, jumpers, and jumper sockets were installed.

The second entry, on October 30, 2015, was needed to determine the cause of the high energy (HE) charging chain drive motor drawing at least 60 amps AC on phase 2 winding at startup, instead of the normal 45 amps AC, thus causing breaker MCP2 in the drive motors control panel to trip off. Initial attempts to solve the problem by rebuilding the HE charging chain drive motor 3-phase high voltage transient suppression device with new replacement SiC thyrite discs did not have any effect. The HE drive motor was replaced with an identical new motor and the problem was resolved. It is suspected that the phase 2 winding of the failed drive motor is shorted to the motor casing, shorted across itself, or shorted to another winding.

May 27, 2015, began the first use of SYLTHERM XLT heat transfer fluid as a replacement for freon 113 in the heat exchange cooling system for the duoplasmatron (DEIS), SpIS, and DECK chopper amplifiers. SYLTHERM XLT is a high-performance silicone polymer manufactured by Dow Corning Corporation and usable in the range of -100° C to 260° C. It has very high resistivity and is used as the coolant for currently manufactured duoplasmatron sources. Tests performed for 6 months at CENPA showed no adverse affects of SYLTHERM XLT or solutions of SYLTHERM XLT and freon 113 on magnet wire varnish, such as exists in windings of the duoplasmatron bottle magnet previously cooled by freon 113. SYLTHERM XLT alone is being added to the cooling system to maintain volume, forming solution with the remaining freon 113 as the two fluids are completely soluble in each other.

ACTIVITY SCHEDULED	**DAYS SCHEDULED**	**PERCENT of TIME**
Nuclear-physics research, accelerator	63	17.3
Development, maintenance, or crew training	30	8.2
Grand total	93	25.5

Table 8.2-1. Tandem Accelerator Operations April 1, 2015, to March 31, 2016.

During this annual reporting period from April 1, 2015, to March 31, 2016, the tandem pellet chains operated 760 hours, the sputter-ion-source (SpIS) operated 0 hours, and the duoplasmatron direct-extraction-ion source (DEIS) operated 947 hours. Additional statistics for accelerator operations are given in Table 8.2-1. Ion beams produced using the DEIS included 17.8 MeV ^{2}H for the ^{6}He experiment, 0.99 – 2.0 MeV ^{1}H for the Physics 576 class, and 15.2 MeV ^{2}H for visiting experimenters.

8.3 Laboratory computer systems

G. T. Holman

CENPA is a mixed shop of Windows 7, XP, Mac OS X and various Linux distributions. Windows 7 is installed on new systems but we are still running a few Windows XP systems for data acquisition. In previous years the IT focus was directed toward server consolidation, network security, process documentation and removal of redundant processes. We continue to utilize Xen virtualization to drive most web pages, Elogs, wiki, calendar, tracking, and document servers. The CENPA website and research group web pages are run on a virtual Debian server and utilize the Drupal web framework. The NPL mail server still provides NPL presence but all email is relayed to UW email hardware. This year we synchronized users on multiple Linux and Windows systems to UW active directory via a delegated organizational unit (OU), which removes the need to run a dedicated domain or LDAP server.

Two Dell 510 20-TB servers (Lisa and Marie) continue to offer user storage, print server capability, and improved backup policy. Linux, Windows and Mac workstations are backed up to the Lisa 20-TB raid farm from which they are written to LTO tape by the Physics Computer Center on a three-month backup retention plan. Lisa runs the Crash Plan Pro backup application which supports all operating systems and provides differential and encrypted backups. Whereas workstations rely on Crash Plan Pro for backups, all servers utilize rsync. Marie provides 20 TB for research, user, and shared group data.

The NPL Data Center (NPLDC) provides critical infrastructure supporting high-performance scientific-computing applications that cannot be efficiently executed on typical commodity server infrastructures (e.g., the Amazon EC2 Cloud). In previous years the space housed a single cluster that was treated as one computational resource, also known as Athena. Today, to meet the wide and highly specialized array of research requirements, the cluster has been separated into two specific cluster instances. The first cluster instance leverages Infiniband interconnects (classified as HPC clusters) and runs the latest open-source Rocks software[1], runs the cvmfs (Cern-VM file system) client, and Frontier local squid cache server. The second cluster, that primarily runs single-threaded applications (non-HPC clusters), uses Rocks version 5.4, and most notably runs COMSOL, root[2], and Geant. Both cluster instances use Torque/Maui via dedicated front ends.

Approximately one third of the rack space is dedicated to non-cluster hardware: scratch

[1]http://www.rocksclusters.org/
[2]http://root.cern.ch/

storage, SQL, elogs, web applications, CAD workstations, and backup storage. These servers constitute over 200 TB of raw disk space.

Our computing and analysis facility consists of:

- The NPL data center as a shared resource with Physics, the Institute for Nuclear Theory (INT), and the Astronomy department.
- A mix of Linux servers: Debian, Redhat, and Ubuntu distributions.
- One VMS/VAXstation for legacy computing.
- Macintosh systems for the SNO+, KATRIN, Majorana, and emiT groups.
- A VAXstation for the linac and vacuum systems control and display system.
- Various Windows XP desktop JAM systems (Java-based software for acquisition and analysis), plus two laptops for transport to other installations.
- A Shorewall Linux-based logical firewall to protect the bulk of CENPA's PCs and servers.
- We provide additional legacy co-location services for the INT and the Physics Nuclear Theory group in the form of one VMS Alphastation 500, which is not directly used by lab personnel.

8.4 Electronic equipment

D. A. Peterson and T. D. Van Wechel

The electronics shop is responsible for the design and construction of new laboratory electronic equipment as well as the maintenance and repair of existing CENPA electronics. Projects undertaken by the electronics shop in the past year include the following:

1. Prototyping $g-2$ 32-channel In Beam Monitoring System.
2. Designed and completed new 40 channel KATRIN Veto system.
3. Completed production of 1300 calorimeter boards for $g-2$.
4. Production of multiplexers and NIM modules for $g-2$ NMR.
5. Production of new KamLAND global trigger units.
6. Continued clean-room soldering of the new Majorana Vespel signal connectors.
7. Development of a new version of the TRIMS pre-amplifiers.
8. Developed a multi-channel buffer for TRIMS instrumentation.

8.5 CENPA instrument shops

T. H. Burritt, J. H. Elms, D. R. Hyde, S. Kimes, and H. Simons

The CENPA instrument shop has given support to CENPA and several UW research groups. Projects completed this year include:

1. Designed and fabricated veto components for KATRIN.
2. Tested assembly of veto into magnet bore.
3. Designed and fabricated fast-closing valve for KATRIN pre-spectrometer including swivel extension supports.
4. Designed and made modifications to TRIMS apparatus.
5. Provided design and fabrication expertise to ADMX project.
6. Designed new Hall probe support for Muon $g-2$ with hydraulic level adjustment ± 0.0005".
7. Fabricated parts for Project 8.
8. Fabricated stand and components for Muon $g-2$ SLAC test.
9. Repaired and fabricated Van De Graaff accelerator components.

The student shop produced several small projects in addition to providing machine-tool training and safety training for the faculty, staff, and students.

1. Built cylindrical tube for differential pumping between 2 vacuum chambers for ^{6}He.
2. Modified test cavity for an electromagnet for ADMX project.
3. Built frames for magnetic coils in order to generate magnetic fields to trap atoms for ^{6}He.
4. Designed, manufactured and installed support platform for translator used on $g-2$ experiment.
5. Modified Macor insulating tube that is used to produce discharges in helium gas for ^{6}He.

8.6 Building maintenance and upgrades

D. I. Will

After several years of large maintenance and upgrade projects funded by the University of Washington, this past year the University funded only one small project at CENPA. The UW Refrigeration Shop maintains cooling towers on campus. Because these cooling towers have been installed at various times by different contractors, the towers have had many different water treatment systems. The Refrigeration Shop obtained funding to replace many of these varied treatment systems with one standard type of water treatment system. This standardizes chemicals and machinery across much of campus. As part of this project our tower water treatment system has been standardized. The project is nearly done with the addition of a pump to circulate the tower water through the treatment loop. This should allow more timely maintenance of our cooling tower and its treatment system.

CENPA has funded two additional upgrade projects this year. In the past, entry door key recovery from students upon graduation and departure has been spotty. Therefore older key-operated exterior door locks have been replaced. The five most used doors have had Trilogy Alarm Locks installed. These locks allow three modes. Everyone on the CENPA telephone list has been issued a six-digit code for keypad entry. Codes can easily be created when a new person arrives and can be readily de-activated upon departure. Some personnel have also been issued radio-frequency identification (RFID) -style key-cards upon request. Finally, brass Medeco security keys are in the hands of several senior personnel for use in case of battery or other electronic failure in the Trilogy locks. The remaining four least-used doors are also in the process of upgrade to the same cut brass Medeco security key.

In 1963 the Van de Graaff Accelerator Building was erected and the tandem installed. The CENPA tandem Van de Graaff accelerator is contained in an American Society of Mechanical Engineers (ASME) Section VIII pressure vessel. It operates at 215 psig of 20% carbon dioxide with balance nitrogen gas to suppress sparking. To facilitate service, a gas-handling system was included to recover and store the insulating gas during tank-entry. This gas handling system includes a high-pressure compressor and 120 storage cylinders, each 20 feet tall and 9 inches diameter and rated 2200 psig working pressure. These steel cylinders were specially ordered by High Voltage Engineering Corporation to meet Interstate Commerce Commission (ICC) standards. In 1978 the Washington State chief boiler inspector required that these be recertified to ASME Section VIII standards for fixed, rather than over-the-road, cylinders (in part because these fixed cylinders could not be re-certified by hydro-test every five or ten years as ICC standards require). As a result, all 120 cylinders were checked for thickness via ultrasound top, middle and bottom that year. Based on those tests, the cylinders were de-rated to about 1635 psig working pressure, and an ASME-rated safety relief valve set for 1350 psig was installed on the output of the compressor to limit pressures well below the 1635 psig working pressure of the cylinders. As ICC-rated pressure vessels, the cylinders each had fusible plugs installed top and bottom in case of fire. This past year the boiler inspector has required us to replace the top fusible plugs with weather-protected burst disks to meet current Section VIII rules. The compressor safety relief is also being replaced and its exhaust plumbed to the building exterior. This work is nearing completion.

This year the University of Washington has begun replacing two aging dormitories, which loom above our laboratory, with five newer energy-efficient residence halls as part of a large North Campus Housing Project. This construction will impact some of our research activities. CENPA staff and faculty are working with the project manager and construction manager to mitigate these impacts.

Again, this year, numerous, smaller, routine and non-routine work orders were placed and the maintenance or repairs completed by the University of Washington's maintenance shops.

9 CENPA Personnel

9.1 Faculty

Eric G. Adelberger[1]	Professor Emeritus
Hans Bichsel[1]	Affiliate Professor
John G. Cramer[1]	Professor Emeritus
Jason Detwiler	Assistant Professor
Peter J. Doe	Research Professor
Sanshiro Enomoto	Research Associate Professor[2]
Svenja Fleischer[1,3]	Research Assistant Professor
Martin Fertl[4]	Acting Assistant Professor
Xavier Fléchard[5,6]	Affiliate Professor
Alejandro García	Professor
Jens H. Gundlach[1]	Professor
Blayne R. Heckel[1]	Professor; Chair
David W. Hertzog	Professor
C. D. Hoyle[1,7]	Affiliate Associate Professor
Peter Kammel	Research Professor
Jarek Kaspar[1]	Acting Assistant Professor
Woo-Joong Kim[8,9]	Affiliate Assistant Professor
Michael L. Miller[1,10]	Affiliate Research Assistant Professor
Diana Parno[1]	Acting Assistant Professor; Associate Director
R. G. Hamish Robertson	Professor; Director
Leslie J Rosenberg[1]	Professor
Gray Rybka[11]	Assistant Professor
Derek W. Storm[1]	Research Professor Emeritus
Nikolai R. Tolich[12]	Assistant Professor
Thomas A. Trainor[13,14]	Research Professor Emeritus
John F. Wilkerson[1,15]	Affiliate Professor

[1] Not supported by DOE CENPA grant.
[2] Commenced Research Associate Professor position in September 2015.
[3] Departed June 30, 2015.
[4] Postdoctoral position ended March 31, 2016. Faculty position commenced April 1, 2016.
[5] Professor from CEA/Saclay, on sabbatical at CENPA.
[6] Arrived April 1, 2016.
[7] Affiliated faculty, Humboldt State University, Arcata, CA.
[8] Assistant professor from Seattle University, on sabbatical at CENPA.
[9] Arrived September 1, 2015.
[10] Affiliated faculty.
[11] Commenced Assistant Professor position in September 2015.
[12] Departed June 15, 2015. Commenced lecturer position in September 2015.
[13] Retired December 2014.
[14] DOE supported through November 2014.
[15] Affiliated faculty, University of North Carolina, Chapel Hill, NC.

9.2 CENPA External Advisory Committee

Robert McKeown[1]	Jefferson Laboratory
Daniel McKinsey[1]	Yale University
Michael Ramsey-Musolf[1]	University of Massachusetts, Amherst

9.3 Postdoctoral Research Associates

Laura Bodine[2]
Clara Cuesta[3]
Mathieu Guigue[3,4]
Charles Hagedorn[5]
Rakshya Khatiwada[3,6]
Kim Siang Khaw[7]
Jared Kofron[8]
Arnaud Leredde[3,9]
Dmitry Lyapustin[3,8]
Ana Malagon[3]
Richard Ottens[3,10]
Daniel Salvat[11]
Matthew Sternberg[12]
Krishna Venkateswara[3]
Frederik Wauters[13]

9.4 Predoctoral Research Associates

Yelena Bagdasarova[3,9]
Christian Boutan[3]
Micah Buuck[3]
Nicole Crisosto[3,14]
Aaron Fienberg
Ali Ashtari Esfahani[3,15]
Nathan Froemming
Brent Graner
Julieta Gruszko[3]
Ian Guinn
Ran Hong[16]
Luke Kippenbrock
John G. Lee[3]
Jonathan Leon[3,17]
Erik Lentz[3,7]
Ting Lin[15]
Eric Machado[15]
Eric Martin

[1] CENPA External Advisory Committee formed January 2014.
[2] Graduated September 2015. Commenced postdoctoral position September 2015. Departed March 2016.
[3] Not supported by DOE CENPA grant.
[4] Arrived February 2016. Supported by Pacific Northwest National Laboratory.
[5] Graduated June 2015. Commenced postdoctoral position June 2015.
[6] Arrived July 2015.
[7] Arrived June 2015.
[8] Graduated March 2015. Commenced postdoctoral position March 2015. Departed May 2015.
[9] Supported by Argonne National Laboratory.
[10] Arrived April 2015.
[11] Arrived August 2015.
[12] Departed August 2015.
[13] Departed September 2015.
[14] Visiting graduate student from University of Florida. Arrived April 2015.
[15] Arrived September 2015.
[16] Graduated March 2016.
[17] On leave of absence beginning January 2016.

Ethan Muldoon[1]	Matthias Smith
Michael Murray	Kerkira Stockton[2,3]
Rachel Osofsky	William Terrano[2,3]
Rachel Ryan	Matthew Turner[2,4]
Erik Shaw[2]	Timothy Winchester[2]
James Sloan[2]	David Zumwalt[2,5]

9.5 University of Washington graduates taking research credit

Raahul Buch	Jason Detwiler, Advisor
Rachel Morris	Alejandro García, Advisor
Matthew Noakes	Nikolai Tolich, Advisor
Diana Thompson	Alejandro García, Advisor

9.6 University of Washington undergraduates taking research credit

Devon Carlton	Alejandro García, Advisor
Ciera Cox	Gray Rybka, Advisor
Justin Jachette Devault	Alejandro García, Advisor
Andrew Eberhardt	Jason Detwiler, Advisor
Nicholas Fong	Sanshiro Enomoto, Advisor
Xavier Frost	Gray Rybka, Advisor
Zhenghao Fu	Jason Detwiler, Advisor
Sean Gilligan	Alejandro García, Advisor
Cole Helling	Alejandro García, Advisor
Jacob Herr	Gray Rybka, Advisor
Andrew Hillman	Alejandro García, Advisor
Dustin Kasparek	Gray Rybka, Advisor
Jacob Johnson	Gray Rybka, Advisor
Matthew Kallander	R. G. Hamish Robertson, Advisor
Aobo Li	Jason Detwiler, Advisor
Benjamin Phillips	Gray Rybka, Advisor
Joshua Povik	Gray Rybka, Advisor
Wade Shaffer	Alejandro García, David W. Hertzog, Advisors
David Smith	Martin Fertl, Advisor
Jordan Stiebritz	Alejandro García, Advisor
Alex Thompson	Jason Detwiler, Advisor
Khang Ton	Jason Detwiler, Advisor
Maarten Van Genabeek	Alejandro García, Advisor
Alex Zderic	Jason Detwiler, Advisor

[1] Arrived June 2015.
[2] Not supported by DOE CENPA grant.
[3] Departed September 2015.
[4] On leave of absence beginning April 2015. Presently at Microsoft.
[5] Graduated June 2015.

9.7 NSF Research Experience for Undergraduates participants

Hector Carranze	California State University, Dominguez Hills	Gray Rybka, Leslie Rosenberg, Advisors
Savanna Starko	Washington and Jefferson College	Alejandro García, Advisor
Tyler Takaro	Cornell University	Jason Detwiler, Advisor

9.8 Visiting students taking research credit

Axel Müller[1]	Peter J. Doe, Advisor
Julian Becker[1]	Peter J. Doe, Advisor

9.9 Professional staff

John F. Amsbaugh	Research Engineer	Engineering, vacuum, cryogenics design
Tom H. Burritt	Shop Supervisor	Precision design, machining
Gary T. Holman	Systems Manager	Computer systems
Hannah LeTourneau	Research Engineer	Helium liquefier
Clifford Plesha[2]	Research Engineer	Helium liquefier
Duncan J. Prindle, Ph.D.	Research Scientist	Heavy ion, muon research
Eric B. Smith	Research Engineer	Accelerator, ion sources
H. Erik Swanson, Ph.D.	Research Physicist	Precision experimental equipment
Timothy D. Van Wechel	Research Engineer	Analog and digital electronics design
Douglas I. Will	Senior Engineer	Cryogenics, ion sources, buildings

9.10 Technical staff

James H. Elms	Instrument Maker
Nick Force[3]	Engineering Technician
David R. Hyde	Instrument Maker
Seth Kimes[4]	Engineering Technician
Joben Pedersen[5]	Research Engineer
David A. Peterson	Electronics Technician
Kiva Ramundo[6,7]	Research Aide
Michael Ross[5,6]	Laboratory Technician

9.11 Administrative staff

Victoria A. Clarkson	Administrator
Ida Boeckstiegel[8]	Fiscal Specialist

[1] Visiting student from Karlsruhe Institute of Technology.
[2] Departed December 2015.
[3] Arrived September 2015.
[4] Arrived July 2015.
[5] Arrived August 2015.
[6] Not supported by DOE CENPA grant.
[7] Arrived June 2015.
[8] Arrived January 2016.

9.12 Part-time staff and student helpers

Marilyn Barnard[1]
Michael Borusinski[2]
Brett Hamre
Cole Helling[3]
Michael Huehn[4]
Callum Lamb[5]
Grant Leum
Lourdes Maganis[6]
Sean MacDonald[7]
Joshua Oppor[8]
Ronaldo Ortez
Gary Plunkett[9]
Josh Reyes[2]
Samuel Sexton
Hendrik Simons
Megan Wachtendonk

9.13 Volunteers

Adam Cox[10]
Michael Kossin[11]

[1] Arrived August 2015. Departed January 2016.
[2] Arrived June 2015.
[3] Arrived March 2015. Departed August 2015.
[4] Arrived July 2015.
[5] Arrived June 2015. Departed September 2015.
[6] Arrived May 2015. Departed August 2015.
[7] Departed December 2015.
[8] Arrived September 2015.
[9] Arrived June 2015. Departed February 2016.
[10] Arrived November 2015.
[11] Arrived June 2015. Departed January 2016.

10 Publications

Publications and presentations with a date of 2015 or 2016 are included below. Some entries from early 2015 may therefore also appear in the 2015 Annual Report.

10.1 Published papers

1. "Precision Measurements of A_1^n in the Deep Inelastic Regime," D. S. Parno*, D. Flay, M. Posik, K. Allada, W. Armstrong, T. Averett, F. Benmokhtar, W. Bertozzi, A. Camsonne, M. Canan, G. D. Cates, C. Chen, J.-P. Chen, S. Choi, E. Chudakov, F. Cusanno, M. M. Dalton, W. Deconinck, C. W. de Jager, X. Deng, A. Deur, C. Dutta, L. El Fassi, G. B. Franklin, M. Friend, H. Gao, F. Garibaldi, S. Gilad, R. Gilman, O. Glamazdin, S. Golge, J. Gomez, L. Guo, O. Hansen, D. W. Higinbotham, T. Holmstrom, J. Huang, C. Hyde, H. F. Ibrahim, X. Jiang, G. Jin, J. Katich, A. Kelleher, A. Kolarkar, W. Korsch, G. Kumbartzki, J. J. LeRose, R. Lindgren, N. Liyanage, E. Long, A. Lukhanin, V. Mamyan, D. McNulty, Z.-E. Meziani, R. Michaels, M. Mihovilovič, B. Moffit, N. Muangma, S. Nanda, A. Narayan, V. Nelyubin, B. Norum, Nuruzzaman, Y. Oh, J. C. Peng, X. Qian, Y. Qiang, A. Rakhman, S. Riordan, A. Saha, B. Sawatzky, M. H. Shabestari, A. Shahinyan, S. Širca, P. Solvignon, R. Subedi, V. Sulkosky, W. A. Tobias, W. Troth, D. Wang, Y. Wang, B. Wojtsekhowski, X. Yan, H. Yao, Y. Ye, Z. Ye, L. Yuan, X. Zhan, Y. Zhang, Y.-W. Zhang, B. Zhao, X. Zheng, Phys. Lett. B **744**, 309 (2015); arXiv:1406.1207 [nucl-ex].

2. "Observation of Gravitationally Induced Vertical Striation of Polarized Ultracold Neutrons by Spin-Echo Spectroscopy," S. Afach, N. J.Ayres, G. Ban, G. Bison, K. Bodek, Z. Chowdhuri, M. Daum, M. Fertl, B. Franke, W. C. Griffith, Z. D. Grujić, P. G. Harris, W. Heil, V. Hélaine, M. Kasprzak, Y. Kermaidic, K. Kirch, P. Knowles, H.-C. Koch, S. Komposch, A. Kozela, J. Krempel, B. Lauss, T. Lefort, Y. Lemière, A. Mtchedlishvili, M. Musgrave, O. Naviliat-Cuncic, J. M. Pendlebury, F. M. Piegsa, G. Pignol, C. Plonka-Spehr, P. N. Prashanth, G. Quéméner, M. Rawlik, D. Rebreyend, D. Ries, S. Roccia, D. Rozpedzik, P. Schmidt-Wellenburg, N. Severijns, J. A. Thorne, A. Weis, E. Wursten, G. Wyszynski, J. Zejma, J. Zenner, and G. Zsigmond, Phys. Rev. Lett. **115**, 162502 (2015); arXiv:1506.00446 [physics.ins-det].

3. "Single-Electron Detection and Spectroscopy via Relativistic Cyclotron Radiation," D. M. Asner, R. F. Bradley, L. de Viveiros, P. J. Doe, J. L. Fernandes, M. Fertl*, E. C. Finn, J. A. Formaggio, D. Furse, A. M. Jones, J. N. Kofron*, B. H. LaRoque, M. Leber, E. L. McBride, M. L. Miller, P. Mohanmurthy, B. Monreal, N. S. Oblath, R. G. H. Robertson*, L. J Rosenberg, G. Rybka*, D. Rysewyk, M. G. Sternberg, J. R. Tedeschi, T. Thümmler, B. A. VanDevender, and N. L. Woods, Phys. Rev. Lett. **114**, 162501(2015); arXiv:1408.5362 [physics.ins-det].†

An * denotes a CENPA author who is the lead author of or major contributor to a publication.
A † denotes a publication describing work fully or partially supported by the DOE grant.

4. "Gravitational depolarization of ultracold neutrons: Comparison with data," S. Afach, N. J. Ayres, C. A. Baker, G. Ban, G. Bison, K. Bodek, M. Fertl, B. Franke, P. Geltenbort, K. Green, W. C. Griffith, M. van der Grinten, Z. D. Grujić, P. G. Harris, W. Heil, V. Hélaine, P. Iaydjiev, S. N. Ivanov, M. Kasprzak, Y. Kermaidic, K. Kirch, H.-C. Koch, S. Komposch, A. Kozela, J. Krempel, B. Lauss, T. Lefort, Y. Lemière, M. Musgrave, O. Naviliat-Cuncic, J. M. Pendlebury, F. M. Piegsa, G. Pignol, C. Plonka-Spehr, P. N. Prashanth, G. Quéméner, M. Rawlik, D. Rebreyend, D. Ries, S. Roccia, D. Rozpedzik, P. Schmidt-Wellenburg, N. Severijns, D. Shiers, J. A. Thorne, A. Weis, E. Wursten, J. Zejma, J. Zenner, and G. Zsigmond, Phys. Rev. D **92**, 052008 (2015); arXiv:1506.06563 [physics.ins-det].

5. "Experimental study of ultracold neutron production in pressurized superfluid helium," P. Schmidt-Wellenburg, J. Bossy, E. Farhi, M. Fertl, K. K. H. Leung, A. Rahli, T. Soldner, and O. Zimmer, Phys. Rev. C **92**, 024004 (2015); arXiv:1506.07785 [nucl-ex].

6. "Reduced Limit on the Permanent Electric Dipole Moment of ^{199}Hg," B. Graner*****, Y. Chen, E. G. Lindahl, and B. R. Heckel, Phys. Rev. Lett. **116**, 161601 (2016); arXiv:1601.04339.**†**

7. "Constraining interactions mediated by axion-like particles with ultracold neutrons," S. Afach, G. Ban, G. Bison, K. Bodek, M. Burghoff, M. Daum, M. Fertl, B. Franke, Z. D. Gruji, V. Hlaine, M. Kasprzak, Y. Kermadic, K. Kirch, P. Knowles, H.-C. Koch, S. Komposch, A. Kozela, J. Krempel, B. Lauss, T. Lefort, Y. Lemire, A. Mtchedlishvili, O. Naviliat-Cuncic, F. M. Piegsa, G. Pignol, P. N. Prashanth, G. Qumner, D. Rebreyend, D. Ries, S. Roccia, P. Schmidt-Wellenburg, A. Schnabel, N. Severijns, J. Voigt, A. Weis, G. Wyszynski, J. Zejma, J. Zenner and G. Zsigmond, Phys. Lett. B **745**, 58–63 (2015); arXiv:1412.3679 [hep-ex].

8. "Focal-plane detector system for the KATRIN experiment," J. F. Amsbaugh, J. Barrett, A. Beglarian, T. Bergmann, H. Bichsel, L. I. Bodine, J. Bonn, N. M. Boyd, T. H. Burritt, Z. Chaoui, S. Chilingaryan, T. J. Corona, P. J. Doe, J. A. Dunmore, S. Enomoto, J. Fischer, J. A. Formaggio, F. M. Fraenkle, D. Furse, H. Gemmeke, F. Glueck, F. Harms, G. C. Harper, J. Hartmann, M. A. Howe, A. Kaboth, J. Kelsey, M. Knauer, A. Kopmann, M. L. Leber, E. L. Martin, K. J. Middleman, A. W. Myers, N. S. Oblath, D. S. Parno*****, D. A. Peterson, L. Petzold, D. G. Phillips II, P. Renschler, R. G. H. Robertson, J. Schwarz, M. Steidl, D. Tcherniakhovski, T. Thuemmler, T. D. Van Wechel, B. A. VanDevender, S. Voecking, B. L. Wall, K. L. Wierman, J. F. Wilkerson, and S. Wuestling, Nucl. Inst. Meth. A **778**, 40-60 (2015); arXiv:1404.2925 [physics.ins-det].**†**

9. "Examination of the calorimetric spectrum to determine the neutrino mass in low-energy electron capture decay," R. G. H. Robertson*****, Phys. Rev. C **91**, 035504 (2015); arXiv:1411.2906 [nucl-th].**†**

An ***** denotes a CENPA author who is the lead author of or major contributor to a publication.
A **†** denotes a publication describing work fully or partially supported by the DOE grant.

10. "Current status of new SAGE project with ^{51}Cr neutrino source," V. Gavrin, B. Cleveland, S. Danshin, S. Elliott, V. Gorbachev, T. Ibragimova, A. Kalikhov, T. Knodel, Yu. Kozlova, Yu. Malyshkin, V. Matveev, I. Mirmov, J. Nico, R. G. H. Robertson, A. Shikhin, D. Sinclair, E. Veretenkin, J. Wilkerson; Phys. Part. Nucl. **46**, 131 (2015).

11. "Test of candidate light distributors for the muon $(g-2)$ laser calibration system," A. Anastasi, D. Babusci, F. Baffigi, G. Cantatore, D. Cauz, G. Corradi, S. Dabagov, G. D. Sciascio, R. D. Stefano, C. Ferrari, A. T. Fienberg, A. Fioretti, L. Fulgentini, C. Gabbanini, L. A. Gizzi, D. Hampai, D. W. Hertzog, M. Iacovacci, M. Karuza, J. Kaspar, P. Koester, L. Labate, S. Mastroianni, D. Moricciani, G. Pauletta, L. Santi, and G. Venanzoni. Nucl. Inst. Meth. A **788**, 43 (2015); arXiv:1504.00132 [physics.ins-det].**†**

12. "Current Status and Future Prospects of the SNO+ Experiment," S. Andringa, E. Arushanova, S. Asahi, M. Askins, D. J. Auty, A. R. Back, Z. Barnard, N. Barros, E. W. Beier, A. Bialek, S. D. Biller, E. Blucher, R. Bonventre, D. Braid, E. Caden, E. Callaghan, J. Caravaca, J. Carvalho, L. Cavalli, D. Chauhan, M. Chen, O. Chkvorets, K. Clark, B. Cleveland, I. T. Coulter, D. Cressy, X. Dai, C. Darrach, B. Davis-Purcell, R. Deen, M. M. Depatie, F. Descamps, F. Di Lodovico, N. Duhaime, F. Duncan, J. Dunger, E. Falk, N. Fatemighomi, R. Ford, P. Gorel, C. Grant, S. Grullon, E. Guillian, A. L. Hallin, D. Hallman, S. Hans, J. Hartnell, P. Harvey, M. Hedayatipour, W. J. Heintzelman, R. L. Helmer, B. Hreljac, J. Hu, T. Iida, C. M. Jackson, N. A. Jelley, C. Jillings, C. Jones, P. G. Jones, K. Kamdin, T. Kaptanoglu, J. Kaspar, P. Keener, P. Khaghani, L. Kippenbrock, J. R. Klein, R. Knapik, J. N. Kofron, L. L. Kormos, S. Korte, C. Kraus, C. B. Krauss, K. Labe, I. Lam, C. Lan, B. J. Land, S. Langrock, A. LaTorre, I. Lawson, G. M. Lefeuvre, E. J. Leming, J. Lidgard, X. Liu, Y. Liu, V. Lozza, S. Maguire, A. Maio, K. Majumdar, S. Manecki, J. Maneira, E. Marzec, A. Mastbaum, N. McCauley, A. B. McDonald, J. E. McMillan, P. Mekarski, C. Miller, Y. Mohan, E. Mony, M. J. Mottram, V. Novikov, H. M. OKeeffe, E. OSullivan, G. D. Orebi Gann, M. J. Parnell, S. J. M. Peeters, T. Pershing, Z. Petriw, G. Prior, J. C. Prouty, S. Quirk, A. Reichold, A. Robertson, J. Rose, R. Rosero, P. M. Rost, J. Rumleskie, M. A. Schumaker, M. H. Schwendener, D. Scislowski, J. Secrest, M. Seddighin, L. Segui, S. Seibert, T. Shantz, T. M. Shokair, L. Sibley, J. R. Sinclair, K. Singh, P. Skensved, A. Srensen, T. Sonley, R. Stainforth, M. Strait, M. I. Stringer, R. Svoboda, J. Tatar, L. Tian, N. Tolich, J. Tseng, H. W. C. Tseung, R. Van Berg, E. Vzquez-Juregui, C. Virtue, B. von Krosigk, J. M. G. Walker, M. Walker, O. Wasalski, J. Waterfield, R. F. White, J. R. Wilson, T. J. Winchester, A. Wright, M. Yeh, T. Zhao, and K. Zuber, Adv. High Energy Phys. **2016** 6194250 (2016); arXiv:1508.05759 [physics.ins-det].**†**

An ***** denotes a CENPA author who is the lead author of or major contributor to a publication.
A **†** denotes a publication describing work fully or partially supported by the DOE grant.

13. "Status of the MAJORANA DEMONSTRATOR: A search for neutrinoless double-beta decay," N. Abgrall, E. Aguayo, F. T. Avignone III, A. S. Barabash, F. E. Bertrand, V. Brudanin, M. Busch, M. Buuck, D. Byram, A. S. Caldwell, Y-D. Chan, C. D. Christofferson, C. Cuesta, J. A. Detwiler, Yu. Efremenko, H. Ejiri, S. R. Elliott, A. Galindo-Uribarri, G. K. Giovanetti, J. Goett, M. P. Green, J. Gruszko, I. S. Guinn, V. E. Guiseppe, R. Henning, E. W. Hoppe, S. Howard, M. A. Howe, B. R. Jasinski, K. J. Keeter, M. F. Kidd, S. I. Konovalov, R. T. Kouzes, B. D. LaFerriere, J. Leon, J. MacMullin, R. D. Martin, S. J. Meijer, S. Mertens, J. L. Orrell, C. O'Shaughnessy, N. R. Overman, A. W. P. Poon, D. C. Radford, J. Rager, K. Rielage, R. G. H. Robertson, E. Romero-Romero, C. Schmitt, B. Shanks, M. Shirchenko, N. Snyder, A. M. Suriano, D. Tedeschi, V. Timkin, J. E. Trimble, R. L. Varner, S. Vasilyev, K. Vetter, K. Vorren, B. R. White, J. F. Wilkerson, C. Wiseman, W. Xu, E. Yakushev, C.-H. Yu, V. Yumatov, Int. J. Mod. Phys. A **30**, 12 (2015).**†**

14. "Assessment of molecular effects on neutrino mass measurements from tritium beta decay," L. I. Bodine*****, D. S. Parno*****, and R. G. H. Robertson*****; Phys. Rev. C **91**, 035505; arXiv:1502.03497 [nucl-ex].**†**

15. "Observation of Gravitational Waves from a Binary Black Hole Merger," B. P. Abbott *et. al.* (LIGO Scientific Collaboration and Virgo Collaboration), Phys. Rev. Lett. **116** 061102 (2016). For full author list see http://journals.aps.org/prl/abstract/10.1103/PhysRevLett.116.061102.

16. "Short-range spin-dependent interactions of electrons: a probe for exotic pseudo-Goldstone bosons," W A. Terrano*****, E. G. Adelberger, J. G. Lee and B. R. Heckel, Phys. Rev. Lett. **115**, 201801 (2015); arXiv:1508.02463 [hep-ex].

17. "Studies of an array of PbF_2 Cherenkov crystals with large-area SiPM readout," A. T. Fienberg*****, L. P. Alonzi, A. Anastasi, R. Bjorkquist, D. Cauz, R. Fatemi, C. Ferrari, A. Fioretti, A. Frankenthal, C. Gabbanini, L. K. Gibbons, K. Giovanetti, S. D. Goadhouse, W. P. Gohn, T. P. Gorringe, D. W. Hertzog, M. Iacovacci, P. Kammel, J. Kaspar*****, B. Kiburg, L. Li, S. Mastroianni, G. Pauletta, D. A. Peterson, D. Počanić, M. W. Smith, D. A. Sweigart, V. Tishchenko, G. Venanzoni, T. D. Van Wechel, K. B. Wall, P. Winter, K. Yai, Nucl. Inst. Meth. A **783**, 12-21 (2015); arXiv:1412.5525 [physics.ins-det].**†**

18. "Low-frequency terrestrial tensor gravitational-wave detector," H. J. Paik, C. E. Griggs, M. V. Moody, K. Venkateswara, H. M. Lee, A. B. Nielsen, E. Majorana, and J. Harms, Classical Quant. Grav. **33**, 075003 (2016).

An ***** denotes a CENPA author who is the lead author of or major contributor to a publication.
A **†** denotes a publication describing work fully or partially supported by the DOE grant.

19. “Measurement of the Formation Rate of Muonic Hydrogen Molecules,” V. A. Andreev, T. I. Banks, R. M. Carey, T. A. Case, S. M. Clayton, K. M. Crowe, J. Deutsch, J. Egger, S. J. Freedman, V. A. Ganzha, T. Gorringe, F. E. Gray, D. W. Hertzog, M. Hildebrandt, P. Kammel*, B. Kiburg, S. Knaack*, P. A. Kravtsov, A. G. Krivshich, B. Lauss, K. R. Lynch, E. M. Maev, O. E. Maev, F. Mulhauser, C. Petitjean, G. E. Petrov, R. Prieels, G. N. Schapkin, G. G. Semenchuk, M. A. Soroka, V. Tishchenko, A. A. Vasilyev, A. A. Vorobyov, M. E. Vznuzdaev, and P. Winter*, Phys. Rev. C **91**, 055502 (2015); arXiv:1502.00913 [nucl-ex].†

20. “Cryogenic distillation facility for isotopic purification of protium and deuterium,” I. Alekseev, Ev. Arkhipov, S. Bondarenko, O. Fedorchenko, V. Ganzha, K. Ivshin, P. Kammel, P. Kravtsov, C. Petitjean, V. Trofimov, A. Vasilyev, T. Vasyanina, A. Vorobyov and M. Vznuzdaev. Rev. Sci. Instrum. **86**, 125102 (2015).†

21. “Low-energy precision tests of the standard model: a snapshot,” D. W. Hertzog*, Ann. Phys. **528** 115-122 (2016).†

22. “Precision Muon Physics,” T. P. Gorringe and D. W. Hertzog*, Prog. Part. Nucl. Phys. **84**, 73 (2015); arXiv:1506.01465 [hep-ex].†

23. “The Measurement of the Anomalous Magnetic Moment of the Muon at Fermilab,” I. Logashenko, J. Grange, P. Winter, R. M. Carey, E. Hazen, N. Kinnaird, J. P. Miller, J. Mott, B. L. Roberts, J. Crnkovic, W. M. Morse, H. Kamal Sayed, V. Tishchenko, V. P. Druzhinin, Y. M. Shatunov, R. Bjorkquist, A. Chapelain, N. Eggert, A. Frankenthal, L. Gibbons, S. Kim, A. Mikhailichenko, Y. Orlov, N. Rider, D. Rubin, D. Sweigart, D. Allspach, E. Barzi, B. Casey, M. E. Convery, B. Drendel, H. Freidsam, C. Johnstone, J. Johnstone, B. Kiburg, I. Kourbanis, A. L. Lyon, K. W. Merritt, J. P. Morgan, H. Nguyen, J.-F. Ostiguy, A. Para, C. C. Polly, M. Popovic, E. Ramberg, M. Rominsky, A. K. Soha, D. Still, T. Walton, C. Yoshikawa, K. Jungmann, C. J. G. Onderwater, P. Debevec, S. Leo, K. Pitts, C. Schlesier, A. Anastasi, D. Babusci, G. Corradi, D. Hampai, A. Palladino, G. Venanzoni, S. Dabagov, C. Ferrari, A. Fioretti, C. Gabbanini, R. D. Stefano, S. Marignetti, M. Iacovacci, S. Mastroianni, G. D. Sciascio, D. Moricciani, G. Cantatore, M. Karuza, K. Giovanetti, V. Baranov, V. Duginov, N. Khomutov, V. Krylov, N. Kuchinskiy, V. Volnykh, M. Gaisser, S. Haciomeroglu, Y. Kim, S. Lee, M. Lee, Y. K. Semertzidis, E. Won, R. Fatemi, W. Gohn, T. Gorringe, T. Bowcock, J. Carroll, B. King, S. Maxfield, A. Smith, T. Teubner, M. Whitley, M. Wormald, A. Wolski, S. Al-Kilani, R. Chislett, M. Lancaster, E. Motuk, T. Stuttard, M. Warren, D. Flay, D. Kawall, Z. Meadows, M. Syphers, D. Tarazona, T. Chupp, A. Tewlsey-Booth, B. Quinn, M. Eads, A. Epps, G. Luo, M. McEvoy, N. Pohlman, M. Shenk, A. de Gouvea, L. Welty-Rieger, H. Schellman, B. Abi, F. Azfar, S. Henry, F. Gray, C. Fu, X. Ji, L. Li, H. Yang, D. Stockinger, D. Cauz, G. Pauletta, L. Santi, S. Baessler, E. Frlez, D. Pocanic, L. P. Alonzi, M. Fertl, A. Fienberg, N. Froemming, A. Garcia, D. W. Hertzog*, P. Kammel, J. Kaspar, R. Osofsky, M. Smith, E. Swanson, and K. Lynch, J. Phys. Chem. Ref. Data **44** 031211 (2015).†

An * denotes a CENPA author who is the lead author of or major contributor to a publication.
A † denotes a publication describing work fully or partially supported by the DOE grant.

24. "High voltage testing for the MAJORANA DEMONSTRATOR," N. Abgrall, I. J. Arnquist, F. T. Avignone III, A. S. Barabash, F. E. Bertrand, A. W. Bradley, V. Brudanin, M. Busch, M. Buuck, D. Byram, A. S. Caldwell, Y-D Chan, C. D. Christofferson, P.-H. Chu, C. Cuesta*, J. A. Detwiler, P. J. Doe, C. Dunagan, Yu. Efremenko, H. Ejiri, S. R. Elliott, Z. Fu, A. Galindo-Uribarri, G. K. Giovanetti, J. Goett, M. P. Green, J. Gruszko, I. S. Guinn, V. E. Guiseppe, R. Henning, E. W. Hoppe, S. Howard, M. A. Howe, B. R. Jasinski, K. J. Keeter, M. F. Kidd, S. I. Konovalov, R. T. Kouzes, B. D. LaFerriere, J. Leon, A. Li, J. MacMullin, R. D. Martin, R. Massarczyk, S. J. Meijer, S. Mertens, J. L. Orrell, C. O'Shaughnessy, A. W. P. Poon, D. C. Radford, J. Rager, K. Rielage, R. G. H. Robertson, E. Romero-Romero, B. Shanks, M. Shirchenko, N. Snyder, A. M. Suriano, D. Tedeschi, A. Thompson, K. T. Ton, J. E. Trimble, R. L. Varner, S. Vasilyev, K. Vetter, K. Vorren, B. R. White, J. F. Wilkerson, C. Wiseman, W. Xu, E. Yakushev, C.-H. Yu, V. Yumatov, Nucl. Inst. Meth. A. **823**, 83 (2016); arXiv:1603.08483 [physics.ins-det].†

25. "A multilayer surface detector for ultracold neutrons," Zhehui Wang, M. A. Hoffbauer, C. L. Morris, N. B. Callahan, E. R. Adamek, J. D. Bacon, M. Blatnik, A. E. Brandt, L. J. Broussard, S. M. Clayton, C. Cude-Woods, S. Currie, E. B. Dees, X. Ding, J. Gao, F. E. Gray, K. P. Hickerson, A. T. Holley, T. M. Ito, C.-Y. Liu, M. Makela, J. C. Ramsey, R. W. Pattie Jr., D. J. Salvat*, D. W. Schmidt, R. K. Schulze, S. J. Seestrom, E. I. Sharapov, A. Sprow, Z. Tang, W. Wei, J. Wexler, T. L. Womack, A. R. Young, B. A. Zeck, Nucl. Inst. Meth. A **798** 30-35 (2015); arXiv:1503.03424 [physics.ins-det].

26. "Upscattering of ultracold neutrons from gases," S. J. Seestrom, E. R. Adamek, D. Barlow, L. J. Broussard, N. B. Callahan, S. M. Clayton, C. Cude-Woods, S. Currie, E. B. Dees, W. Fox, P. Geltenbort, K. P. Hickerson, A. T. Holley, C.-Y. Liu, M. Makela, J. Medina, D. J. Morley, C. L. Morris, J. Ramsey, A. Roberts, D. J. Salvat*, A. Saunders, E. I. Sharapov, S. K. L. Sjue, B. A. Slaughter, B. VornDick, P. L. Walstrom, Z. Wang, T. L. Womack, A. R. Young, and B. A. Zeck, Phys. Rev. C **92**, 065501 (2015).

27. "Charge multiplicity dependence of single-particle transverse-rapidity y_t and pseudorapidity densities and 2D angular correlations from 200 GeV p-p collisions," T. A. Trainor* and D. J. Prindle, Phys. Rev. D **93**, 014031 (2016); arXiv:1512.01599 [hep-ph].†

28. "Transverse-rapidity $\mathbf{y_t}$ dependence of the nonjet azimuth quadrupole from 62 and 200 GeV Au-Au collisions," D. T. Kettler, D. J. Prindle and T. A. Trainor*, Phys. Rev. C **91**, 064910 (2015); arXiv:1504.02741 [hep-ph].†

An * denotes a CENPA author who is the lead author of or major contributor to a publication.
A † denotes a publication describing work fully or partially supported by the DOE grant.

29. "Event-wise mean-pt fluctuations vs minimum-bias jets (minijets) at the LHC," T. A. Trainor*, Phys. Rev. C **92**, 024915 (2015); arXiv:1503.02197 [hep-ph].†

30. "Optimal modeling of 1D azimuth correlations in the context of Bayesian inference," M. B. De Kock, H. C. Eggers and T. A. Trainor*, Phys. Rev. C **92**, 034908 (2015); arXiv:1502.04475 [hep-ph].†

31. "Predicting minimum-bias trigger-associated dijet correlations in p-p collisions," T. A. Trainor*, J. Phys. G **42**, 085105 (2015); arXiv:1407.6422 [hep-ph].†

32. "Questioning tests of hadron production models based on minimum-bias distributions on transverse energy," T. A. Trainor*, Phys. Rev. C **91**, 044905 (2015); arXiv:1402.4071 [hep-ph].†

10.2 Invited talks at conferences

1. "QCD prediction of jet structure in 2D trigger-associated momentum correlations and implications for multiple parton interactions," T. A. Trainor*, EPJ Web Conf. **90** 02003, ISMD 2014 Bologna, (2015); arXiv:1412.0082 [hep-ph].†

2. "Status of the Majorana Demonstrator," C. Cuesta*, N. Abgrall, I. J. Arnquist, F. T. Avignone III, C. X. Baldenegro-Barrera, A. S. Barabash, F. E. Bertrand, A. W. Bradley, V. Brudanin, M. Busch, M. Buuck, D. Byram, A. S. Caldwell, Y-D. Chan, C. D. Christofferson, P.-H. Chu, J. A. Detwiler, Yu. Efremenko, H. Ejiri, S. R. Elliott, A. Galindo-Uribarri, T. Gillis, G. K. Giovanetti, J. Goett, M. P. Green, J. Gruszko, I. S. Guinn, V. E. Guiseppe, R. Henning, E. W. Hoppe, S. Howard, M. A. Howe, B. R. Jasinski, K. J. Keeter, M. F. Kidd, S. I. Konovalov, R. T. Kouzes, B. D. LaFerriere, J. Leon, J. MacMullin, R. D. Martin, R. Massarczyk, S. J. Meijer, S. Mertens, J. L. Orrell, C. O'Shaughnessy, A. W. P. Poon, D. C. Radford, J. Rager, K. Rielage, R. G. H. Robertson, E. Romero-Romero, B. Shanks, M. Shirchenko, N. Snyder, A. M. Suriano, D. Tedeschi, J. E. Trimble, R. L. Varner, S. Vasilyev, K. Vetter, K. Vorren, B. R. White, J. F. Wilkerson, C. Wiseman, W. Xu, E. Yakushev, C.-H. Yu, V. Yumatov, I. Zhitnikov, AIP Conf. Proc. **1686**, 020005 (2015).†

3. "Electron Detection for KATRIN," D. S. Parno*, Invited talk, Determination of the Absolute Electron (Anti)-Neutrino Mass Workshop, ECT*, Trento, Italy, April, 2016.†

4. "KATRIN: Seeking the Neutrino Mass," D. S. Parno*, Physics Division Seminar, Argonne National Laboratory, October, 2015.†

An * denotes a CENPA author who is the lead author of or major contributor to a publication.
A † denotes a publication describing work fully or partially supported by the DOE grant.

5. "Background Model for the MAJORANA DEMONSTRATOR," C. Cuesta*, N. Abgrall, E. Aguayo, F. T. Avignone III, A. S. Barabash, F. E. Bertrand, M. Boswell, V. Brudanin, M. Busch, D. Byram, A. S. Caldwell, Y-D. Chan, C. D. Christofferson, D. C. Combs, J. A. Detwiler, P. J. Doe, Yu. Efremenko, V. Egorov, H. Ejiri, S. R. Elliott, J. E. Fast, P. Finnerty, F. M. Fraenkle, A. Galindo-Uribarri, G. K. Giovanetti, J. Goett, M. P. Green, J. Gruszko, V. E. Guiseppe, K. Gusev, A. L. Hallin, R. Hazama, A. Hegai, R. Henning, E. W. Hoppe, S. Howard, M. A. Howe, K. J. Keeter, M. F. Kidd, O. Kochetov, S. I. Konovalov, R. T. Kouzes, B. D. LaFerriere, J. Leon, L. E. Leviner, J. C. Loach, J. MacMullin, A. MacMullin, R. D. Martin, S. J. Meijer, S. Mertens, M. Nomachi, J. L. Orrell, C. O'Shaughnessy, N. R. Overman, D. G. Phillips II, A. W. P. Poon, K. Pushkin, D. C. Radford, J. Rager, K. Rielage, R. G. H. Robertson, E. Romero-Romero, M. C. Ronquest, A. Schubert, B. Shanks, T. Shima, M. Shirchenko, K. J. Snavely, N. Snyder, A. M. Suriano, J. Thompson, V. Timkin, W. Tornow, J. E. Trimble, R. L. Varner, S. Vasilyev, K. Vetter, K. Vorren, B. R. White, J. F. Wilkerson, C. Wiseman, W. Xu, E. Yakushev, A. R. Young, C.-H. Yu, V. Yumatov, Phys. Procedia **61**, 821 (2015); arXiv:1405.1370 [physics.ins-det].†

6. "Next Generation Muon g-2 Experiment at FNAL," M. Fertl*, Invited talk, Symmetries in Subatomic Physics 2015, Victoria, BC, Canada.†

7. "Status of the ANAIS experiment," C. Cuesta* on behalf of the ANAIS Collaboration, Conference presentation, UCLA Dark Matter, Los Angeles, CA, February, 2016.

8. "Status of the MAJORANA DEMONSTRATOR," C. Cuesta* on behalf of the MAJORANA Collaboration, Conference presentation, Matrix Elements for the Double-beta-decay Experiments, Prague, Czech Republic, June, 2015.†

9. "Table-top tests of gravity, etc.," E. G. Adelberger*, Invited talk, Probing the Mystery: Theory and Experiment in Quantum Gravity, Galiano Island, Canada, August 17-20, 2015.

10. "Tests of Einstein's equivalence principle and Newton's inverse-square law," E. G. Adelberger*, Invited talk, A Century of General Relativity, Berlin, Germany, November 30 - December 2, 2015.

11. "The New Muon $g-2$ Experiment at Fermilab," D. W. Hertzog*, Invited talk, LFC15: physics prospects for Linear and other Future Colliders after the discovery of the Higgs, Trento, Italy, September 7-11, 2015.

12. "Next Generation Muon $(g-2)$," D. W. Hertzog*, Invited talk, FCCP2015: Flavour changing and conserving processes, Capri Island, Italy, September 10-12, 2015.

13. "The Muon $g-2$: probing the physics beyond the Standard Mode," K. S. Khaw*, Invited talk, UWPA Annual Research Symposium 2015, Seattle, WA, December 8, 2015.

An * denotes a CENPA author who is the lead author of or major contributor to a publication.
A † denotes a publication describing work fully or partially supported by the DOE grant.

14. "*p*-*p* minimum-bias dijets and nonjet quadrupole in relation to conjectured collectivity (flows) in high-energy nuclear collisions," T. A. Trainor*, XLV International Symposium on Multiparticle Dynamics, arXiv:1512.01857, October 4-9, 2015.†

15. "Progress toward measuring the mass of the neutrino," R. G. H. Robertson*, Colloquium, Washington State University Sept. 22, 2015.

16. "Double Beta Decay," M. J. Ramsey-Musolf and R. G. H. Robertson*, Invited briefing to Acting Director, Office of Science, DOE, April 22, 2015.†

10.3 Abstracts and contributed talks

1. "Low background signal readout electronics for the Majorana Demonstrator," I. S. Guinn*, N. Abgrall, F. T. Avignone III, A. S. Barabash, F. E. Bertrand, V. Brudanin, M. Busch, M. Buuck, D. Byram, A. S. Caldwell, Y-D. Chan, C. D. Christofferson, C. Cuesta, J. A. Detwiler, Yu. Efremenko, H. Ejiri, S. R. Elliott, A. Galindo-Uribarri, G. K. Giovanetti, J. Goett, M. P. Green, J. Gruszko, V. E. Guiseppe, R. Henning, E. W. Hoppe, S. Howard, M. A. Howe, B. R. Jasinksi, K. J. Keeter, M. F. Kidd, S. I. Konovalov, R. T. Kouzes, B. D. LaFerriere, J. Leon, J. MacMullin, R. D. Martin, S. J. Meijer, S. Mertens, J. L. Orrell, C. O'Shaughnessy, N. R. Overman, A. W. P. Poon, D. C. Radford, J. Rager, K. Rielage, R. G. H. Robertson, E. Romero-Romero, M. C. Ronquest, B. Shanks, M. Shirchenko, N. Snyder, A. M. Suriano, D. Tedeschi, J. E. Trimble, R. L. Varner, S. Vasilyev, K. Vetter, K. Vorren, B. R. White, J. F. Wilkerson, C. Wiseman, W. Xu, E. Yakushev, C.-H. Yu, V. Yumatov, J. Phys. Conf. Ser. **606**, 012009 (2015); arXiv:1502.03174 [physics.ins-det].†

2. "Low background signal readout electronics for the Majorana Demonstrator," I. S. Guinn*, N. Abgrall, I. J. Arnquist, F. T. Avignone III, C. X. Baldenegro-Barrera, A. S. Barabash, F. E. Bertrand, A. W. Bradley, V. Brudanin, M. Busch, M. Buuck, D. Byram, A. S. Caldwell, Y-D. Chan, C. D. Christofferson, C. Cuesta, J. A. Detwiler, Yu. Efremenko, H. Ejiri, S. R. Elliott, A. Galindo-Uribarri, T. Gillis, G. K. Giovanetti, J. Goett, M. P. Green, J. Gruszko, V. E. Guiseppe, R. Henning, E. W. Hoppe, S. Howard, M. A. Howe, B. R. Jasinski, K. J. Keeter, M. F. Kidd, S. I. Konovalov, R. T. Kouzes, B. D. LaFerriere, J. Leon, J. MacMullin, R. D. Martin, S. J. Meijer, S. Mertens, J. L. Orrell, C. O'Shaughnessy, A. W. P. Poon, D. C. Radford, J. Rager, K. Rielage, R. G. H. Robertson, E. Romero-Romero, B. Shanks, M. Shirchenko, N. Snyder, A. M. Suriano, D. Tedeschi, J. E. Trimble, R. L. Varner, S. Vasilyev, K. Vetter, K. Vorren, B. R. White, J. F. Wilkerson, C. Wiseman, W. Xu, E. Yakushev, C.-H. Yu, V. Yumatov, I. Zhitnikov, AIP Conf. Series **1672**, 030001 (2015); arXiv:1506.04279 [physics.ins-det].†

3. "Status of the KATRIN Neutrino-Mass Experiment," D. S. Parno*, APS April Meeting, Baltimore, MD, April, 2015.†

An * denotes a CENPA author who is the lead author of or major contributor to a publication.
A † denotes a publication describing work fully or partially supported by the DOE grant.

4. "Background analysis and status of the ANAIS dark matter project," J. Amaré, S. Cebrián, C. Cuesta*, E. García, C. Ginestra, M. Martínez, M. A. Oliván, Y. Ortigoza, A. Ortiz de Solórzano, C. Pobes, J. Puimedón, M. L. Sarsa, J. A. Villar, P. Villar, AIP Conf. Proc. **1672**, 10001 (2015); arXiv:1506.03210 [astro-ph.IM].

5. "Status of the MAJORANA DEMONSTRATOR," C. Cuesta*, N. Abgrall, E. Aguayo, F. T. Avignone III, A. S. Barabash, F. E. Bertrand, V. Brudanin, M. Busch, M. Buuck, D. Byram, A. S. Caldwell, Y-D. Chan, C. D. Christofferson, J. A. Detwiler, Yu. Efremenko, H. Ejiri, S. R. Elliott, A. Galindo-Uribarri, G. K. Giovanetti, J. Goett, M. P. Green, J. Gruszko, I. S. Guinn, V. E. Guiseppe, R. Henning, E. W. Hoppe, S. Howard, M. A. Howe, B. R. Jasinski, K. J. Keeter, M. F. Kidd, S. I. Konovalov, R. T. Kouzes, B. D. LaFerriere, J. Leon, J. MacMullin, R. D. Martin, S. J. Meijer, S. Mertens, J. L. Orrell, C. O'Shaughnessy, N. R. Overman, A. W. P. Poon, D. C. Radford, J. Rager, K. Rielage, R. G. H. Robertson, E. Romero-Romero, C. Schmitt, B. Shanks, M. Shirchenko, N. Snyder, A. M. Suriano, D. Tedeschi, V. Timkin, J. E. Trimble, R. L. Varner, S. Vasilyev, K. Vetter, K. Vorren, B. R. White, J. F. Wilkerson, C. Wiseman, W. Xu, E. Yakushev, C.-H. Yu, V. Yumatov, Nucl. Part. Phys. Proc. **265**, 70 (2015).†

6. "Analysis techniques for background rejection at the MAJORANA DEMONSTRATOR," C. Cuesta*, N. Abgrall, I. J. Arnquist, F. T. Avignone III, C. X. Baldenegro-Barrera, A. S. Barabash, F. E. Bertrand, A. W. Bradley, V. Brudanin, M. Busch, M. Buuck, D. Byram, A. S. Caldwell, Y-D. Chan, C. D. Christofferson, J. A. Detwiler, Yu. Efremenko, H. Ejiri, S. R. Elliott, A. Galindo-Uribarri, T. Gillis, G. K. Giovanetti, J. Goett, M. P. Green, J. Gruszko, I. S. Guinn, V. E. Guiseppe, R. Henning, E. W. Hoppe, S. Howard, M. A. Howe, B. R. Jasinski, K. J. Keeter, M. F. Kidd, S. I. Konovalov, R. T. Kouzes, B. D. LaFerriere, J. Leon, J. MacMullin, R. D. Martin, S. J. Meijer, S. Mertens, J. L. Orrell, C. O'Shaughnessy, A. W. P. Poon, D. C. Radford, J. Rager, K. Rielage, R. G. H. Robertson, E. Romero-Romero, B. Shanks, M. Shirchenko, N. Snyder, A. M. Suriano, D. Tedeschi, J. E. Trimble, R. L. Varner, S. Vasilyev, K. Vetter, K. Vorren, B. R. White, J. F. Wilkerson, C. Wiseman, W. Xu, E. Yakushev, C.-H. Yu, V. Yumatov, I. Zhitnikov, AIP Conf. Proc. **1672**, 140006 (2015); arXiv:1506.03202 [physics.ins-det].†

7. "Testing molecular effects for tritium-based neutrino mass measurements," D. S. Parno*, DNP Fall Meeting, Santa Fe, NM, October, 2015.†

8. "Analysis Techniques for the MAJORANA DEMONSTRATOR," M. Buuck* on behalf of the MAJORANA Collaboration, 43rd SLAC Summer Institute: The Universe of Neutrinos, Menlo Park, California, USA, August, 2015.†

9. "Background Reduction Strategies for the MAJORANA DEMONSTRATOR," I. S. Guinn* on behalf of the MAJORANA Collaboration, 43rd SLAC Summer Institute: The Universe of Neutrinos, Menlo Park, California, USA, August, 2015.†

An * denotes a CENPA author who is the lead author of or major contributor to a publication.
A † denotes a publication describing work fully or partially supported by the DOE grant.

10. "Status Update of the MAJORANA DEMONSTRATOR Neutrinoless Double Beta Decay Experiment," J. Gruszko*, N. Abgrall, I. J. Arnquist, F. T. Avignone III, A. S. Barabash, F. E. Bertrand, A. W. Bradley, V. Brudanin, M. Busch, M. Buuck, D. Byram, A. S. Caldwell, Y-D. Chan, C. D. Christofferson, P. Chu, C. Cuesta, J. A. Detwiler, C. Dunagan, Yu. Efremenko, H. Ejiri, S. R. Elliott, A. Galindo-Uribarri, T. Gillis, G. K. Giovanetti, J. Goett, M. P. Green, I. S. Guinn, V. E. Guiseppe, R. Henning, E. W. Hoppe, S. Howard, M. A. Howe, B. R. Jasinski, K. J. Keeter, M. F. Kidd, S. I. Konovalov, R. T. Kouzes, B. D. LaFerriere, J. Leon, J. MacMullin, R. D. Martin, R. Massarczyk, S. J. Meijer, S. Mertens, J. L. Orrell, C. O'Shaughnessy, A. W. P. Poon, D. C. Radford, J. Rager, K. Rielage, R. G. H. Robertson, E. Romero-Romero, B. Shanks, M. Shirchenko, N. Snyder, A. M. Suriano, D. Tedeschi, J. E. Trimble, R. L. Varner, S. Vasilyev, K. Vetter, K. Vorren, B. R. White, J. F. Wilkerson, C. Wiseman, W. Xu, E. Yakushev, C.-H. Yu, V. Yumatov, I. Zhitnikov, Proceedings, Meeting of the APS Division of Particles and Fields (DPF 2015), CNUM: C15-08-04, (2015); arXiv:1511.00395 [physics.ins-det].†

11. "Status Update of the MAJORANA DEMONSTRATOR Neutrinoless Double Beta Decay Experiment," J. Gruszko* on behalf of the MAJORANA Collaboration, APS Division of Particles and Fields Meeting at University of Michigan, Ann Arbor, MI, USA, August, 2015.†

12. "The Muon Capture Rate on the Deuteron in the MuSun Experiment," M. H. Murray*, APS April Meeting 2015, Baltimore, MD, April, 2015.†

13. "The MuSun Experiment: Calibration of Weak Reactions in the Two Nucleon System," R. A. Ryan*, 6th International Symposium on Symmetries in Subatomic Physics, Victoria, Canada, June, 2015.†

14. "Muon capture on the deuteron: the MuSun experiment," F. Wauters*, European Nuclear Physics Conference 2015, University of Groningen, Groningen, The Netherlands, September, 2015.†

10.4 Papers submitted or to be published

1. "A high-finesse Fabry-Perot cavity with a frequency-doubled green laser for precision Compton polarimetry at Jefferson Lab," A. Rakhman, M. Hafez, S. Nanda, F. Benmokhtar, A. Camsonne, G. Cates, M. Dalton, G. B. Franklin, M. Friend, R. Michaels, V. Nelyubin, D. S. Parno, K. Paschke, B. Quinn, P. A. Souder, W. A. Tobias, arXiv:1601.00251 [physics.ins-det]. Submitted to Nucl. Inst. Meth. A.

An * denotes a CENPA author who is the lead author of or major contributor to a publication.
A † denotes a publication describing work fully or partially supported by the DOE grant.

2. "Measurements of d_2^n and A_1^n: Probing the Neutron Spin Structure," D. Flay, M. Posik, D. S. Parno*, K. Allada, W. Armstrong, T. Averett, F. Benmokhtar, W. Bertozzi, A. Camsonne, M. Canan, G. D. Cates, C. Chen, J.-P. Chen, S. Choi, E. Chudakov, F. Cusanno, M. M. Dalton, W. Deconinck, C. W. de Jager, X. Deng, A. Deur, C. Dutta, L. El Fassi, G. B. Franklin, M. Friend, H. Gao, F. Garibaldi, S. Gilad, R. Gilman, O. Glamazdin, S. Golge, J. Gomez, L. Guo, O. Hansen, D. W. Higinbotham, T. Holmstrom, J. Huang, C. Hyde, H. F. Ibrahim, X. Jiang, G. Jin, J. Katich, A. Kelleher, A. Kolarkar, W. Korsch, G. Kumbartzki, J. J. LeRose, R. Lindgren, N. Liyanage, E. Long, A. Lukhanin, V. Mamyan, D. McNulty, Z.-E. Meziani, R. Michaels, M. Mihovilovič, B. Moffit, N. Muangma, S. Nanda, A. Narayan, V. Nelyubin, B. Norum, Nuruzzaman, Y. Oh, J. C. Peng, X. Qian, Y. Qiang, A. Rakhman, S. Riordan, A. Saha, B. Sawatzky, M. H. Shabestari, A. Shahinyan, S. Širca, P. Solvignon, R. Subedi, V. Sulkosky, W. A. Tobias, W. Troth, D. Wang, Y. Wang, B. Wojtsekhowski, X. Yan, H. Yao, Y. Ye, Z. Ye, L. Yuan, X. Zhan, Y. Zhang, Y.-W. Zhang, B. Zhao, X. Zheng, arXiv:1603.03612 [nucl-ex]. Submitted to Phys. Rev. D.

3. "The Majorana Demonstrator Radioassay Program," N. Abgrall, I. J. Arnquist, F. T. Avignone III, H. O. Back, A. S. Barabash, F. E. Bertrand, M. Boswell, A. W. Bradley, V. Brudanin, M. Busch, M. Buuck, D. Byram, A. S. Caldwell, Y-D. Chan, C. D. Christofferson, P.-H. Chu, C. Cuesta, J. A. Detwiler*, J. A. Dunmore, Yu. Efremenko, H. Ejiri, S. R. Elliott, P. Finnerty, A. Galindo-Uribarri, V. M. Gehman, T. Gilliss, G. K. Giovanetti, J. Goett, M. P. Green, J. Gruszko, I. S. Guinn, V. E. Guiseppe, R. Henning, E. W. Hoppe, S. Howard, M. A. Howe, B. R. Jasinski, R. A. Johnson, K. J. Keeter, M. F. Kidd, O. Kochetoi, S. I. Konovalov, R. T. Kouzes, B. D. LaFerriere, J. Leon, J. C. Loach, J. MacMullin, S. MacMullin, R. D. Martin, R. Massarczyk, S. Meijer, S. Mertens, M. L. Miller, J. L. Orrell, C. OShaughnessy, N. R. Overman, A. W. P. Poon, K. Pushkin, D. C. Radford, J. Rager, K. Rielage, R. G. H. Robertson, E. Romero-Romero, M. C. Ronquest, A. G. Schubert, B. Shanks, M. Shirchenko, K. J.Snavely, N. Snyder, D. Steele, A. M. Suriano, D. Tedeschi, J. E. Trimble, R. L. Varner, S. Vasilyev, K. Vetter, K. Vorren, B. R. White, J. F. Wilkerson, C. Wiseman, W. Xu, E. Yakushev, C.-H. Yu, V. Yumatov, I. Zhitnikov, arXiv:1601.03779. Submitted to Nucl. Inst. Meth. A.†

4. "Next Generation Muon g-2 Experiments," D. W. Hertzog*, (2015); arXiv:1512.00928 [hep-ex].†

5. "Charge-multiplicity and collision-energy dependence of $\mathbf{p_t}$ spectra from p-p collisions at the relativistic heavy-ion collider and large hadron collider," T. A. Trainor, arXiv:1603.01337.

An * denotes a CENPA author who is the lead author of or major contributor to a publication.
A † denotes a publication describing work fully or partially supported by the DOE grant.

6. “The Muon Flux Measurements at the Davis Campus of the Sanford Underground Research Facility with the MAJORANA DEMONSTRATOR Veto System,” N. Abgrall, E. Aguayo, F. T. Avignone III, A. S. Barabash, F. E. Bertrand, A. W. Bradley, V. Brudanin, M. Busch, M. Buuck, D. Byram, A. S. Caldwell, Y-D. Chan, C. D. Christofferson, P.-H. Chu, C. Cuesta, J. A. Detwiler, C. Dunagan, Yu. Efremenko, H. Ejiri, S. R. Elliott, A. Galindo-Uribarri, T. Gilliss, G. K. Giovanetti, J. Goett, M. P. Green, J. Gruszko, I. S. Guinn, V. E. Guiseppe, R. Henning, E. W. Hoppe, S. Howard, M. A. Howe, B. R. Jasinski, K. J. Keeter, M. F. Kidd, S. I. Konovalov, R. T. Kouzes, B. D. LaFerriere, J. Leon, A. M. Lopez, J. MacMullin, R. D. Martin, R. Massarczyk, S. J. Meijer, S. Mertens, J. L. Orrell, C. O’Shaughnessy, N. R. Overman, A. W. P. Poon, D. C. Radford, J. Rager, K. Rielage, R. G. H. Robertson, E. Romero-Romero, M. C. Ronquest, C. Schmitt, B. Shanks, M. Shirchenko, N. Snyder, A. M. Suriano, D. Tedeschi, J. E. Trimble, R. L. Varner, S. Vasilyev, K. Vetter, K. Vorren, B. R. White, J. F. Wilkerson, C. Wiseman, W. Xu, E. Yakushev, C.-H. Yu, V. Yumatov, I. Zhitnikov, arXiv:1602.07742. Submitted to Astroparticle Physics.†

7. “Commissioning of the vacuum system of the KATRIN Main Spectrometer,” M. Arenz, M. Babutzka, M. Bahr, J. P. Barrett, S. Bauer, M. Beck, A. Beglarian, J. Behrens, T. Bergmann, U. Besserer, J. Blümer, L. I. Bodine, K. Bokeloh, J. Bonn, B. Bornschein, L. Bornschein, S. Büsch, T. H. Burritt, S. Chilingaryan, T. J. Corona, L. De Viveiros, P. J. Doe, O. Dragoun, G. Drexlin, S. Dyba, S. Ebenhöch, K. Eitel, E. Ellinger, S. Enomoto, M. Erhard, D. Eversheim, M. Fedkevych, A. Felden, S. Fischer, J. A. Formaggio, F. Fränkle, D. Furse, M. Ghilea, W. Gil, F. Glück, A. Gonzalez Urena, S. Görhardt, S. Groh, S. Grohmann, R. Grössle, R. Gumbsheimer, M. Hackenjos, V. Hannen, F. Harms, N. Haussmann, F. Heizmann, K. Helbing, W. Herz, S. Hickford, D. Hilk, B. Hillen, T. Höhn, B. Holzapfel, M. Hötzel, M. A. Howe, A. Huber, A. Jansen, N. Kernert, L. Kippenbrock, M. Kleesiek, M. Klein, A. Kopmann, A. Kosmider, A. Kovalík, B. Krasch, M. Kraus, H. Krause, M. Krause, L. Kuckert, B. Kuffner, L. La Cascio, O. Lebeda, B. Leiber, J. Letnev, V. M. Lobashev, A. Lokhov, E. Malcherek, M. Mark, E. L. Martin, S. Mertens, S. Mirz, B. Monreal, K. Müller, M. Neuberger, H. Neumann, S. Niemes, M. Noe, N. S. Oblath, A. Off, H.-W. Ortjohann, A. Osipowicz, E. Otten, D. S. Parno, P. Plischke, A. W. P. Poon, M. Prall, F. Priester, P. C.-O. Ranitzsch, J. Reich, O. Rest, R. G. H. Robertson, M. Röllig, S. Rosendahl, S. Rupp, M. Rysavy, K. Schlösser, M. Schlösser, K. Schönung, M. Schrank, J. Schwarz, W. Seiler, H. Seitz-Moskaliuk, J. Sentkerestiova, A. Skasyrskaya, M. Slezak, A. Spalek, M. Steidl, N. Steinbrink, M. Sturm, M. Suesser, H. H. Telle, T. Thümmler, N. Titov, I. Tkachev, N. Trost, A. Unru, K. Valerius, D. Venos, R. Vianden, S. Vöcking, B. L. Wall, N. Wandkowsky, M. Weber, C. Weinheimer, C. Weiss, S. Welte, J. Wendel, K. L. Wierman, J. F. Wilkerson, D. Winzen, J. Wolf, S. Wüstling, M. Zacher, S. Zadoroghny, M. Zboril, arXiv:1603.01014 [physics.ins-det]. Submitted to J. Inst.†

An * denotes a CENPA author who is the lead author of or major contributor to a publication.
A † denotes a publication describing work fully or partially supported by the DOE grant.

8. "Neutron spectrometry with scintillating bolometers of LiF and sapphire," N. Coron, C. Cuesta, E. García, C. Ginestra, J. Gironnet, P. de Marcillac, M. Martínez, Y. Ortigoza, A. Ortiz de Solórzano, J. Puimedón, T. Redon, T. Rolón, M. L. Sarsa, L. Torres, J. A. Villar. submitted to IEEE Nuclear and Plasma Sciences Society.

10.5 Reports and white papers

1. "Muon Capture on the Deuteron: Progress Report 2015," P. Kammel*, C. Petitjean, and A. A. Vasilyev; PSI Experiment R-08-01 Experimental Report (2015).

2. "The COHERENT Experiment at the Spallation Neutron Source," D. Akimov, P. An, C. Awe, P. S. Barbeau, P. Barton, B. Becker, V. Below, A. Bolozdynya, A. Burenkov, B. Cabrera-Palmer, J. I. Collar, R. J. Cooper, R. L. Cooper, C. Cuesta, D. Dean, J. Detwiler, Y. Efremenko, S. R. Elliott, N. Fields, W. Fox, A. Galindo-Uribarri, M. Green, M. Heath, S. Hedges, N. Herman, D. Hornback, E. B. Iverson, L. Kaufman, S. R. Klein, A. Khromov, A. Konovalev, A. Kumpan, C. Leadbetter, L. Li, W. Lu, A. Melikyan, D. Markoff, K. Miller, M. Middlebrook, P. Mueller, P. Naumov, J. Newby, D. Parno, S. Penttila, G. Perumpilly, D. Radford, H. Ray, J. Raybern, D. Reyna, G. C. Rich, D. Rimal, D. Rudik, K. Scholberg, B. Scholz, W. M. Snow, A. Sosnovchev, A. Shakirov, S. Suchyta, B. Suh, R. Tayloe, R. T. Thornton, A. Tolstukhin, K. Vetter, C. H. Yu; arXiv:1509.08702 [physics.ins-det] (2015).

3. "Fundamental symmetries, neutrinos, neutrons, and astrophysics: a White Paper on progress and prospects," A. Aprahamian, F. Cavanna, V. Cianciolo, V. Cirigliano, A. de Gôuvéa, D. J. Dean, J. A. Detwiler, T. DeYoung, J. Engel, J. Erler, B. W. Filippone, N. Fomin, J. A. Formaggio, G. Fuller, D. Geesaman, W. C. Haxton, A. Hayes, D. W. Hertzog, P. Huber, T. M. Ito, J. R. Klein, Yu. G. Kolomensky, K. S. Kumar, C. Y. Liu, J. C. Long, R. G. Milner, J. G. Morfín, U. Mosel, G. D. Orebi Gann, J. L. Orrell, A. Piepke, B. Plaster, A. Pocar, A. W. P. Poon, D. C. Radford, M. J. Ramsey-Musolf, D. G. Richards, A. Ritz, R. G. H. Robertson, K. Scholberg, S. J. Seestrom, W. M. Snow, J. Singh, M. Thoennessen, S. E. Vigdor, D. L. Wark, J. F. Wilkerson, J. Wuertele, and A. Young; white paper on Fundamental Symmetries and Neutrinos in preparation for 2015 Nuclear Physics Long Range Plan.

4. "Reaching for the horizon: The 2015 long range plan for nuclear science," A. Aprahamian, R. Atcher, H. Caines, G. Cates, J. Cizewski, V. Cirigliano, D. Dean, A. Deshpande, R. Ent, R. Fatemi, B. Filippone, G. Fuller, C. Gagliardi, H. Gao, D. Geesaman, G. L. Greene, J. C. Hardy, K. M. Heeger, D. W. Hertzog, C. Howell, A. Hutton, P. Jacobs, X. Ji, R. Kruecken, S. Kuhn, K. Kumar, S. Lapi, M. Lisa, Z. Lu, A. Macchiavelli, N. C. R. Makins, P. Mantica, Z. Meziani, R. Milner, B. Mueller, J. Nagle, W. Nazarewicz, F. Nunes, E. Ormand, J. Piekarewicz, D. Radford, K. Rajagopal, M. J. Ramsey-Musolf, R. G. H. Robertson, T. Roser, P. Rossi, M. Savage, G. Savard, H. Schellman, K. Scholberg, J. Schukraft, M. Shepherd, J. Velkovska, R. Venugopalan, S. Vigdor, M. Wiescher, J. F. Wilkerson, and W. Zajc; Department of Energy and National Science Foundation Report [refereed], (2015).

An * denotes a CENPA author who is the lead author of or major contributor to a publication.
A † denotes a publication describing work fully or partially supported by the DOE grant.

10.6 Book publications

1. "The Quantum Handshake: Entanglement, Nonlocality and Transactions," John G. Cramer*, Publisher: Springer International Publishing (2016), ISBN 978-3-319-24642-0.

10.7 Ph.D. degrees granted

Developments for a measurement of the beta-nu correlation and determination of the recoil charge-state distribution in ^{6}He decay, Ran Hong (March, 2016).

Molecular Effects in Tritium Beta-Decay Neutrino-Mass Measurements, Laura I. Bodine (August, 2015).

A Sub-Millimeter Parallel-Plate Test of Gravity, Charles A. Hagedorn (August, 2015).

Torsion Pendulum Searches for Macroscopic Spin-Interactions as a Window on New Physics, William A. Terrano (August, 2015).

Towards a new search of tensor currents using trapped ^{6}He, David W. Zumwalt (June, (2015).

A novel method for electron energy measurement: Cyclotron Radiation Emission Spectroscopy, Jared N. Kofron (March, 2015).

An improved low-temperature RF-cavity search for dark-matter axions, Dmitry Lyapustin (March, 2015).

An * denotes a CENPA author who is the lead author of or major contributor to a publication.
A † denotes a publication describing work fully or partially supported by the DOE grant.